SYNTHESIS, CHARACTERIZATION AND PHOTOLUMINESCENCE PROPERTIES OF RARE EARTH IONS DOPED $BiPO_4$ PHOSPHORS

A THESIS SUBMITTED IN PARTIAL FULFILLMENT OF THE REQUIREMENTS FOR THE DEGREE OF DOCTOR OF PHILOSOPHY

NAOREM RAMANANDA SINGH

MZU REGISTRATION NO. : 1600780

Ph.D REGISTRATION NO.: MZU/Ph.D/1005 of 15.05.2017

DEPARTMENT OF CHEMISTRY
SCHOOL OF PHYSICAL SCIENCES

MARCH, 2021

SYNTHESIS, CHARACTERIZATION AND PHOTOLUMINESCENCE PROPERTIES OF RARE EARTH IONS DOPED $BiPO_4$ PHOSPHORS

BY

NAOREM RAMANANDA SINGH

Department of Chemistry

Under the supervision of

Dr. N. MOHONDAS SINGH

Submitted

In partial fulfillment of the requirement of the Degree of Doctor of Philosophy in Chemistry of Mizoram University, Aizawl.

MIZORAM UNIVERSITY

DEPARTMENT OF CHEMISTRY

MIZORAM : AIZAWL – 796004

Dr. N. Mohondas Singh

Associate professor

CERTIFICATE

This is to certify that the thesis entitled **"*Synthesis, Characterization and Photoluminescence Properties of Rare Earth Ions Doped $BiPO_4$ Phosphors*"** submitted to Mizoram University, Aizawl for the award of the degree of Doctor of Philosophy by ***Mr. Naorem Ramananda Singh*** **(Regd. No.: MZU/Ph. D./1005 of 15.05.2017)**, research scholar in the Department of Chemistry, is the record of original research work carried out under my supervision. He has been duly registered and the thesis presented is worthy of being considered for the award of the Ph.D. degree. This work has not been submitted elsewhere for any degree in any other Universities.

Date: (Dr. N. MOHONDAS SINGH)

Place: Supervisor

Phone: (0389) 2330860/2330832 Fax : (0389) 2330860 nmdas08@rediffmail.com

Declaration of the Candidate

Mizoram University

March, 2021

I, Naorem Ramananda Singh, hereby declare that the subject matter of this thesis is the record of work done by me, that the contents of this thesis did not form basis of the award of any previous degree to me or to do the best of my knowledge to anybody else, and that the thesis has not been submitted by me for any research degree in any other University/ Institute.

This is being submitted to the Mizoram University for the degree of Doctor of Philosophy in Chemistry.

(NAOREM RAMANANDA SINGH)

Candidate

(Prof. MUTHUKUMARAN R.)

Head

(Dr. N. MOHONDAS SINGH)

Supervisor

ACKNOWLEDGEMENT

First and foremost, I would like to express all my profound sense of gratitude to my honored supervisor Dr. Nongmaithem Mohondas Singh, Associate Professor, Department of Chemistry, School of Physical Science, Mizoram University, Aizawl for his constant inspiration at every stage of my research work. His serious involvement, thoughtfulness and patience helped me to complete my work in time. It was an invaluable experience to work under him and also gained a tremendous knowledge through his supervision. His guidance will remain unforgettable throughout my journey.

I would like to express my sincere thanks to Dr. L. Robindra Singh, Assistant Professor, Department of Nanotechnology, NEHU for providing me PL facility. His suggestions and advices were lots to me.

I am very thankful to Dr. Naorem Premjit Singh, Assistant Professor, A.R.S.D College, Delhi for his persistent support, guidance and invaluable helps throughout my research journey.

My sincere thanks also goes to Prof. Diwakar Tiwari, Dean of School of Physical Science, Prof. Muthukumuran R, HOD Department of Chemistry and other faculty members Dr. Zodinpuia Pachuau, Dr. Ved Prakash Singh, and Dr. Bimolini Devi, Department of Chemistry, Mizoram University, for their kind support and continue to motivate during the course of my research work.

I am very thankful to my parents, (L) Naorem Shyamchandra Singh and Naorem Chandrajini Devi, my uncle Naorem Lukhoi Singh and my brothers and sisters for their endless love, support, care etc. during my academic career.

I also would like to thank Mr. Brojendro Singh Shagolsem, Senior Laboratory Technician, Department of Chemistry, MZU and other non-teaching staffs for their help and co-operation during my research work.

I am very thankful to Dr. Nurpen Meitei Thangjam, Aosanen Ozukum, Yaongam Ramsan, Gabriel Lalchandama, Sarikokba Jamir, Senjrang Momin and MSA for their physical and moral supports.

I am very thankful to Mr. Wangkhem Paikhomba Singh, Research Scholar (Chemistry) NEHU, Mr. Ningthoujam Premananda Singh, Research Scholar (Chemistry) Manipur University, Dilliraj Upadhaya Research Scholar (Physics) NIT Nagaland and my fellow labmates Dr. Olivia Lalmuanzuali, Mr. Naorem Herojit Singh, Mr. Jogat Gogoi and all the Research Scholars in the Department of Chemistry, Mizoram University, for their co-operations and helps.

Lastly I would like to thank Almighty God, without his grace, none of this would be possible.

Date:

Place:

(NAOREM RAMANANDA SINGH)

TABLE OF CONTENTS

CONTENTS

LISTS OF TABLES

LISTS OF FIGURES

Lists of Figures (continued) **Page**

Lists of Figures (continued) **Page**

Lists of Figures (continued) **Page**

Lists of Figures (continued) **Page**

ABBREVIATIONS

AFM	Atomic Force Microscope
CCD	Charged Coupled Device
CCT	Color co-relation temperature
CIE	Commission International de L'Eclairage
CRI	Color Rendering Index
CTAB	Cetyl trimethylammonium bromide
DEG	Diethylene glycol
EDAX	Energy Dispersive X-Ray Analysis
FESEM	Field Emission Scanning Electron Microscope
FTIR	Fourier Transform Infrared Spectroscopy
FWHM	Full Width at Half Maximum
HP	Hexagonal Phase
HRTEM	High Resolution Transmission Electron Microscope
HTMP	High Temperature Monoclinic Phase
ICDD	International Centre for Diffraction Data
JCPDS	Joint Committee on Powder Diffraction Standards
kV	Kilo volts
LCD	Liquid Crystal Display
LED	Light Emitting Diode
LTMP	Low Temperature Monoclinic Phase
MB	Methylene Blue
MRI	Magnetic Resonance Imaging
NIR	Near Infrared
NMR	Nuclear Magnetic Resonance
OLED	Organic Light Emitting Diode
PL	Photoluminescence
PLE	Photoluminescence Excitation
SAED	Selected Area Electron Diffraction
SEM	Scanning Electron Microscope
TEM	Transmission Electron Microscope

TVs	Televisions
UC	Upconversion
UV	Ultraviolet
wLED	White Light Emitting Diode
XRD	X-Ray Diffraction

CHAPTER-1

GENERAL INTRODUCTION

CHAPTER-2

INSTRUMENTATION

CHAPTER-3

SYNTHESIS, CHARACTERIZATION, PHOTOLUMINESCENCE AND PHOTOCATALYTIC STUDIES OF $BiPO_4:Ce^{3+}$

CHAPTER-4

PHOTOLUMINESCENCE PROPERTIES OF Tb^{3+} DOPED $BiPO_4$ NANOPHOSPHOR SYNTHESIZED BY CO-PRECIPITATION METHOD USING ETHYLENE GLYCOL

CHAPTER-5

SYNTHESIS, CHARACTERIZATION AND PHOTOLUMINESCENCE PROPERTIES OF Eu^{3+} IONS DOPED $BiPO_4$ NANOPHOSPHORS

CHAPTER-6

ROOM TEMPERATURE SIMPLE PRECIPITATION METHOD FOR THE PREPARATION OF Sm^{3+} ION DOPED $BiPO_4$ AND EFFECT OF ANNEALING TEMPERATURES ON THEIR PHOTOLUMINESCENCE PROPERTY

SUMMARY AND CONCLUSION

Chapter 1

General Introduction

1.1 Introduction to Lanthanides

The elements in which the atomic number starting from 57 i.e. lanthanum upto the element with atomic number 71 (Lutetium) are collectively known as lanthanides. These elements are also called f-block elements due to their gradual filling of electrons in the antepenultimate shell of f-orbital except lanthanum. The lanthanide series elements have almost similar physical and chemical properties. Lanthanide ions are showing +3 oxidation states, and their stability is explained by analysis of ionization energies. The ionization energies of lanthanides are given in figure 1.1. Even if +3 oxidation state of lanthanides ions are stable, +2 oxidation state of Samarium, Europium and ytterbium are also relatively stable due to their high value of the third ionization energy compared to the rest of the lanthanides. Cerium has the lowest ionization energy compared to the rest of the lanthanide and it also can adopt +4 oxidation state. These can be explained by using their electronic structure. Lanthanides generally show $[Xe]4f^n5d^{0-1}6s^2$ (n=1-14) electronic configuration but Ce, Gd, Lu show $[Xe]4f^n5d^16s^2$ to keep the electron count favorable in f-orbital. The electrons in d and s orbitals ionize first as they are farther from the nucleus than 4f orbital. Certain lanthanides favor to show +2 and +4 oxidation states due to the relative stability of empty and half-filled orbitals, Ce, while removing the 4 electrons, the electronic configuration becomes the electronic configuration of Xenon which is very stable. Eu^{2+}, removing the third electron disturb its half-filled orbital, and hence it is very difficult to remove electrons. The same thing happened in case of Yb^{2+}, removing the third electron results in the distortion of fully filled f orbital which is energetically unfavorable [Aspinall, (2001); King, (2008)]. The 4f orbitals of lanthanides are being shielded by 5s and 5p orbitals. This makes them very interesting to study the chemical and spectroscopic properties of their ions.

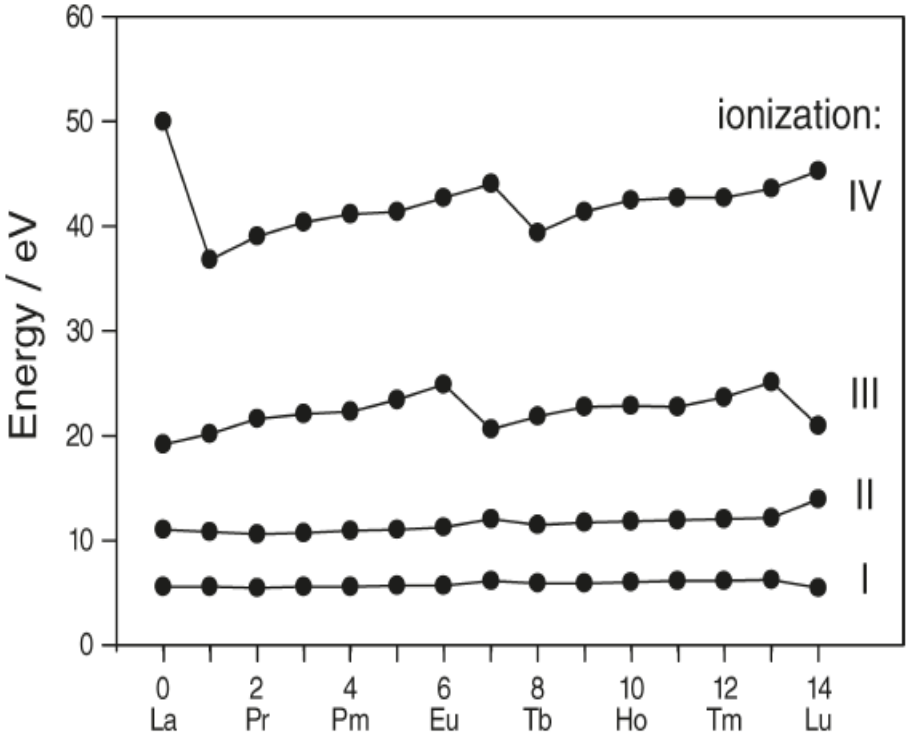

Figure 1.1 The ionization energies of different lanthanides.

The 6s and 5d orbitals are more attracted towards the nucleus as the atomic number increases due to less shielding of 4f orbitals resulting in higher charge density and lower ionic radius. The ionic radii of lanthanide elements decrease from left to right along the period. Consequently, the size are smaller than expected ionic radii. This decreased in ionic radii of lanthanide series elements are known as lanthanide contraction [Cotton, (2006)]. Lanthanide contraction happens due to less shielding of the nuclear charge by 4f electrons as moving from left to right and the electrons in the 6s orbitals are attracted towards the nucleus making the size smaller. Lanthanide ions are hard lewis acid, hence they prefer to make bonds with the atoms having an electron-donating property like O, N, etc. Lanthanides naturally form ionic complexes. They have a good tendency to form oxide. So, they prefer to bond with water than other ligands. The oxides are readily formed by thermal decomposition of co-ordination compound,

and further carbonates and hydroxides can be formed by reacting with carbondioxide and water, respectively [Rizkalla and Choppin, (1994)].

As lanthanide ions have ionic character, they exhibited weak stereo chemical preferences and labile co-ordination sphere enabling them to show variable co-ordination numbers and geometries. In solid form, lanthanide ions normally show co-ordination geometries like dodecahedral, anti-prismatic, bicapped dodecahedral, tricapped trigonal prismatic etc., but in the case of solution, it is very difficult to predict the co-ordination geometries of these lanthanide ions [Bünzli and Tang, (1995)].

1.2 Lanthanide Spectroscopy

Becquerel found sharp peaks for the first time while performing lanthanide ions absorption measurements in 1906 [Becquerel, (1906)]. Later on, Bethe, Kramers and Becquerel proposed that the sharp peaks may be due to f-f transition [Bethe, (1930); Kramers, (1930); Becquerel, (1929)]. As the 4f orbitals are well shielded by 5s and 5p orbitals, the f orbitals electron do not take part in chemical bonding, which results in the lanthanide ion to exhibit sharp peaks. Every lanthanide ion exhibited its characteristic absorption and emission spectra and they enable to emit in near UV, visible, NIR regions of the electromagnetic spectrum. Laporte selection rule says that the state of opposite parity is responsible for the generation of spectra associated with electric dipole transition. In case of non-centrosymmetric system, the electric dipole transitions must be induced by the mixture of opposite parity configurations and charge-transfer states [Vleck, (1937)]. Magnetic dipole transitions are allowed in the case of lanthanide ions, and their intensities do not depend on the surrounding environment. Ligand fields are responsible for the production of electric dipole transition in lanthanide ions and the strength of these transitions are strongly sensitive towards the surrounding environment. Hence, the intensities of their spectra highly depend on the ligand characteristics. The selection rules for f-f transitions of lanthanides are given below:

Table 1.1: Selection rules for lanthanide ions transitions. (S=total spin angular momentum; L=total atomic orbital angular momentum and J=total angular momentum)

Electric dipole transitions	Magnetic dipole transitions
$\Delta S = 0$	$\Delta S = 0$
$\Delta L \leq 6$	$\Delta L = 0$
$\Delta J \leq 6$; $\Delta J = 2,4,6$	$\Delta J = 0, \pm 1$; $0 \leftrightarrow 0$ = forbidden

The transitions (electric and magnetic dipole transitions) of lanthanide ions are very weak as they are forbidden transitions that are distinguished by narrow and sharp emission peaks with a long lifetime (milliseconds). Due to forbidden transitions of lanthanide ions, the direct excitation of the electron is very difficult, but this difficulty can be overcome using organic chromophores having a large absorption cross-section [Malba, (2013)]. The charge transfer process from organic chromophores to lanthanide ions can be understood using the Antenna effect. Lanthanide ions also form complexes with organic ligands like pyridines, calixarenes, polyaminopolycarboxylic acid etc. Ligands with appropriate photophysical properties can be used to design lanthanide ions to get highly luminescent lanthanide complexes. Some of the lanthanide ions which emit light in the visible regions are Eu^{3+}, Tb^{3+}, Sm^{3+}, Tm^{3+} etc. [Malba, (2013)].

1.3 Applications of Lanthanides

Lanthanide ions are very important in this modern era as they are having number of applications. These applications include catalysis, batteries, permanent magnets, optics etc. [Cotton, (1991); Digonet, (1993)]. Moreover, their luminescence property is responsible for making them applicable in the field of magnetic resonance imaging (MRI), metallurgy, medical diagnostics, nuclear magnetic resonance (NMR), imaging, sensors, high-temperature superconductors, magnetoptical discs, rechargeable Nickel-metal batteries etc. [Bunzli, (2006)]. Lanthanide ions are used as one of the important material in making positive pole of batteries which is almost 26% by weight of the total

weight [Xia *et al.*, (2018)]. In terms of consumable products, they are also used in TVs, computer hard drives, plasma, LCD screens etc. Lanthanides are used in motors and making generators of hybrid cars. They are also used in fuel injectors, airbags, seat belt sensors etc. [Binnemans *et al*., (2013); Curtis, (2010); Tanaka *et al*., (2013)]. Lanthanides are used in large quantities (2 tons) in constructing wind turbines which are almost 70% more efficient than the standard one; they are used as a catalyst that increases not only gasoline production by 5% but also the capacity of refinery equipment by 30% [Kołodyńska and Hubicki (2012)]. The optical property of lanthanide plays a big role when techniques are established to separate the lanthanide ions into their purest forms. Their optical applications have been increasing over the last few years. For example, Eu^{3+} is used to make cathode ray tubes required for computer and laser amplifiers, Er^{3+} is used to enhance the optical signals. Those lanthanide ions which are emitted in the NIR region of the spectrum are beneficial in laser designing and communication devices [Stouwdam *et al*., (2003)]. In the last few years, lanthanides doped inorganic phosphors are becoming very interesting due to their applications in fluorescent lamps, plasma display panels, solid-state lasers, watches, luminescence markers etc. [Wang and Gao (2006); Neeraj *et. al*. (2004); Riwotzki *et. al*. (2000); Nazarov *et. al*. (2004); Singh *et. al*. (2010)].

1.4 Luminescence

The German physicist namely Wiedemann used the word Lumin which is a Latin word and also the origin of the word Luminescence in 1888. In Latin, the term Lumin means light [Bernard and Mario, (2011)]. The phenomenon involving absorption and emission of light from excited atoms or molecules, not from black body radiation is termed as Luminescence and the materials which cause luminescence are referred to as phosphors. Phosphors emit light after they have been exposed to light. The term phosphor was coined by an Italian alchemist named Vincentinus Casciarolo in the 17^{th} century. He found a stone and heated it with the intention to convert it into noble gas. Instead of converting it into a gas, he discovered a material that emits light in the dark

after exposure to sunlight [Murthy and Virk, (2014)]. There are two types of phosphors namely inorganic and organic phosphors. Generally, organic phosphors don't have specific emission centres. Inorganic solid phosphors consist of host lattice and generally, they are insulators or semiconductors. The emission centres in inorganic phosphors take place according to the doping impurity ion [Singh, (2018)]. These impurity ions are also known as activator ions. These activator ions may be transition metal ions, lanthanide ions or any other impurity ions.

In the process of luminescence, an energy source is responsible for pumping up an electron from its ground state to an excited state after absorbing its required energy. Then, the excited electron returns to its initial ground state by emitting energy radiatively in the form of light, generally in the visible region. According to this mechanism, it can be assumed that every ion or material can show luminescence. However, this assumption is not correct because there are lots of non-radiative transitions. Hence, two types of radiations are observed when an electron returns from its excited state to its ground state. Generally, non-radiative transitions occur due to multiphonon relaxation. In this process, energy transfer occurs between similar ions and different ions or releases heat to the lattice. Schematic representation of excitation and emissions (radiatively and non-radiatively) of an atom R is showing below in the diagram.

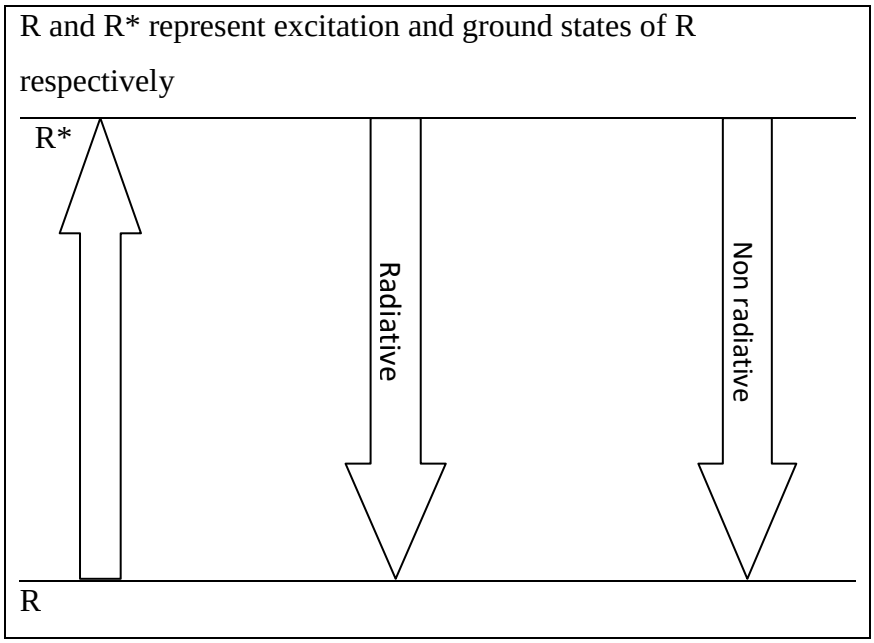

Figure 1.2: Scheme showing excitation, radiative and non-radiative emissions of R.

In inorganic phosphors, the energy required for the material to excite is absorbed by the host lattice or by the doped impurity ions intentionally. In most cases, emission takes place due to impurity ions that generate desired emission. These impurity ions are also known as activators. When the activator ions show a very weak absorption, a second impurity (sensitizer) can be used to increase the luminescence efficiency. In this case, the sensitizer is responsible for the absorption of the required energy. Subsequently, that energy is further transferred to the activator, which results in radiative emission [Blasse and Grabmaier, (1994)]. In this particular process, energy transfer takes place through phosphors. Most frequently, several impurity ions were used to adjust the required emission keeping the host lattice unchanged. Lanthanide ions had been used as impurity ions as their emission spectra are hardly disturbed by their

chemical environment. Figure 1.3 represents the schematic diagram showing the basic mechanism involved in luminescent centres.

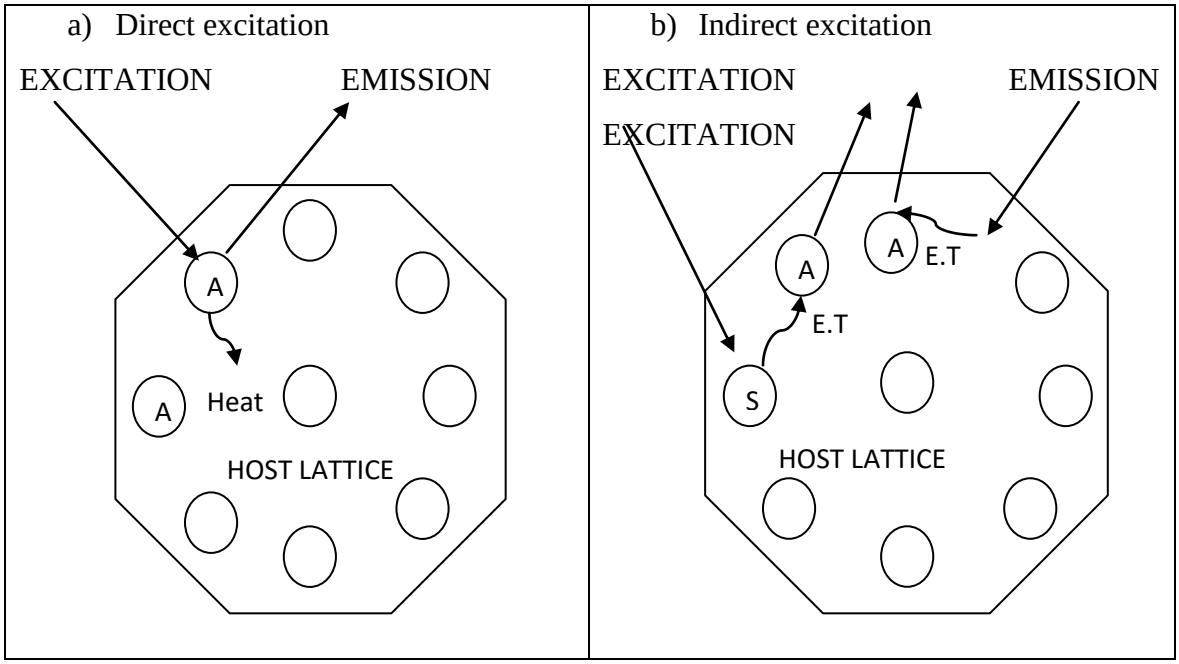

Figure 1.3: Schematic representation of a) Direct excitation of activator ion b) Indirect excitation of activator ions through energy transfer from sensitizer or host lattice. (E.T means Energy transfer).

Depending on the excitation energy source, luminescence can also be classified into several types. Some of them are given below:

Types of luminescence	Energy source
Chemiluminescence	Chemical reaction
Bioluminescence	Biochemical reactions in a living organism
Electrochemiluminescence	Electrochemical reaction
Crystalloluminescence	Energy produced during crystallization

Electroluminescence	Electric current
Cathodoluminescence	Energetic electron
Photoluminescence	Photon
Thermoluminescence	Heat
Radioluminescence	Bombarded by ionization radiation

In case of photoluminescence, the energy which is needed for the molecule to excite is given by photon. The emission of the absorbed light takes place with characteristic time (t_c) which allows luminescence to be classified into two types based on the duration of emission. The two types of luminescence are

a) Fluorescence where $t_c<10^{-8}$s (Temperature independent process), and
b) Phosphorescence where $t_c> 10^{-8}$s (Temperature-dependent process).

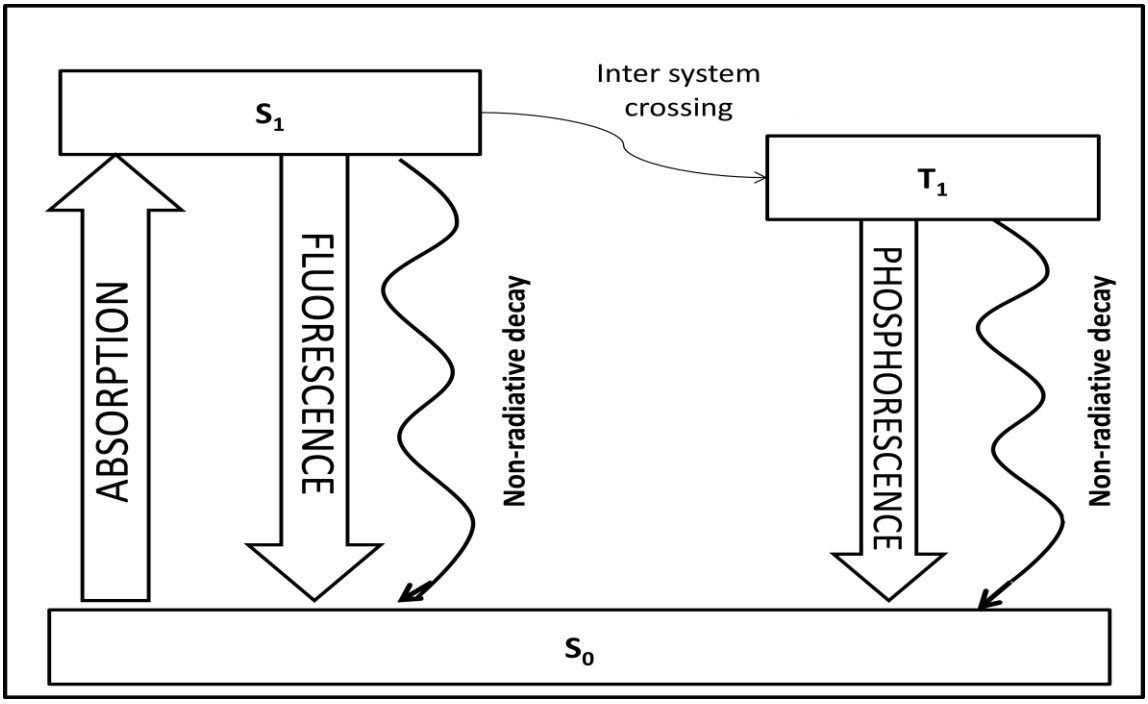

Figure 1.4: Schematic diagram showing the mechanism of Fluorescence and Phosphorescence.

The above diagram shows the schematic mechanism of fluorescence and phosphorescence. Fluorescence light is generated directly from the excited singlet state without changing its spin state and normally exhibited a shorter time even if the material has long-live fluorescence. The fluorescence light vanishes just after the excitation source is pulled out [Bernard and Mario, (2011)]. Whereas, in photoluminescence, the exciting material in the singlet state is again passed through an intermediate, i.e. from excited singlet state to excited triplet state by changing its spin state. Generally, in photoluminescence, the fluorescence light has a long lifetime period. It persevered its luminescence even after the excitation source is removed and it may be continued upto hours or even days in some particular materials [Francis, (1929)]. The long lifetime of phosphorescence emission is due to the change of its spin state from singlet to triplet state by a system called inter system crossing. Due to quantum mechanically forbidden transition, the material can't come back quickly to the ground state once the spin has changed. Further, photoluminescence can be divided into two categories based on emission time duration; a) short period and b) long period. In short period photoluminescence, the emission time is less than 10^{-4}s, whereas the emission time period is greater than 10^{-4}s then it is considered a long period photoluminescence. All of them have their own significance in science and technology. Schematic diagram of different types of luminescence based on their emission time is given below (figure 1.5):

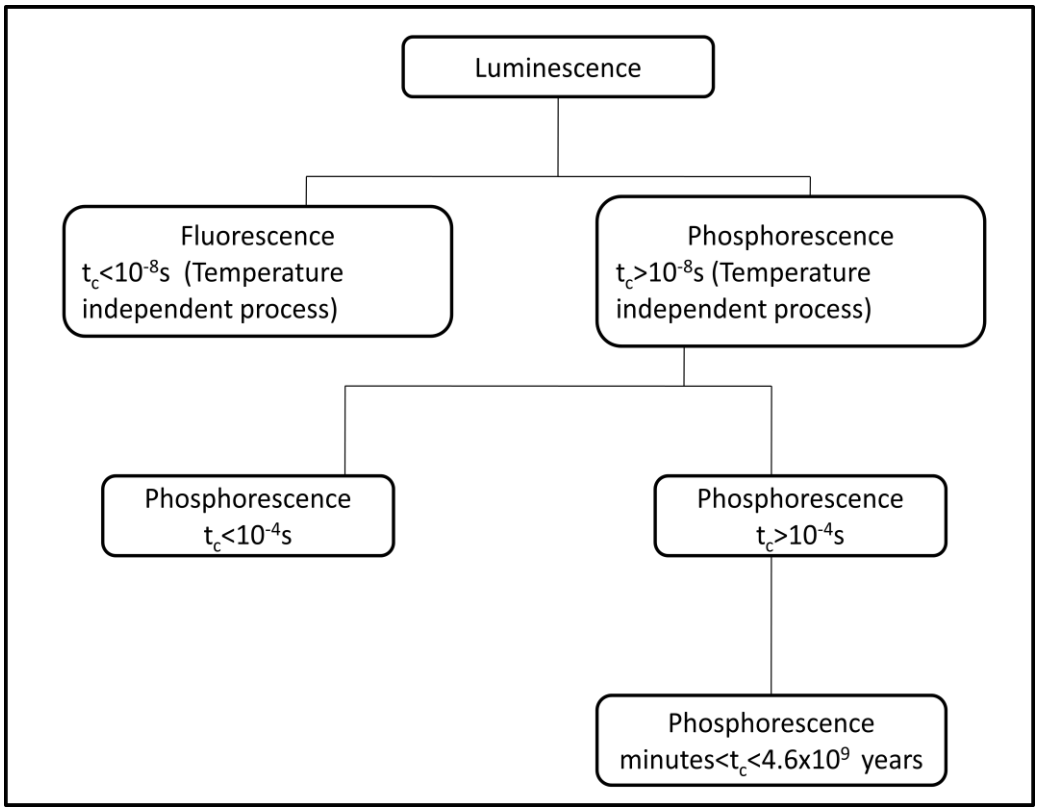

Figure 1.5: Classification of luminescence on the basis of emission time.

1.5 Luminescence of trivalent lanthanide ion

Lanthanides are the elements that follow the general electronic configuration of $[Xe]4f^n5d^{0-1}6s^2$(where n=1-14). The 4f shells of these elements are successively filled up, and these elements show the same valence electrons (except europium and ytterbium). Hence they all show quite similar reactivity as well as co-ordination behaviour. Some of the lanthanide ions even exhibit luminescence in their divalent states (Eu^{2+}, Sm^{2+}). The luminescence behaviour of lanthanide ions arose due to the electronic transitions occurring within the 4f shell. Even though the electronic transition occurring in lanthanide ions is parity forbidden, there occurs transition as a result of mixing up of orbitals which relaxes the selection rule. Since the transition that occurred within lanthanide ions is forbidden, the absorption co-efficient is low and the luminescence lifetime of these ions is long which ranges usually from microseconds to several

milliseconds. The 4f shell of lanthanide ions is strongly shielded by 5s and 5p orbitals which results the luminescence property of these ions are not affected by the environment. Hence the absorption and emission peaks of lanthanide ions are narrow and sharp except in the case of cerium ions. Due to the strong shielding of the 4f electrons by 5s and 5p electrons, the crystal field cannot affect the energy level. Hence the position of absorption and emission spectra of lanthanide ions are same irrespective of host materials. However, their crystal symmetry and quenching may lead to a significant change in their optical properties. Photoluminescence and magnetic properties of lanthanide ions make them very attractive in modern research. Doping of different lanthanide ions into a host material give different emission colours. It means that different lanthanide ions show emission peaks at different wavelengths. Sm^{3+} ion exhibits red/orange/pink colour, Tb^{3+} ion produces green emission light, Dy^{3+} ion usually emits in yellow colour, Eu^{3+} ion shows red colour and Tm^{3+} in the blue region etc.

As said above, 4f electrons are responsible for the luminescence property in lanthanide ions. In an orbital, there are several microstates; in these microstates, the 4f electrons are allocated. Different configurations produced different numbers of microstates depending upon the number of electrons present in the particular shell. Some microstates are more stable than others. The ground state is the most stable microstate where the electrons are distributed to provide maximum spin multiplicity. In free state, orbitals of 4f shell are generally in degenerate states and filled the electrons according to the Hund'srule. In case of combined state, the energies of 4f orbitals are perturbed by many forces such as Coulombic force, spin-orbit coupling and crystal field. Out of these three forces, Coulombic force perturbed most other than the rest two forces followed by spin-orbit coupling and crystal field [Gschneidner and Eying, (1996)]. Hence, the splitting of 4f energy levels are largely contributed by the Coulombic interaction force, and the energy separation between the energies of 4f states produced by the Coulombic interaction is in the order of 10^4 cm^{-1}. Further, these energy states are split by spin-orbit

interaction into different energy levels. The difference in energy between these split energy levels is in the order of 10^3 cm^{-1} [Gschneidner and Eying, (1996)]. These energy states are characterized using the term symbol $^{(2S+1)}L_J$. Here, L can be denoted as S,P,D,F…., corresponding to different values of L=0,1,2,3….., respectively [Hendersion and Imbusch, (1989)]. And the spin multiplicity is denoted by (2S+1) which provides permitted values of J for a particular value of L. J indicates the total angular momentum which is resulted from the coupling between spin angular momentum(S) and orbital angular momentum (L). The permitted values of J are 0 and positive but not negative. When organic or inorganic ligands surround lanthanide ions, they produce a crystal field that affects not only the strength of f-f transition but also splits J levels into different sub-levels. The splitting is observed as a fine structure in the emission band [Bunzli, (2010)]. Figure 1.6 shows the schematic splitting diagram of 4f energy levels caused due to different forces.

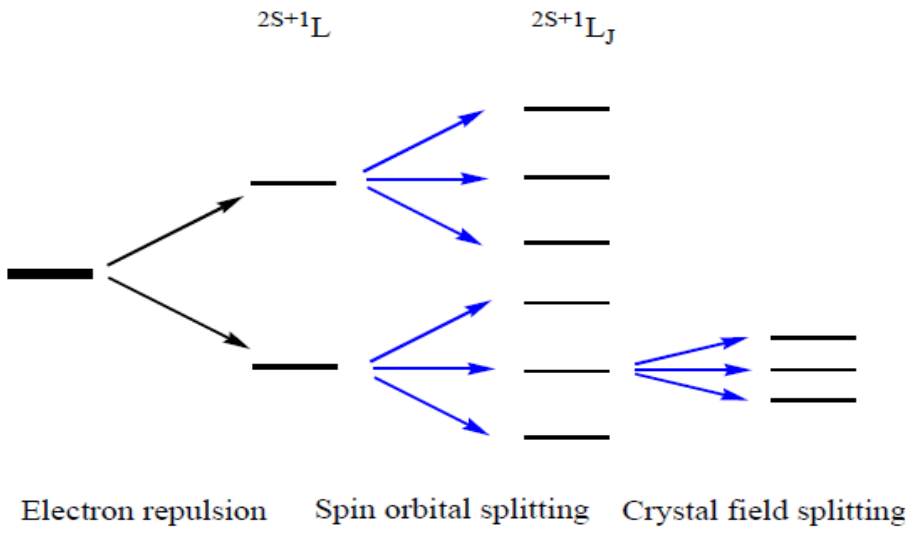

Figure 1.6: Energy levels splitting for the lanthanide ions with $4f^n$ configuration.

The ground state which is the most stable state has the highest spin multiplicity. In case if it has more than one term of the same spin, then the higher value of L will be

considered as the ground state and again if there are same values of L and (2S+1) but the difference is only in their J value then the ground state term can be found out using Hund's rule. In a particular orbital, if the electrons are half-filled or less than half-filled then the lowest value of J will be considered as a ground state while the electrons are filled more than half. In this case, the highest value of J will be considered as the ground state. Table 1.2 shows the ground state electronic configuration along with their corresponding total angular momentum (J), spin angular momentum (S) and orbital angular momentum (L).

Table 1.2: Electronic configuration of Ln^{3+} ion in the ground state.

Elements $\Sigma(L+S)$	Atomic number	electronic configuration	4f electrons	S=	Σs L=	Σl J=
Ce^{3+}	58	[Xe] $4f^1$	↑	1/2	3	5/2
Pr^{3+}	59	[Xe] $4f^2$	↑↑	1	5	4
Nd^{3+}	60	[Xe] $4f^3$	↑↑↑	3/2	6	9/2
Pm^{3+}	61	[Xe] $4f^4$	↑↑↑↑	2	6	4
Sm^{3+}	62	[Xe] $4f^5$	↑↑↑↑↑	5/2	5	5/2
Eu^{3+}	63	[Xe] $4f^6$	↑↑↑↑↑↑	3	3	0
Gd^{3+}	64	[Xe] $4f^7$	↑ ↑ ↑ ↑ ↑ ↑ ↑	7/2	0	7/2
Tb^{3+}	65	[Xe] $4f^8$	↑↓ ↑ ↑ ↑ ↑ ↑ ↑	3	3	6
Dy^{3+}	66	[Xe] $4f^9$	↑↓ ↑↓ ↑ ↑ ↑ ↑ ↑	5/2	5	15/2
Ho^{3+}	67	[Xe] $4f^{10}$	↑↓ ↑↓ ↑↓ ↑ ↑ ↑ ↑	2	6	8
Er^{3+}	68	[Xe] $4f^{11}$	↑↓ ↑↓ ↑↓ ↑↓ ↑ ↑ ↑	3/2	6	15/2
Tm^{3+}	69	[Xe] $4f^{12}$	↑↓ ↑↓ ↑↓ ↑↓ ↑↓ ↑ ↑	1	5	6
Yb^{3+}	70	[Xe] $4f^{13}$	↑↓ ↑↓ ↑↓ ↑↓ ↑↓ ↑↓ ↑	½	3	7/2
Lu^{3+}	71	[Xe] $4f^{14}$	↑↓ ↑↓ ↑↓ ↑↓ ↑↓ ↑↓ ↑↓	0	0	0

The energy level diagram of various lanthanide ions was shown in figure 1.7 [Carnall *et al*., (1989)]. As stated above, the 4f electrons in lanthanides are strongly shielded by 5s and 5p electrons, hence the crystal field is unable to affect the energy levels. Moreover, J energy level is well defined and turned out sharp spectra [Frey and Horrocks, (1995)]. For this reason, lanthanide energy level diagram can be used in all sorts of host materials. But, in case of La^{3+} and Lu^{3+}, they have empty and completely filled 4f shells respectively and hence they exhibited no optical transitions. Ce^{3+} has only one excited energy level as there is only one electron is available in 4f orbital. The light-induced due to electronic transition is mainly due to magnetic dipole and electric dipole interaction. Electric dipole transition is normally site-selective. Whenever lanthanide ion occurs in a crystal lattice having inversion symmetry, the transitions are very weak, and sometimes no transition is exhibited as electric dipole transition is forbidden while magnetic dipole transitions exhibit a strong intensity since magnetic dipole transition is allowed. If lanthanide ion detains in the lattice site with non-inversion symmetry, a more intense peak is observed in the case of electric dipole transition than magnetic dipole transition as electric dipole transition is allowed and magnetic dipole transition is forbidden. The selection rule for allowed electronic dipole and allowed magnetic dipole transitions are $\Delta l = \pm 2$, $\Delta J = \pm 2$ and $\Delta l = \pm 1$, $\Delta J = \pm 1$ (except for $0 \rightarrow 0$), respectively. Hence, in a crystal, the symmetry around lanthanide can be found out using the intensity ratio of the electric dipole to the magnetic dipole transitions.

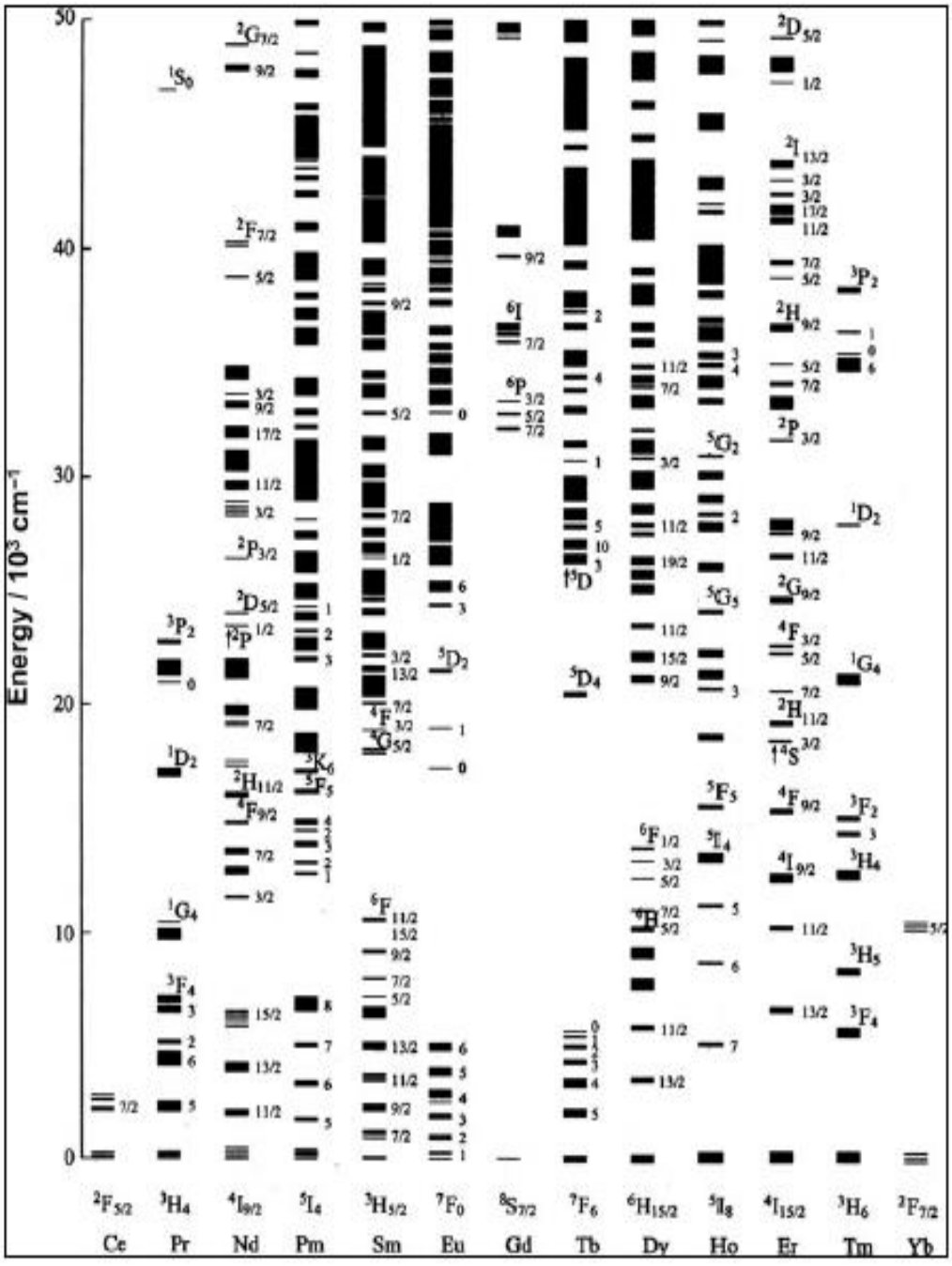

Figure 1.7: Energy level diagram of Ln^{3+}ions.

1.6 Charge Transfer

Lanthanide compounds usually exhibit sharp and narrow absorption or emission spectra but sometimes, broad absorption and emission bands are also observed. In this case, charge transfer transition is used to explain this broad band. In this type of transition, the distribution of charge on the optical centre alters strongly which again results in the change of their chemical bonding. Usually, this kind of transition takes place in different orbitals or in between different electronic states of different ions [Ronda, (2009)]. Charge transfer transition is normally exhibited either of the two ways 1) within host materials containing lanthanide ion or 2) in between lanthanide ion and host material. The latter one takes place either by transferring charge from lanthanide ion to the host material or from host to lanthanide ion [Boutinaud *et al*., (2007)].

1.7 Quenching of Luminescence

In some cases, it is unable to meet the condition for efficient luminescence emission. Here, non-radiative transition dominates radiative transition, consequently results in the decrease of the luminescence emission intensity which is known as quenching. Quenching of luminescence occurs due to many processes. However, few common mechanisms are as follows:

a) Cross relaxation

It is a kind of non-radiative energy transfer. However, the whole excited ions transfer some amount of energy to another ion, this process is known as cross-relaxation. Such quenching mechanism is connected with energy interaction between lanthanide ions and is normally seen when the concentration of lanthanide ions is high. The schematic representation of cross-relaxation between two ions R is shown in figure 1.8. Here, the original system losses some of its energy and comes down to the lower energy state while another system gains the energy to acquire to the higher energy state.

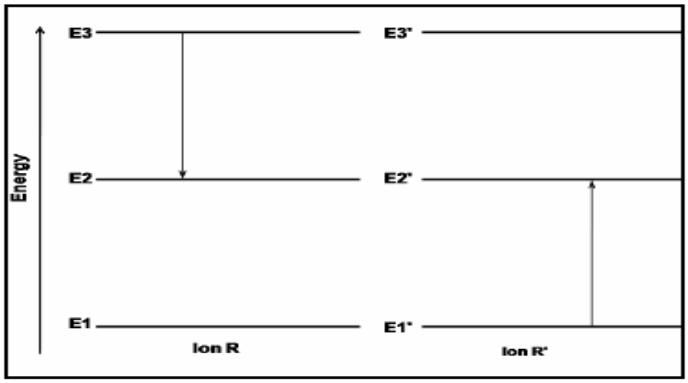

Figure 1.8: Graphical presentation of the cross-relaxation between two pairs of R.

b) Multi phonon relaxation

Luminescence emissions are also quenched by a non-radiative transition process resulted from the surrounding's phonon vibration (phonon emission). This kind of quenching is termed as multi phonon relaxation. The non-radiative return of the excited state to its ground state can be done if it fulfils the conditions i.e. the difference in energy (ΔE) has to be the same or less than 4-5 times the vibrational frequency of the surroundings.

1.8 Literature Reviews

Rare-earth ions doped materials have drawn a particular attention since they are applicable in laser materials, flat panel displays, cathode ray tubes, up conversion materials etc. [Balakrishnaniah *et al.*, (2010); Wang *et al.*, (2010)]. Likewise, rare-earth doped phosphate compounds also have potential applications in the fields of laser, ceramic, sensor, phosphor, heat resistant materials, field-effect transition and also in optoelectronics, medical and biological labels, solar cells and fluorescent light sources [Di *et al*., (2004); Sun and Sirringhaus, (2005); Talapin and Murray, (2005); Huang and Lieber, (2004); Law *et al*., (2005); Chiang *et al*., (2005)]. The photoluminescence property of rare-earth ions is considered as one of the most interesting features. Some of the rare-earth ions show luminescence in the visible regions while some others are in the

near-infrared spectral regions upon UV light excitation. They have potential applications in the fields such as fluorescent lamp phosphors [Shionoya and Yen,(1999)], organic light-emitting diodes (OLED) [Reyes *et al.*, (2004); Kido and Okamota, (2002)], optical fibres for telecommunications**,** contrast agents for magnetic resonance imaging [Faulkner *et al*., (2005)], biological assays [Matsumoto and Yuan, (2003); Faulkner and Matthews, (2004)]. Those rare earth ions which give emission near-infrared region are useful for laser applications**,** telecommunication and optical amplifiers [Sahu *et al.*, (2012)].

On the other hand, $BiPO_4$ is considered as one of the best host materials for photoluminescence due to its isostructural to metal phosphate, very high Physico-chemical stability [Clavier *et al.*, (2011); Tang *et al.*, (2005); Naidu *et al.*, (2012)]. $BiPO_4$ has three different phases i.e. hexagonal, low-temperature monoclinic and high-temperature monoclinic phases [Naidu *et al.*, (2012); Zhao *et al*., (2013)]. The hexagonal phase of $BiPO_4$ can be transformed into low-temperature monoclinic phase on heating above 600^oC [Romero *et al.*, (1994)]. High-temperature monoclinic phase of $BiPO_4$ is seldom reported, owing to its metastable feature [Zhao *et al*., (2013)]. Hexagonal and monoclinic essentially differ in the co-ordination number of Bi^{+3}. In case of hexagonal $BiPO_4$, Bi^{3+} ions are surrounded by eight neighbours oxygen atoms forming square anti-prism geometry around Bi^{3+}, whereas in monoclinic $BiPO_4$, Bi^{3+} has a co-ordination number nine similar to the monazite structure of lanthanide phosphate [Ni *et al.*, (1995)]. The luminescence from Bi^{3+} species in different inorganic hosts are also quite interesting due to its $6s^2$ configuration and significant Stoke shift associated with its emission–absorption characteristics [Wolfert *et al.*,(1985)]. Upon UV-excitation, both the phases of $BiPO_4$ i.e. hexagonal and monoclinic emit light around 437 nm and this has been attributed to the $^3P_1$–$^1S_0$ transition of the Bi^{3+} ion in the lattice. The comparable ionic sizes of Bi^{3+} and rare earth ions may make $BiPO_4$ as one of the best host for the dopant of rare-earth ions. [Naidu *et al.*, (2012)].

Fu and his group prepared Eu^{3+} doped $BiPO_4$ by precipitation method and studied the effect of solvents in phase structure as well as photoluminescence property. Hexagonal phase (HP) was obtained for the samples prepared using organic solvents which have hydrophobic in nature. In their study, alcohols having hydrophilic nature which contains one hydroxyl group were used as solvents and confirmed the formation of low-temperature monoclinic phase (LTMP). But mixed-phase (HP and LTMP) was confirmed when alcohols having hydrophilic in nature containing more than one hydroxyl group were used as a solvent. The formation of mixed phases of Eu^{3+} doped $BiPO_4$ was due to the presence of C−O−C and C=O groups in the solvents. Different particle sizes were noticed for the two phases and a larger particle size was observed in the case of HP than LTMP. During photoluminescence investigation, it was observed that the LTMP exhibited higher quantum yield and longer lifetime than HP [Fu *et al.*,(2012)]. Zhao *et al.* reported the synthesized of $BiPO_4$:Eu^{3+} by room temperature co-precipitation method followed by annealing of the precipitate formed. The HP was observed for the sample synthesized at room temperature. Upon further heating of the as-prepared sample in between 400°C to 600°C for 2hrs, a change of phase from HP to LTMP was observed. However, on annealing the sample at 800°C for 2 hrs, high-temperature monoclinic phase (HTMP) was formed. A change of morphology from nanorods to spherical shape was also observed when the sample is annealed at 600°C. Photoluminescence study showed the highest emission intensity for LTMP samples followed by HTMP and HP [Zhao *et al.*, (2012)]. Liu and his co-workers synthesized $BiPO_4$ co-doped with Eu^{3+} and Dy^{3+}phosphor by solid-state method. A change of phase from HTMP to LTMP was reported on increasing the concentration of Dy^{3+} ions. It was also reported that the concentration of doping material plays an important role in the crystallinity of the prepared phosphors and the characteristic peaks of Eu^{3+} and Dy^{3+} were split due to this phase transition upon excitation at different wavelengths. They also reported that the phosphor could show a shifting of colour from the red-orange region to the blue-green region depending on the excitation wavelengths [Liu *et al.*, (2013)]. Tb^{3+} ions doped $BiPO_4$ nanowire was synthesized by Yan using hydrothermal

method at 200°C. They studied the effect of different reaction times (1.5hrs, 2.5hrs and 3.5hrs) on phase and photoluminescence properties. The samples prepared with a reaction time of 1.5hrs and 2.5hrs showed hexagonal and mixture of hexagonal and monoclinic phases respectively while the sample prepared with a reaction time of 3.5hrs showed pure monoclinic structure which resulted in the exhibition of highest emission intensity other than 1.5hrs and 2.5hrs of reaction times [Yan, (2015)]. Zheng and his co-workers enhanced the stability of LTMP of $BiPO_4$ by doping rare-earth ions such as La, Ce, Nd, Eu, Er. Doping of a small amount of Ln^{3+} ions ≤9% retarded the structure transition to HTMP and resulted in the formation of more stabilized LTMP. Annealing of codoped sample (5% La^{3+}, 5% Nd^{3+}, 5% Ce^{3+} with 2% Eu^{3+}) at 900°C not only enhanced the percentage content of LTMP upto 89%, 87%, and 96% respectively as compared to undoped $BiPO_4$ but also increased the photoluminescence emission intensities [Zheng *et al.,* (2014)]. Nanostar morphology $BiPO_4$:Eu^{3+} phosphors were synthesized by Becerro and co-workers using the co-precipitation method at 120°C. The effect of doping Eu^{3+} ion concentrations was investigated. The phosphor showed red-orange colour resulted from the emission peaks of Eu^{3+} having transitions $^5D_0 - ^7F_J$ (J = 0, 1, 2, 3, or 4) and 2mmol% of Eu^{3+} ion was found to be the optimum concentration [Becerro *et al.,* (2014)].

The hydrothermal synthesized of Sm^{3+} ions doped $BiPO_4$ were reported by Shi *et al.* They investigated the effects of pH of the reaction medium and Sm^{3+} ion doping concentration on the structural and photoluminescence properties of Sm^{3+} ions doped $BiPO_4$. The phase transition was observed from LTMP to HP on increasing the pH of the reaction medium as well as Sm^{3+} ion concentration. The morphologies were also changed from octahedron-like to mixed morphologies of irregular polyhedron and short rod-like shapes as the pH increased from 0.5 to 3. But, the transition due to Sm^{3+} ion could be suppressed at a pH of 0.5. The optimum concentration of Sm^{3+} ion was reported as 11% when pH of the solution was 0.5 [Shi *et al.*, (2014)]. Yang and his co-workers reported the synthesis of $BiPO_4$:Tb^{3+}/ Ce^{3+}nanofibre by using an electrospinning

process followed by calcination. They observed that the Ce^{3+} ion enhanced the photoluminescence properties of $BiPO_4$:Tb^{3+} by charge transfer process from Ce^{3+} ion to Tb^{3+} ion. The concentration quenching was observed after 15mmol% of Tb^{3+} ion [Yang *et al.,* (2016)].

Yan and Long studied the charge transfer property from Sm^{3+} ions to Eu^{3+} ions in $BiPO_4$ co-doped with Sm^{3+} ions and Eu^{3+} ions synthesized by hydrothermal method. They observed that Sm^{3+} ion could enhance the excitation and emission intensities of Eu^{3+} ion by transferring the excitation energy efficiently. This transfer of charge is due to the overlapping of excitation energy of Eu^{3+} with the emission energy of Sm^{3+} [Yan and Long, (2016)]. Ma *et al.*, studied the effects of pH of the reaction medium and the amount of CTAB surfactant on the photoluminescence properties of 5% Eu^{3+} ion-doped $BiPO_4$. They observed that both pH and the amount of CTAB gave a strong influence on the photoluminescence property. When the amount of CTAB was 0-4mM, LTMP was formed whereas HP nanoparticles was obtained upon increasing the amount of CTAB to 6mM. 2mM of CTAB was exhibited the highest emission intensity. The morphology and phase were found to change from LTMP micro rod to HP nanoparticles with an increase of pH value. The strongest luminescence intensity was observed when the pH of the solution is 0.5 [Ma *et al.*, (2017)]. In 2008, Guan *et al.*, synthesized undoped urchinlike $BiPO_4$ structure and Dy^{3+} doped $BiPO_4$. The pure and Dy^{3+} doped $BiPO_4$ showed strong blue emission and white emission respectively. These blue and white emissions are exhibited due to $^3P_1$-$^1S_0$ transition of Bi^{3+} and $^4F_{9/2}$-$^6H_{15/2}$ (480 nm, blue), $^4F_{9/2}$-$^6H_{13/2}$ (572 nm, yellow), and $^4F_{9/2}$-$^6H_{11/2}$ (664 nm, red) of Dy^{3+} transitions of Dy^{3+} [Guan *et al.*, (2008)].

Roming synthesized $BiPO_4$:Tb^{3+} by polyol mediated method. He studied the effect of calcination on their quantum efficiency and observed an increase in the quantum efficiency of the prepared $BiPO_4$:Tb^{3+} upon calcination at 750°C. The prepared $BiPO_4$:Tb^{3+} may be re-dispersed further using ethanol or diethylene glycol [Roming and

Feldmann, (2009)]. The effect of different surfactants on phase structure as well as photoluminescence properties of Ce^{3+} co-doped $BiPO_4:Tb^{3+}$ was studied by Lakshminarayana and his co-workers. The formation of hexagonal nanostructure of Ce^{3+}co-doped $BiPO_4:Tb^{3+}$ with no agglomeration and limiting the structure growth was observed in oleic acid unlike other surfactants, namely glycerol, water glycerol solution, water ethylene glycol solution and pure ethylene glycol. Moreover, it has also been observed that the photoluminescence property of Ce^{3+}co-doped $BiPO_4:Tb^{3+}$ is showing more intense green emission in oleic acid as compared to other mentioned surfactants and transfer of charge from Ce^{3+} to Tb^{3+} was observed during photoluminescence study [Lakshminarayana *et al.,* (2015)]. The influences of ageing time on phase, morphology and photoluminescence properties were studied by synthesizing $BiPO_4:Er^{3+}$, Yb^{3+} phosphors using solvothermal method. The extension of ageing time resulted in the change of phase from hexagonal to monoclinic phase and also the morphology changes from nanorods to micro-octahedra through nano rugbies. In case of hexagonal phase, the photoluminescence property was observed very weak due to the presence of water molecules while maximum photoluminescence emission intensity was observed in case of monoclinic phase. $BiPO_4:Er^{3+}$, Yb^{3+} showed green and red upconversion emission (UC)**.** The direct proportionality of UC emission with pumping power was also mentioned in their study. It has also been concluded that two-photon processes were involved in green and red UC emission [Liu *et al.,* (2015)]. The hexagonal phase of $BiPO_4:Eu^{3+}$ was synthesized by polyol-mediated route using Diethylene glycol (DEG) as reacting medium as well as a capping agent. The presence of DEG stabilizes $BiPO_4:Eu^{3+}$ nanoparticles and allow them to arrange into cocoon-like crystals. The size of the particles remain the same even after heating at 600^oC, but the change of phase from hexagonal to monoclinic was observed. The hexagonal phase of $BiPO_4:Eu^{3+}$ exhibited very weak emission intensity due to the presence of surface-bound DEG residual molecules. This was further removed by heating at 600^oC along with the enhancement of emission intensity [Arunkumar *et al.,* (2012)].

Cybinska and his group used ionic liquids (butylammoniumdihydrogenphosphate) for the preparation of water free monazite $BiPO_4:Ln^{3+}$ (Ln = Sm, Eu, Tb, Dy) by microwave method at 120^oC. The ionic liquid acts not only as solvent, microwave susceptor but also particle stabilizer. As prepared nanoparticles were free from water as well as from surface-bound water, hence heating is not required which causes particles growth and migration of lanthanide ions leading to aggregation. Depending upon the type of dopants, the synthesized nanomaterials showed different emission colours such as orange (Sm^{3+}), red (Eu^{3+}), green (Tb^{3+}), white (Dy^{3+}) etc. But in case of $BiPO_4:Eu^{3+}$, a high quantum efficiency ranging from 49-65.5% were observed [Cybinska *et al.,* (2016)]. Han prepared $BiPO_4:Ce^{3+}$, Tb^{3+} by solvothermal method using 2:1 mixture of glycerin and water as solvent. The charge transferred from Ce^{3+} to Tb^{3+} was observed as the emission wavelength of Ce^{3+} and excitation wavelength of Tb^{3+} were well matched which results in the production of more intense emission peak as compared to $BiPO_4$: Tb^{3+} [Han *et al.,* (2014)]. Eu^{3+}/Sm^{3+} co-doped micro-sized shuttle shape with smooth surface $BiPO_4$ was synthesized by facile hydrothermal method in surfactant-free environment. The photoluminescence study of Eu^{3+}/Sm^{3+} co-doped $BiPO_4$ showed a wide excitation band along with the emission of orange-red colour. In this study, it had also been observed that the transfer of charge from Sm^{3+} to Eu^{3+} consequently enhanced the photoluminescence property of Eu^{3+}/Sm^{3+} co-doped $BiPO_4$ [Jianming *et al.,* (2014)]. Monoclinic phase of $BiPO_4:Yb^{3+}/ Er^{3+}$ was prepared using two different methods such as solvothermal method and solid-state method. Further, the effect on upconversion (UC) luminescence properties was studied by co-doping different concentrations of Sc^{3+} to $BiPO_4:Yb^{3+}/ Er^{3+}$. Strong dual-wavelength sensitive UC emission properties due to $BiPO_4:Yb^{3+}/ Er^{3+}/Sc^{3+}$ were noticed. The UC emission intensity is further enhanced by controlling the appropriate concentration of Sc^{3+}. The colour co-ordinates resulted from $BiPO_4$:15% Yb^{3+}, 2% Er^{3+}, x% Sc^{3+} (x=0, 1, 3 and 5) prepared by solid-state method and solvothermal synthesis were found in the green or yellow-green region upon excitation at 980 nm or 1550 nm. The optimum concentration of Sc^{3+} was found to be 3% which enhanced UC emission

intensity 250/8 times than Sc^{3+} free samples under excitation at 980 nm/1550 nm[Li *et al.,* (2018)].

Li *et al.,* observed the change in the phase transition of $BiPO_4$: Eu^{3+} by controlling the concentration of PO_4^{3-} ion under reaction solution. The change of phase from hexagonal to low-temperature monoclinic phase was observed due to the change of free energy in the crystallographic system at which a lower energy crystallography phase is formed. The study also confirmed the higher luminescence property of monoclinic phase over hexagonal phase due to non-radiative process in the lattice [Li *et al.,* (2019)]. Zhao *et al.,* studied the phase change of $BiPO_4$:Eu^{3+} upon increasing the doping concentration of Eu^{3+} using hydrothermal method. Monoclinic phase of undoped $BiPO_4$ was obtained when the sample is prepared at 100^oC. When the concentration of Eu^{3+} ions is increased upto 0.068 then the monoclinic phase changed to hexagonal phase. The hexagonal phase of $BiPO_4$:Eu^{3+} is further transformed into a monoclinic phase upon heating at 400^oC which is just the opposite of doping. Enhanced luminescence property of monoclinic phase was reported as compared to hexagonal. It is necessary to account into the structural changes due to different chemical natures to enhance the luminescence applicability [Zhao *et al*., (2012)]. The photoluminescence lifetimes of three different phases such as hexagonal phase, low-temperature monoclinic phase and high-temperature monoclinic phase of undoped $BiPO_4$ were discussed by preparing the samples using co-precipitaion method, hydrothermal method and calcination of hydrothermally synthesized sample respectively. Broad band emission of all the three phases was confirmed from the photoluminescence emission spectra centring at 540nm resulting from the recombination of electrons and holes generated due to UV illumination. Moreover, Bi^{3+} ion containing materials usually exhibited broad emission spectra upon UV excitation due to $^3P_1$ to $^1S_0$ transition. The photoluminescence lifetime study showed the maximum lifetime for the sample with high-temperature monoclinic phase [Wang *et al.,* (2013)]. Different polymorphs of $BiPO_4$:Eu^{3+} were prepared using hydrothermal method. Hexagonal phase of the phosphor was obtained when prepared at

100^{o}C, when the temperature is increased upto 160^{o}C, monoclinic phase is obtained. Again, the temperature is increased beyond 180^{o}C, hexagonal phase is observed. But the hexagonal phase obtained under different temperatures can be transformed in monoclinic phase upon annealing at 400^{o}C. There occurred a change of morphology from nanorods to prism-like shape, the lattice strains also vary from tensile to compressive and then again returned to tensile. The effects of polymorphs on their luminescence property were shown by the increase of a) decay time b) quantum efficiency c) non-radiative transitions. Monoclinic phase was reported as the best phase for photoluminescence applications [Zhao *et al.*,(2012)]. Shi *et al.,* investigated the effect of cation/anion molar ratio $[Bi^{3+} + Eu^{3+}]/[PO_4^{3-}]$ on the structural morphology as well as the photoluminescence properties of $BiPO_4$:Eu^{3+} prepared under a simple hydrothermal method. In their study, it had been observed a) change of phase from hexagonal to monoclinic phase along with the change of morphology from nanoparticles to octahedron like and finally rod-like respectively, b) increase of particle size from 150nm to 10micro meters when the molar ratio of cation/anion changes from 1:0.5 to 1:2.5. The weak emission intensity of 1:0.5 molar ratio is attributed to OH oscillators of H_2O present in hexagonal nanomaterials whereas, rod-like monoclinic exhibited strong emission due to its high crystalline nature [Shi *et al.,* (2015)].

$BiPO_4$ doped with Ce^{3+} and Eu^{3+} ions singly and Ce^{3+} co-doped $BiPO_4$: Eu^{3+}were prepared by simple precipitation method. The photoluminescence study showed the exhibition of blue emission for $BiPO_4$ doped with Ce^{3+} and yellowish-orange for $BiPO_4$: Eu^{3+} were observed due to 5d → 4f and $^5D_0 \rightarrow {}^7F_1$ of Ce^{3+} and Eu^{3+} respectively. Tunable emission in blue and orange regions was observed from Ce^{3+}co-doped $BiPO_4$: Eu^{3+} depending upon the excitation wavelength in a single sample. No charge transfer from Ce^{3+} to Eu^{3+} and vice-versa was observed due to the unavailability of metastable excitation levels for Ce^{3+} and Eu^{3+} ions. Moreover, there is no spectral overlap between the emission spectra of Ce^{3+} and excitation spectra of Eu^{3+} ions [Singh *et al.,* (2015)]. Tunable photoluminescence properties associated with Tb^{3+} and Eu^{3+}codoped $BiPO_4$

synthesized by hydrothermal method was firstly demonstrated by Wang and his co-workers. Change of emission colour from green to yellow and red was confirmed by co-doping Tb^{3+} and Eu^{3+} to $BiPO_4$ and by changing their doping ratio respectively. Moreover, there occurred an efficient charge transfer from Tb^{3+} to Eu^{3+} ions. Interestingly, 9% Tb^{3+} and 3% Eu^{3+}co-doping exhibited warm white light emission was reported successfully in their study [Wang *et al.,* (2015)]. Rice shape lanthanide ions (Yb^{3+}, Er^{3+}, Tm^{3+} and Ho^{3+}) doped $BiPO_4$ upconversion submicron particles (SMPs) were prepared by facile precipitation method at room temperature followed by subsequent calcination. The upconversion luminescence was observed for monoclinic phase upon excitation at 980nm laser diode. Red, Green and Blue emission lights have been observed for Yb^{3+} and Ho^{3+}/Er^{3+}/Tm^{3+} co-doped $BiPO_4$ SMPs. It was also reported the emission of warm white light by $BiPO_4$:20% Yb^{3+}/1% Er^{3+}/0.5% Tm^{3+}/0.15% Ho^{3+} which was also confirmed by the calculated chromaticity coordinates of (0.318, 0.356), which fall in the white region and are very close to the standard energy of white light coordinates (0.333, 0.333) [Wang *et al.,* (2013)].

pH also plays a vital role in photoluminescence property. In 2015, Yan investigated the effect of pH on the structure and photoluminescence properties of $BiPO_4$: Eu^{3+}. During their study, a decrease in crystallinity, destruction of regular rod-like crystals, formation of small particles were observed with increase of pH. With increased of pH, the particles are aggregated more and formed aggregated rod shape structure which lowers the photoluminescence property [Yan, (2015)]. Zhang *et al.*, studied the effect of PO_4^{3-} ion concentration on the structure, morphology and luminescence properties of $BiPO_4$: Dy^{3+}. The crystal structure having growth-oriented along (120) plane, change of morphology from irregular polyhedron like to rod-like were observed when the concentration of PO_4^{3-} ion is increased. Moreover, it had also been reported that the excessive presence of PO_4^{3-} ion enhanced the photoluminescence property which makes them a good reference to design better luminescent materials [Zhang *et al.,* (2017)]. Zhou *et al.*, enhanced the luminescence property of $BiPO_4$: Eu^{3+}

by introducing Li^+ in it. By the presence of Li^+ helps in the improvement of symmetry and it also prevents the agglomeration of the particles and resulted in the enhancement of emission intensity [Zhou *et al.*, (2011)]. Recently, an innovative approach has been made for the preparation of colloidal photoluminescent $BiPO_4$: Ln^{3+} (Eu^{3+}, Tb^{3+}) using oleic acid as surfactant and $H_6P_4O_{13}$ as PO_4^{3-} source by using solvothermal method. The adsorbed oleic acid during synthesis made the nanoparticles hydrophobic in nature. The colloidal solutions of $BiPO_4$: Eu^{3+} and $BiPO_4$: Tb^{3+} showed organic red and green colours respectively. And it has also been reported that the synthesized nanoparticles are having promising applications in water painting [Huang *et al.*, (2019)].

1.9 Scope of Studies

The scope of the study will include the photoluminescence property of lanthanide ions doped $BiPO_4$ phosphors. The photoluminescence property depends on some factors such as concentration, annealing effects will be discussed as it is important to find out the optimum concentration to apply into applications and the same is required for annealing also. So, the main objective of the current thesis will be

- To synthesize the rare earth ions doped $BiPO_4$ phosphor samples
- To characterize the rare earth ions doped phosphor samples by using the characterization technique XRD (X-ray Diffraction), TEM (Transmission electron microscope), PL etc.
- To study the photoluminescence properties of the rare earth ions doped phosphor samples with different concentrations of dopant ions.
- To study the effect of annealing temperature of the rare earth ions doped phosphor samples on photoluminescence properties.

1.10 Methodology

1.10.1 Synthesis of rare-earth doped $BiPO_4$ phosphors

The rare-earth ions doped $BiPO_4$ phosphors were synthesized by co-precipitaion method. Co-precipitation method is considered as one of the simplest way to synthesize phosphors and it is cost-effective and have so many advantages over solid-state method with regards to the temperature requirement, homogeneity of the product obtained. The solid-state method required frequent grinding of the sample during the synthesis process and needs a high temperature to get the desired product, while in case of co-precipitation method the synthesize of the phosphor usually take place in liquid state. Hence, grinding is not required during the synthesis process and need comparatively lower temperature compared to solid-state method. The details of co-precipitation synthesis steps will be given in the coming chapters in detail.

1.10.2 Characterization techniques

- **X-Ray diffraction (XRD)**

The phase purity as well as the crystal structures of the synthesized phosphors are determined by using XRD patterns study of the phosphors. The XRD patterns of the phosphors were measured by XRD machine. For this, the dried phosphor is kept in a sample holder or in a glass slide and then it is put inside the machine. Further, the machine is run at different 2 theta ranges as per the requirement of the phosphors and all the measurements are done at room temperature.

- **Scanning Electron Microscope (SEM) and (EDAX)**

The morphology and elements present in the synthesized phosphors were measured by SEM and EDAX spectra. For these measurements, a few amounts of the phosphor was put on carbon-coated tape and it is blown using a blower. Further, the tape is inserted inside the sample chamber of the SEM machine and then it is scanned by applying high voltage. The resultant SEM image was recorded. While the EDAX spectra were measured by scanning a particular area of the SEM image. Then, the elements

present in that particular area were shown as a spectra type image which is saved for further use.

- **Transmission Electron Microscope (TEM)**

Transmission electron microscopy is used to find out the shape, crystallinity and size of the sample using the TEM images, HRTEM and SAED pattern obtained from the analysis of Transmission electron microscopy technique. Recording of the above-mentioned images required the synthesized powder sample to be dispersed into a solvent such as methanol under ultrasonic vibration for around 1hr. Then, few drops of the dispersed particles were taken out and put over a copper grid that had already been coated with carbon. Further, it is dried in an ambient atmosphere and inserted into the instrument to get the required images.

- **Fourier Transform Infrared (FT-IR) Spectroscopy**

The vibrational spectra of a material can be found out using FT-IR spectroscopy technique. If the sample contained adsorbed water molecule from the synthesis process can be easily investigated from the FT-IR spectra. Measurement of FT-IR spectra is carried out using a few amounts of the powder sample and measured generally in the wavelength ranges from 400-4000cm^{-1}. The beam splitter used in FT-IR technique is KBr generally. Shimadzu Iraffinity-1s FT-IR spectrometer using KBr as beam splitter was used for recording the FT-IR spectra of the entire prepared phosphors.

- **Photoluminescence Spectroscopy**

Photoluminescence spectroscopy is used generally to find out the excitation and emission wavelength of a sample. Finding out an emission wavelength in this particular spectroscopy required an excitation wavelength (wavelength having maximum absorption) and vice versa. Generally, second-order spectra are also shown in the photoluminescence spectra and it can be removed using appropriate filters.

Chapter 2

Instrumentation

2.1 Introduction

After the completion of synthesizing steps, characterization of the synthesized phosphors is an important step required to discover the properties of the phosphors using required instruments. The properties of a material depend on the morphology as well as the size of the synthesized particles. Hence it is very important to find out the particle size as well as the morphology of the particles formed. Generally, characterization can be classified into two main categories, such as spectroscopy techniques and microscopic techniques. The microscopic techniques consist of Scanning electron microscopy (SEM), Transmission electron microscopy (TEM), Atomic force microscopy (AFM) etc. while spectroscopy techniques consist of UV-Visible spectroscopy, Fourier transform infrared spectroscopy (FTIR), Photoluminescence (PL) spectroscopy etc. Generally, X-Ray Diffraction (XRD), High-resolution transmission electron microscope (HRTEM) and selected area electron diffraction (SAED) are used to determine the crystal structure, phase composition and crystallinity of a material. In this chapter, it will be discussed about the instruments which are generally used for the characterization of materials.

2.2 X-Ray Diffraction (XRD)

X-Ray Diffraction is considered as one of the basic techniques to characterize a) the crystalline nature of solids including semiconductors, organic materials, insulators, ceramics, metals, polymers etc. b) symmetry of the atomic arrangement c) crystalline/particle sizes as well as the position of the atoms present in the crystal. A German physicist named Wilhelm Conrad Rontgen discovered X-Ray Diffraction in the year 1895. X-Ray Diffractometers are of two types namely single crystal x-ray diffractometer which is usually used for molecular structure and powder x-ray diffractometer for phases. Hence the atomic structure as well as molecular structure,

preferred crystal orientation, crystal defects etc. of a material can be determined by using X-ray diffraction [Bob, (1954); Cullity, (1956)]. X-ray corresponds to the electromagnetic radiation in which the wavelength used in X-ray diffraction is 1Å. This electromagnetic radiation is obtained when a high energy electron of several thousand electron volts is stopped or decelerated by a heavy metal target (Cooper or Molybdenum etc.). Constructive and destructive phenomena take place when the crystalline or molecular structures are exposed to X-rays. Only in a few directions, the constructive interferences may be noticed while their waves are in phase. So, every crystalline sample exhibited its characteristic diffraction patterns. The X-ray diffraction pattern is used to obtain only when the condition satisfies Bragg's law.

$$n\lambda = 2d\text{Sin}\Theta$$

Where, d=interplanar spacing, Θ=incident angle (Bragg angle), λ=wavelength of the incident x-ray. Figure 2.1 shows the schematic diagram of x-ray diffraction from a crystal.

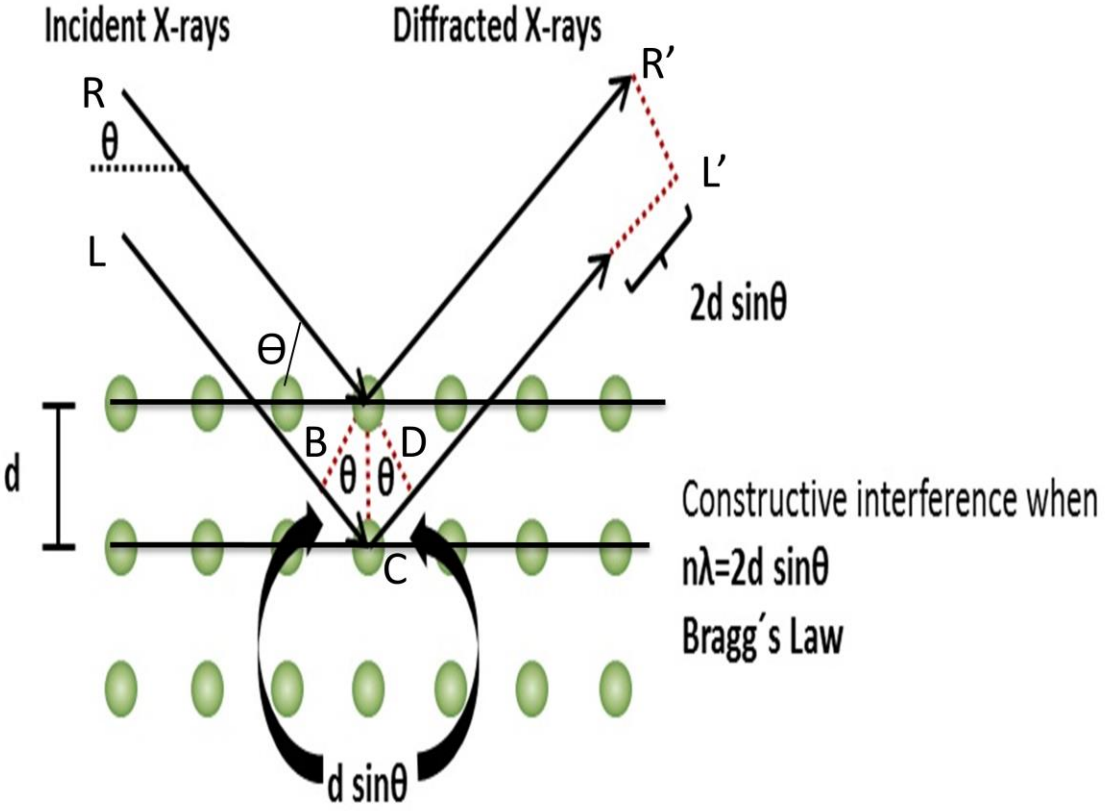

Figure 2.1: Schematic diagram of X-Ray diffraction from a crystal.

Bragg's law is derived as follows. Two incident beams of light (R and L) making an angle Θ to the two adjacent planes separated by a distance of d are reflected (R' and L') within the crystal. The reflected beams will have maximum intensity only when their characteristic waves are in phase. Beam L travelled an extra distance compared to beam R. Hence there occur a path difference between the beams R and beam L. The distance i.e. BCD must be equal to a whole number of the wavelength (λ). The d-spacing and angle of incidence or Bragg's angle 'Θ' are related to the distance BC or CD as follows:

$$BC = CD = d\sin\Theta;\ BCD = BC+CD = 2d\sin\Theta$$

And, $$BCD = n\lambda$$

Therefore, $$n\lambda = 2d\sin\Theta$$

The incident ray made an angle Θ with a fixed plane and the same angle was also formed by the reflected ray, the reflected beam made an angle of 2Θ with the incident beam. Using the diffraction peaks corresponding to 2Θ values, it is also easy to identify the phase of materials comparing with the database available at the Joint Committee on Powder Diffraction Standards (JCPDS) or International Centre for Diffraction Database (ICDD). By knowing the value of d-spacing and their corresponding *hkl* planes, the lattice parameters of the materials can be calculated as follows:

i) For cubic systems, $\frac{1}{d^2} = \frac{h^2+k^2+l^2}{a^2}$

ii) For tetragonal systems, $\frac{1}{d^2} = \frac{h^2+k^2}{a^2} + \frac{l^2}{c^2}$

iii) For hexagonal systems, $\frac{1}{d^2} = \frac{4}{3}\left(\frac{h^2+k^2+l^2}{a^2}\right) + \frac{l^2}{c^2}$

iv) For monoclinic systems, $\frac{1}{d^2} = \frac{1}{Sin^2\beta}\left(\frac{h^2}{a^2} + \frac{k^2Sin^2\beta}{b^2} + \frac{l^2}{c^2} - \frac{2hCos\beta}{ac}\right)$

Where, a,b,c are the lattice parameters of the crystal and β is the angle. The average sizes of the crystal can be evaluated using the Scherrer equation,

$$D = \frac{k\lambda}{\beta Cos\Theta}$$

Where, D = average crystalline size of the material, k = shape factor ($\sim$0.9), λ = wavelength of the x-ray, β = full width at half maximum (FWHM) in radian and Θ = Bragg's angle [Klong and Alexander, (1954); Scherrer, (1918); Patterson, (1939)]. Figure 2.2: shows the schematic diagram of full width half maximum.

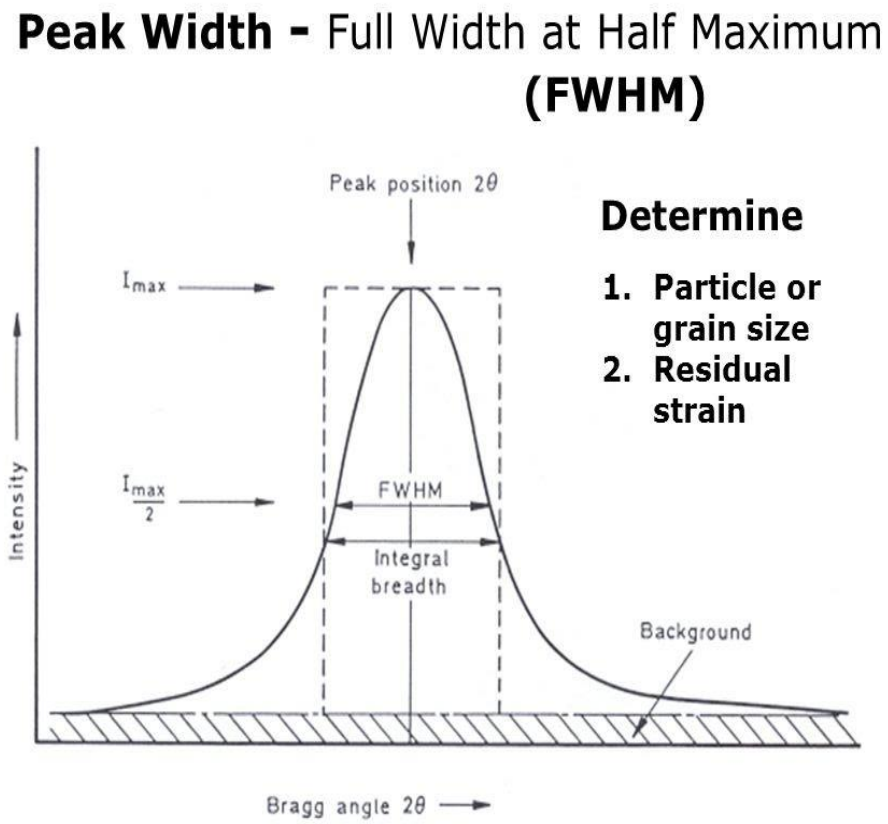

Figure 2.2: Schematic diagram of full width half maximum.

2.3 Transmission Electron Microscope (TEM)

It is a high-resolution characterization technique that has the capability to image atoms in crystalline specimens with resolutions upto 0.1nm, smaller than interatomic distance. This type of analysis technique is tremendously essential for characterizing the materials at a scale ranging from atoms to nanometres. The information regarding the particle size, shape, crystallinity and interparticle interaction can be demonstrated using TEM analysis. It is an important microscopic technique in which an electron beam from an electron gun is passed through an ultra-thin specimen less than 100nm thick. The interaction of the electron with the specimen resulted in the formation of an image when the electron beam is transmitted through the specimen. The image thus formed can be

magnified further and then focused onto an imaging device such as a layer of photographic film, fluorescent screen, or sensors such as scintillator attached to charge couple devices. TEM was illustrated by Max Knoll and Ernst Ruska for the first time in the year 1931 and the first commercial TEM was launch in 1939. In 1986, Ruska was honoured with the Nobel Prize in Physics for the development of TEM. Its working principle is based on the electron's wave nature and the wavelength λ which is given by,

$$\lambda = \frac{h}{p} = \frac{h}{(mv)} = \frac{h}{\sqrt{2mE}} = \frac{h}{\sqrt{2meV}}$$

This equation is also known as de-Broglie equation. Where, *h* represents Planck's constant, m is the mass of the electron, *v* represents the velocity of the electron, *E* is energy and the applied potential *V*. The wavelength associated with the electron decreases when the voltage is higher and thus allowing the electrons to penetrate a distance of microns into a solid. Hence, it enabled to image and structure of material upto the atomic level.

Resolution is very important for an image to distinguish one from another. The resolving power of a microscope is different from its magnifying power. Even though an image is magnified with a power lens, the image will not be cleared and it will be difficult for the image to read and hence the magnification will not enhance the resolution power of a microscope. Resolution *d* of a microscope is related to wavelength as:

$$d = \frac{\lambda}{2NA}$$

where, *NA* represents the numerical aperture of the system. De Broglie wavelength of electron (= 2.85x10-3 nm at 160 kV) is very short as compared to the wavelength of visible light by about one million times. TEM can magnify the image about one million times than the optical microscope. Figure 2.3 shows the schematic diagram for a TEM.

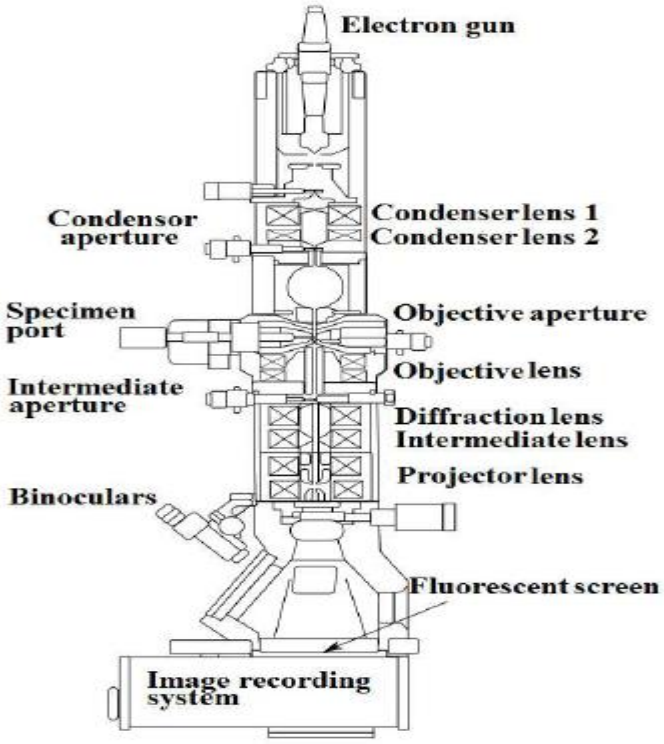

Figure 2.3: Schematic diagram of TEM

Generally, a TEM is composed of the basic components, namely an electron source, vacuum, specimen stage, electromagnetic lens and detectors. When the pin-shaped cathode is heated up the current, the electrons ray is turned out. This electron ray is vacuumed up at anode using high voltage. As the voltage is higher, the wavelength turned out to be shorter which results in the higher resolution of the electron microscope. The accelerated electrons are further moved to the drill-hole at the bottom of the anode. The electronic coils generate an electromagnetic field in the lens system. The condenser lens first focused on the electron ray and then passed through the object. The scattered electrons after passing through the object are collected by an objective. Thus an image is formed. The image so formed can be enlarged using an additional lens (projective with an electron microscope) and visualized on the fluorescent screen of the CCD camera. High-resolution TEM (HRTEM) enabled to observe the rearrangement of atoms directly in a sample. SAED provides a set of diffraction spots or rings of the crystal lattice when

the lattice diffracted the high energy electrons. These diffracted rings are of great use for evaluating the interplanar spacing using the formula;

$$d_{h,k,l} = \frac{L\lambda}{R}$$

Where, L is a constant for the particular (the length of the camera), λ is the wavelength of the electron and R is the radius of the diffraction ring.

Sample preparation for TEM, HRTEM or SAED analysis is as follow, the sample is first ground into powders and then dispersed using dispersive solvents. Few drops of the dispersed solution are put on the copper grid which is already coated with carbon. Then it is put into the sample holder and inserted into the instrument. The sample is scanned by applying a high voltage.

2.4 SEM and EDX

The main components of SEM consist of an illumination system, specimen stage, objective lens, magnification system, data recorder system, chemical analysis system. Tungsten filaments are usually used as an illumination system and magnetic lens as magnification. Like TEM, there are two or three lenses above the specimen which acts as a condenser and the final lens also known as the objective lens which narrows the incident beam upto~10nm. Figure 2.4 shows the schematic representation of SEM. In the process, the electron probe scanned across the specimen horizontally in two perpendiculars (x and y) directions. Sawtooth-wave generator generated the x-scan which is relatively fast. This generator gives scanning current to the two coils which are connected in series on either side of the optic axes. Further, these coils create a magnetic field in the y-direction, creating a force on the electron (travelling in the z-direction)that deflects in the x-direction. Y-scan is relatively slow and it is resulted due to the second sawtooth-wave generator. In such kind of process, the electron losses its energy due to repeated random scattering and absorption occurred within specimen volume. The exchange energy that occurred between the electron and sample within the specimen

volume is responsible for the electrons to get reflected through elastic scattering, emission of electromagnetic radiation, emission of the secondary electron through inelastic scattering, which is detected in the detector. The amplified output signals are fed to cathode-ray tubes and thus, images are captured using cameras with the high-resolution ability [Egerton, (2016); Singh, (2011)]. Moreover, the emitted x-rays are also utilized for the sample to determine its chemical composition using suitable electron voltage (EDAX). For the entire process, the sample should be conductive or it will be made conductive.

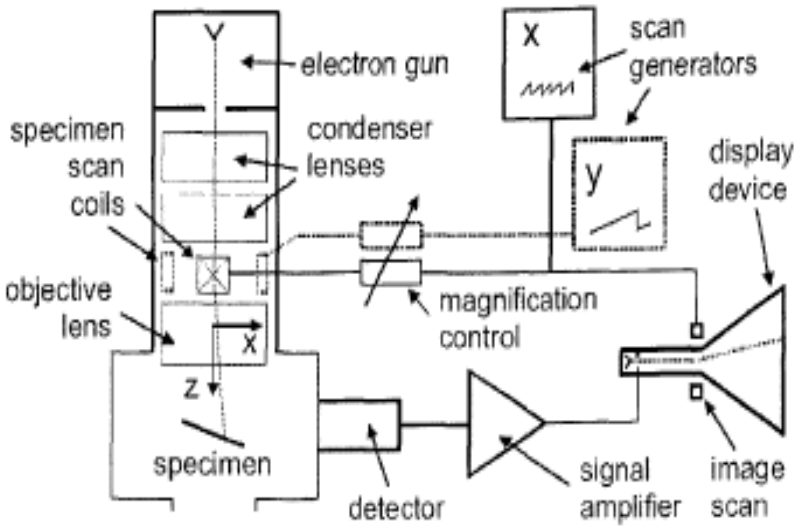

Figure 2.4: Schematic representation of SEM.

EDAX (Energy-dispersive analysis of x-ray) is one of the essential techniques to find the constituent elements present in a particular sample. It works on the fact that every element has a different atomic structure, so there are different peaks for different atoms in the x-ray spectrum [Goldstein, (2003)]. Only the electrons in the inner shells are responsible for the exhibition of x-rays and the energy or frequency resulted from the observed x-rays are related to the atomic number as:

$$E = C_1(Z-C_2)^2$$

Here, C_1 and C_2 are constants that depend on the types of lines. The atomic number of an element that produces lines can be determined if the energy of K,L,M lines are given [Goldstein, (2003)]. The schematic diagram which shows the electron transition in an atom is shown in figure 2.5. Measuring the elemental composition as well as the surface morphology need the sample to be ground and dispersed using suitable solvents. Then, it is transferred to the carbon-coated film and inserted inside the SEM instrument. Low pressure is evacuated inside the chamber. The sample is scanned applying high voltage. Thus the surface morphology as well as the elemental composition is evaluated using the images obtained.

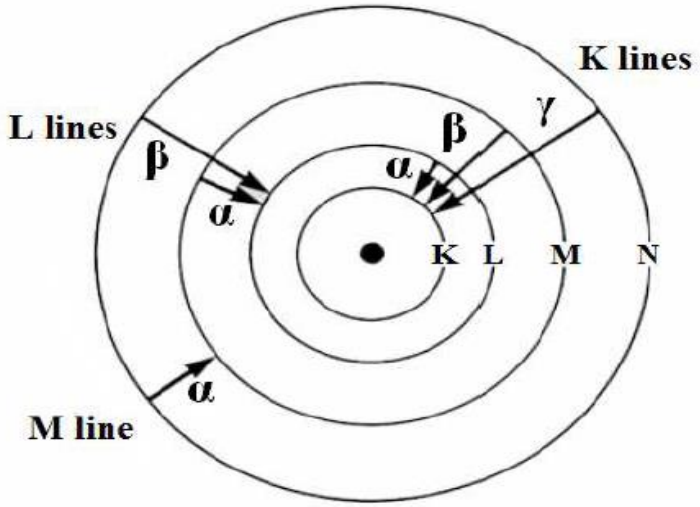

Figure 2.5: The schematic diagram which shows the electron transition in an atom.

2.5 FT-IR Spectrometer

FT-IR spectroscopy is an economical, rapid, easy, and non-destructive technique deserving wider use for material analysis. Infra-red spectroscopy is used to get an infrared spectrum of emission, absorption, Raman scattering of a solid, liquid or gas. When infra-red radiation passed through a material, some of the radiations are being transmitted while some of them get absorbed by the sample. Hence the FT-IR spectrum is consisting of molecular absorption as well as transmission. FT-IR spectroscopy analysis is useful to obtain information regarding the vibration and rotational of chemical bonding and molecular structure. FT-IR peaks are resulted due to the frequencies of vibration between the atomic bonds of the materials. The fingerprint of a sample can be represented by FT-IR spectrum as different materials show different FT-IR spectrum i.e. no two different materials are having the same FTIR spectrum. So, effective identification of a material can be done using FTIR spectra [Banwell and McCash, (1994); Colthup *et. al*., (1964)]. From FT-IR spectra, it is possible to indicate the amount of material present depending on the size of the peaks obtained. Depending on its frequency range IR region can be divided into three different regions, namely near IR, mid-IR and far IR.

In FT-IR instrument, a prism or grating allowed to separate the energy which was emitted from the infra-red source into different frequencies like a prism separates the white light into seven different colours. FT-IR took a long time to scan, hence it was developed using an optical device known as an interferometer to measure all the IR frequencies at a time instead of measuring one after another. The signals produced using an interferometer are very unique as all the IR frequencies are coded into it. Hence, it takes significantly less time to measure the signals. When the signals obtained using an interferometer is unable to define directly, decoding an individual frequency is required to interpret the signal. This decoding of signal can be done using Fourier transformation. A schematic diagram of FT-IR spectrometer is shown below:

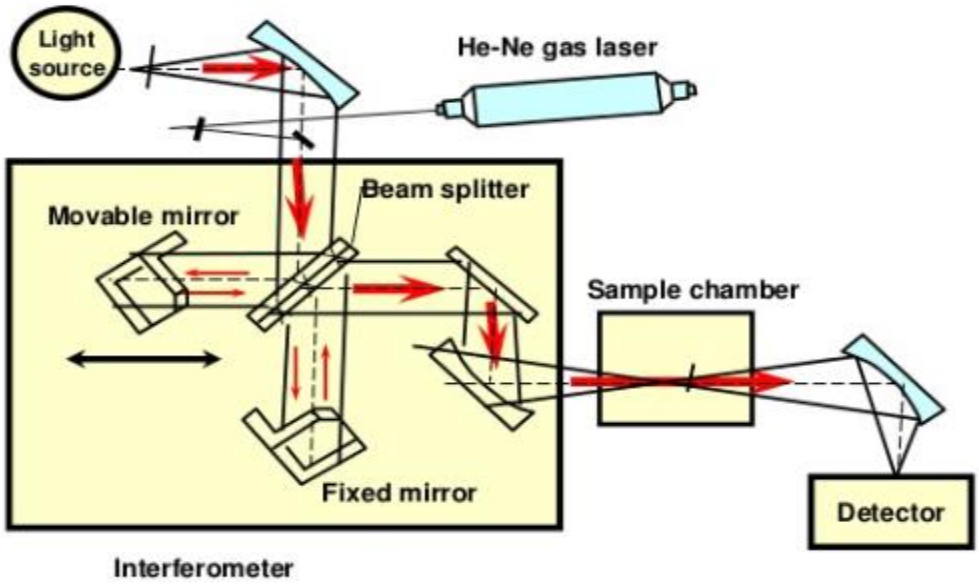

Figure 2.6: Schematic diagram of FT-IR

FT-IR consists of the main components such as source, interferometer and detector. A glowing black body is generally used as an IR source that releases IR energy. The IR energy from the source is first passed through an aperture to control the energy required for the material to be analyzed. Then it passed through the interferometer. Michelson interferometer is one of the most commonly used interferometers. This kind of interferometer consists of a fixed as well as a movable mirrors along with a beam splitter. The beam splitter splits the incoming IR energy into two components, one component directed towards the fixed mirror while the other component directed towards the movable mirror. The two energy components are further recombined together at the beam splitter due to the generation of path difference between the beams since one beam is used to travel upto a fixed length as it is reflected from the fixed mirror while the other component travelled with constantly changing its length as the mirror moves. The interfering of these two beams resulted in the production of signals known as an interferogram. The signals (interferogram) are further passed through the sample chamber and thereby generating IR signals and finally reached to the detector.

2.6 Photoluminescence spectrometer

It is a process of spontaneous emission of light due to the optical excitation of a material. Photoluminescence (PL) studies are very useful for the characterization of several parameters of a material. PL spectroscopy exhibited electrical information and it is a very sensitive probe for electronic states. The emission spectra resulted from PL measurement is capable of distinguishing surfaces, interfaces, impurity levels etc. The lifetime of a bulk state of the non-equilibrium interface can be obtained from the transient PL intensity resulted from pulsed excitation. PL emission intensity is affected by the change in temperature. Time-resolved PL is fast and it is also important for characterizing a rapid process that takes place within a material. Materials with low radiative efficiency are unable to analyze by ordinary PL. The optical activity of material plays an important role in determining its impurity level. The excitation as well as the emission of a material can be recorded using a fluorometer. Fluorometer is of two types namely Filter fluorometer and Spectrofluorometer. In case of filter fluorometer, a filter is generally used to isolate the emission and incident light whilst a spectrofluorometer used a diffraction grating monochromator to do the same. Comparing the two fluorometers, spectrofluorometer is more advantageous than that of filter fluorometer as spectrofluorometer can scan a sample in a wide range of wavelengths but it is more expensive. The working principles of the two fluorometers are the same.

The light which comes from the light source in the excitation wavelength range of material is passed through a monochromator or an excitation filter. Then, only the required energy range is allowed to pass through the sample. The sample is further excited by absorbing the light coming from the monochromator or a filter and produced fluorescence when it gets back to the ground state again. The produced emission light is emitted in all directions and some of it passed through a second monochromator or filter before it goes to the detector. This second type of filter is responsible for screening out the light (Rayleigh and Raman scatter) emitted from the sample. Generally, the second type of filter or emission filter is used to keep at 90^{o} with the incident light to let the

transmitted light reaching the detector without disturbances. Hence, a better signal-noise ratio is obtained by lowering the detection limit compared to the 180^{o} geometry [Rendell, (1987)]. A schematic diagram of Spectrofluorometer is shown below in figure 2.7.

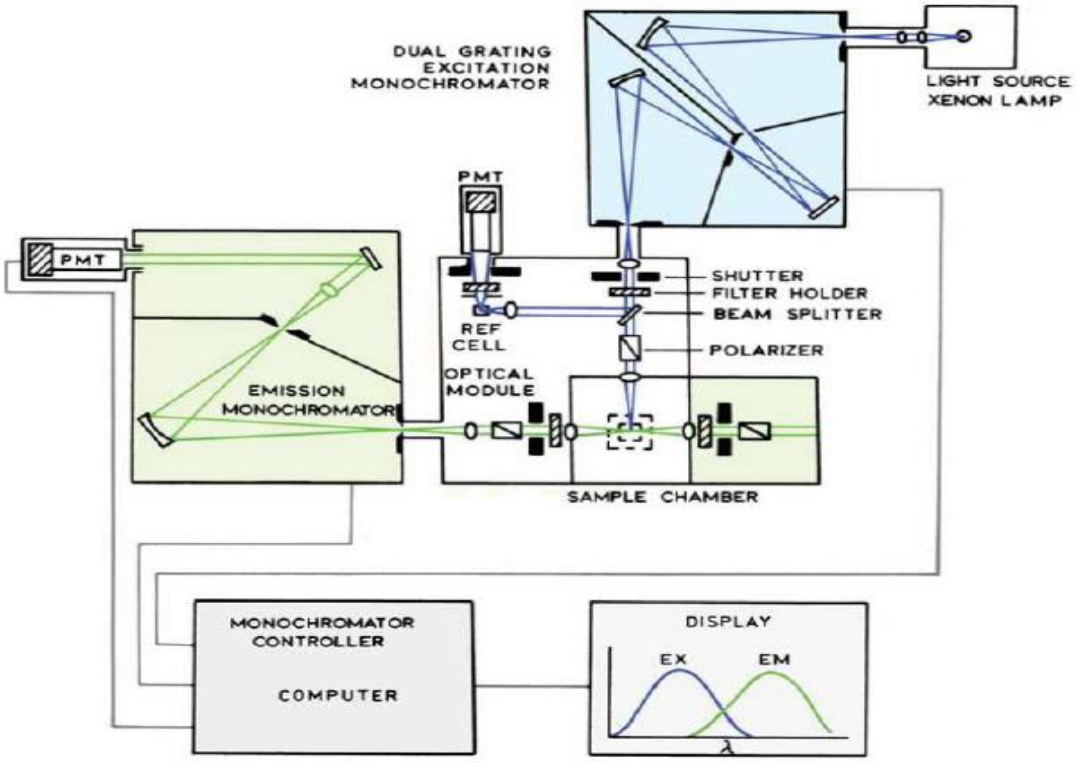

Figure 2.7: Schematic diagram of a Spectrofluorometer.

Xenon arc lamp, xenon-mercury arc lamp, high-pressure mercury vapour lamp, LED etc. are generally used as a light source in fluorometers [Lakowics, (1983)]. Even though the fluorometer with laser as a light source doesn't require an excitation filter or a monochromator due to the narrow emission wavelength, it is very inconvenient as the wavelength cannot be changed. LEDs as a light source for fluorometer is having many advantages like low power consumption, long lifetime, wide range of wavelength etc. So, this light source is considered as a good source even for the near future. Lamps are also one of the good light sources producing a wide wavelength range other than the

required to excite the material. Xenon lamp is one of the most commonly used light sources which emits light with a wavelength range of 190nm to 1200nm. Mercury vapour lamp is not suitable for fluorometer as it gives intensified light with wavelength concentrated only in Hg spectrum. Photomultiplier which consists of 6-12 diodes exhibited an anodic current corresponding to the light intensity. The supplied voltage affects greatly to the intensity of the signal as well as noise. Noises are greater when the supplied voltage is high enough. Hence, balancing the sensitivity and noise is much required.

Chapter 3

Synthesis, Characterization, Photoluminescence and Photocatalytic studies of $BiPO_4:Ce^{3+}$

3.1 Introduction

Rare-earth ions doped luminescent materials have attracted much attention because of their wide applicability in the fields of lighting and display devices, optoelectronics etc. [Park *et al.,* (2013); Singh *et al.,* (2019); Yang *et al.,* (2013)]. Among the rare-earth ions, Ce^{3+} is very much sought after due to its low cost, spin and parity allowed optical 4f–5d transitions and its applications in scintillators, light-emitting diodes and field emission displays etc. [Dabre *et al.,* (2014)]. Moreover, Cerium ions doped phosphors could absorb in UV region with a large cross-section and emit in the blue region of the visible radiation due to allowed electric dipole transitions, which makes them suitable for applications in the fields of lithography, imaging, optical data recording [Lai *et al.,* (2008)].

In the last few years, phosphate based luminescent materials have drawn a considerable attention because of their potential applications in photoluminescence, photocatalysis, superionic conductors, moreover, they have high physio-chemical stability [Ganguli *et al.,* (2015); Naidu *et al.,* (2012); Guan *et al.,* (2008)]. As a member of phosphate family, $BiPO_4$ is considered as one of the most suitable host for doping rare earth ions because of their comparable in size of Bi^{3+} with the trivalent rare-earth ions. $BiPO_4$ normally crystallizes in three crystallographic forms: Hexagonal phase, low-temperature monoclinic and high-temperature monoclinic phases [Zhao *et al*., (2013)]. Hexagonal phase is generally formed at lower temperature and it can be converted into low-temperature monoclinic phase on heating above 600˚C. High-temperature monoclinic phase of $BiPO_4$ is rarely reported due to their metastable feature [Zhao *et al*., (2013)]. Hexagonal and Monoclinic structures of $BiPO_4$ essentially differ in the co-ordination number of Bi^{3+}. In case of hexagonal phase, Bi^{3+} ions are surrounded by eight

neighbouring oxygen atoms and forming square anti-prism geometry.Whereas in case of monoclinic phase nine near oxygen atoms surround Bi^{3+} ions. In hexagonal phase, BiO_8 polyhedra and PO_4 tetrahedra with lattice water molecules located in channels are symmetrically arranged in a chain form parallel to the c-axis [Naidu *et al.,* (2012); Arunkumar *et al.,* (2012)]. But in monoclinic phase, the chains are unsymmetrically arranged [Arunkumar *et al.,* (2012)]. Monoclinic phase exhibited superior photoluminescence and photocatalytic activity than the hexagonal phase [Achary *et al.,* (2013)]. Additionally, the luminescence arising from the Bi^{3+} species is also quite interesting because of its electron transition between the $6s^2$ ground states and the 6s6p excited states and significant Stoke shift associated with its emission–absorption characteristics [Naidu *et al.,* (2012)].

On the other hand, semiconductor photocatalysis has become the most attractive research topic among researchers in the past few years as it is considered as the most promising method to solve energy problems and environment-related problems [Wang *et al.,* (1997); Kamat, (1993)]. It has potential applications in water splitting to generate hydrogen and decomposition of organic dyes in waste-water. The organic dyes present in waste-water are very stable in the natural cycle. Therefore, it causes hazardous effects on living beings (both aquatic and surface environments). It also caused carcinogenic, mutagenic to human being as well [Lellis *et al.,* (2019), Berradi*et al.,* (2019)]. Hence, the degradation of these organic dyes is of great importance before entering into the fresh water bodies. In this regard, $BiPO_4$ is considered as a good UV-light active photocatalyst semiconductor due to its high efficiency to separate the electrons and holes, low cost, high stability etc. It has also been reported that $BiPO_4$ has greater activity on the degradation of some organic dyes, phenol, benzene than the P25 under UV light irradiation [Pan and Zhu (2010); Pan *et al.,* (2012); Xu *et al.,* (2013)]. Moreover, doping of Ce^{3+} ion into semiconductor leads to increase its surface area and also enhances the electron-hole charge separation which higher its photocatalytic activity [Reli *et al.,* (2019); Regmi *et al.,* (2018)]. Therefore, the present study is focused

on the investigation of photoluminescence and photocatalytic properties of Ce^{3+} doped $BiPO_4$ prepared by co- precipitation method using ethylene glycol as reaction medium.

3.2 Experimental details

3.2.1 Materials

The chemicals used for the synthesis of Ce^{3+} doped $BiPO_4$ are cerium nitrate hexahydrate ($Ce(NO_3)_3.6H_2O$) (with 99.99% purity), Bismuth nitrate pentahydrate ($Bi(NO_3)_3 \cdot 5H_2O$) (with 98% purity), Ammonium dihydrogen phosphate ($NH_4H_2PO_4$) (with 98% purity). All chemicals were purchased from Alfa Aesar. The solvent ethylene glycol was purchased from Merck.

3.2.2 Preparation of Cerium ions doped Bismuth Phosphate

In a typical synthesis, the stoichiometric amount of $Bi(NO_3)_3 \cdot 5H_2O$ was added into a round bottom flask containing 70 ml of ethylene glycol. The solution was stirred in a magnetic stirrer for 30 minutes. Then, the stoichiometric amounts of $NH_4H_2PO_4$ and $Ce(NO_3)_3.6H_2O$ were added into the above solution and it is refluxed at a temperature of 160˚C for 2hrs. The solution was then allowed to cool down at room temperature and then the precipitate thus formed was washed with distilled water several times and then with ethanol. After that, the sample was dried in an oven at a temperature of 80^{o}C for 12 hrs [Naidu *et al.,* (2012)]. Similar process was followed for preparing different doping concentrations of Ce^{3+}.

3.2.3 Characterizations

Bruker D2 phaser XRD machine equipped with Cu Kα radiation (λ=1.5406Å, Ni filter, 2Θ = 15° to 60° operated at 30kV and 100mA) was used to determine the crystal structure of the prepared samples. The vibrational spectra of the prepared sample were analyzed using Shimadzu Iraffinity-1s FT-IR spectrometer using KBr as beam splitter. Field emission scanning electron microscopy (FESEM) was recorded by Jeol JSM-6390 in order to see the morphologies of the samples. The absorption band and the

photocatalytic activities of the samples were recorded by Jasco V-730 UV-Visible spectrophotometer. Hitachi (F-7000) fluorescence spectrophotometer having xenon discharge lamp as excitation source was used for the recording of excitation and emission spectra. All the measurements were taken at room temperature.

3.2.4 Photocatalytic activity measurement

Methylene blue was chosen as a target pollutant for evaluating the photocatalytic activity of the prepared $BiPO_4$:7at. $\%Ce^{3+}$ because it is one of the most commonly used dye in industries, mainly for printing, textiles and leather industries [Mills *et al.,* (2011)]. It causes environmental and biological problems [Jalali *et al.,* (2019)]. It also causes headache, shortness of breath, high blood pressure to human being [Zhang *et al.,* (2013)]. The photocatalytic activity of the prepared $BiPO_4$:Ce^{3+} (7at. %) sample was analyzed through the degradation of methylene blue dye under UV-light irradiation (Spectroline E-Series UV lamp with 254nm). The details of the procedure are as follow, 10 ppm of methylene blue solution was prepared in an aqueous solution. Then 100mg of the catalyst was suspended in 100ml of above methylene blue solution. The solution was stirred using a magnetic bar for 15 minutes and then kept in the dark place for about 30 minutes in order to achieve adsorption-desorption equilibrium. Then the solution was irradiated by UV light at a wavelength of 254 nm. Every 10 minutes, the absorbance of the sample was recorded using UV–Vis spectrophotometer. The discolouration efficiency (I %) was calculated using the formula

$$\text{I (\%)} = \frac{C_o - C_t}{C_o} X100$$

Where, C_o isthe initial concentration of the dye and C_t is the concentration of the dye after UV-light irradiation at time t.

3.3 Results and Discussions

3.3.1 XRD study

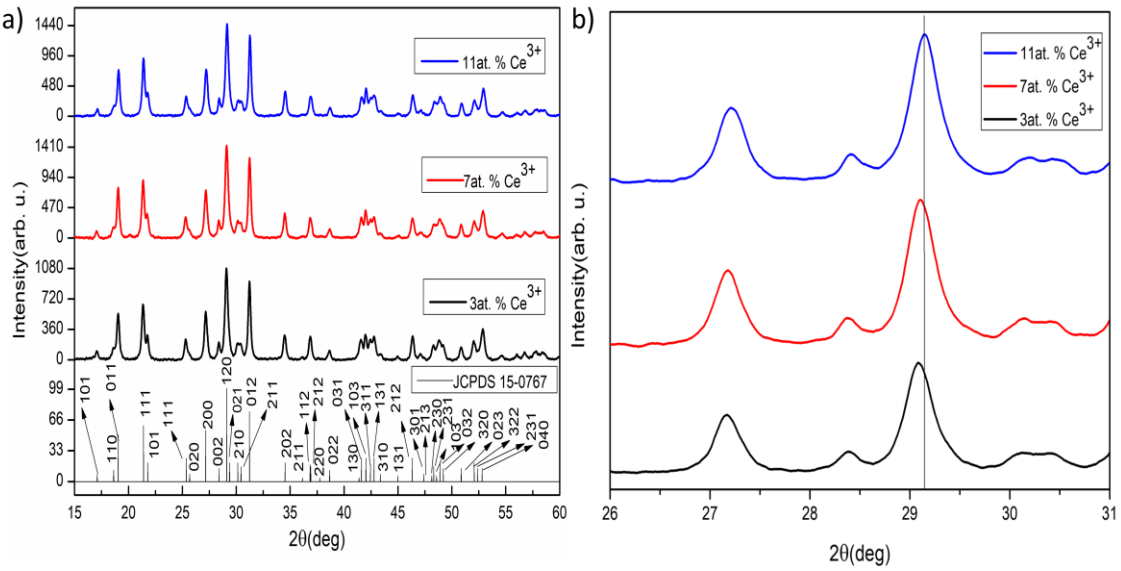

Figure 3.1: a) XRD patterns of the prepared $BiPO_4$:xCe^{3+} (x = 3, 7, 11at. %). b) Expanded view of the diffraction peaks in the 2θ range from 26 to 31 which shows the deflection of the peak with concentrations.

Figure 3.1(a) shows the XRD patterns of Ce^{3+} (3, 7 and 11at. %) ions doped $BiPO_4$ phosphors. The diffraction peaks of the prepared samples are well-matched with the low-temperature monoclinic phase of the $BiPO_4$ according to the JCPDS No. 15-0767 [Guan *et al.,* (2008)]. The observed diffraction peaks were strong and sharp indicating that the prepared samples are well crystallized. Further, no possible impurity phases were detected, showing that the prepared samples are crystallized in pure low-temperature monoclinic phase. Figure 3.1(b) showed the shifting of diffraction peak to the higher angle as the concentrations of dopant Ce^{3+} ion increases which is due to the smaller size of Ce^{3+} ion (1.07 Å) as compared to Bi^{3+} ion (1.17 Å) [Li *et al.,* (2018); He *et al.,* (2016)]. This shifting of diffraction peaks confirmed the successful doping of Ce^{3+} ions into the interstitial site of $BiPO_4$ [Shannon, (1976); İlhan *et al.,* (2018); İlhan,

(2017)]. The calculated lattice parameters and cell volumes are shown in table 3.1. It is seen that the cell volume is decreased with the increase of Ce^{3+} ion concentration which is due to the smaller size of Ce^{3+} ion as compared to the Bi^{3+} ion. The substitution of Bi^{3+} ion by Ce^{3+} ion is also supported by the reduction in cell volume.

Table 3.1: Calculated lattice parameters and cell volumes of Ce^{3+} ions doped $BiPO_4$.

Dopant Ceriumion concentrations (atomic percentage)	Lattice parameters			Cell volume (V) $Å^3$
	a(Å)	b(Å)	c(Å)	
3	6.754	6.937	6.47	294.465
7	6.752	6.936	6.469	294.277
11	6.741	6.934	6.463	293.572

3.3.2FT-IR and SEM Image study

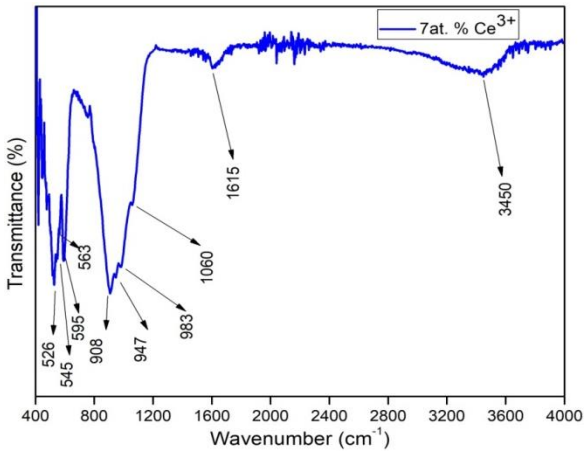

Figure 3.2: FT-IR spectrum of $BiPO_4$: Ce^{3+} (7at. %).

The FT-IR spectrum of $BiPO_4$:Ce^{3+} (7at. %) is shown in figure 3.2. The bands observed at 3450 and 1615 cm^{-1} correspond to the stretching and bending vibrations of O–H bond that is originated from the adsorbed H_2O molecules on the surface of the

sample [Huang *et al.,* (2011); Li *et al.,* (2005)]. The bands observed at 947, 983 and 1060 cm^{-1} are attributed to the symmetric stretching vibrational modes of O-P–O bond and the band observed at 908 cm^{-1} can be assigned to the symmetric stretching vibrational mode of O-P-O bond within the PO_4^{3-} group [Naidu *et al.,* (2012); Pawlig *et al.,* (2001)]. The bands observed at 595, 563, 545 and 526 cm^{-1} correspond to the bending vibrational modes of O-P-O linkage [Pawlig *et al.,* (2001)]. All these observed bands are the characteristic bands of PO_4^{3-} group of a monoclinic structure. So, the formation of monoclinic phase is further supported by the above analysis. The rice shape morphology of $BiPO_4:Ce^{3+}$ (7at. %) phosphor was observed from SEM image analysis and the SEM images of $BiPO_4:Ce^{3+}$ (7at. %) is shown in figure 3.3.

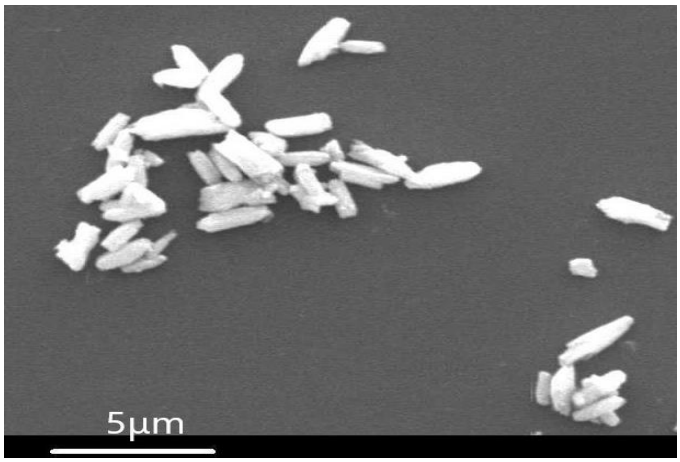

Figure 3.3: SEM image of BiPO4:Ce^{3+} (7at. %).

3.3.3 Photoluminescence study

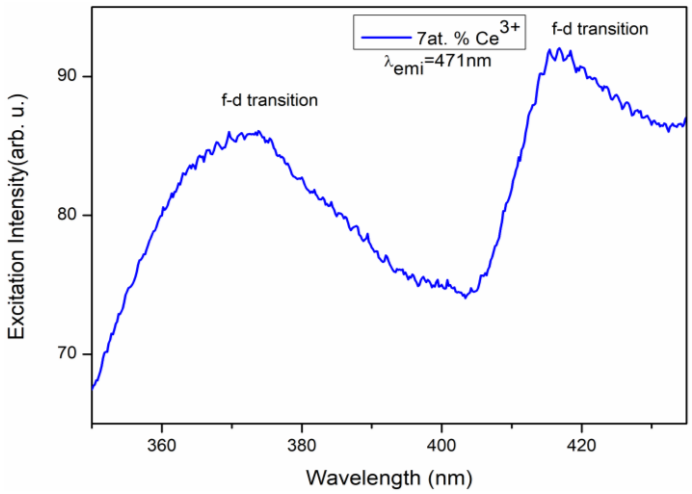

Figure 3.4: PLE spectrum of $BiPO_4$: Ce^{3+} (7at. %) (λemi= 471nm).

Figure 3.4 showed the photoluminescence excitation spectrum of prepared $BiPO_4$:Ce^{3+} (7at. %). The excitation spectrum was recorded by monitoring the emission wavelength at 471 nm. The spectrum consists of two emission bands centring at 370 and 417 nm which correspond to $^2F_{5/2}$→5d transitions of Ce^{3+} ion [Wang *et al.*, (2018); Singh *et al.*, (2015); Yang *et al.*, (2016)].

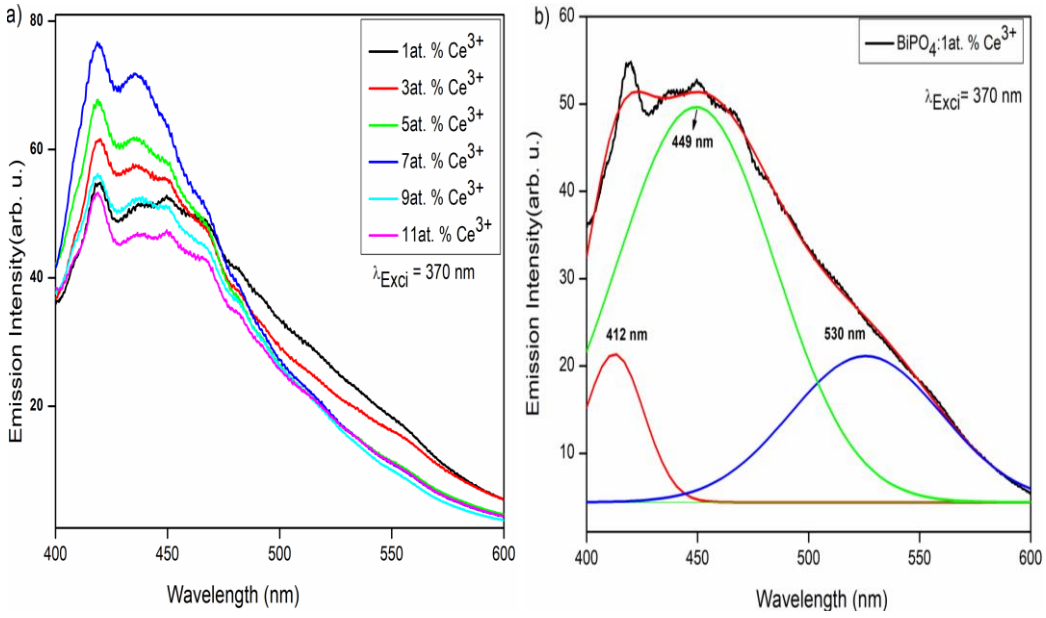

Figure 3.5: a) PL spectra of $BiPO_4$:$x$$Ce^{3+}$, ($\lambda_{emi}$=370nm) ($x$=1,3,5,7,9,11at. %) b) Gaussian fitting of the peak of $BiPO_4$:1at. % Ce^{3+}.

Under excitation at the wavelength of 370 nm, a broad emission band extending upto 600 nm having maximum at 419 nm was observed which is due to the 5d-$^2F_{5/2}$, $^2F_{7/2}$ allowed transition of Ce^{3+} ion resulted from the coupling of 5d electron with the host lattice (as shown in figure 3.5) [Yang *et al.*, (2016); Talewar *et al.*, (2018)]. This broad emission band can be split into three different bands at 412, 449 and 526nm by Gaussian curve fitting and these bands are resulted due to the transition from ground state to different field-splitting 5d levels of Ce^{3+} ions [Pawlig *et al.*, (2001); He *et al.*, (2016); Shi *et al.*, (2014)]. However, under excitation at 417 nm, the observed emission band is extended from 465 to 480 nm with maximum peak intensity at 471 which is due to the 5d $\rightarrow$$^2F_{7/2}$ transition of Ce^{3+} ions and is fall in the blue region of the electromagnetic wave (as shown in figure 3.6) [Pawlig *et al.*, (2001)]. Except the photoluminescence intensity, there is no significant change in the peak profile with the change of Ce^{3+} ion concentration. The photoluminescence intensity was found to increase with the increase of Ce^{3+} till it reaches 7at. %. Beyond this concentration, the intensity was found to

decrease upon excitation at both the wavelengths 370 and 417 nm. This decreased in the photoluminescence intensity beyond 7at. % Ce^{3+} is due to the concentration quenching [Katelnikovas *et al.*, (2008)]. This can be explained as the concentration of Ce^{3+} ion increases, inter-ionic distances between the Ce^{3+} ions decreases. When the inter-ionic distances among Ce^{3+} ions are lower than the critical distance, the non-radiative energy transfer among the Ce^{3+} ions increased. This results in the quenching of emission intensities [Singh *et al.*, (2018)].

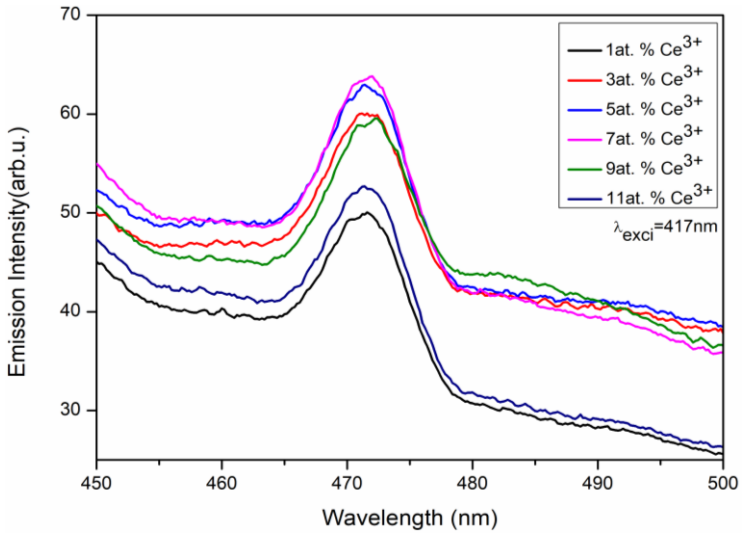

Figure 3.6: PL spectra of $BiPO_4$:$x$$Ce^{3+}$, ($\lambda_{emi}$=417nm) ($x$=1, 3, 5, 7, 9, 11at. %).

3.3.4 Optical property study

The absorption spectra of $BiPO_4$: Ce^{3+} (7at. %) is shown in figure 3.7 (a). The figure showed that the absorption band is extended in a wide range from UV to visible with maximum absorption in the UV region which indicates that the sample can use as a photocatalyst under UV-light irradiation. The energy band gap was determined using the formula for optical absorption:

$$\alpha h\nu = A(h\nu - E_g)^{n/2}$$

Where α is the absorption co-efficient, h is the Planck's constant, ν is the photonic frequency, A is the constant relative to the material, E_g is the absorption energy gap and

n depends on the type of transitions (for direct transition, n=1 and for indirect transition, n=4). As $BiPO_4$ exhibits indirect transition, the absorption energy band-gap is determined by extrapolating the linear portion of the plot of $(\alpha hv)^{0.5}$ *Vs hv*and it is shown in figure 3.7 (b) [Pan and Zhu (2010)]. The estimated energy band gap was found to be 3.81eV. This observed energy band gap is almost the same as that reported in the literature [Xu *et al.,* (2013)].

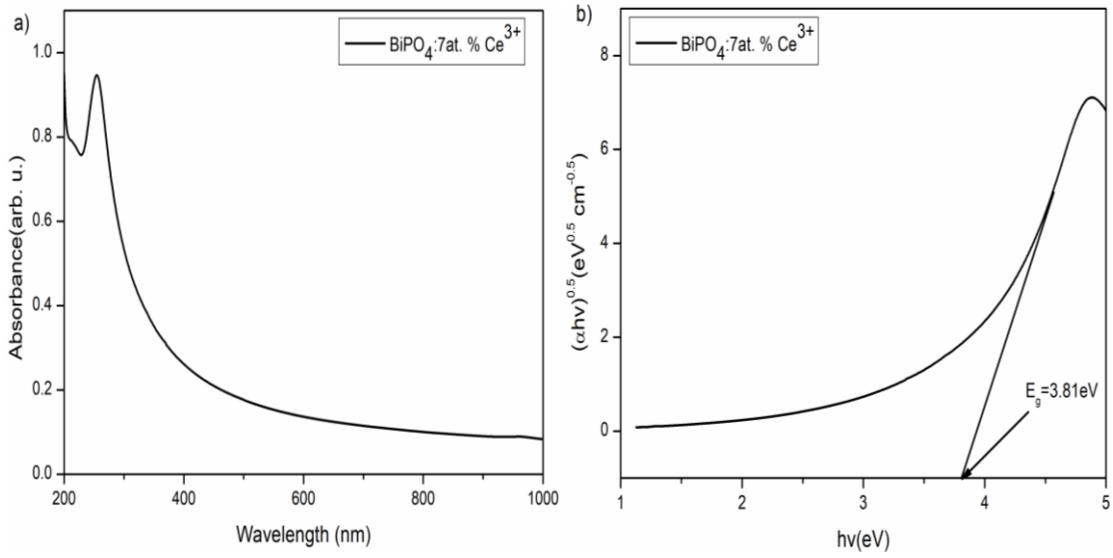

Figure 3.7: a) Absorbance spectra of $BiPO_4$:7 at. % Ce^{3+} b) Band-gap of $BiPO_4$:7at. % Ce^{3+} calculated using Tauc plot. (α - absorption co-efficient, h – Planck's constant, v - photonic frequency, Eg - absorption energy gap, eV – electron volts).

3.3.5 Photocatalytic activity study

The photocatalytic activity of the prepared $BiPO_4$:Ce^{3+} (7at. %) was examined through the degradation of methylene blue dye under UV-irradiation. Figure 3.8 shows the absorbance spectra of methylene blue dye at different time intervals. It was reported that methylene blue dye doesn't degrade itself [Hou *et al.,* (2018)]. However, with the addition of the prepared catalyst, the absorption spectrum was significantly decreased. The absorbance was recorded every 10 minutes and after 120 minutes of UV light irradiation, 90% of the dye was degraded. On irradiation under UV light, the

photogenerated electrons are introduced in the conduction band and photogenerated holes are produced in the valence band which is responsible for the degradation of methylene blue dye [Chang *et al.*, (2018)]. The electrons in the conduction band of $BiPO_4$ adsorbed O_2 from the water molecule and formed $O_2^{-\bullet}$, while the holes in the valence band interact with absorbed H_2O molecules to form hydroxyl radicals. The $O_2^{-\bullet}$and $OH^{\bullet}$ decomposed Methylene blue to CO_2 and H_2O [Lu *et al.*, (2015)]. From this investigation, it is believed that the prepared sample may have potential application in degrading the colouring organic dyes present in waste-water.

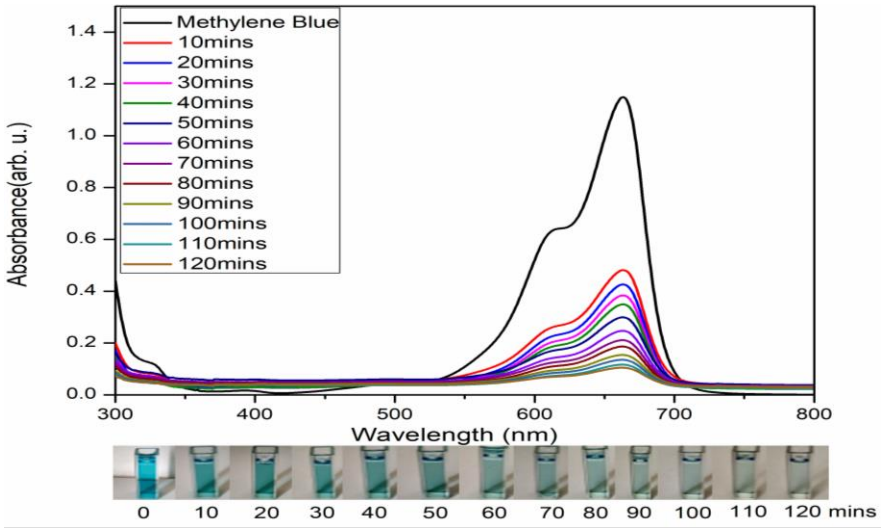

Figure 3.8: Photodegradation of Methylene blue under UV-light irradiation using $BiPO_4$:7at. % Ce^{3+}.

3.3.6 Kinetics study

The kinetics involving the rate of degradation of methylene blue under UV-light irradiation was discussed. The order of the reaction was calculated by plotting a graph between ln [C_t] vs time, where C_t is the concentration of the dye at time t. The graph exhibited a negative slope which confirmed the reaction followed a first-order kinetic figure 3.9(a). Further, ln [C_o/C_t] vs time graph was plotted as shown in figure 3.9(b) which showed that the degradation of methylene blue followed first-order Langmuir-

Hinshelwood kinetics model and pseudo first-order kinetics equation is given below [Naciri *et al.,* (2019)]

$$\ln(C_o/C_t)=kt$$

Where C_o and C_t represent the initial concentration of methylene blue and final concentration of methylene blue at time t respectively, k represents the first-order kinetic rate constant and t is the time. The rate constant was calculated and found to be 2.56395 $\times 10^{-2}$ min^{-1}.

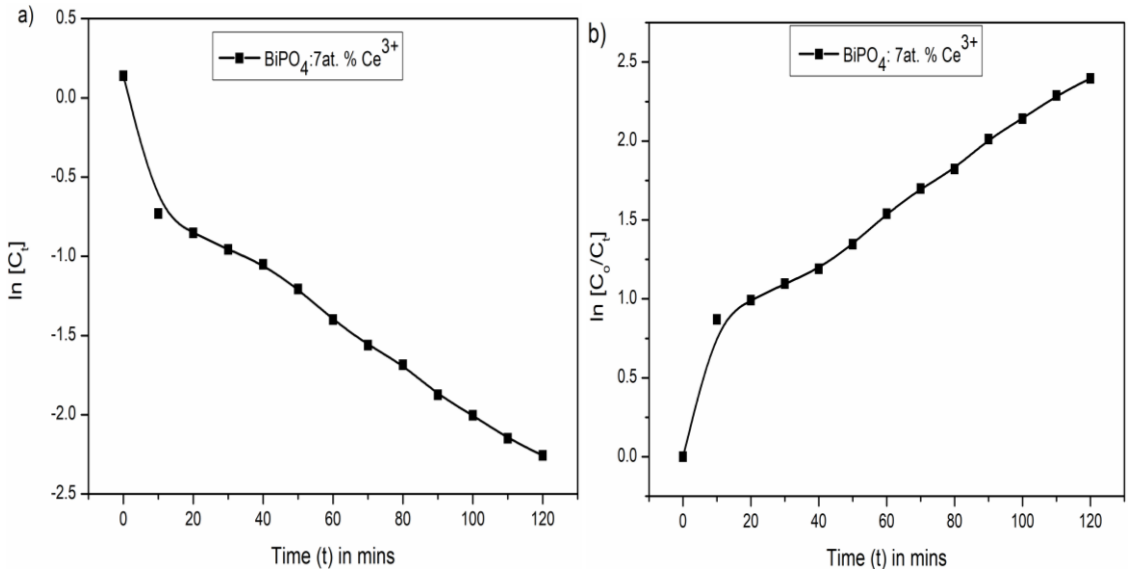

Figure 3.9: a) Plot of $\ln[C_o]$ Vs Time in minutes b) Linear transform $\ln(C_o/C_t)$ Vs Time in minutes of the kinetic curves of Methylene blue degradation. (ln – natural logarithm, C_o – initial concentration, C_t – concentration at time t).

3.4 Conclusions

$BiPO_4$:xCe^{3+} (x=1,3,5,7,9,11) phosphors were synthesized successfully by co-precipitaion method using ethylene glycol as reaction medium as well as capping agent. The prepared phosphors were characterized by XRD, UV-Vis spectroscopy, SEM and PL. Low-temperature monoclinic phase of the prepared phosphors was confirmed from XRD analysis. The prepared phosphors were found to have rice shape morphology. The

PL study showed a broad emission band extending from blue to green region upon excitation at 370 nm. The optimum concentration of Ce^{3+} was found to be 7at. %. Photocatalytic analysis of $BiPO_4:Ce^{3+}$ (7at. %) sample revealed that 90 % of the dye methylene blue could be degraded within 120 minutes of UV light irradiation. From the results, it is concluded that the prepared samples may have potential applications in lighting as well as photocatalysis for the degradation of organic dyes.

CHAPTER-4

Photoluminescence properties of Tb^{3+} doped $BiPO_4$ nanophosphor synthesized by co-precipitation method using ethylene glycol

4.1 Introduction

Nanotechnology is one of the fastest-growing technologies in this modern era and it has been becoming an important tool for manufacturing advanced materials. Nano-sized materials exhibited unique physical and chemical properties rather different from counterpart bulk materials because of their smaller size, large surface area to volume ratio, a large number of loosely bound bonds and unsaturated atoms on the surface [Guisbiers *et al*., (2012); Hong, (2019)]. In addition to this, they also have advantageous features such as reduced scattering of light, surface defect concentration etc. [Hong, (2019); Khan *et al*., (2017)]. Moreover, quantum dots or nanomaterials in which sizes less than 10nm are becoming a hot area of research owing to their outstanding optical and physico-chemical properties and their wide range of applications [Joshi *et al*., (2018); Jia and Misra (2013)]. In the past few decades, ZnO, TiO_2 and CuO nanoparticles are widely studied because of their excellent performance in the fields of photocatalysis, sensors, quantum dots, biomedicals etc. [Jayaprakash *et al*., (2020); Depan and Misra (2014); Venkatasubramanian *et al*., (2013); Gao *et al*., (2016)].

It has been found that rare-earth ion-doped inorganic phosphor materials have applications in various kinds of fields, including solid-state physics, photochemistry, biophysics, etc. [Naorem *et al*., (2020); Singh *et al*., (2020); Selvin, (2002)]. These materials consist of two components: host material and activator, rare earth ion acts as activator ion [Xu *et al*., (2015)]. Among the various host materials, phosphate based materials have been attracted as one of the best hosts due to their high physico-chemical and thermal stability [Shi *et al*., (2015); Hou *et al*., (2019)]. Among phosphate family, $BiPO_4$ has several interesting properties such as high absorption edge, high stability in terms of chemical and mechanical stability, as well as the ionic size of Bi^{3+} is

Similar to that of lanthanide ions [Roming and Feldmann (2009); Naidu *et al*., (2012)] and it also has many potential applications in different fields such as ion sensing, catalysis, radioactive element separation etc. [Charyulu *et al*., (2002); Zhang *et al*., (2020)]. In addition, $BiPO_4$ can be crystallized in three different crystallographic forms: Hexagonal, low-temperature monoclinic and high-temperature monoclinic. In hexagonal structure, Bi^{3+} ion is surrounded by eight oxygen atoms, whereas in case of monoclinic phase, Bi^{3+} ion is surrounded by nine oxygen atoms [Naidu *et al*., (2012)]. The luminescent property of a phosphor is strongly dependent on its phase structure and many researchers have reported that low-temperature monoclinic structure of $BiPO_4$ exhibits the strongest luminescent property in comparison with other phases in case of $BiPO_4$ [Naidu *et al*., (2012); Naorem *et al*., (2020)].

In lanthanide ions doped luminescent materials, the luminescence property is generally originated from the electronic transition within the 4f electrons of doping lanthanide ions and since the 4f electrons of rare-earth ion are shielded by 6s and 5p orbitals, the f-f electronic transition of rare-earth ions is not influenced by the outside environment thereby producing sharp absorption and emission bands. Doping of different rare-earth ions into the host lattice exhibited different emission colours. For example, Ce^{3+} ion normally emits blue colour, Eu^{3+} exhibits red colour and Sm^{3+} exhibits orange colour [Xia *et al*., (2018); Xia *et al*., (2020); Cybinska *et al*., (2016); Huang *et al*., (2019)]. Trivalent terbium ion generally gives green colour due to the $^5D_4 \rightarrow {}^7F_5$ electronic transition of Tb^{3+} ion [Huang *et al*., (2019)], and it has potential applications in various fields including traffic signal, decoration, lighting and display etc. Moreover, it is one of the components of white light. Therefore, the present study investigated the luminescence property of Tb^{3+} ion-doped $BiPO_4$ synthesized by co-precipitation method using ethylene glycol as a reacting medium. Since the luminescence property is strongly influenced by the concentration of doping ion, the effect of Tb^{3+} ion concentration has been investigated to get optimum emission and the

effect of annealing temperatures on the photoluminescence property were also discussed in this chapter.

4.2 Experimental details

4.2.1 Sample preparation

For the synthesis of $BiPO_4:Tb^{3+}$ phosphors, the chemicals used were Terbium nitrate hydrate ($Tb(NO_3)_3.xH_2O$) with 99.99% purity (Alfa Aesar), Bismuth nitrate pentahydrate ($Bi(NO_3)_3{\cdot}5H_2O$) with a purity of 98% (Alfa Aesar), Ammonium dihydrogen phosphate ($NH_4H_2PO_4$) of 98% purity (Alfa Aesar) and the solvent ethylene glycol (Merck). The typical synthesis steps are given as follows; first, the stoichiometric amounts of $Bi(NO_3)_3{\cdot}5H_2O$ was mixed with 70 mL of ethylene glycol in a round bottom flask. Stoichiometric amounts of $NH_4H_2PO_4$ and $Tb(NO_3)_3.xH_2O$ were added to the above solution. The solution was then refluxed at a temperature of 160˚C for 2 hrs. The white precipitate thus obtained was centrifuged, washed with distilled water or about 4-5 times and then finally with acetone. The sample was dried in an oven at a temperature of 80˚C for 12 hrs. The same procedure was followed for preparing different doping concentrations of Tb^{3+} ions. The effect of annealing temperatures on photoluminescence property was studied by annealing $BiPO_4$:3at. % Tb^{3+} at 400^{o}C, 600^{o}C, 800^{o}C and 1000^{o}C.

4.2.2 Characterization of the samples

The prepared samples were characterized by different characterization techniques. The crystal structure and the phase composition of the prepared samples were determined using Bruker D2 phaser XRD with Cu Kα radiation (λ = 1.5406 A, Ni filter, 2θ=15°-60° operated at 30 kV and 100 mA) and Bruker (eco D8, Advance) employing Cu Kα radiation. Shimadzu Iraffinity-1s FT-IR spectrometer was used for recording the vibrational spectra. Field emission scanning electron microscopy (FESEM) image was recorded by FEI Quanta 200 3D to see the morphology of the sample. JEOL JEM-2100, Transmission Electron Microscope operating at 200 kV was used for studying the shape

and size of the materials. The photoluminescence excitation spectra, emission spectra and decay time were recorded by Horiba FluoroMax-4CP Spectrofluorometer with 150W xenon lamp and 25W μsec flash lamp as excitation light sources and Hitachi (F-7000) fluorescence spectrophotometer having xenon discharge lamp as excitation source. All the measurements were performed at room temperature.

4.3 Results and Discussions

4.3.1 XRD study

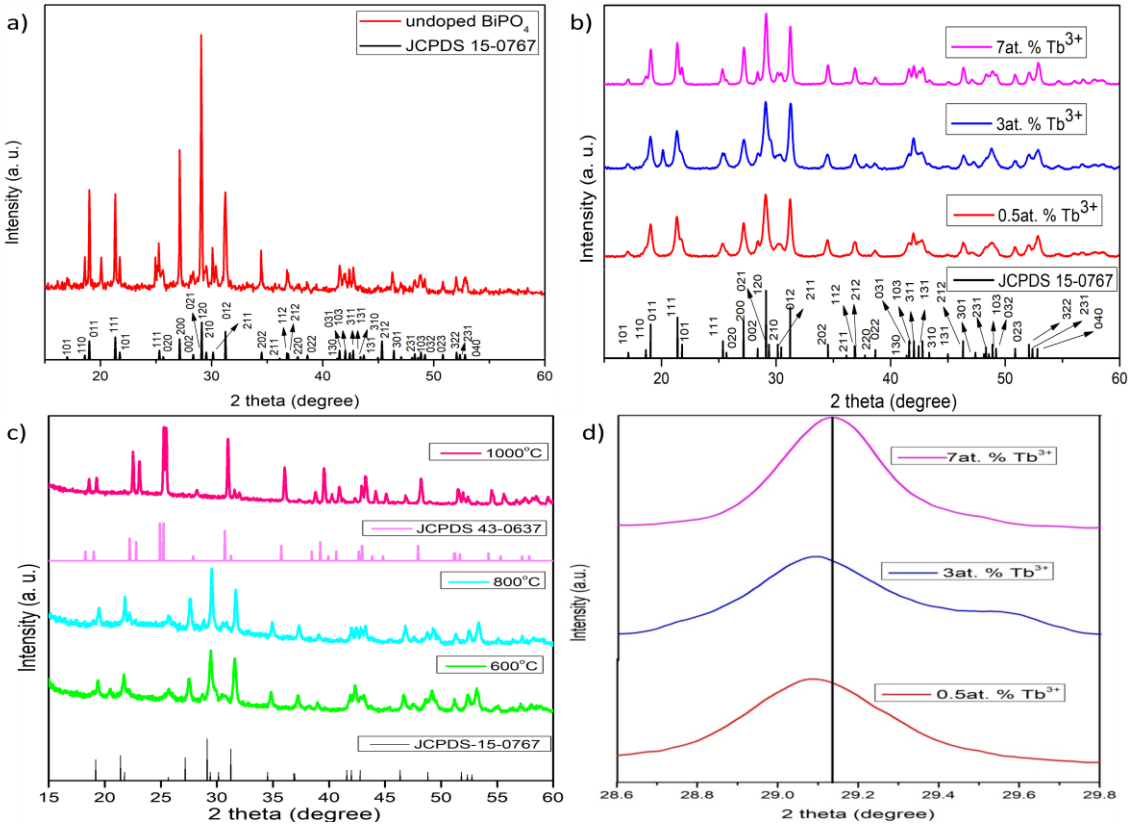

Figure 4.1: a) XRD patterns of the prepared undoped $BiPO_4$ b) XRD patterns of the prepared $BiPO_4$:$x$$Tb^{3+}$ (x = 0.5, 3, 7at. %), c) XRD patterns of 600^oC, 800^oC and 1000^oC annealed samples (2 hrs) of $BiPO_4$:Tb^{3+} (3at. %). d) Expanded view of the diffraction peaks in the 2θ range from 28.6 to 29.8 of figure 4.1(b) which shows the deflection of the peak with concentrations.

The XRD patterns of the prepared undoped $BiPO_4$ and 0.5, 3 and 7at. % of Tb^{3+} ions doped $BiPO_4$ nanophosphors are shown in figures 4.1(a) and 4.1(b) respectively. The XRD patterns of both doped and undoped $BiPO_4$ nanophosphors showed low-temperature monoclinic phase according to JCPDS card no. 15-0767 [Guan *et al*., (2008); Gao *et al*., (2016)]. The diffraction peaks are sharp and well defined, revealing that the phosphors are well crystallized in pure low-temperature monoclinic phase. No impurity peaks were detected in the XRD patterns of concentrations of 0.5 and 7at. % while peak due to impurity was detected at 2θ degree around 20 degree in the pattern of 3at. % Tb^{3+} doped $BiPO_4$ and undoped $BiPO_4$ nanophosphors. The diffraction plane (120) is shifted toward the higher angle (as shown in figure 4.1(d)) with the increase of Tb^{3+} ion doping concentration which is because of the substitution of larger size Bi^{3+} (1.15Å) by smaller size Tb^{3+} (1.01Å) [Li *et al*., (2018), Singh *et al*., (2018)]. The calculated unit cell volume decreased with an increase of Tb^{3+} ion concentration. From these above results, it is indicated that the dopant Tb^{3+} ion has been successfully doped into the $BiPO_4$. The calculated lattice parameters, cell volume along with average crystallite sizes are provided in Table 4.1. Figure 4.1(c) showed the XRD spectra of 600^{o}C, 800^{o}C and 1000^{o}C annealed samples (3at. % Tb^{3+} doped $BiPO_4$). The diffraction patterns of the samples annealed at 600^{o}C and 800^{o}C were found to be in low-temperature monoclinic phase according to JCPDS card no. 15-0767 indicating that the phase structure of the samples remain unchanged even upto 800^{o}C while the sample is annealed at 1000^{o}C, there occurred a change in phase structure from low-temperature monoclinic phase to high-temperature monoclinic phase according to JCPDS card no. 43-0637 [Zhao *et al*., (2013)].

Table 4.1: Calculated lattice parameters, cell volumes and crystallite sizes of undoped $BiPO_4$ and Tb^{3+} ions doped $BiPO_4$.

Tb^{3+} ion doping concentrations (atomic percentage)	Lattice parameters			Cell volume (V) $Å^3$	Crystallite size (nm)
	a(Å)	b(Å)	c(Å)		
0	6.801	6.795	6.392	290.584	30.45
0.5	6.790	6.793	6.390	290.250	28.29
3	6.777	6.695	6.386	289.602	20.70
7	6.770	6.691	6.382	289.158	25.02

The average crystallite size was calculated using the Scherrer equation

$$D = 0.9\lambda/\beta\cos\theta$$

Where, D represents the crystallite diameter, λ is the incident x-ray wavelength which has a value of 1.5406 Å, β is the full width at half maximum and θ represents the angle of diffraction.

4.3.2 FT-IR spectroscopy and SEM study

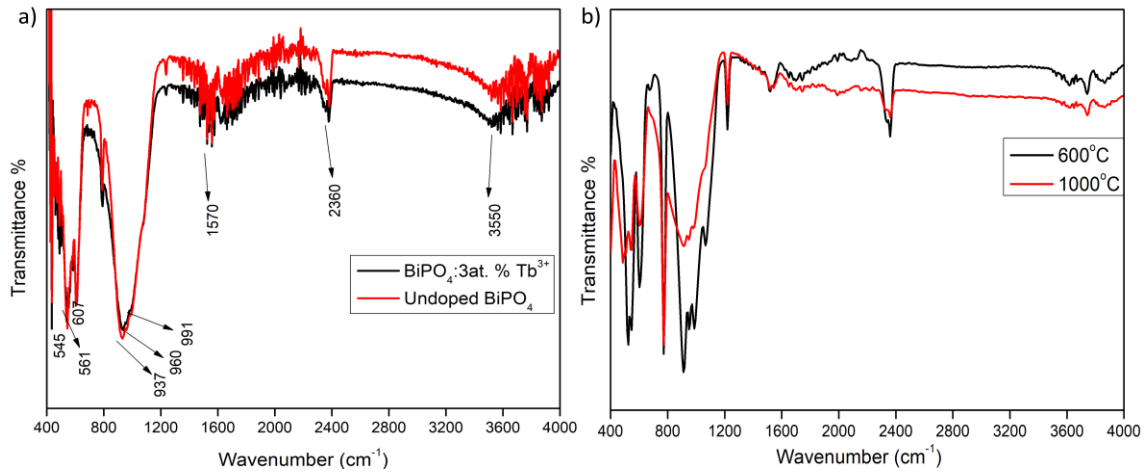

Figure 4.2: FT-IR spectra of a) undoped $BiPO_4$ and $BiPO_4$: Tb^{3+} (3at. %), b) annealed samples at 600°C and 1000°C.

Figure 4.2 showed the FT-IR spectrum of undoped $BiPO_4$, $BiPO_4:Tb^{3+}$ (3 at. %) and annealed samples of $BiPO_4:Tb^{3+}$ (3 at. %) at 600^oC and 1000^oC for 2hrs. The peaks centring at around 1570 and 3550 cm^{-1}correspond to the bending and stretching vibrations of adsorbed water molecules [Xue *et al*., (2009); Singh *et al*., (2019)]. The peak observed at around 2360 cm^{-1} is ascribed to the ν_3 anti-symmetric stretching mode of CO_2 molecule adsorbed from the atmosphere [Iskra *et al*., (2017)]. The bands observed in the range of 400 cm^{-1} and 1100 cm^{-1} are the characteristic bands of PO_4^{3-}. The bands observed at 937, 960 and 991 cm^{-1} are ascribed to the stretching symmetric vibrations (v_1) of O-P-O linkage, whereas the bands observed at 545, 561, and 607 cm^{-1} are attributed to the bending vibrations of O-P-O linkage [Xue *et al*., (2009), Pawlig *et al*., (2001)]. These observed bands are the characteristic bands of PO_4^{3-} group in low-temperature monoclinic structure. So the formation of low-temperature monoclinic structure in the sample was supported by this FTIR study. No significant change in the FT-IR spectra of undoped $BiPO_4$ and $BiPO_4:Tb^{3+}$ (3 at. %) was observed. This may be due to very low doping concentration of Tb^{3+}. While in case of annealed samples, the FT-IR peaks are more sharper than the unheated sample. No significant change in the peaks was noticed. But, for the sample which was annealed at 1000^oC, the FT-IR peaks in the range of 900 cm^{-1} to 1100 cm^{-1} are becoming complicated which indicated the change of phase structure from low-temperature monoclinic phase to high-temperature monoclinic phase [Zhao *et al*., (2013)]. The field emission scanning electron microscopic image is used to examine the morphology of samples. The FESEM image of the synthesized $BiPO_4:Tb^{3+}$ (3at. %) is shown in figure 4.3. It is seen that there is no clear shape observed and the particles have existed as agglomeration.

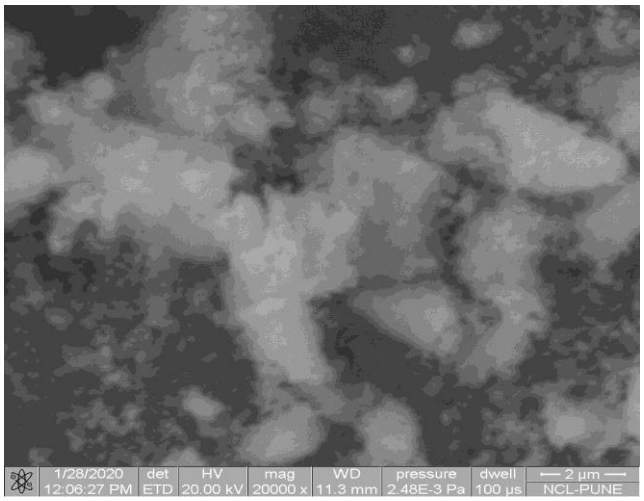

Figure 4.3: FESEM image of $BiPO_4$: Tb^{3+} (3at. %).

4.3.3 TEM Study

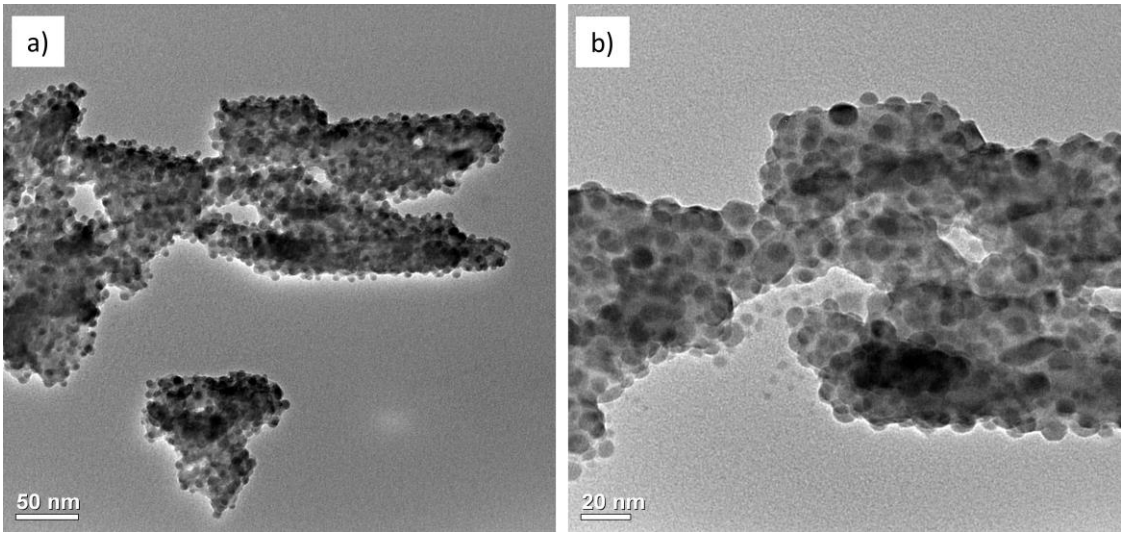

Figure 4.4: TEM image of $BiPO_4$:3at. % Tb^{3+} at a) low resolution b) high resolution.

4.4(a) and 4.4(b) showed TEM images of $BiPO_4$:3at. % Tb^{3+} at low and high resolutions respectively. It is seen from the figure that $BiPO_4$:3at. % Tb^{3+} exhibited hexagonal in shape with crystallite sizes ranges from 8-20nm. SAED and HRTEM images of $BiPO_4$:3at. % Tb^{3+} were shown in figure 4.5(a) and 4.5(b) respectively. SAED pattern was exhibiting dotted bright spots which show the well crystalline nature of the

phosphor. From the HRTEM image, a well separation of the inter-planar lattice fringes was noticed which confirmed the formation of highly crystalline phosphors. The lattice distances between the two fringes were found to be 3.16Å, 3.37Å, 2.68Å which correspond to (200), (110), (102) diffraction peaks of the XRD pattern respectively [Singh *et al*., (2019)].

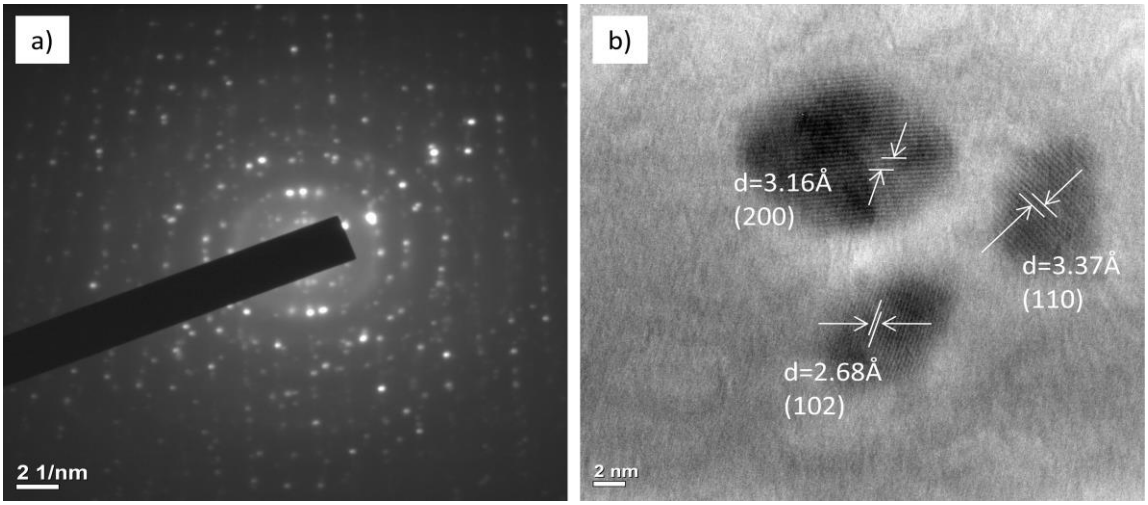

Figure 4.5: a) SAED image of $BiPO_4$:3at. % Tb^{3+} b) HRTEM image of $BiPO_4$:3at. % Tb^{3+}.

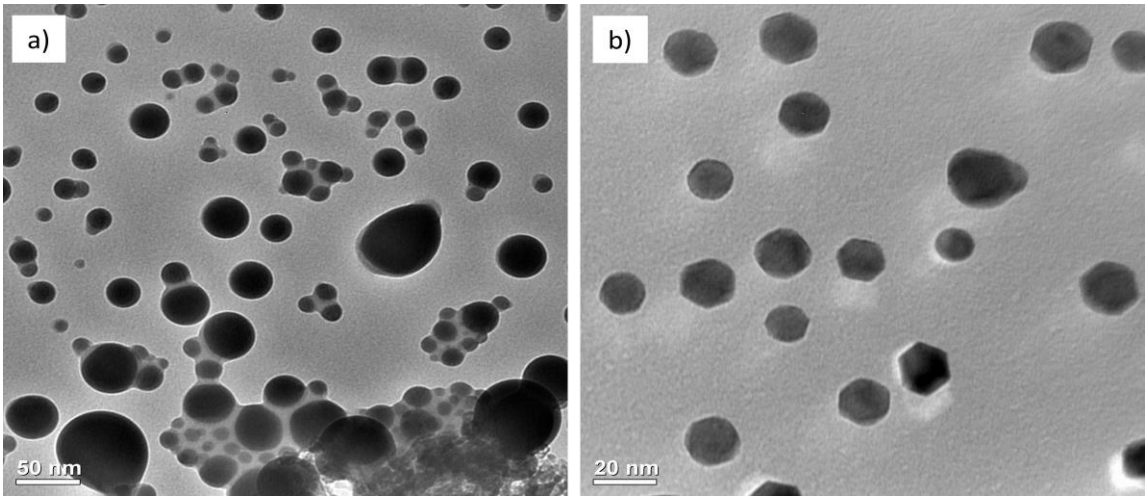

Figure 4.6: TEM image of $BiPO_4$:3at. % Tb^{3+} (annealed at 800^oC) at a) low resolution b) high resolution.

The TEM images of $BiPO_4$:3at. % Tb^{3+} annealed at 800^oC with different resolutions were shown in figures 4.6(a) and 4.6(b) respectively. It showed hexagonal shape morphology having sizes range from 10-70nm. SAED and HRTEM images showed a well crystalline nature of the synthesized phosphors as shown in figures 4.7(a) and 4.7(b) respectively.SAED pattern exhibited dotted bright spots which revealed the well crystalline nature of the phosphor. Separation of inter-planar lattice fringes was noticed well in HRTEM image, indicating the crystalline nature of the phosphors. The lattice distance was found out to be 3.51Å which corresponds to (111) of the diffraction peak in XRD pattern of $BiPO_4$:3at. % Tb^{3+} annealed at 800^oC. The formation of hexagonal shape morphology was also clearly seen in HRTEM image.

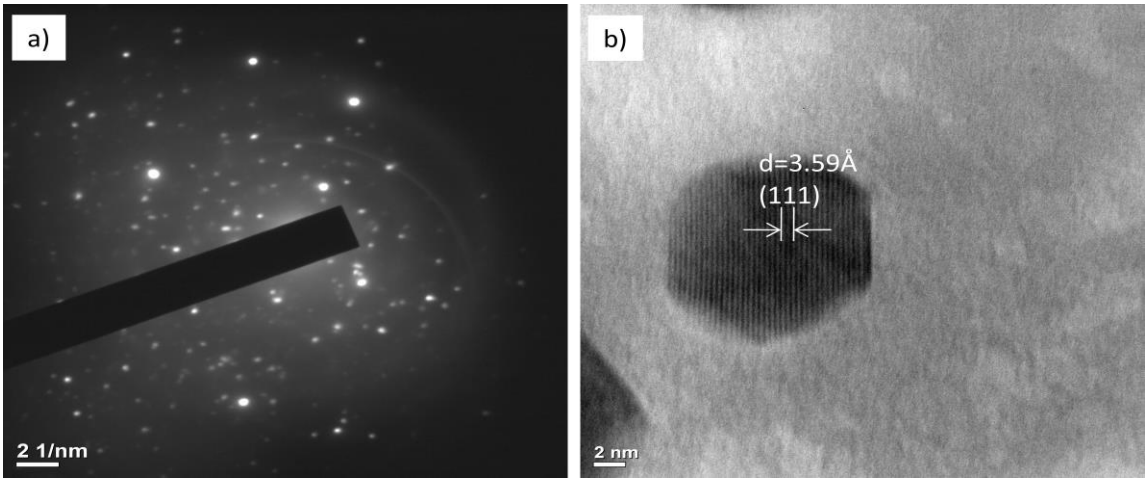

Figure 4.7: a) SAED image of $BiPO_4$:3at. % Tb^{3+} (annealed at 800^oC)b)HRTEM image of $BiPO_4$:3at. % Tb^{3+} (annealed at 800^oC).

4.3.4 Photoluminescence study:

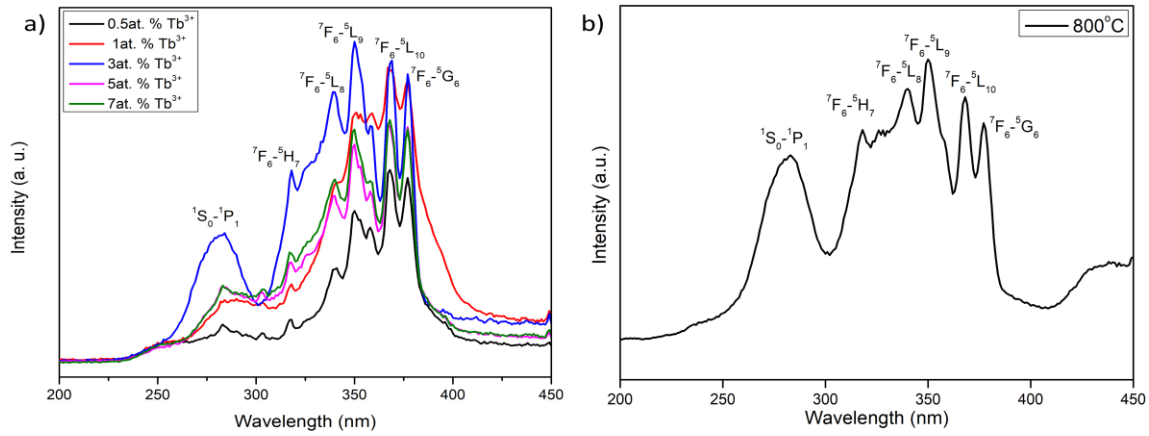

Figure 4.8: PLE spectra of a) BiPO4:x Tb^{3+} (x = 0.5,1,3,5,7at. %), b) Annealed at 800°C of 3at. % Tb^{3+} doped $BiPO_4$ sample. (λ_{emi} = 544 nm).

The photoluminescence excitation spectra of different doping concentrations of Tb^{3+} into $BiPO_4$ and annealed at 800°C of 3at. % Tb^{3+} doped $BiPO_4$ samples are shown in figures 4.8(a) and 4.8(b) respectively. The spectra (both 4.8(a) and 4.8(b)) were measured with the emission wavelength of 544 nm. The spectra (both 4.8(a) and 4.8(b)) consist of a broad band at 285 nm originated from the $^1S_0 \rightarrow {}^1P_1$ electronic transition of Bi^{3+} ion [Li *et al*., (2017)] and sharp bands due to the electronic transitions within the 4f energy levels of doping Tb^{3+} ion. These sharp bands are observed at 377, 369, 351, 340 and 318 nm and they can be ascribed to the 4f electronic transitions such as $^7F_6 \rightarrow {}^5G_6$, $^7F_6 \rightarrow {}^5L_{10}$, $^7F_6 \rightarrow {}^5L_9$, $^7F_6 \rightarrow {}^5L_8$ and $^7F_6 \rightarrow {}^5H_7$ of Tb^{3+} ion respectively [Yan, (2015); Lakshminarayana *et al*., (2015)]. Bi^{3+} can also have an electronic transition i.e. $^1S_0 \rightarrow {}^3P_1$ at 351 nm [Li *et al*., (2017); Kaur *et al*., (2014)]. Hence the excitation peak observed at 351 nm may be attributed to the overlapping of $^1S_0 \rightarrow {}^3P_1$ transition with f-f transition of Tb^{3+} ion. As the peak due to $^7F_6 \rightarrow {}^5L_9$ transition is stronger in terms of intensity than the other excitation peaks, the emission spectra of all the samples were measured with the excitation wavelength of 351 nm. Figure 4.9(a) shows the emission spectra of $BiPO_4$ nanophosphors doped with different concentrations of Tb^{3+} ion. The spectra consist of a broad band with maximum at 419 nm and four sharp peaks centring at 488, 544, 582 and

620 nm, this broad band at 419 nm is due to the electronic transition from $^3P_1 \rightarrow {}^1S_0$ of Bi^{3+} ion [Kaur *et al*., (2014); Lee *et al*., (2018)] and the sharp peaks are attributed to the $^5D_4 \rightarrow {}^7F_6$, $^5D_4 \rightarrow {}^7F_5$, $^5D_4 \rightarrow {}^7F_4$ and $^5D_4 \rightarrow {}^7F_3$ transitions of Tb^{3+} ion respectively [Yang *et al*., (2016); Gayatri and Singh (2013)]. It is also known that Bi^{3+} ion exhibited emission band in the wavelength range between 450 to 650 nm [Scarangella *et al*., (2019); Pan *et al*., (2020)]. Therefore the emission band observed from 450 to 650 nm may be due to the overlapping of emissions from Tb^{3+} ion and Bi^{3+} ion. With the increase of Tb^{3+} ion doping concentration, the emission band at 419 nm originated from Bi^{3+} ion is found attenuated and the emission band at 544 nm originated from Tb^{3+} ion was found increased. Further, the emission intensity is attenuated beyond 3at. % of Tb^{3+} ion doping concentration, it is due to the concentration quenching effect. So, the optimum concentration of Tb^{3+} is found to be 3 at. %. Due to the increase in the concentration of Tb^{3+} ion, the inter-ionic distance between the Tb^{3+} ions decreased. When the distance is lower than its critical distance, non-radiative energy transfer among the doped Tb^{3+} takes place which leads to attenuation of emission intensity [Chen *et al*., (2015)]. The photoluminescence emission profile of as-prepared (3at. % Tb^{3+} doped $BiPO_4$), and the samples annealed at 400^{o}C, 600^{o}C, 800^{o}C, 1000^{o}C monitored at λ_{exci}=351nm are demonstrated in figure 4.9(b). There occurred no change in the emission peaks profile of Tb^{3+} doped $BiPO_4$ except their emission intensities. The emission intensity was observed accentuated with increase of annealing temperature upto 800^{o}C then decreased when it reached 1000^{o}C. This increased in emission intensity upon annealing upto800^{o}C is due to the increase in their crystallinity and also decreased in the number of quenchers like OH groups present on the surface of nanophosphors [Luwang *et al*., (2010)]. This result is also in concurrence with the FT-IR spectra depicted in figure 4.3(b). The optimum emission intensity was achieved for the sample which was annealed at 800^{o}C. For 1000^{o}C annealed sample, the emission intensity decreased due to the change of their phase structure from low-temperature monoclinic phase to high-temperature monoclinic phase shown in XRD pattern figure 4.1(c).

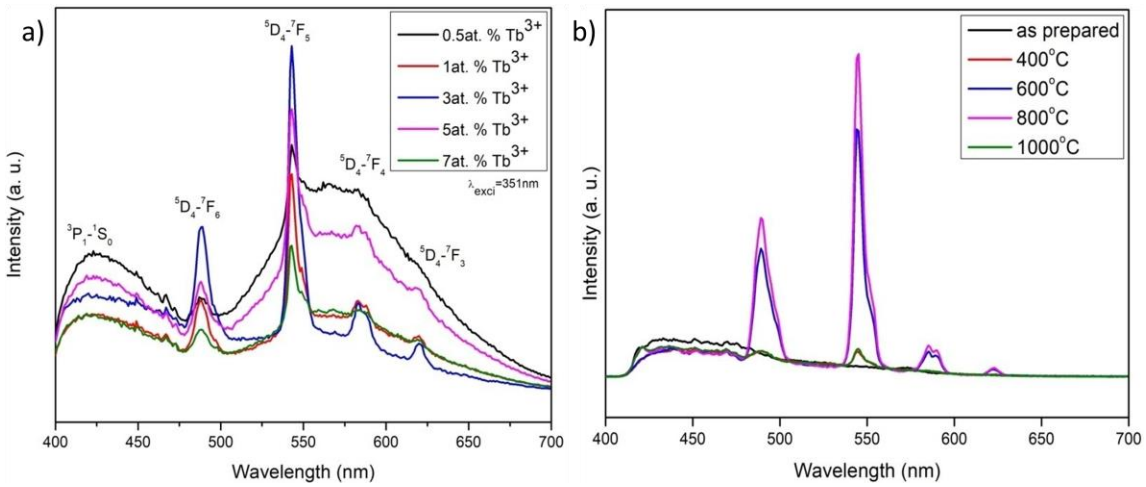

Figure 4.9: PL spectra of a) $BiPO_4$:xTb^{3+}, (λ_{exci} = 351 nm) (x = 0.5,1,3,5,7at. %), b) $BiPO_4$:3at. % Tb^{3+} annealed at 400°C, 600°C, 800°C, 1000°C, (λ_{exci} = 351 nm).

4.3.5 Lifetime study

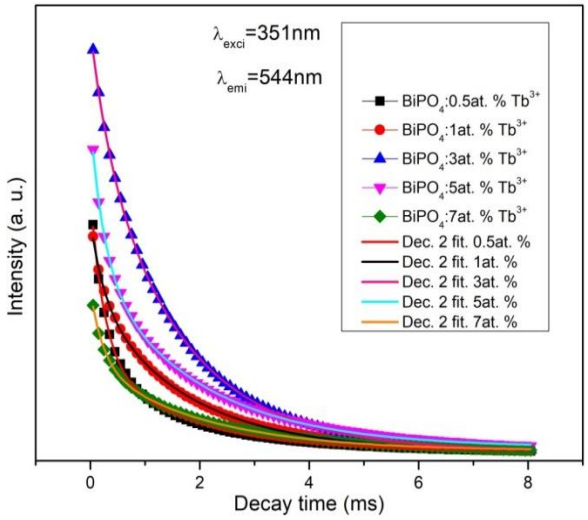

Figure 4.10: Photoluminescence decay curve of $BiPO_4$:$x$$Tb^{3+}$ with bi-exponential fitting(x = 0.5,1,3,5,7at. %).

The luminescence decay curves of the prepared Tb^{3+} ion-doped $BiPO_4$ nanophosphors have been evaluated. The decay curves were measured by fixing the

excitation and emission wavelengths at 351 and 544 nm respectively for all the concentrations. The measured decay curves are shown in figure 4.10. All the observed decay curves are well fitted by using bi-exponential equation [Devi *et al*., (2014)].

$$I = I_1 \exp(-t/\tau_1) + I_2 \exp(-t/\tau_2)$$

Here I_1 and I_2 represent the intensities at two different time intervals and τ_1 and τ_2 represent their corresponding decay times. The decay behaviour for bi-exponential curve fitting of a phosphor lies on a) non-homogeneous distribution of dopant ions into the host lattice b) energy transfer from donor atom and c) defects present in the host and the presence of impurity [Sharma and Singh (2013)]. The average decay time can be evaluated by using the following equation

$$\tau_{ave} = (I_1\tau_1^2 + I_2\tau_2^2)/(I_1\tau_1 + I_2\tau_2)$$

The calculated average lifetime for the Tb^{3+} concentrations of 0.5, 1, 3, 5 and 7% are found to be 1.31, 1.49, 1.56, 1.76, and 1.83 ms respectively and their goodness of fitting (R^2) for the above concentrations is 0.99958, 0.99978, 0.99994, 0.99972 and 0.99969 respectively. These obtained lifetime values are in agreement with those reported in the literatures [Naidu *et al*., (2012), Xu *et al*., (2014)]. And the parameters involved in the lifetime study are listed in Table 4.2.

Table 4.2: Parameters involved in the lifetime study of Tb^{3+}ions doped $BiPO_4$.

Sample	y_0	I_1	τ_1	I_2	τ_2
0.5at. % Tb^{3+}	5446.102	148804.387	1.59449	250764.978	0.24823
1at. % Tb^{3+}	4920.868	118326.036	0.24715	242288.363	1.71372
3at. % Tb^{3+}	5364.018	512514.805	1.56957	145013.291	0.35325
5at. % Tb^{3+}	10654.841	228505.424	0.25884	279435.395	1.93152
7at. % Tb^{3+}	5352.537	113296.454	0.23191	137220.138	1.98890

4.3.6 CIE study

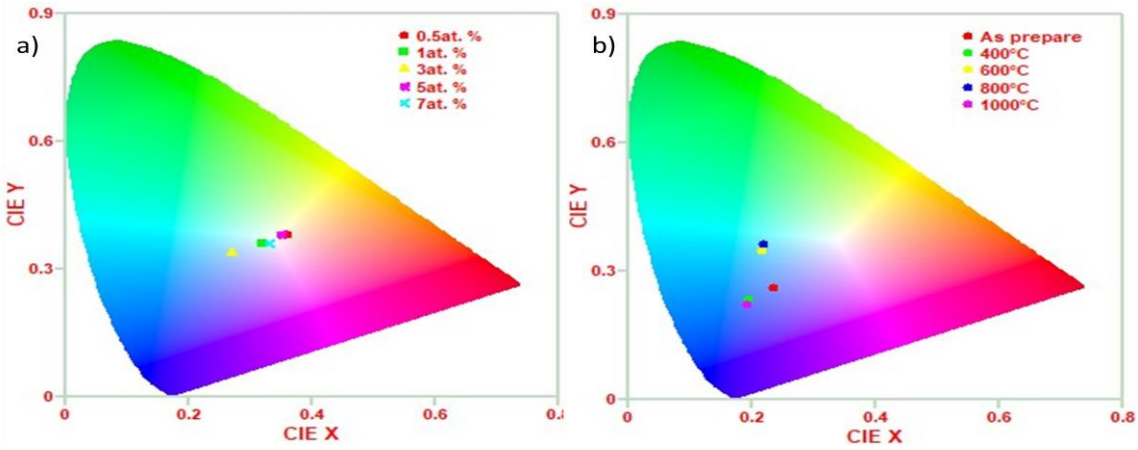

Figure 4.11: CIE chromaticity diagrams of a) $BiPO_4$:xTb^{3+} nanophosphors. (x = 0.5, 1, 3, 5 and 7at. %), b) as prepared, 400°C, 600°°C, 800°C and 1000°C annealed samples.

The Commission International de L'Eclairage (CIE) chromaticity diagram reveals the co-ordinates that are very useful in determining the perceived colour of the emission of a phosphor [Singh *et al*., (2018), Sharma *et al*., (2014)]. The calculated colour co-ordinates from the emission spectra and their corresponding co-related colour temperature are given in Table 4.3. The co-related colour temperatures (CCT) for Tb^{3+} ions doped $BiPO_4$ were calculated by using McCamy's equation [Du *et al*., (2016), Ryadun *et al*., (2020)]:

$$CCT = -437n^3 + 3601n^2 - 6861n + 5514.31 \text{ and } n = (x-x_e)/(y-y_e),$$

Where x and y represent the calculated colour co-ordinates. The CIE chromaticity diagrams for the prepared $BiPO_4$ doped with different concentrations of Tb^{3+} ion and for the samples annealed at 400°C, 600°C, 800°C and 1000°C upon excitation at 351 nm were shown in figure 4.11(a) and 4.11(b) respectively. This diagram showed that the prepared samples emit nearly white colour under excitation at 351nm while the annealed samples showed cyan colour emissions.

Table 4.3: CIE chromaticity coordinates and CCT of the BiPO4:Tb^{3+} nanophosphors upon excitations at 351 nm.

% of Tb^{3+} doped into $BiPO_4$ lattice	x	y	CCT
0.5	0.36	0.38	4601
1	0.32	0.36	6007
3	0.27	0.34	8886
5	0.35	0.38	4912
7	0.33	0.36	5596
As prepare	0.24	0.26	1700
400^oC	0.20	0.23	2284
600^oC	0.21	0.35	4281
800^oC	0.22	0.36	3887
1000^oC	0.19	0.22	3489

4.4 Conclusion

In conclusion, low-temperature monoclinic structure of Tb^{3+} doped $BiPO_4$ nanophosphors have been prepared successfully by co-precipitation method using ethylene glycol as reaction medium. The phase structure of the sample changed from low-temperature monoclinic phase to high-temperature monoclinic phase upon annealing at 1000^oC. TEM analysis showed the formation of hexagonal shape morphology of the prepared nanophosphors. Photoluminescence analysis revealed the typical emission spectra of Tb^{3+} with maximum emission intensity at 544 nm due to $^5D_4$-$^7F_5$ under excitation at 351 nm. The optimum concentration of Tb^{3+} was found to be at 3at. %. Beyond this concentration, the emission intensity decreases as a result of concentration quenching effect. The emission intensity of 3at. % Tb^{3+} doped $BiPO_4$ increased with increase of annealing temperature upto 800^oC. At 1000^oC annealing temperature, the emission intensity becomes attenuated due to the change of phase structure from low-temperature monoclinic phase to high-temperature monoclinic phase. From the CIE diagram, it is observed that the prepared nanophosphors emitted to nearly white colour whereas the annealed samples exhibited an emission of cyan colour. These results revealed that the prepared nanophosphors may have potential applications in the fields of lighting, displays and other optical devices etc.

Chapter 5

Synthesis, Characterization and Photoluminescence properties of Eu^{3+} ions doped $BiPO_4$ nanophosphors

5.1 Introduction

In the last few years, research on wLED is becoming a hot area of research owing to its high efficiency, low energy consumption, long lifetime etc. [Xiang *et al.,* (2019); Luo *et al.,* (2016); Bidikoudi *et al.,* (2018)]. With this regard, a number of researches have been approached for producing wLED. For example, a combination of yellow YAG:Ce^{3+} material with blue chips have been used commercially [Xia and Meijerink (2017)]. Nevertheless, it has so many disadvantages due to its low colour rendering index (CRI) and high co-related colour temperature (CCT) [Wang *et al.,* (2015)]. Further, a new type of wLED which is composed of blue, green and red light materials excited by near UV light has been introduced. These materials have good CRI and exhibited a stable colour [Chen *et al.,* (2016)]. Red emitting materials have been attracted the interest of many researchers as it is one of the major components of white light and moreover, the number of commercially available red phosphor materials are very few compared to green and blue phosphors. So, exploring materials exhibiting red emission colour which show stable photoluminescence property with good colour purity and low cost is much desirable for wLED.

In search of red colour emission phosphors in which the electrons can be pumped up using near UV light, Mn^{4+} ion-doped oxides/fluorides red phosphors or nitride based red phosphors seem to be promising candidates while they are less favourable because of their high cost and low luminous efficiency [Pust *et al.,* (2014); Xie *et al.,* (2011); Jiang *et al.,* (2014); Wang *et al.,* (2016); Zhang *et al.,* (2017)]. Moreover, Mn^{4+} ion-doped oxides phosphors are thermally unstable as well as they are easily degradable in high humidity conditions [Chen *et al.,* (2016)]. The optimal red phosphor material which can be used for wLED exhibiting high colour purity, high quantum efficiency etc., normally

has a narrow emission band. In this respect, Eu^{3+} ion-doped phosphor materials will be of wise choice as these materials are exhibiting high luminescence properties, strong red emission, long lifetime and they produced narrow emission band resulting from 4f-4f transitions [Zhang *et al.,* (2017); Zukauskas *et al.,* (2008); Seo, (2014); Xu *et al.,* (2014); Geng *et al.,* (2013)]. The 4f-4f electronic transition can be affected by local Eu^{3+} symmetry and hence they are used as a structural probe for studying crystallographic sites [Morozov *et al.,* (2013)]. Moreover, Eu^{3+} emission is suitable for display devices producing a high purity red emission colour and hence Eu^{3+} doped Y_2O_2S and $(Y,Gd)VO_4$ phosphors are even used commercially by producing a stable luminescence property but there is still limitation for these materials as they showed low energy efficiency compared to other blue and green phosphors [Huang *et al.,* (2007); Pust *et al.,* (2014); Xin *et al.,* (2015)]. Hence choosing a good host for doping lanthanide ion is still fascinating.

On the other hand, phosphate based phosphors have been paid more attention due to their strong absorption in UV region and they also have high chemical and thermal stability and relatively low cost [Xin *et al.,* (2018); Wu *et al.,* (2010)]. Moreover, they have a wide variety of applications such as plasma display panels (PDPs), luminescence host, photocatalysis, sensors etc. [Verma and Baghel (2017); Lin *et al.,* (2010); Gao *et al.,* (2018)]. As a part of phosphate family, $BiPO_4$ is considered as one of the best host for lanthanide ion doping owing to their several attractive properties such as high chemical and mechanical stability, high adsorption edge, their similarity in ionic sizes with the lanthanide ions etc. and they are applicable in various fields like lighting, supercapacitor, biomedical etc. [Roming and Feldmann (2009); Naidu *et al.,* (2012); Sahu and Mula (2019); Vadivel *et al.,* (2016); Shahbazi *et al.,* (2020)]. $BiPO_4$ crystallizes in three different crystallographic forms namely hexagonal, low temperature monoclinic and high-temperature monoclinic phases [Naidu *et al.,* (2012); Zhao *et al.,* (2013)]. Normally, the hexagonal phase of $BiPO_4$ is obtained at low temperature below 400^oC whereas, low-temperature monoclinic phase and high-temperature monoclinic

phase are obtained at higher temperature such as 600^{o}C and above 800^{o}C respectively [Naidu *et al.,* (2012)]. Hexagonal and monoclinic phases differ in their co-ordination number of Bi^{3+} ion. Bi^{3+} ions in hexagonal phase are being surrounded by eight oxygen atoms forming square anti-prism geometry while the Bi^{3+} ions in monoclinic phase are co-ordinated by nine oxygen atoms similar to the monazite structure of lanthanide phosphate [Naorem *et al.,* (2020)]. Hexagonal phase is associated with water molecules and forms an open framework structure as BiO_8 polyhydra, PO_4 tetrahedra with zeolitic water molecules arranged in a symmetrical chain parallel to c-axis. While in monoclinic phase, the chains are asymmetrically arranged and hence space-filling compact networks are formed. When it comes to luminescence, $BiPO_4$ has a unique feature as Bi^{3+} ion itself acted as a sensitizer for dopant lanthanide ions [Arunkumar *et al.,* (2012); Yaba *et al.,* (2020)].

The pH, capping agents and synthesis methods played an important role in controlling the morphology of a nanophosphor. The morphology of a nanophosphor changed as the above mentioned conditions of the reaction medium are changed and consequently affect the luminescence property of a nanophosphor. Hence, Eu^{3+} ion doped $BiPO_4$ nanophosphors were synthesized by co-precipitation method and the photoluminescence properties resulted due to different doping concentrations of Eu^{3+} ions, the effect of different annealing temperatures, the effect of different pH and lastly the effect of different concentrations of CTAB of the reaction medium were discussed in this chapter.

5.2 Experimental details

5.2.1 Materials and methods

The materials used for the synthesis of $BiPO_4$:Eu^{3+} phosphors are Europium nitrate hexahydrate ($Eu(NO_3)_3.6H_2O$) with 99.99% purity (Alfa Aesar), Ammonium dihydrogen phosphate ($NH_4H_2PO_4$) of 98% purity (Alfa Aesar), Bismuth nitrate pentahydrate ($Bi(NO_3)_3 \cdot 5H_2O$) with purity of 98% (Alfa Aesar), and the solvent used is ethylene glycol (Merck). The synthesis procedures are as follows, the stoichiometric amounts of

$Bi(NO_3)_3 \cdot 5H_2O$ was mixed with 70 ml of ethylene glycol in a round bottom flask. Stoichiometric amounts of $NH_4H_2PO_4$ and $Eu(NO_3)_3 \cdot 6H_2O$ were added into the above solution. The solution was then refluxed at a temperature of 130˚C for 2 hrs. The white precipitate thus obtained was centrifuged, washed with distilled water for about 4-5 times and then finally washed with acetone. The sample was dried in an oven at a temperature of 80˚C for 12hrs. Different doping ion concentrations of Eu^{3+} were prepared using the same procedure. $BiPO_4$:8at. % Eu^{3+} phosphors were synthesized at 0.5, 1, 3, 6 and 10mM concentrations of CTAB using the same procedure. 8at. % Eu^{3+} ion doped $BiPO_4$ were also prepared at different pH and the pH of the reaction medium was adjusted using NaOH and HCl. In order to see the effect of annealing temperatures, $BiPO_4$:8at. % Eu^{3+} was annealed at 500^{o}C, 600^{o}C, 700^{o}C and 800^{o}C.

5.2.2 Characterization of the samples

The crystal structures of the prepared materials were characterized using XRD spectroscopic technique and the XRD machine used is PANalytical's X-ray diffractometer (X'-PertPRO) with CuKα (1.5406Å) radiation with Ni filter. The vibrational spectra of the samples were analyzed using Shimadzu Iraffinity-1s FT-IR spectrometer. Sigma 300, Carl Zeiss Field Emission Scanning Electron Microscope was used for morphology analysis of the sample. JEOL JEM-2100, Transmission Electron Microscope operating at 200 kV was used for studying the shape and size of the materials. The photoluminescence excitations as well as emissions spectra were recorded using Hitachi (F-7000) fluorescence spectrophotometer having xenon discharge lamp as excitation source. All the measurements were carried out at room temperature.

5.3 Results and Discussions

5.3.1 XRD study

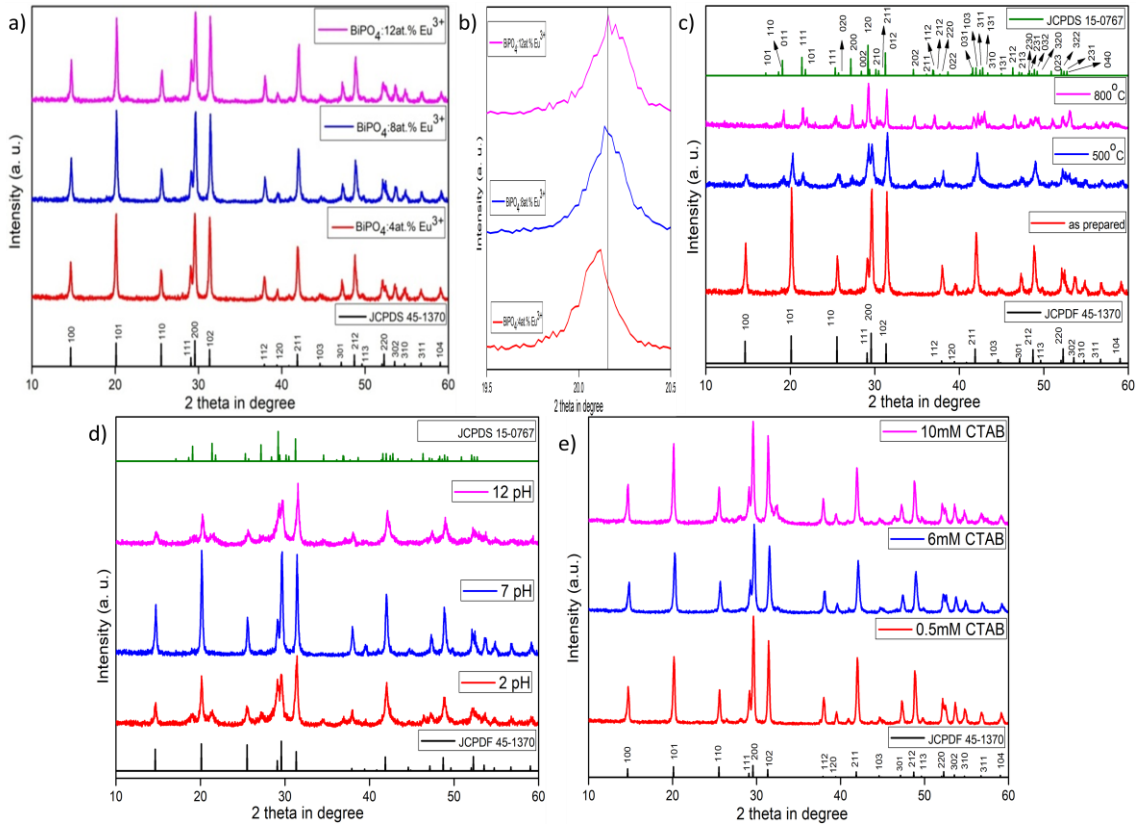

Figure 5.1: XRD patterns of a) $BiPO_4$:xEu^{3+} (x=4, 8, 12at. %), b) Expanded view of the diffraction peaks in the 2θ range from 19.5 to 20.5 of figure 5.1(a) which shows the deflection of the peak with concentrations, c) (as prepared) $BiPO_4$:8at. % Eu^{3+}, samples annealed at 500°Cand 800°C d) $BiPO_4$:8at. % Eu^{3+}prepared at pH= 2,7,12 e) $BiPO_4$:8at. % Eu^{3+}prepared at 0.5, 6, 10mM CTAB.

The XRD patterns of different concentrations of Eu^{3+} doped $BiPO_4$; 8at. % Eu^{3+} doped $BiPO_4$ (as prepared), samples annealed at 500°C and 800°C; 8at. % Eu^{3+} doped $BiPO_4$ prepared at pH= 2, 7 and 12 and 8at. % Eu^{3+} doped $BiPO_4$ prepared at 0.5, 1, 6 and 10mM CTAB of the reaction medium were depicted in figures 5.1(a), 5.1(c), 5.1(d) and 5.1(e) respectively. All the diffraction peaks in figure 5.1(a) exhibited hexagonal phase of $BiPO_4$ according to JCPDS card no. 45-1370 [Zhao *et al.,* (2013)]. The

diffraction peak having 101 Miller Indices is found shifted towards a higher angle as doping concentration of Eu^{3+} increases as shown in figure 5.1(b). This shifting of the diffraction peak to higher angle is due to the smaller size of Eu^{3+} (0.947Å) as compared to Bi^{3+} (1.17Å) and this result revealed that Eu^{3+} is successfully doped into the interstitial site of $BiPO_4$ [Singh *et al.,* (2019)]. The lattice parameter as well as cell volumes of $BiPO_4$ doped with different concentration of Eu^{3+} were also calculated and listed in table 5.1. From this table, it can be seen vividly that the cell volume decreased with increase of Eu^{3+} concentration due to the smaller size of Eu^{3+} as compared to Bi^{3+}. When the sample $BiPO_4$:8at. % Eu^{3+} is annealed at 500°C for 2hrs, the hexagonal phase of the as-prepared sample changed into mixed phase of hexagonal and low-temperature monoclinic phase according to JCPDS card no. 15-0767 and card no. 45-1370 [Zhao *et al.,* (2013); Naorem *et al.,* (2020)]. Further increase of annealing temperature upto 800°C leads to the formation of pure low-temperature monoclinic phase according to JCPDS card no. 15-0767 [Naorem *et al.,* (2020)]. The effect of pH on the phase structure of 8at. % Eu^{3+} doped $BiPO_4$ was also discussed in figure 5.1(d). Mixed phase structure of hexagonal and monoclinic phases was observed in both pH2 and pH12 of the reaction medium [Zhao *et al.,* (2013); Naorem *et al.,* (2020)]. But, a pure hexagonal phase was formed for the sample prepared at pH7 of the reaction medium. The XRD patterns of 8at. % Eu^{3+} doped $BiPO_4$ prepared at different concentrations of CTAB was depicted in figure 5.1(e). All the samples exhibited hexagonal phase indicating that the concentration of CTAB does not alter the phase of 8at. % Eu^{3+} doped $BiPO_4$.

Table 5.1: Calculated lattice parameters, cell volumes and crystallite sizes of Eu^{3+} ions doped $BiPO_4$.

Eu^{3+} ion doping concentrations (atomic percentage)	Lattice parameters		Cell volume (V) A^3	Crystallite size (nm)
	a=b	c		
4	6.9787	6.4705	272.91	38
8	6.9767	6.4602	272.32	35
12	6.9748	6.4573	272.05	34

5.3.2 FT-IR study

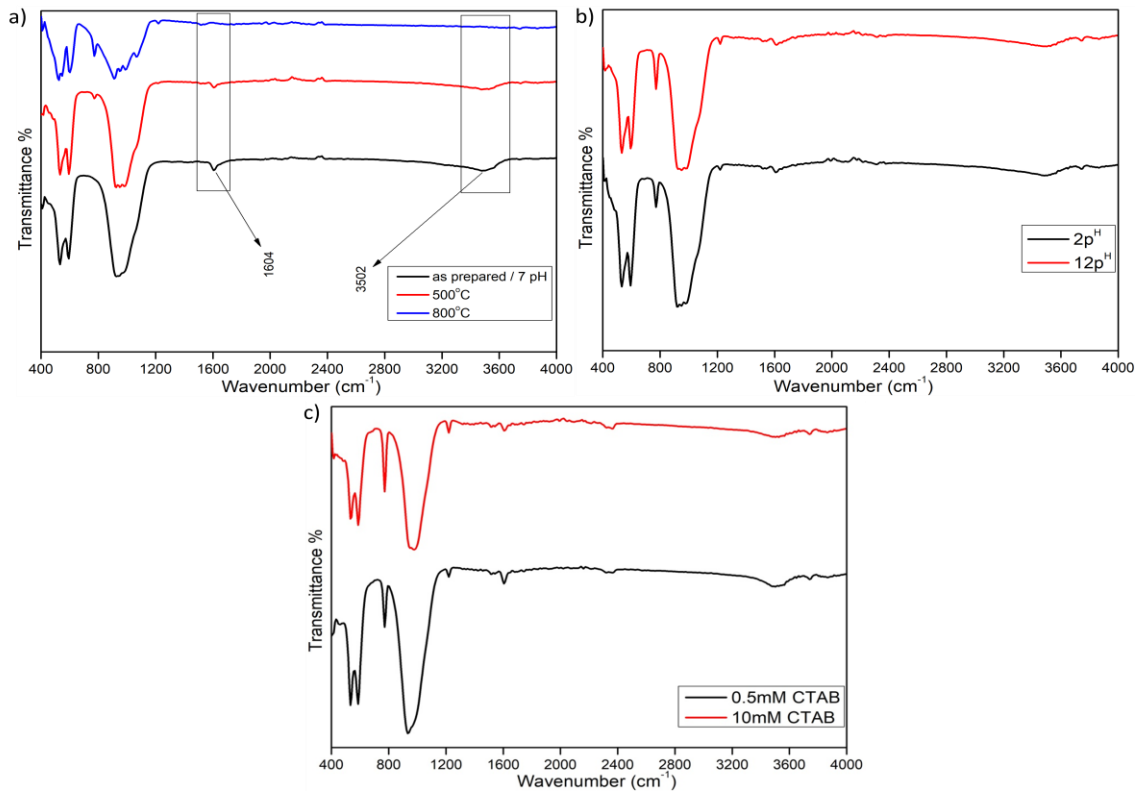

Figure 5.2: FT-IR spectra of a) $BiPO_4$:8at. % Eu^{3+}, $BiPO_4$:8at. % Eu^{3+} annealed at 500°C and 800°C b) $BiPO_4$:8at. % Eu^{3+} prepared at pH=2 and 12 c) $BiPO_4$:8at. % Eu^{3+} prepared in 0.5 and 10mM CTAB.

The FT-IR spectra of $BiPO_4$:8at. % Eu^{3+}, $BiPO_4$:8at. % Eu^{3+} annealed at 500^oC and 800^oC, $BiPO_4$:8at. % Eu^{3+} prepared in pH=2 and 12, $BiPO_4$:8at. % Eu^{3+} prepared in 0.5 and 10mM CTAB were shown in figure 5.2(a), 5.2(b) and 5.2(c) respectively. All the FT-IR spectra showed a similar peak profile and the spectra consist of different peaks in the range of 400cm^{-1} to 1200cm^{-1} corresponding to PO_4^{3-} group. The peaks beyond 1200cm^{-1} are attributed to adsorbed water molecules. The peaks observed at 532 $cm^{-1,}$ 588 cm^{-1}, 596 cm^{-1} are resulted due to bending vibrations of O-P-O linkage [Zhao *et al.,* (2013)]. Whereas, the most intense peaks at 939cm^{-1}corresponds to the stretching symmetric vibrations (*v*1) of O-P-O bond [Lakshminarayana *et al.,* (2015); Xue *et al*., (2009), Pawlig *et al*., (2001)]. The two bands centring at 1604 cm^{-1} and 3502cm^{-1} are ascribed to bending and stretching vibrations of water molecules adsorbed on the surface of the nanoparticles [Zhao *et al.,* (2011)]. The observed FT-IR peaks are well-matched with the FT-IR peaks hexagonal phase of $BiPO_4$ of reported literature [Zhao *et al.,* (2013)]. For 500^oC annealed sample, the most intense band centring at 939cm^{-1} is distorted a bit and three peaks were observed at 922cm^{-1}, 948cm^{-1} and 986cm^{-1}. These peaks are not distinct enough which may be due to the formation of mixed phase structure (hexagonal and low temperature monoclinic). Further increase of annealing temperature upto 800^oC resulted in the formation of more distinct peaks in the range of 700cm^{-1}-1200cm^{-1} due to the formation of pure low-temperature monoclinic phase [Xue *et al.,* (2009); Naorem *et al.,* (2020)].

5.3.3 SEM and EDAX study

The FE-SEM images of 8at. % Eu^{3+} doped $BiPO_4$, 8at. % Eu^{3+} doped $BiPO_4$ prepared at pH of 2 and 12 of the reaction medium, 8at. % Eu^{3+} doped $BiPO_4$ prepared at 0.5, 6 and 10mM concentration of CTAB were depicted at figure 5.3(a), 5.3(b), 5.3(c), 5.3(d), 5.3(e) and 5.3(f) respectively. The sample with 8at. % Eu^{3+} doped $BiPO_4$ was found hexagonal in shape with grain size in the range of 40nm to 140nm. The formation of hexagonal shape morphology can be seen clearly in TEM image also. Agglomerations of the nanoparticles were found for the samples prepared at pH of 2 and 12 of the

reaction medium. So, it is difficult to determine the shapes and sizes in these cases. Hexagonal shape morphology for the sample prepared using 0.5mM of CTAB of the reacting medium was observed from the FE-SEM image. The grain size of the hexagonal shape nanophosphors were found in the range of 25nm to 188nm. The morphology of the nanoparticles changed as the concentration of CTAB of the reacting medium increased and the morphology were found as cucumber seed-like structure for the sample prepared in 6mM of CTAB and the grain sizes were also calculated in the range of 31nm to 425nm. In case of the sample prepared at 10mM CTAB of the reacting medium, the morphology was found to be sea flower-like morphology with diameter of around 500nm. It is also notable that the particles look incorporated and embedded with the next adjacent particles and hence the structure thus formed seems incomplete. Moreover, agglomerations of the particles are also noticed in some parts of the image. The EDAX spectra of Eu^{3+} doped $BiPO_4$, samples prepared at different pH of the reaction medium and the samples prepared at different concentrations of CTAB were depicted in figure 5.4. All the spectra showed the respective elements present such as Bi, P, O and Eu indicating the successful doping of Eu^{3+} into the interstitial sites of $BiPO_4$.

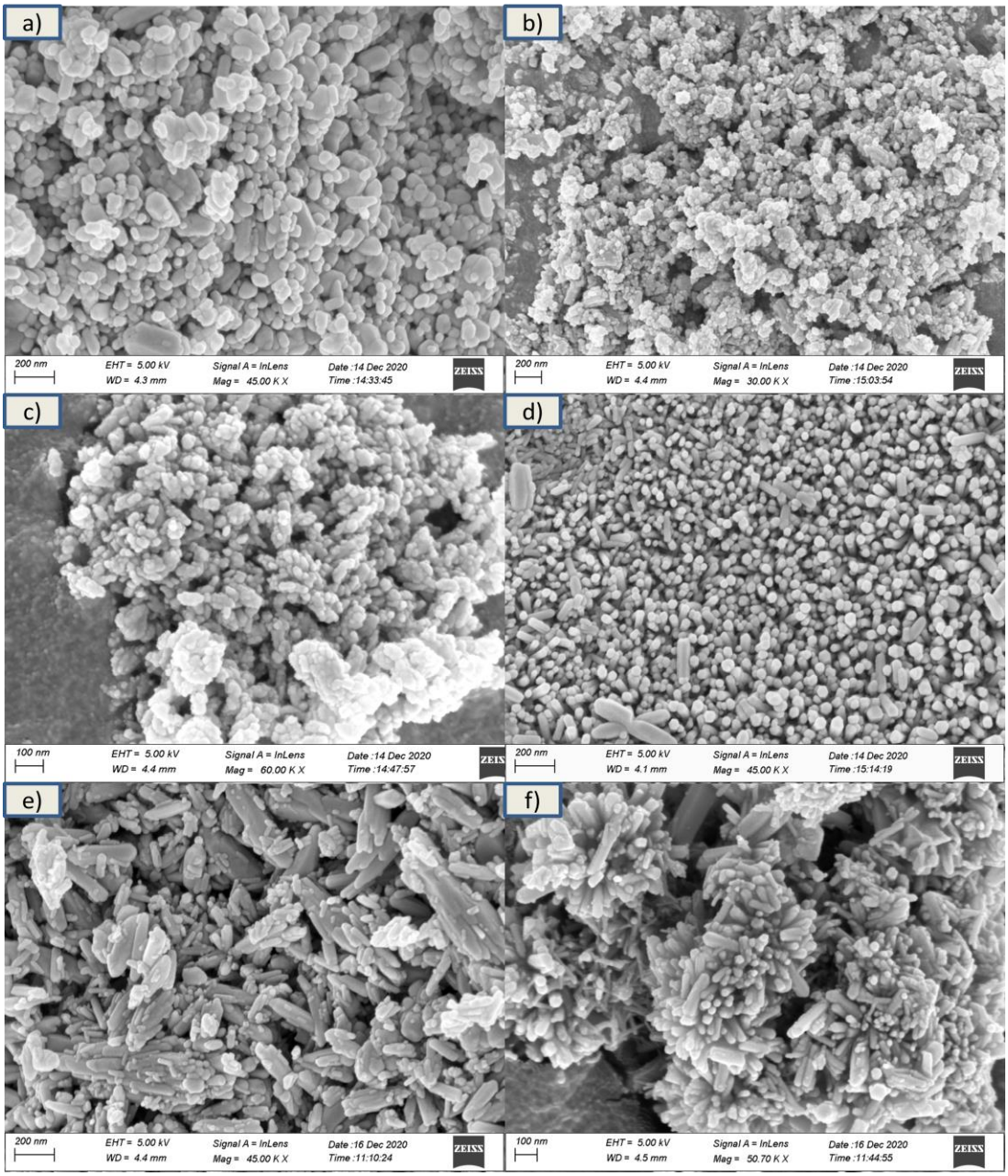

Figure 5.3: a) FE-SEM image of 8 at. % Eu^{3+} doped $BiPO_4$, FE-SEM images of 8 at. % Eu^{3+} doped $BiPO_4$ synthesized at b) acidic (pH2) c) basic (pH12), FE-SEM image of 8 at. % Eu^{3+} doped $BiPO_4$ prepared at d) 0.5mM CTAB e) 5mM CTAB f) 10mM CTAB.

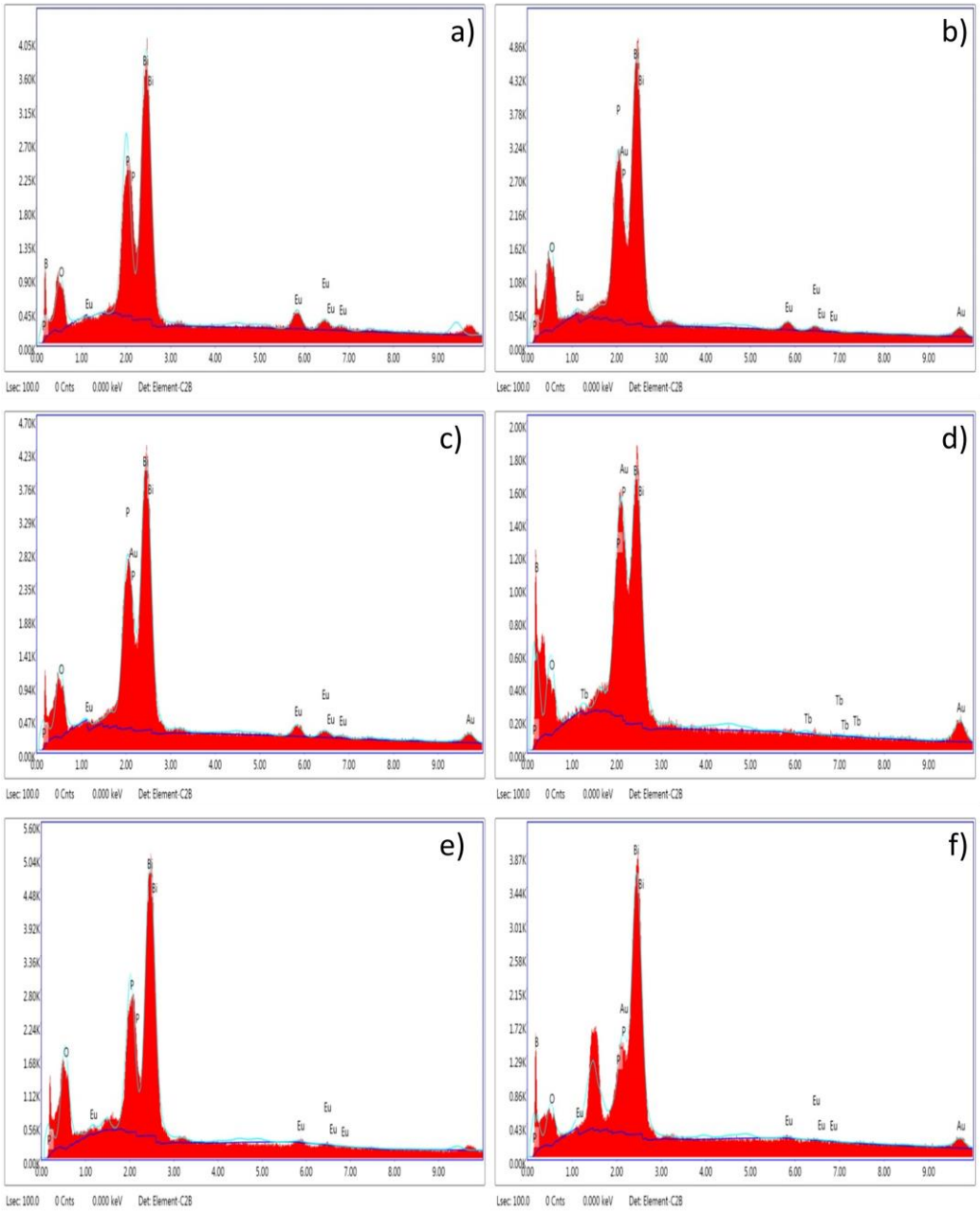

Figure 5.4: a) EDAX spectra of 8 at. % Eu^{3+} doped $BiPO_4$, EDAX spectra of 8 at. % Eu^{3+} doped $BiPO_4$ synthesized at b) acidic (pH2) c) basic (pH12), EDAX spectra of 8 at. % Eu^{3+} doped $BiPO_4$ prepared at d) 0.5mM CTAB e) 6mM CTAB f) 10mM CTAB.

5.3.4 TEM study

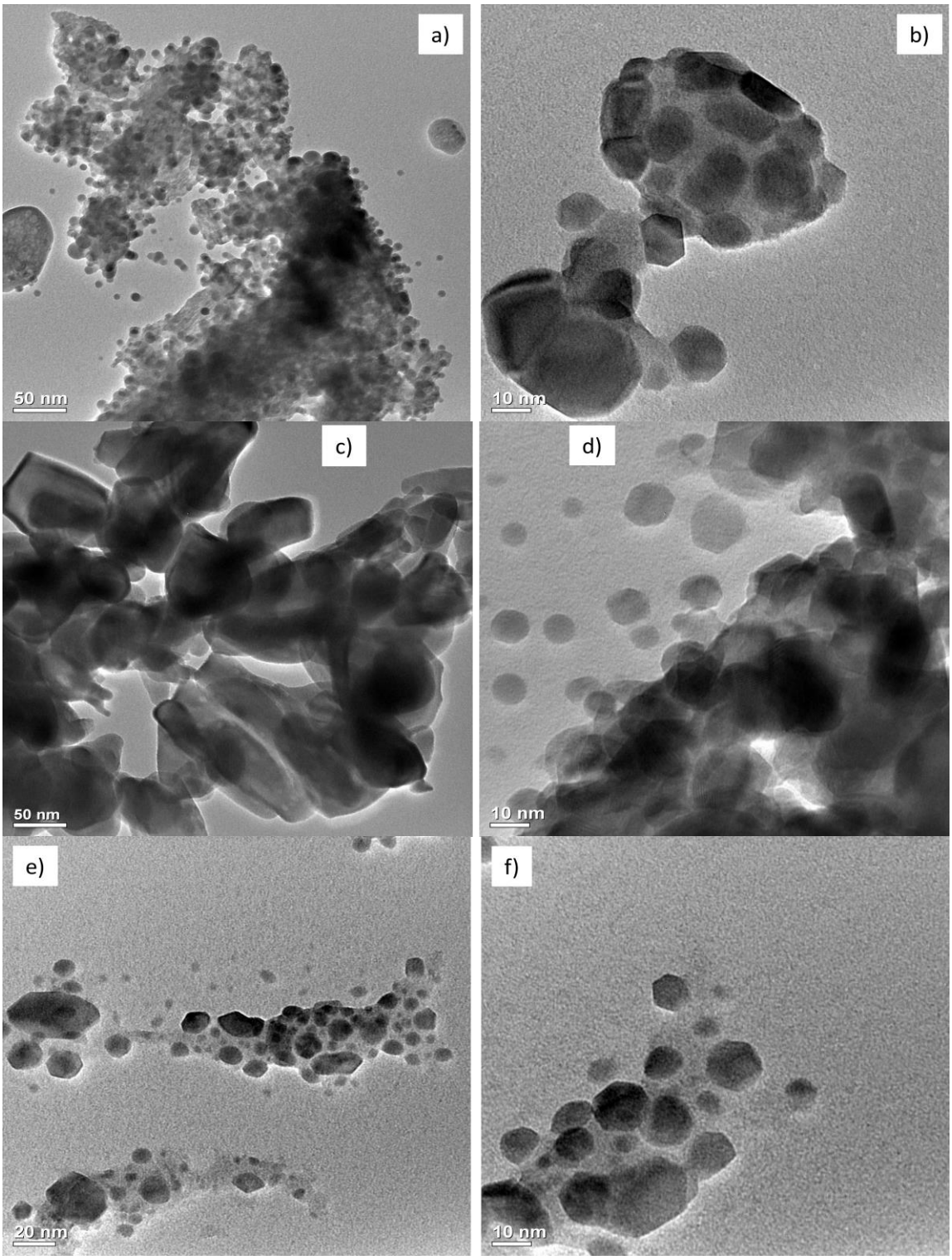

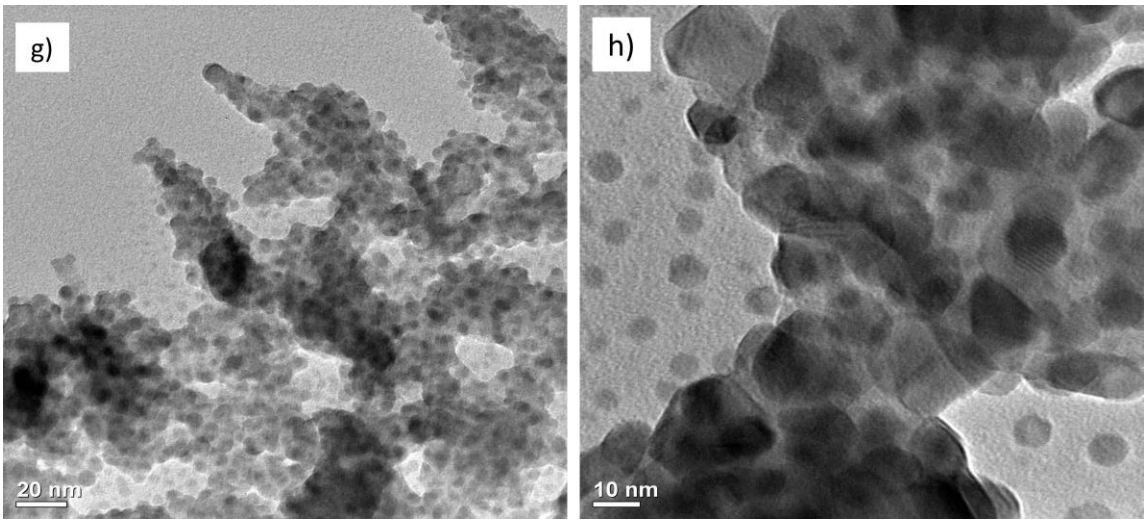

Figure 5.5: TEM images of as-prepared 8at. % Eu^{3+} doped $BiPO_4$ a) at low-resolution b) at high resolution, TEM images of 8at. % Eu^{3+} doped $BiPO_4$ annealed at 800^oC c) at low-resolution d) at high resolution, TEM images of 8at. % Eu^{3+} doped $BiPO_4$ synthesized at pH 2 e) at low-resolution f) at high resolution, TEM images of 8at. % Eu^{3+} doped $BiPO_4$ synthesized at pH12 g) at low-resolution h) at high resolution.

TEM images of as-prepared 8at. % Eu^{3+} doped $BiPO_4$, annealed samples and 8at. % Eu^{3+} doped $BiPO_4$ prepared at different pH were shown in figure 5.5. All the TEM images of the prepared nanophosphors showed hexagonal shape morphology with different crystallite sizes. The crystallite sizes were found in the range of 9nm-26nm for as-prepared sample and that of 800^oC annealed samples were measured in the range of 17nm-35nm. The crystallite sizes of 8at. % Eu^{3+} doped $BiPO_4$ synthesized at pH2 and pH12 were found to be 7nm-30nm and 8nm-20nm respectively. SAED and HRTEM images of as-prepared 8at. % Eu^{3+} doped $BiPO_4$, 800^oC annealed samples (8at. % Eu^{3+} doped $BiPO_4$) and 8at. % Eu^{3+} doped $BiPO_4$ prepared at different pH (2 and 12) were depicted in figure 5.6. Dotted rings of bright spots were noticed in all the SAED images which indicate the formation of well crystalline nature of the prepared phosphors [Singh *et al*., (2019)]. Moreover, HRTEM image exhibited well separated inter-planar lattice fringes for all the samples indicating that the samples are highly crystalline in nature [Singh *et al*., (2019)]. The lattice distance of as-prepared sample was calculated and

found to be 2.99Å which corresponds to (200) plane of Eu^{3+} doped $BiPO_4$ hexagonal phase. For 800^oC annealed sample, the inter-planar lattice distance was coming out to be 3.07Å, corresponding to (120) plane of low-temperature monoclinic phase of Eu^{3+} doped $BiPO_4$. 2.12Å and 3.17Å were calculated as inter-planar lattice distances for the sample prepared at pH2 corresponding to (211) and (200) planes of hexagonal phase of Eu^{3+} doped $BiPO_4$ respectively. Lastly, for the sample prepared at pH12, the lattice distance was calculated as 2.35Å attributed to (112) plane of hexagonal phase of Eu^{3+} doped $BiPO_4$.

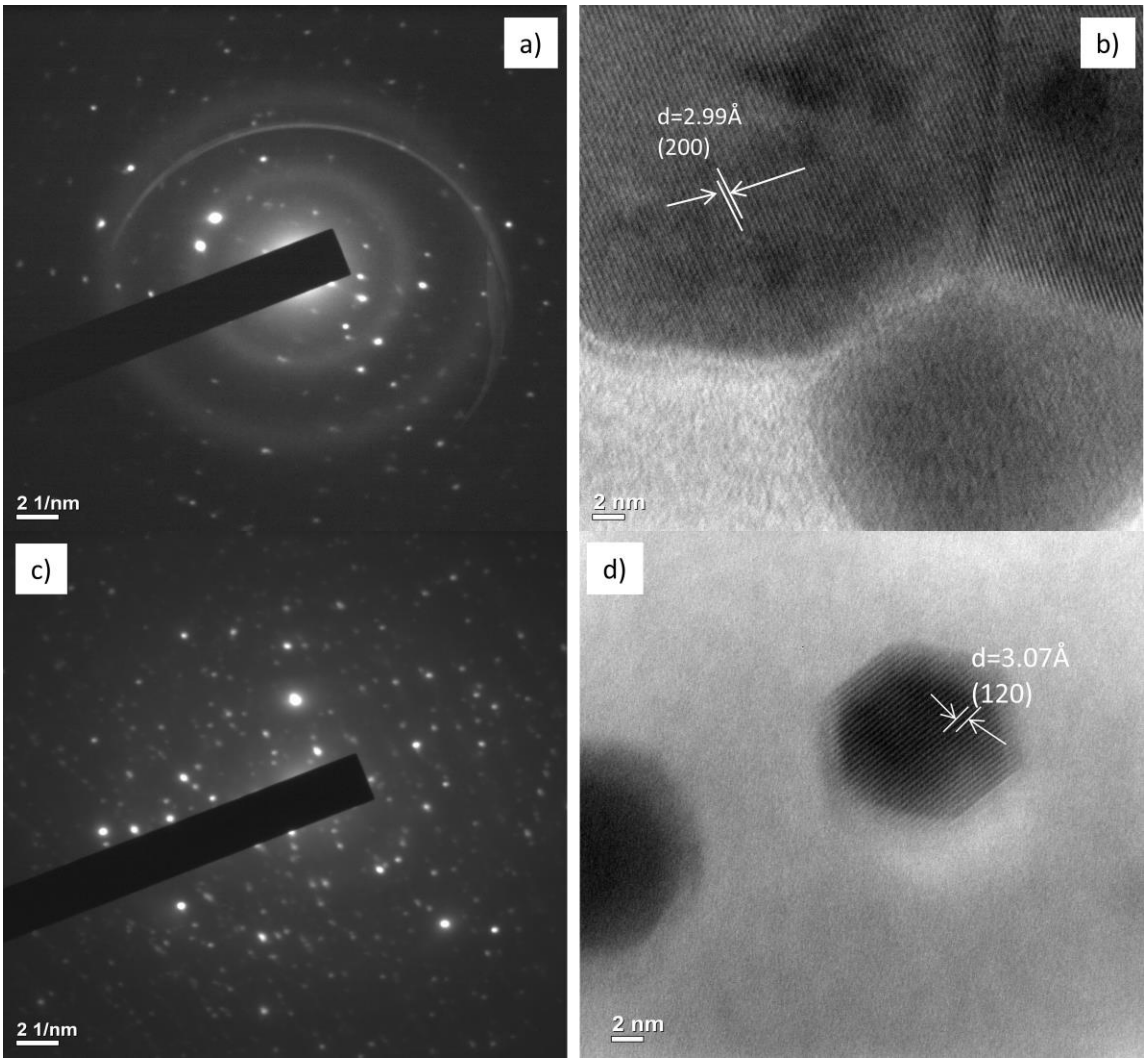

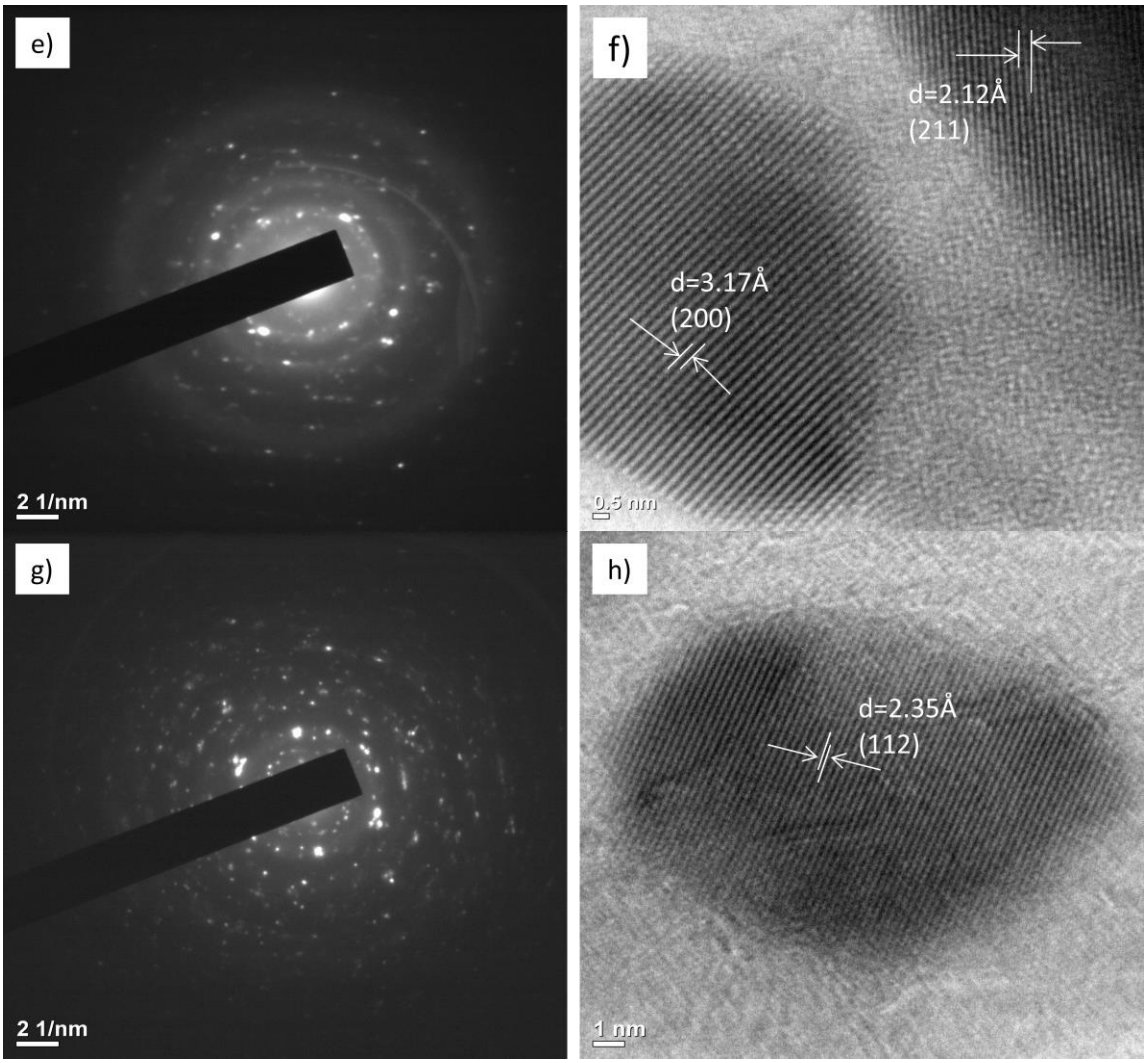

Figure 5.6: a) SAED of 8at. % Eu^{3+} doped $BiPO_4$, b) HRTEM images of 8at. % Eu^{3+} doped $BiPO_4$, c) SAED of8at. % Eu^{3+} doped $BiPO_4$ annealed at 800^oC d) HRTEM images of 8at. % Eu^{3+} doped $BiPO_4$ annealed at 800^oC, e) SAED of 8at. % Eu^{3+} doped $BiPO_4$ synthesized at pH2 f) HRTEM images of 8at. % Eu^{3+} doped $BiPO_4$ synthesized at pH2, g) SAED of 8at. % Eu^{3+} doped $BiPO_4$ synthesized at pH12 h) HRTEM images of 8at. % Eu^{3+} doped $BiPO_4$ synthesized at pH12.

5.3.5 Photoluminescence study

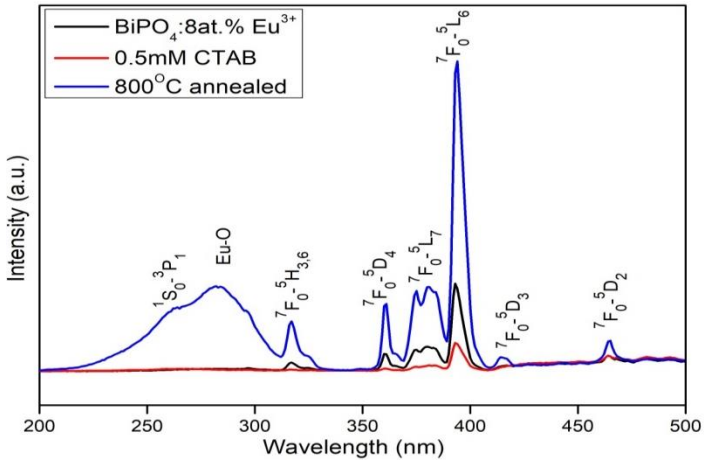

Figure 5.7: The PL excitation spectra of 8at. % Eu^{3+} doped $BiPO_4$, 8at. % Eu^{3+} doped $BiPO_4$ nanophosphors prepared at 0.5mM CTAB and 8at. % Eu^{3+} doped $BiPO_4$ sample annealed at 800^oC. (λ_{emi}=594nm).

The excitation spectra of 8at. % Eu^{3+} doped $BiPO_4$, 8at. % Eu^{3+} doped $BiPO_4$ nanophosphors prepared at 0.5mM CTAB and 8at. % Eu^{3+} doped $BiPO_4$ sample annealed at 800^oC were demonstrated in figure 5.7. The excitation spectra were recorded using an emission wavelength of 594nm and the excitation spectra consist of several excitation peaks resulted from Bi^{3+}, Eu^{3+} and Eu-O [Ma *et al.*, (2017)]. All the spectra showed similar excitation peak profiles except their peak intensities. The small shoulder peak at around 260nm and a broad band centring at 280nm was attributed to $^1S_0$-$^1P_1$ transition of Bi^{3+} and Eu-O respectively [Ma *et al.*, (2017); Zhao *et al.*, (2012)].Bi^{3+} also exhibits $^1S_0$-$^1P_1$transition at a wavelength of 285nm. Hence, the broad band centring at 280nm may be resulted from the overlapping of $^1S_0$-$^1P_1$ transition of Bi^{3+} and Eu-O [Li *et al.*, (2017); Zhao *et al.*, (2012)]. Several sharp peaks which are located at 316, 360, 384, 394, 416 and 464nm are corresponded to the intrinsic transitions i.e. $^7F_0$-$^5H_{3,6}$, $^7F_0$-$^5D_4$, $^7F_0$-$^5L_7$, $^7F_0$-$^5L_6$, $^7F_0$-$^5D_3$, $^7F_0$-$^5D_2$respectively of Eu^{3+} [Zhao *et al.*, (2012)]. Amongst the various excitation peaks, the peak centring at 394nm having the transition $^7F_0$-$^5L_6$ was observed to have maximum excitation peak intensity. Hence, the emission spectra of all the prepared nanophosphors were recorded using 394nm as excitation wavelength.

The emission spectra of different doping concentrations of Eu^{3+} into $BiPO_4$ were recorded by using an excitation wavelength of 394 nm and the emission spectra were depicted in figure 5.8(a). The emission spectra consist of different emission peaks which are originated from $^5D_0$ state of Eu^{3+} and $^3P_1$ of Bi^{3+}. The broad band centring at around 420nm is attributed to $^3P_1 \rightarrow {}^1S_0$ transition of Bi^{3+}. The sharp emission bands centring at 594nm with a shoulder peaking at 589nm, peaks at 614nm with a shoulder peaking at 618nm, 654nm and the emission band in the range of 687nm to 701nm are attributed to $^5D_0$-$^7F_1$, $^5D_0$-$^7F_2$, $^5D_0$-$^7F_3$ $^5D_0$-$^7F_4$ transitions of Eu^{3+} ion respectively [Zhao *et al.,* (2012); Li *et al.,* (2010)]. It has been observed from the emission spectra that the emission intensity of Eu^{3+} increases with increase of Eu^{3+} ion concentration upto 8at. % further increase of Eu^{3+} doping concentration leads to attenuation of the emission intensity which is due to the concentration quenching effect. The effect of annealing temperature on the photoluminescence property of 8at. % doped $BiPO_4$ nanophosphors were also discussed in figure 5.8(b). From this figure, the emission intensities of the samples were found accentuated with increase of annealing temperatures (500^{o}C, 600^{o}C, 700^{o}C and 800^{o}C) and maximum intensity was observed for the sample which was annealed at 800^{o}C. This increased in emission intensity with temperature is due to the change of phase structure from mixed phase structure of hexagonal and low-temperature monoclinic phases to pure low-temperature monoclinic phase [Naidu *et al.,* (2012)]. The effect of pH on the photoluminescence property was also investigated in figure 5.8(c). The optimum emission intensity of Eu^{3+} was achieved when the pH of the reaction medium is 7. Minimum emission intensities were observed for 8at. % Eu^{3+} doped $BiPO_4$ prepared at a pH of 2 and 12 due to the formation of less crystalline sample compared to 8at. % Eu^{3+} doped $BiPO_4$ prepared at a pH of 7. Moreover, 8at. % Eu^{3+} doped $BiPO_4$ particles formed at a pH of 2 and 12 of the reaction medium were found agglomerated which reduces the emission intensity. Further, the effect of CTAB concentrations of the reaction meadium on the photoluminescence property was discussed in figure 5.8(d). The emission intensity of 8at. % Eu^{3+} doped $BiPO_4$ was found maximum for the sample prepared in 0.5mM CTAB concentration. With the increased of CTAB concentration of

the reaction medium, the emission intensity decreases. This is due to the formation of larger particle size, passivation of 8at. % Eu^{3+} doped $BiPO_4$ nanoparticles surface defects by surfactant molecules which lower the active sites on the surface of Eu^{3+} doped $BiPO_4$ and change of morphology from hexagonal to cucumber like shape and later on to sea flower upon increasing the concentration of CTAB from 0.5mM to 6mM and later on to 10mM respectively. And also some areas of the FE-SEM image of the sample prepared at 10mM showed agglomeration of the particles which decreases the photoluminescence intensities. Moreover, the grain sizes of the particles were also increased as the concentration of CTAB increases. Hence, the photoluminescence intensity was observed to decrease when the concentration of CTAB increases.

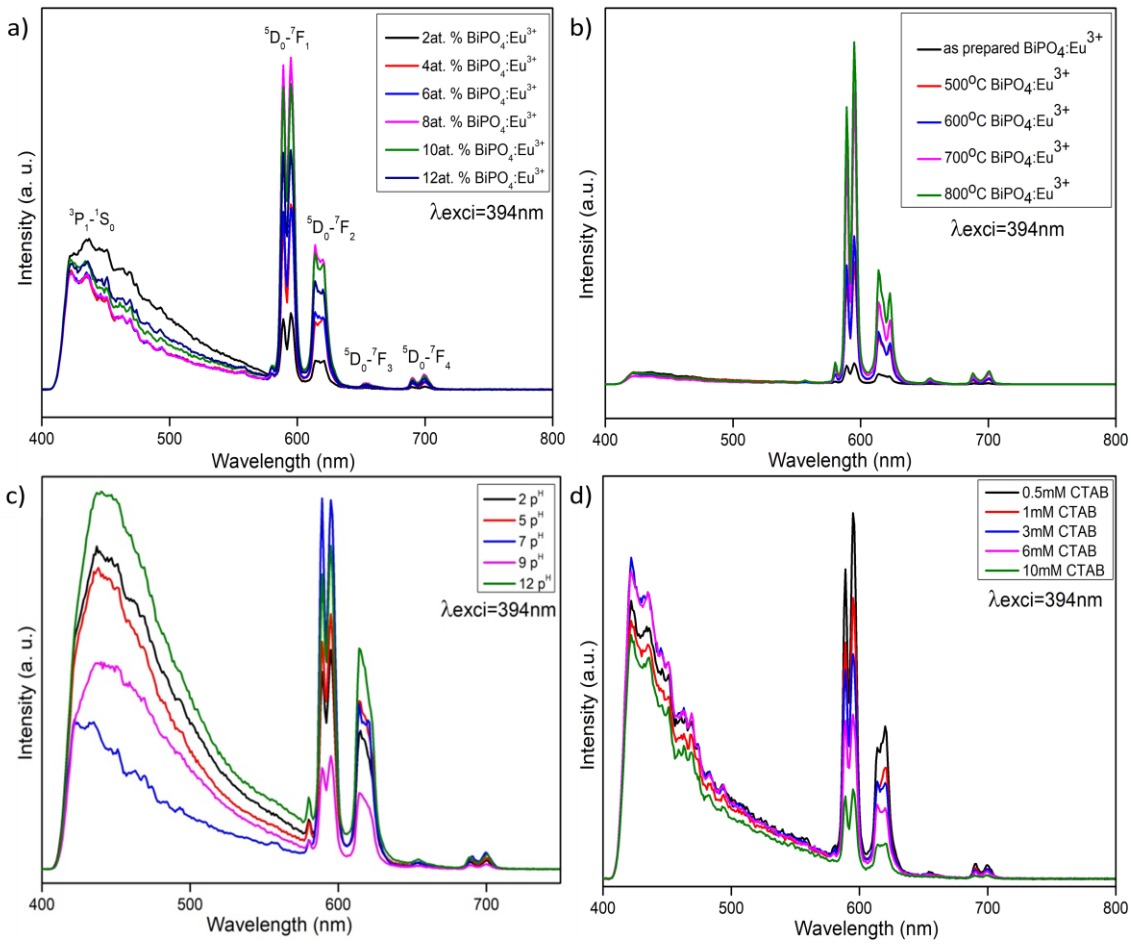

Figure 5.8: The PL emission spectra of a) $BiPO_4$:xEu^{3+} (x=2,4,6,8,10,12at. %), b) as prepared $BiPO_4$:8at. % $Eu^{3+}$and annealed samples at 500^{o}C, 600^{o}C, 700^{o}C, 800^{o}C c) $BiPO_4$:8at. % Eu^{3+}prepared at pH=2,5,7,9,12 d) $BiPO_4$:8at. % Eu^{3+} prepared using 0.5mM, 1mM, 3mM, 6mM,10mM, recorded using excitation wavelength of 394nm.

5.3.6 CIE diagram

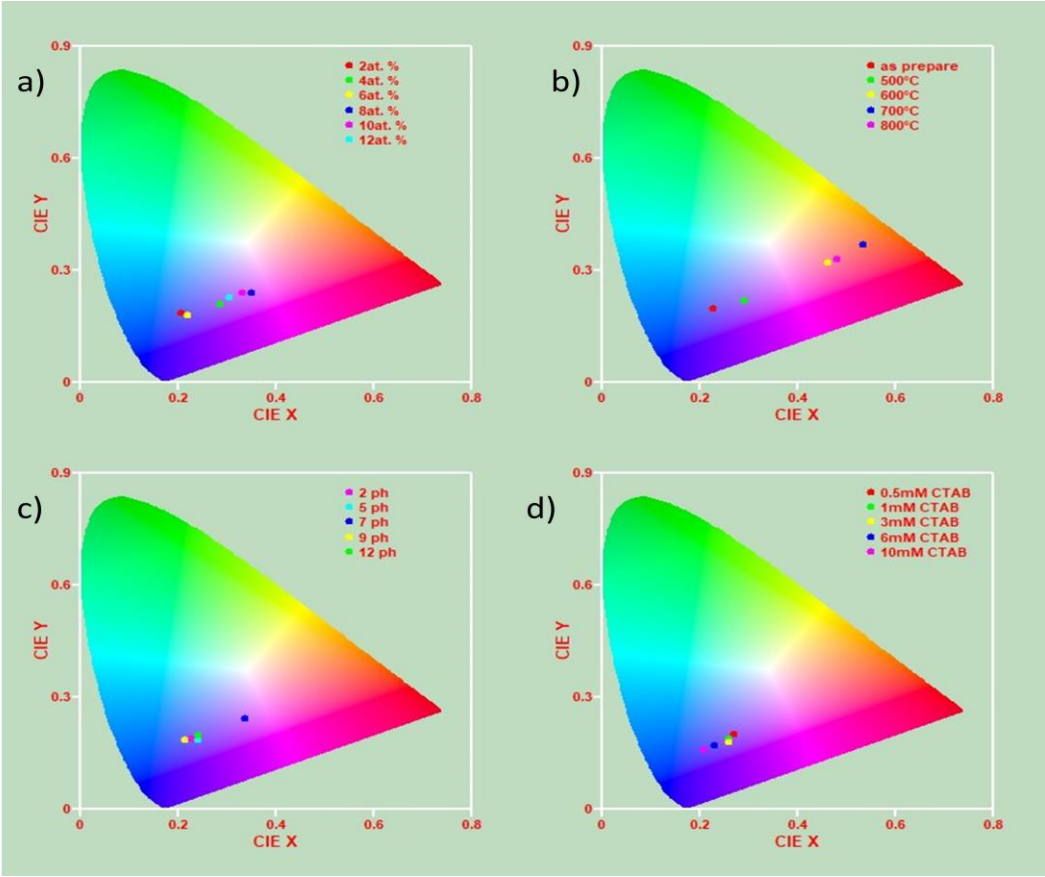

Figure 5.9: CIE chromaticity diagrams of a) $BiPO_4$:xEu^{3+} (x=2,4,6,8,10,12 at. %), b) 8at. % Eu^{3+} doped $BiPO_4$ annealed at 500°C, 600°C, 700°C, 800°C, c) 8at. % Eu^{3+} doped $BiPO_4$ prepared in pH =2, 5, 7, 9, 12 and d) 8at. % Eu^{3+} doped $BiPO_4$ prepared in different CTAB (0.5, 1, 3, 6, 10mM) concentrations.

The colour timbre of the emitted light can be comprehended using CIE co-ordinates. The CIE co-ordinates were calculated from their emission spectra excited at 394nm and they are listed in table 5.2. The CIE chromaticity diagrams of $BiPO_4$:xEu^{3+} (x=2,4,6,8,10,12at. %), 8at. % Eu^{3+} doped $BiPO_4$ annealed at 500°C, 600°C, 700°C, 800°C, 8at. % Eu^{3+} doped $BiPO_4$ synthesized in different pH (2, 5, 7, 9, 12) and in different CTAB (0.5, 1, 3, 6, 10mM) concentrations were shown in figure 5.9(a), 5.9(b), 5.9(c) and 5.9(d) respectively. The diagram showed emission of Bluish purple color for

$BiPO_4$:*x*Eu^{3+} (*x*=2,4,6,8,10,12at. %), 8at. % Eu^{3+} doped $BiPO_4$ samples synthesized at different pH and in different CTAB concentrations. But for the annealed samples, the emission colours vary with annealing temperature. It exhibited Bluish purple colour for as-prepared sample, Reddish purple colour for 500^oC, Pink colours for 600^oC, 800^oC and Orange pink for 700^oC annealed samples.

Table 5.2: CIE chromaticity coordinates of the $BiPO_4$:Eu^{3+} nanophosphors upon excitations at 394 nm.

Sample		x	y
% of Eu^{3+} doped into $BiPO_4$ lattice	2	0.205	0.186
	4	0.286	0.210
	6	0.219	0.181
	8	0.350	0.244
	10	0.332	0.241
	12	0.302	0.229
As prepared		0.226	0.197
500^oC		0.292	0.220
600^oC		0.460	0.323
700^oC		0.481	0.330
800^oC		0.534	0.369
pH of the reaction medium	2	0.226	0.190
	5	0.241	0.187
	7	0.335	0.244
	9	0.213	0.185
	12	0.240	0.185
CTAB concentration of the reaction medium (in mM)	0.5	0.273	0.202
	1	0.259	0.194
	3	0.259	0.183
	6	0.227	0.167
	10	0.207	0.159

5.4 Conclusion

Hexagonal phase of Eu^{3+} doped $BiPO_4$ nanophosphors was synthesized by co-precipitation method using ethylene glycol as reaction medium. Change of phase structure from hexagonal to mixed phase of hexagonal and low-temperature monoclinic phases and later on to pure low-temperature monoclinic phase upon annealing at 500^oC and 800^oC respectively were confirmed from XRD study. TEM images revealed the hexagonal shape morphology of the synthesized nanophosphors. Photoluminescence emission spectra showed the characteristic emission peaks of Bi^{3+} as well as Eu^{3+} and the optimum concentration of Eu^{3+} ion for doping was found to be 8at. %. Further, the photoluminescence emission intensity increased with increase of annealing temperature due to the change in their phase structure from hexagonnnal to low-temperature monoclinic phase. The effect of pH of the reaction medium on the photoluminescence property of Eu^{3+} doped $BiPO_4$ nanophosphors was discussed and emission intensity was found maximum at pH 7. 0.5mM exhibited maximum emission intensity and the emission intensity decreased as CTAB concentration of the reaction medium increased due to the formation of agglomerated particles and larger particle size of the nanoparticles. CIE diagram showed the emission of Bluish purple colour of the synthesized nanophosphors while the emission colour varies for the samples annealed at 500^oC, 600^oC, 700^oC, 800^oC and their emission colours were found to be Reddish purple for 500^oC, Pink colour for 600^oC and 800^oC, Orange pink for 700^oC annealed samples. From these results, it is concluded that the synthesized nanophosphors may have application in lighting, optical devices, biomedical imaging etc.

CHAPTER-6

Room temperature simple precipitation method for the preparation of Sm^{3+} ion doped $BiPO_4$ and effect of annealing temperatures on their photoluminescence property

6.1 Introduction

Lanthanide ions doped inorganic luminescent materials have been given considerable attention because of their significant importance. They are used as catalysts, sensors, high-performance luminescent devices, other functional materials etc. based on their electronic, optical and chemical characteristics [Eliseevaab and Bunzli (2011); Hou *et al.,* (2012)]. Out of various lanthanide ions, Sm^{3+} has $4f^5$ electronic configuration and absorbed the interest of researchers due to their high quantum efficiency [Singh *et al.,* (2018)]. Due to $^4G_{5/2}$-$^6H_{J/2}$ (J = 5, 7, 9, 11) transitions, Sm^{3+} ion normally produced emission of yellowish-orange/reddish-orange/orange colour and has a wide range of applications in the field of sensors, solid-state laser, undersea communication fluorescence devices etc. [Hussain *et al.,* (2009); Bahadur *et al.,* (2014)]. Lanthanide ion alone showed low luminescence efficiency due to poor cross-section resulted from their f-f forbidden transitions [Liu *et al.,* (2010); Vranjeˇs *et al.,* (2013); Ningthoujam *et al.,* (2012)]. Hence, it is needed to encompass into a host material.

As Bi^{3+} have similar ionic size with lanthanide ions, $BiPO_4$ has been considered as one of the most suitable host material for doping lanthanide ion [Naidu *et al.,* (2012)]. Moreover, $BiPO_4$ has comparatively low cost, excellent physio-chemical properties such as high absorption edge, high stability in terms of chemical and mechanical stability etc. [Roming and Feldmann, (2009)]. Moreover, Bi^{3+} ion itself acted as a sensitizer and the luminescence resulted from Bi^{3+} ions are very attractive due to the electronic transition between $6s^2$ and 6s6p and Stoke shift associated with its absorption-emission characteristics [Naorem *et al.,* (2020)]. The composition and phase structure of the host materials also play an important role in controlling the optical, chemical and physical

properties of the materials as luminescence property depends on optical, chemical and physical properties of the materials [Naidu *et al.,* (2012); Naorem *et al.,* (2020); Naorem*et al.,* (2020),]. In this regard, synthetic route played a vital role in controlling chemical and physical properties. Wet chemical synthetic routes such as hydrothermal method, sol-gel, co-precipitation methods etc. are commonly employed as it is easy to control pH, reaction temperature, solution concentrations etc. Amongst these wet chemical methods, co-precipitation is one of the easiest, low cost, energy-saving method for the synthesis of lanthanide ion-doped luminescent material. However, luminescent material which is synthesized using wet chemical method generally adsorbed luminescent quenchers such as OH^-, CO_3^{2-} etc. on the surface of the material and even co-ordinated with lanthanide ion [Mass *et al.,* (2002); Jiang *et al.,* (2003)]. In most cases, OH^- is responsible for luminescent quenching of the lanthanide ion-doped luminescent material [Mass *et al.,* (2002); Luwang *et al.,* (2010)]. In wet chemical synthetic route, water molecules are associated with the phase structure of the material and it is difficult to control in this synthetic route. However, these luminescent quenchers can be removed by heating the material at high temperatures [Luwang *et al.,* (2010)]. Hence, in this chapter, Sm^{3+} ion-doped $BiPO_4$ phosphor was prepared using room temperature simple precipitation method. Their photoluminescence properties resulted due to annealing at different temperatures were discussed.

6.2 Experimental details

6.2.1 Sample preparation

Samarium nitrate hexahydrate ($Sm(NO_3)_3.6H_2O$) with 99.99% purity, Bismuth nitrate pentahydrate ($Bi(NO_3)_3{\cdot}5H_2O$) with purity percentage of 98%, ammonium dihydrogen phosphate ($NH_4H_2PO_4$) of 98% purity purchased from Alfa Aesarwere used for the synthesis of Sm^{3+} ions doped $BiPO_4$. The synthesis steps are given as follows, firstly the stoichiometric amount of $Bi(NO_3)_3{\cdot}5H_2O$ was mixed with 70 ml of water into a beaker and it was stirred in a magnetic stirrer for 15mins. Stoichiometric amounts of $NH_4H_2PO_4$ and $Tb(NO_3)_3$ were further added to the above solution. The solution is

further stirred for 2hrs at room temperature to get white precipitate. The white precipitate formed was washed 4-5 times with distilled water and lastly with acetone. The sample thus obtained was dried in an oven at a temperature of 80^{o}C for 12 hrs. Different doping concentrations of Sm^{3+} ion into $BiPO_4$ were also prepared following the same procedure. 5at. % Sm^{3+} doped $BiPO_4$ which has the highest emission intensity was further annealed at different temperatures i.e. 500^{o}C, 600^{o}C, 700^{o}C, 800^{o}C.

6.2.2 Characterization of the samples

PANalytical's X-ray diffractometer (X'-PertPRO) with CuKα (1.5406 A˚) radiation with Ni filter was used to determine the crystal structure of the prepared samples. The vibrational spectra of the prepared sample were analyzed using Shimadzu Iraffinity-1s FT-IR spectrometer using KBr as a beam splitter. Field emission scanning electron microscopy (FESEM) was recorded by Sigma 300, Carl Zeiss in order to see the morphologies of the samples. Hitachi (F-7000) fluorescence spectrophotometer having xenon discharge lamp as excitation source was used for the recording of excitation and emission spectra. All the measurements were taken at room temperature.

6.3 Results and Discussions

6.3.1 XRD study

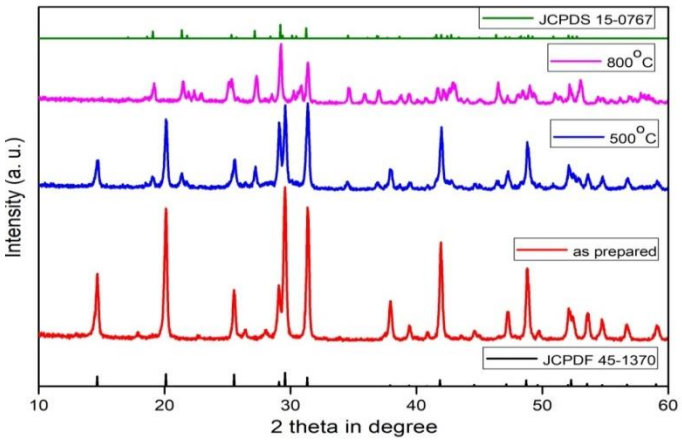

Figure 6.1: XRD patterns of as prepared $BiPO_4$:5at. % Sm^{3+}, 500^{o}C and 800^{o}C annealed samples.

The XRD patterns of as-prepared 5at. % Sm^{3+} ion doped $BiPO_4$, 500^oC and 800^oC annealed samples were shown in figure 6.1. The diffraction patterns showed the hexagonal phase for as prepared sample with respect to JCPDS card no. 45-1370 [Zhao *et al.,* (2013)]. The observed diffraction peaks are sharp and strong showing well crystallization of the samples. Further, no impurity peak is observed indicating the formation of well-crystallized pure hexagonal phase of the prepared sample. The XRD patterns of 500^oC annealed sample exhibited a mixed phase structure of hexagonal and low-temperature monoclinic phases of $BiPO_4$ according to JCPDS card no. 45-1370 and card no. 15-0767 [Zhao *et al.,* (2013); Naorem *et al.,* (2020)]. Further, change of phase structure from mixed phase to low-temperature monoclinic phase was observed when the sample is annealed at 800^oC as the diffraction peaks are corresponded to low-temperature monoclinic phase of $BiPO_4$ according to JCPDS card no. 15-0767 [Naorem *et al.,* (2020)]. No impurity peak was observed even in the annealed samples also revealing the formation of pure low-temperature monoclinic phase.

6.3.2 FT-IR study

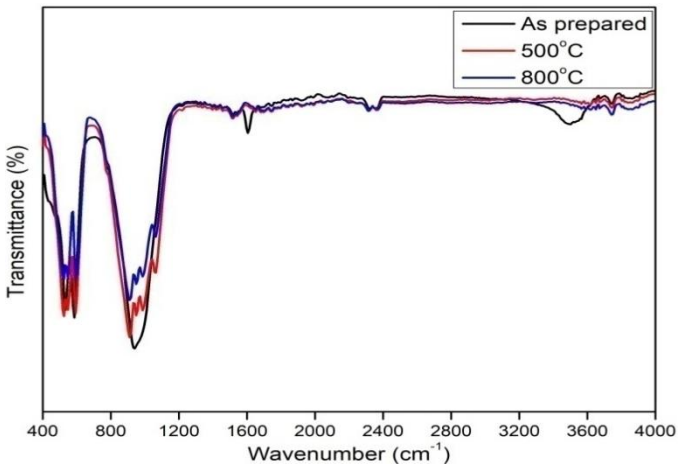

Figure 6.2: FT-IR spectra of as-prepared ($BiPO_4$:5at. % Sm^{3+}) and annealed samples at 500^oC and 800^oC.

The vibrational properties of PO_4^{3-} group in different phases were discussed using FT-IR spectra. The FT-IR spectrum of 5at. % of Sm^{3+} doped $BiPO_4$ was shown in

figure 6.2. The most intense band centring at 941cm^{-1} is attributed to the symmetric stretching vibrational modes of O-P–O bond [Lakshminarayana *et al.,* (2015); Xue *et al*., (2009), Pawlig *et al*., (2001)]. The other bands centring at 532 cm^{-1} and 586cm^{-1} are resulted due to bending vibrational modes of O–P–O linkage [Zhao *et al.,* (2013); Achary *et al.,* (2013)]. The two bands at 1605cm^{-1} and 3480cm^{-1} are associated with ν(O–H) and δ(H–O–H) [Zhao *et al.,* (2011)]. These all characteristic bands correspond to the hexagonal phase. The FT-IR spectra for the samples annealed at different temperatures were also displayed in figure 6.2. The FT-IR spectra for the sample annealed at 800^{o}C showed splitting of the absorption band centring at 941cm^{-1} into four peaks at 910, 948, 987 and 1064 cm^{-1} in the fingerprint region which are corresponded to the monoclinic phase of $BiPO_4$ [Xue *et al.,* (2009)]. In case of 500^{o}C annealed sample, the absorption band centring at 941cm^{-1} was split which may be due to the presence of monoclinic phase in their phase structure. Moreover, no absorption bands were observed at 1605cm^{-1} and 3480cm^{-1} indicating that the samples were free from water [Singh *et al*., (2019)].

6.3.3 SEM and EDAX study

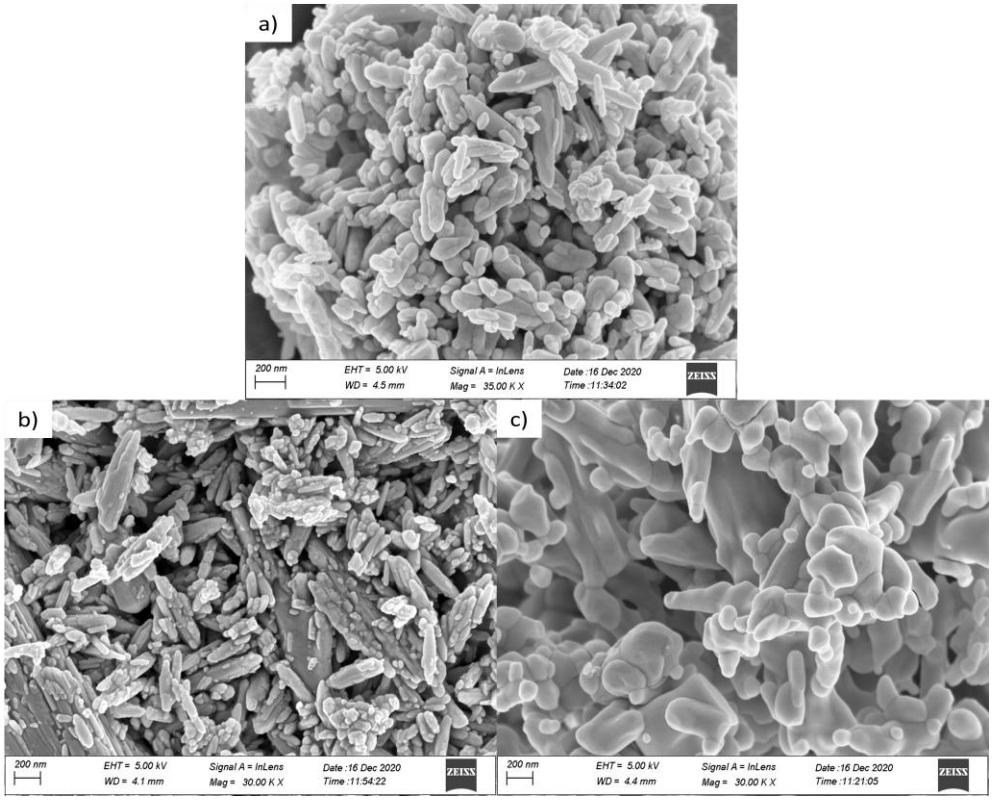

Figure 6.3: SEM image of a) as prepared ($BiPO_4$:5at. % Sm^{3+}), b) 500^oC annealed sample c) 800^oC annealed sample.

The morphology of the as-prepared sample as well as the samples annealed at 500°C and 800°C were contemplated using Scanning Electron Microscopy (SEM). The above figure 6.3(a), 6.3(b),6.3(c) showed SEM images of as-prepared (5at. % Sm^{3+} doped $BiPO_4$) sample, the samples annealed at 500°C and 800°C respectively. It has been disclosed from the figure that the nano-rod morphology of as-prepared sample with grain sizes range from 30nm to 600nm were observed. The sample which was annealed at 500°C also showed nano-rod morphology of the particles with grain sizes ranged from 60nm to 750nm while the sample which was annealed at 800°C revealed irregular shape and sizes range from 100nm to 1µm. The EDAX spectra of as-prepared (5at. % Sm^{3+} doped $BiPO_4$) sample, the samples annealed at 400°C and 1000°C were shown in figure 6.4. It has been clearly revealed that the spectra consist of peaks emanated from the

elements i.e. Bi, P, O and Sm. These EDAX spectra also support the successful doping of Sm^{3+} into $BiPO_4$ lattice.

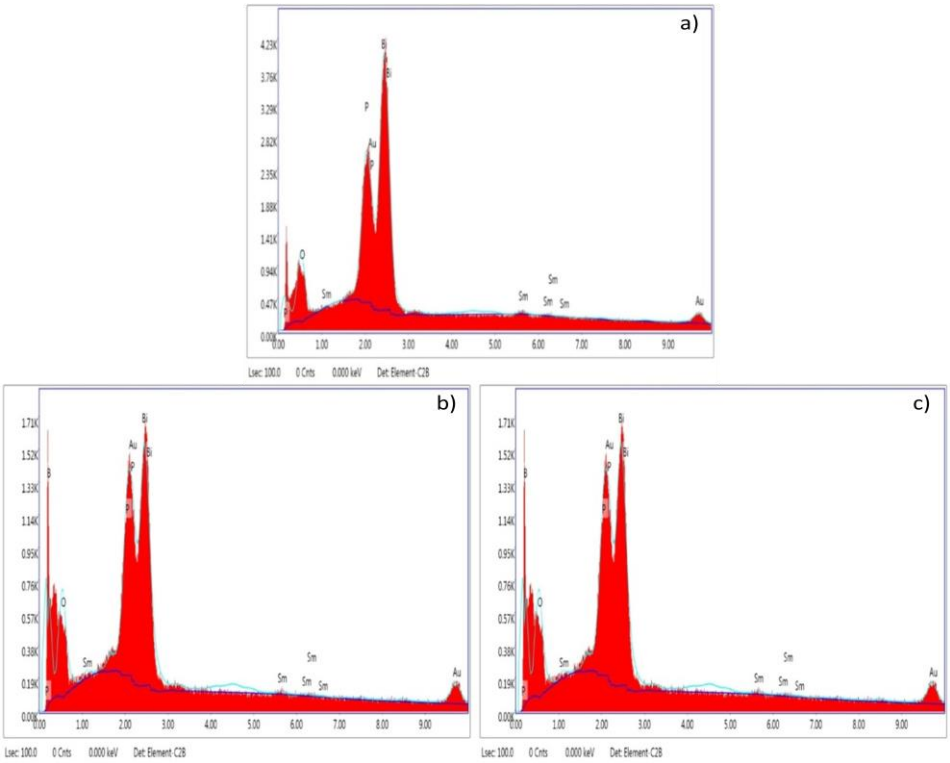

Figure 6.4: EDAX spectra of a) as prepared, b) 500^{o}C and c) 800^{o}C annealed samples.

6.3.4 Photoluminescence study

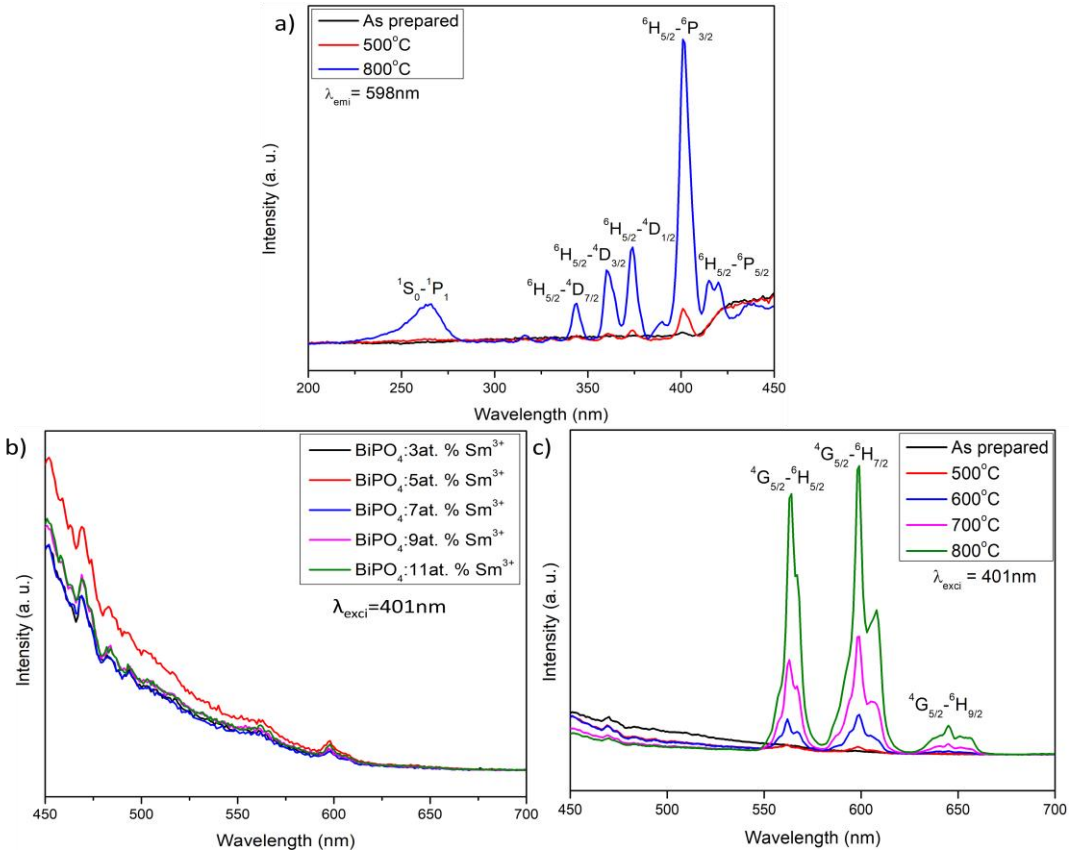

Figure 6.5: a) PL excitation spectra of as prepared (5at. % Sm^{3+} doped $BiPO_4$) sample, annealed samples at 500°C and 800°C with emission wavelength of 598nm b) PL emission spectra of $BiPO_4$:xSm^{3+} (x=3,5,7,9,11at. %) (λ_{exci}=401nm) c) Emission spectra of as prepared(5at. % Sm^{3+} doped $BiPO_4$) sample, 500°C, 600°C, 700°C, 800°C annealed samples for 2hrs (λ_{exci}=401nm).

The photoluminescence excitation spectra of as-prepared sample, 500°C and 800°C annealed samples were shown in figure no. 6.5(a). The excitation spectra were recorded using the emission wavelength of 598nm. The spectra consist of six absorption bands which are centring at 265nm, 344nm, 360nm, 374nm, 401nm and 415nm. The peak at 265nm is attributed to $^1S_0$-$^1P_1$ transition resulted from Bi^{3+} [Zhao *et al.*, (2013)]. The other remaining peaks correspond to $^6H_{5/2}$-$^4D_{7/2}$, $^6H_{5/2}$-$^4D_{3/2}$, $^6H_{5/2}$-$^4D_{1/2}$, $^6H_{5/2}$-$^6P_{3/2}$

and $^6H_{5/2}$-$^6P_{5/2}$ transitions originated from Sm^{3+} respectively [Shi *et al.,* (2015); Chanu and Singh (2020)]. Figure 6.5(b) and 6.5(c) showed the emission spectra of $BiPO_4$:*x*Sm^{3+} (*x*=3,5,7,9,11at. %) and the samples annealed at 500^{o}C, 600^{o}C, 700^{o}C and 800^{o}C respectively. The emission spectra were recorded with an excitation wavelength of 401nm as $^6H_{5/2}$-$^6P_{3/2}$ was giving the highest excitation peak intensity. The emission spectra consist of three emission bands centring at 563nm, 598nm and 645nm which are attributed to $^4G_{5/2}$-$^6H_{5/2}$, $^4G_{5/2}$-$^6H_{7/2}$, $^4G_{5/2}$-$^6H_{9/2}$ transitions of Sm^{3+}respectively [Chanu and Singh (2017); Okram *et al.,* (2013)]. No significant change in their emission intensities was observed for different doping concentrations of Sm^{3+} while 5at. % of Sm^{3+} was found a little bit higher in emission intensity as compared to other doping concentrations. So, the sample with 5at. % of Sm^{3+} doping concentration was further annealed at different temperatures such as 500^{o}C, 600^{o}C, 700^{o}C, 800^{o}C. The photoluminescence emission intensities were found accentuated with increased of annealing temperatures. This increased in photoluminescence emission intensity upon heating is due to the change of phase structure from hexagonal to low-temperature monoclinic phase and the absconding of luminescent quenchers at a temperature of 800^{o}C [Naidu *et al.,* (2012); Luwang *et al.,* (2010)].

6.3.5 CIE study

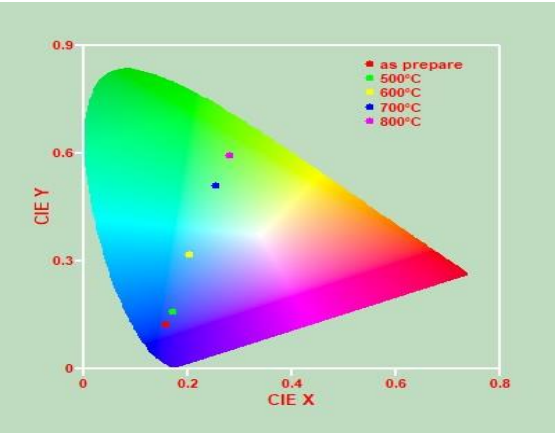

Figure 6.6: CIE chromaticity diagrams of as prepared $BiPO_4$:5at. % Sm^{3+} nanophosphor and the samples annealed at 500^{o}C, 600^{o}C, 700^{o}C, 800^{o}C.

The CIE chromaticity diagram of as prepared 5at. % Sm^{3+} doped $BiPO_4$ and samples (5at. % Sm^{3+} doped $BiPO_4$) annealed at 500^oC, 600^oC, 700^oC, 800^oC for 2hrs are depicted in figure 6.6. The CIE colour co-ordinates of the samples were calculated from the emission spectra obtained upon excitation at 401nm and the calculated co-ordinates were listed in table 6.1. From the CIE diagram study, it was observed that as prepared (5at. % Sm^{3+} doped $BiPO_4$) sample showed emission in the blue region of the electromagnetic radiation. As the sample is annealed at 500^oC, the emission colour shifted slightly towards cyan region but for the sample which was annealed at 600^oC exhibited purely cyan colour emission while 700^oC annealed sample showed emission of greenish cyan colour and lastly, the sample annealed at 800^oC exhibited emission of light green colour. The calculated colour co-ordinates for all the samples were calculated by usingMcCamy's equation [Du *et al*., (2016), Ryadun *et al*., (2020)]:

$$CCT = -437n^3 + 3601n^2 - 6861n + 5514.31 \text{ and } n = (x-x_e)/(y-y_e),$$

Where x and y represents the calculated colour co-ordinates.The CCT values werelisted in table 6.1.

Table 6.1: CIE chromaticity coordinates and CCT of the $BiPO_4:Sm^{3+}$ nanophosphors upon excitations at 401 nm.

Sample	x	y	CCT
As prepare	0.157	0.122	2331
500$^{\circ}C$	0.171	0.158	1527
600^oC	0.204	0.318	2072
700^oC	0.252	0.511	3114
800^oC	0.281	0.594	6146

6.4 Conclusion

In conclusion, BiPO4:xSm^{3+} (x=3,5,7,9,11at. %) nanophosphors were synthesized by co-precipitation method using water as reaction medium followed by heating of $BiPO_4$:5at. % Sm^{3+} at different temperatures i.e. 500^{o}C, 600^{o}C, 700^{o}C, 800^{o}C for 2 hrs. The hexagonal phase of the as-prepared sample was observed from the XRD study and the change of phase structure from hexagonal phase to low-temperature monoclinic phase was noticed upon annealing the sample at 800^{o}C. Rod-shaped morphology of size ranging from 30nm to 600nm of the as-prepared nanophosphors was detected from SEM image. There occurred no change in morphology of the nanophosphors upon heating at 500^{o}C but the size of the nanophosphors increased (60nm to 750nm) while change of morphology from nano rod shape morphology to irregular morphology upon heating at 800^{o}C was noticed and the sizes were also found increased (100nm to 1µm). Sm^{3+} doped $BiPO_4$ showed excitation spectra consisting six excitation peaks resulted from Bi^{3+} and Sm^{3+}, the transition $^6H_{5/2}$-$^6P_{3/2}$ at 401nm was found as the highest excitation peak. The characteristic emission peaks of Bi^{3+} and Sm^{3+} were observed in the emission spectra of Sm^{3+} doped $BiPO_4$ and the optimum concentration of Sm^{3+} was found to be 5at. %. The emission intensity was found accentuated with increased of heating temperature which is due to the change of phase structure from hexagonal to low-temperature monoclinic phase upon annealing at 800^{o}C. CIE study showed the exhibition of blue colour emission for as-prepared sample, bluish cyan for 500^{o}C annealed sample, cyan for 600^{o}C annealed sample, greenish cyan for 700^{o}C annealed sample and light green for the sample which was annealed at 800^{o}C. The above results showed that the prepared nanophosphors may have potential applications in fluorescence lamp, optical devices, displays etc.

Summary and conclusion

In summary, $BiPO_4:Ln^{3+}$ (Ln^{3+} = Ce^{3+}, Tb^{3+}, Eu^{3+}, Sm^{3+}) phosphors were synthesized by co-precipitation method using ethylene glycol and water as reaction mediums. The prepared phosphors were characterized by using the techniques such as XRD, FT-IR, UV-Vis spectroscopy, FE-SEM, EDAX, TEM, HRTEM, SAED and PL. The effect of lanthanide ions doping concentrations and also the effect of annealing temperature on their photoluminescence intensities were studied. The photoluminescence properties resulted from different pH and CTAB concentrations of the reaction medium were also investigated and the following results were observed:

- The formation of low-temperature monoclinic phase of Ce^{3+} ion doped $BiPO_4$ phosphors was confirmed from XRD and FT-IR studies. SEM study revealed the rice shape morphology of $BiPO_4:Ce^{3+}$ (7at.%). Photoluminescence analysis showed a broad emission band extending in a wide wavelength range with maxima around 419 and 470 nm was observed under excitation at 370 and 417 nm, respectively attributed to $5d \rightarrow {}^2F_{5/2}$, ${}^2F_{7/2}$ transitions of Ce^{3+} ion. The optimum concentration of Ce^{3+} ion was found to be 7at. %. $BiPO_4:Ce^{3+}$ (7at.%) was able to degrade 90% of methylene blue under 120 minutes of UV light irradiation.

- The XRD and FT-IR studies showed low-temperature monoclinic phase of the prepared Tb^{3+} ions doped $BiPO_4$ phosphors. Change of phase structure from low-temperature monoclinic phase to high-temperature monoclinic phase upon annealing at 1000^oC was observed through XRD analysis. Agglomerations of particles were noticed from SEM image analysis. TEM image revealed the formation of hexagonal shape morphology with particle size in the range of 8-20nm. In the photoluminescence study, the emission spectra showed four

emission peaks centring at 488nm, 544nm, 582nm and 620nm under excitation at 351nm. These emission peaks were resulted due to $^5D_4 \rightarrow {}^7F_6$, $^5D_4 \rightarrow {}^7F_5$, $^5D_4 \rightarrow {}^7F_4$ and $^5D_4 \rightarrow {}^7F_3$ transitions of Tb^{3+} respectively. The optimum concentration of Tb^{3+} was found to be 3at. %. Same emission peaks profiles were observed for annealed samples except their emission peak intensities. The emission peaks intensities were found to increase with increase of annealing temperature upto 800^oC, then decreased when the annealing temperature reached 1000^oC due to change of phase structure from low-temperature monoclinic phase to high-temperature monoclinic phase. The decay lifetime of the prepared samples were also investigated and found 1.8346 ms as the maximum lifetime. Emissions in near white region of the prepared phosphors were observed from their CIE diagram study.

- The XRD patterns of the prepared $BiPO_4$: Eu^{3+} showed hexagonal phase while change of phase from hexagonal to mixed phase of hexagonal and low-temperature monoclinic phases and later on to pure low-temperature monoclinic phase were noticed upon annealing at 500^oC and 800^oC respectively. Hexagonal shape morphologies of the synthesized nanophosphors were observed from TEM images. Photoluminescence emission spectra showed the characteristic emission peaks resulted from Bi^{3+} and Eu^{3+} ions. $^5D_0$-$^7F_1$ transition of Eu^{3+} ion was found to exhibit maximum emission intensity and the optimum concentration of Eu^{3+} was found to be 8at. %. Further, the photoluminescence emission intensity increased with increase of annealing temperature upto 800^oC due to the change in their phase structure from hexagonal phase to pure low-temperature monoclinic phase. 8at. % Eu^{3+} doped $BiPO_4$ prepared at pH=7 exhibited maximum emission intensity comparing to the samples prepared at acidic as well as in basic mediums. 8at. % Eu^{3+} doped $BiPO_4$ prepared at 0.5mM CTAB concentration exhibited maximum emission intensity and the emission intensity decreased as CTAB concentration of the reaction medium increased due to the

formation of agglomerated particles and larger particle size of the nanoparticles. From CIE diagram study, all the synthesized nanophosphors emitted in Bluish purple colour region and the annealed samples showed different emission colours such as Reddish purple for 500^{o}C, Pink colour for 600^{o}C and 800^{o}C, Orange pink for 700^{o}C annealed samples

- Hexagonal phase of the prepared Sm^{3+} ions doped BiPO4 phosphors were confirmed from XRD study. And change of phase from hexagonal phase to low-temperature monoclinic phase was also observed upon annealing at 800^{o}C. Change of morphology from rod-shaped to nearly spherical shape was noticed upon annealing at 800^{o}C and the sizes were also found to increase upon annealing. The emission peaks were observed at 563nm, 598nm and 645nm which are attributed to $^{4}G_{5/2}$-$^{6}H_{5/2}$, $^{4}G_{5/2}$-$^{6}H_{7/2}$, $^{4}G_{5/2}$-$^{6}H_{9/2}$ transitions of Sm^{3+} respectively. The maximum emission intensity was observed for $^{4}G_{5/2}$-$^{6}H_{7/2}$ transition and the optimum concentration of Sm^{3+} was found to be 5at. %. The emission intensity was found accentuated with increased of heating temperature due to the change of phase from hexagonal to low-temperature monoclinic phase and the abscondence of luminescent quenchers at higher temperatures. From CIE study, switching of emission colour from region to light green region was observed upon annealing.

From the above results, it is suggested that the prepared phosphors may have potential application in the fields of lighting, photocatalyst, sensors, bio-imaging, scintillators, display devices, biological assays, undersea communications etc. In future, the applicability of the prepapred samples in the field of photocatalysis, sensors and supercapacitor will be studied.

References

Achary S. N., Errandonea D., Munoz A., RodrıguezH. P., Manj´on F. J., Krishna P. S. R., Patwe S. J., Grover V., Tyagi A. K., (2013), Experimental and theoretical investigations on the polymorphism and metastability of $BiPO_4$ *Dalton Trans*., **42**:14999.

Arunkumar P., Jayajothi C., Jeyakumar D., Lakshminarasimhan N., (2012), Structure–property relations in hexagonal and monoclinic $BiPO_4:Eu^{3+}$ nanoparticles synthesized by polyol-mediated method, *RSC Adv.*,**2**:1477–1485.

Aspinall H., (2001), Chemistry of the f-Block Elements, Gordon and Breach Science Publishers, Amsterdam

Bahadur A., Dwivedi Y., Rai S. B., (2014), Enhanced luminescence and energy transfer study in Tb: sm co-doped lead fluoro tellurite glass, *Spectrochim. Acta A: Mol. Biomol. Spectrosc*.**118**:177–181.

Balakrishnainah R., Kim D. W., Yi S. S., Kim S. H., Jang K., Lee H. S., Moon B. K. and Jeong J. H., (2010), Enhanced photoluminescence properties of Li/Al doped YPO_4:Eu phosphors, *NSTI-nanotech*, vol. 3. https://briefs.techconnect.org/wp-content/volumes/Nanotech2010v3/pdf/1491.pdf

Banwell C. N., McCash E. M., (1994), Fundamental of molecular spectroscopy, 4th edition, McGraw-Hill, London.

Becerro A. I., Criado J., Gontard L. C., Obregón S., Fernández A., Colón G., and Ocaña M., (2014), Bifunctional, Monodisperse $BiPO_4$-Based Nanostars: Photocatalytic Activity and Luminescent Applications., *Cryst. Growth Des.*,**14:** 3319−3326.

Becquerel J., (1906), Sur les variations des bandesd'absorption d'un crystal dansun champ magnétique. *Compt. Rend. Hebd. Acad. Sci*., **142**: 775–779.

Becquerel J., (1929), Einleitung in eineTheorie der magneto-optischenErscheinungen in Kristallen, *Z Physik*, **58**: 205.

Bernard V., Mario N. B. S., (2011), A brief history of fluorescence and phosphorescence before the emergence of quantum theory, *J. Chem. Educ.*, **88:**731-738.

Berradi M., Hsissou R., Khudhair M., et al. (2019), Textile finishing dyes and their impact on aquatic environs. *Heliyon* **5:** Article e02711. https://doi.org/10.1016/j.heliyon.2019.e02711.

Bethe H., (1930), ZurTheorie des Zeeman effektesan den Salzen der seltenenErden Z. *Physik*, **60**: 218-233.

Bidikoudi M., Fresta E., Costa R. D., (2018), White perovskite based lighting devices. *ChemCommun***54**:8150–8169.

Binnemans K., Jones P. T., Blanpain B., Gerven T. V., Yang Y., Walton A., Buchert M., (2013), Recycling of rare earths: a critical review, *J. Clean. Prod.*,**51**:1-22

Blasse G. and Grabmaier B.C., (1994), Luminescent materials., Springer-Verlag, Berlin

Bob B. H., (1954), Two dimensional X-ray diffraction, John Wiley & Sons, Inc.

Boutinaud P., Cavalli E., Bettinelli M., (2007), Emission quenching induced by intervalence charge transfer charge transfer in Pr^{3+} and Tb^{3+} doped $YNbO_4$ and $CaNb_2O_6$, *J. Phys.:Condens. Matter*, **19**:386230.

Bünzl J.C. G., (2010), Lanthanide luminescence for biomedical analyses and imaging.,*Chem. Rev.*, **110**:2729-2755.

Bünzli J. C. G., Tang A. M., (1995), Solvation and anion interaction in organic solvents. In Handbook on the Physics and Chemistry of Rare Earths, Karl A. Gschneidner; Eyring, L., Eds. Elsevier, Amsterdam, 305-366.

Bünzli J.C. G., (2006), Benefiting from the unique properties of lanthanide ions.,*Acc. Chem. Res.*, **39**:53-61.

Carnall W. T., Goodman G. L., Rajnak K., Rana R. S., (1989), A systematic analysis of the spectra of lanthanides doped into single crystal LaF_3.*J Chem. Phys*., **90**:3443-3457.

Chang W., Xuan Q., Shan L., (2018), Enhanced Photocatalytic Activity of $BiPO_4$ Photocatalyst by Surface Modification of Fe(III) Cocatalyst. *J. Wuhan Univ. Technol.-Mat.Sci.* **33**: 871–875.

Chanu T. T., Singh N. R., (2017), Multicolor luminescence of $PbWO_4$:RE^{3+}(Sm^{3+},Dy^{3+},$Eu^{3+}$and Tb^{3+}) phosphor prepared via hydrothermal method *J Mater Sci: Mater Electron***28**:3909–3916.

Chanu T. T., Singh N. R., (2020), Influence of Sm3þ concentration on structural and spectroscopic properties of orange-red emitting $PbWO_4$ phosphor: An energy transfer study *J. Solid State Chem.*, **284**:121190.

Charyulu M., Chetty K. V., Phal D., Sagar V., Naronha D. M.,Pawar S. M., Swarup R., Ramakrishna V. V., Venugopal V., (2002), Recovery of americium from nitric acid solutions containing calcium by different co-precipitation methods, *J. Radioanal. Nucl. Chem.***251**:153.

Chen D. Q., Zhou Y., Zhong J. S., (2016), A review on Mn^{4+} activators in solids for warm white light-emitting diodes. *RSC Adv.* **6**:86285–86296.

Chen M., Xia Z., Liu Q., (2015),Luminescence properties and energy transfer of Ce^{3+}/Tb^{3+} co-doped $Ca_6Ba(PO_4)_4O$ phosphor for near-UV pumped light-emitting diodes *J. Mater. Chem. C*.**3**:4197.

Chen X., Lv F. Z., Ma Y., Zhang Y. H., (2016), Preparation and spectroscopic investigation of novel $NaAlP_2O_7:Eu^{2+}$ phosphors for white LEDs. *J Alloys Compd.,* **680**:20.

Chiang H. Q., Wager J. F., Hoffman R. L., Jeong J. and Keszler D. A., (2005), High mobility transparent thin-film transistors with amorphous zinc tin oxide channel layer, *Appl. Phys. Lett.,***86**: 13503-13505.

Clavier N., Podor R., and Dacheux N., (2011), Crystal chemistry of the monazite structure.,*J. Eur. Ceram. Soc.,***31:** 941–976.

Colthup N. B., Daly L. H., Wiberly S, E,, (1964), Introduction to infrared and Raman Spectroscopy, Academic Press, New York; London.

Cotton S., (1991), Lanthanides and Actinides, Macmillan Education: Basingstoke.

Cotton S., (2006), Lanthanides and Actinides, Wiley, England.

Cullity B. D., (1956), Elements of X-ray diffraction, Addison-Wesley Pub. Co., Massachusetts, U.S.A.

Curtis N., (2010), Rare earths, we can touch them everyday. In: Lynas Presentation at the JP Morgan Australia Corporate Access Days, New York, 27.

Cybinska J., Lorbeer C., Mudring A. V., (2016), Ionic liquid assisted microwave synthesis route towards color-tunable luminescence of lanthanide-doped $BiPO_4$, *J. Lumin.,***170**:641-647.

Dabre K. V., Dhoble S. J., Lochab J., (2014), Synthesis and luminescence properties of Ce^{3+} doped MWO_4 (M=Ca, Sr and Ba) microcrystalline phosphors**.***J. Lumin.,***149**:348–352.

Depan D., Misra R. D. K., (2014), Structural and physico-chemical aspects of silica encapsulated ZnO quantum dots with high quantum yield and their natural uptake in hela cells. *J Biomed Mater Res A.*,**102**:2934–2941.

Devi C. V., Phaomei G., Yaiphaba N., Singh N. R., (2014), Luminescence behavior of YVO4:Dy^{3+} phosphors with enhanced photoluminescence on co-doping Bi^{3+} ions *J. Alloys Compd.*,**583**:259.

Di W., Chen J., Wang X., and Chen B., (2004), Investigation of phase structure transformation and VUV excitation of YPO_4:Tb synthesized by solution precipitation route *Chem. Letters,* **33**:1448-1449.

Digonet M. J. F., (1993), Rare earth doped fiber laser and amplifiers, Dekker: New York.

Du P., Wu S., Yu J. S., (2016), Synthesis, electronic structure and luminescence properties of color-controllable Dy^{3+}/Eu^{3+}-codoped $CaWO_4$ phosphors. *J. Lumin.*,**173**:192.

Egerton R.F., (2016), The Scanning Electron Microscope. In: Physical Principles of Electron Microscopy. Springer, Cham.https://doi.org/10.1007/978-3-319-39877-8_5

Eliseevaab S. V., Bunzli J. C. G., (2011), Rare earths: jewels for functional materials of the future. *New J. Chem*., **35**:1165–1176.

Faulkner S. and Matthews J. L., (2004), Fluorescent complexes for biomedical applications, *Comprehense Coordination Chemistry II*, **9**:913-944.

Faulkner S., Pope S. J. A., Burton-Pye, Benjamin P., (2005), Lanthanide Complexes for Luminescence Imaging Applications,*Appl. Spectrosc. Rev.*,**40**:1-31.

Francis P., (1929),*Ann. Phys.*,**12**:169-275, Paris, France.

Frey S. T., Horrocks W. D. J., (1995), On correlating the frequency of the $^7F_0$ - $^5D_0$ transition in Eu^{3+} complexes with the sum of 'nephelauxetic parameters' for all of the coordinating atoms. *Small,* **229**:383-390.

Fu C., Li G., Zhao M., Yang L., Zheng J., and Li L., (2012), Solvent-Driven Room-Temperature Synthesis of Nanoparticles $BiPO_4$:Eu^{3+}, *Inorg. Chem.,* **51:** 5869−5880.

Ganguli S., Hazra C., Chatti M., Samanta T., Mahalingam V., (2015), A Highly Efficient UV–Vis–NIR Active Ln^{3+}-Doped $BiPO_4/BiVO_4$ Nanocomposite for Photocatalysis Application.*Langmuir*,**32**:247-253.

Gao M., Zhang D., Pu X., Ma H., Su C., Gao X., Dou J., (2016), Surface decoration of BiOBr with $BiPO_4$ nanoparticles to build heterostructurephotocatalysts with enhanced visible-light photocatalytic activity. *Sep. Purif. Technol*.,**170**:183-189.

Gao M., Zhang D., Pu X., Shao X., Li H., Lv D., (2016), Combustion Synthesis and Enhancement of BiOCl by Doping Eu^{3+} forPhotodegradation of Organic Dye. *J. Am. Ceram. Soc.*,**99 (3)**:881–887.

Gao Y., Cheng Y., Huang F., Lin H., Xu J., Wang Y. S., (2018) Sn^{2+}/Mn^{2+}codoped strontium phosphate ($Sr_2P_2O_7$) phosphor for high temperature optical thermometry, *J. Alloys Compd.*, **735**:1546-1552.

Gayatri S. K., Singh N. R., (2013), Re-dispersible $CaWO_4:Tb^{3+}$ nanoparticles: Synthesis, characterization, and photoluminescence studies.*J. Lumin.*,**139**:98.

Geng J., Yu C. S., Wu H., Wu B. J., Tian L. H., (2013), Photoluminescence characteristics of red-emitting Eu^{3+}-activated $Ca_4GdNbMo_4O_{20}$ phosphor. *J. Lumin.*,**140**:71–73.

Goldstein J., (2003), Scanning electron microscopy and X-ray micro analysis, 3rd edition, Kluwer academy/ Plenum publishers, New York.

Gschneidner K. A. Jr., Eyring L., (1996), Handbook on the Physics and Chemistry of Rare Earths, Elsevier Science, Amsterdam Lausanne, vol. 23, New York.

Guan M., Sun J., Tao F., and Xu Z. (2008), A Host Crystal for the Rare-Earth Ion Dopants: Synthesis of Pure and Ln-Doped Urchinlike $BiPO_4$ Structure and Its Photoluminescence, *Cryst. Growth Des.*,**8:** 2694-2697.

Guisbiers G., Rosales S. M., Deepak F. L., (2012), Nanomaterial Properties: Size and Shape Dependencies. *Journal of Nanomaterials* **2012**: Article ID 180976, 2 pages, https://doi.org/10.1155/2012/180976.

Han X., Zhang G., Qi X., Wang X., Li M., Sun X., WeiC., (2014), Synthesis and luminescence properties of $BiPO_4$:Ce,Tb nanorods, *J. Lumin.*, **152**:37–39.

He X., Liu X., Li R., et al. (2016), Effects of local structure of Ce^{3+} ions on luminescent properties of $Y_3Al_5O_{12}$:Ce nanoparticles.*Sci Rep.*,**6**:22238-22248.

Henderson B., Imbusch G. F., (1989), Optical Spectroscopy of Inorganic Solids, Oxford University Press, Oxford, New York 645.

Hong N. H., (2019), Introduction to Nanomaterials: basic properties, synthesis, and characterization. *Nano-Sized Multifunctional Materials*. (pp. 1–19). https://doi.org/10.1016/B978-0-12-813934-9.00001-3.

Hou C., Hu B., Zhu J., (2018), Photocatalytic Degradation of Methylene Blue over TiO_2 Pretreated with Varying Concentrations of NaOH.*Catalysts*,**8**: 575-587.

Hou J., Pan C., Chen X., Zhao G., Liu Y., Li Y., Fang Y., (2019), White-light-emitting from single-phased $(Ca,Eu,Mn)_9Al(PO_4)_7$ phosphor with blue-white-yellow tunable luminescence properties for UV-based LEDs, *Mater. Technol.*,**34**:135.

Hou Z., Li G., Lian H., Lin J., (2012), One-dimensional luminescent materials derived from the electrospinning process: preparation, characteristics and application *J. Mater. Chem*., **22**:5254.

Huang M., Xu Z., Hou C., Jia H. L., Sun J., Guan M., (2019), Facile synthesis of colloidal photoluminescent $BiPO_4$:Ln (Eu,Tb) nanoparticles well-dispersed in polar solvents *CrystEngComm,* **21**:278-282.

Huang X. H., Tay C. B., Zhan Z. Y., et al. (2011), Universal photoluminescence evolution of solution-grown ZnO nanorods with annealing: important role of hydrogen donor.*CrystEngComm.*,**13**: 7032–7036.

Huang Y. and Lieber C. M., (2004), Integratednanoscale electronics and optoelectronics: Exploring nanoscale science and technology through semiconductor nanowires, *Pure Appl. Chem.,* **76:**2051-2068.

Huang Y., Wang X., Lee H., Cho E., Jang K., Tao Y., (2007), Synthesis, vacuum ultraviolet and ultraviolet spectroscopy of Ce^{3+} ion doped olgite Na(Sr, Ba)PO_4*Phys. D: Appl. Phys.*,**40**:7821.

Hussain N. S., Hungerford G., El-Mallawany R., Gomes M. J. M., Lopes M. A., Ali N., Santos J. D., Buddhudu S., (2009), Absorption and Emission analysis of RE^{3+}(Sm^{3+} and Dy^{3+}): lithium borotellurite glasses, *J. Nanosci. Nanotechnol.*,**9**:3672–3677.

İlhan M., (2017), Synthesis, structural characterization, and photoluminescence properties of TTB-type PbTa2O6:Eu^{3+} phosphor. *Int J Appl Ceram Technol.*,**00**:1-7.

İlhan M., Keskin İ. Ç., Çatalgöl Z., Samur R., (2018), NIR photoluminescence and radioluminescence characteristics of Nd^{3+} doped $BaTa_2O_6$ phosphor. *Int J Appl Ceram Technol.*,**15**:1594–1601.

Iskra A., Gentleman A. S., Kartouzian A., Kent M. J., Sharp A. P., Mackenzie S. R., (2017), Infrared Spectroscopy of Gas-Phase $M^+(CO_2)_n$ (M = Co, Rh, Ir) Ion-Molecule Complexes *J. Phys. Chem., A.***121**:133.

Jalali K., Pajootan E., Bahrami H., (2019), Elimination of hazardous methylene blue from contaminated solutions by electrochemically magnetized graphene oxide as a recyclable adsorbent.*Adv Powder Technol.*,**30**:2352–2362.

Jayaprakash N., Suresh R., Rajalakshmi S., Raja S., Sundaravadivel E., Gayathri M., SridharanM., (2020), One-step synthesis, characterisation, photocatalytic and bio-medical applications of ZnOnanoplates, *Mater Technol.*,**35**:112-124

Jia Z., Misra R. D. K., (2013), Tunable ZnO quantum dots for bioimaging: synthesis and photoluminiscence. *Mater Technol.*,**28**:221–227.

Jiang X. C., Yan C. H., Sun L. D., Wei Z. G., Liao C. S. *J.*, (2003),Hydrothermal homogeneous urea precipitation of hexagonal YBO_3:Eu^{3+} nanocrystals with improved luminescent properties*Solid State Chem.*,**175**:245.

Jiang X., Pan Y., Huang S., Chen X., Wang J., Liu G., (2014), Hydrothermal synthesis and photoluminescence properties of red phosphor BaSiF6: Mn^{4+} for LED applications. *J.Mater. Chem. C*,**2:**2301–2306.

Jianming Z., Weiren Z., Licai L., Jianqing W., (2014), Hydrothermal synthesis and luminescence properties of Eu^{3+} and Sm^{3+}codoped $BiPO_4$, *J. Rare Earths*, **32(1)**:5-11.

Joshi P. N., Mathias A., Mishra A., (2018), Synthesis of ecofriendly fluorescent carbon dots and their biomedical and environmental applications, *Mater Technol.*,**33:10**:672-680.

Kamat P. (1993), Photochemistry on nonreactive and reactive (semiconductor) surfaces.*Chem. Rev.*,**93:** 267–300.

Katelnikovas A., Jüstel T., Uhlich D., Jorgensen J. E., Sakirzanovas S., Kareiva A., (2008), Characterization of Cerium-Doped Yttrium Aluminium Garnet Nanopowders Synthesized via Sol-Gel Process.*Chem Eng Comm.*,**195**:758–769.

Kaur G., Kumar B., Verma R. K., Rai S. B., (2014), Bismuth induced enhanced green emission from terbium ions and their complex in thin films. *Dalton Trans.*,**43**:11014.

Khan I., Saeed K., Khan I., (2017), Nanoparticles: Properties, applications and toxicities. *Arabian.JChem.*, **12**:908.

Kido J., Okamoto Y., (2002), Organo lanthanide metal complexes for electroluminescent materials, *Chem. Rev.*, **102**: 2357-2368.

King S., (2008), Synthesis and Characterisation of Lanthanide Complexes as Possible Single-Molecule Magnets, School of Chemistry and NowNano Doctoral Training Centre University of Manchester, England.

Klong H. P., Alexander L.F., (1954), X-ray Diffraction procedure for crystalline and amorphous materials, Wiley, New York.

Kołodyńska D., Hubicki Z., (2012), Investigation of Sorption and Separation of Lanthanides on the Ion Exchangers of Various Types. *Ion Exch. Technol.*,**8**:193–240.

Kramers H. A., (1930), La rotation paramagnétique du plan de polarisationdans les cristauxuniaxes de terresrares, *Proc. Acad. Sci.*,**32**:1176-1189.

Lai H., Bao A., Yang Y., et al. (2008), UV Luminescence Property of YPO_4:RE (RE = Ce^{3+}, Tb^{3+}).*J. Phys. Chem. C.*,**112**:282-286.

Lakowicz J. R., (1983), Principles of Fluorescence Spectroscopy, Plenum Press, New York.

Lakshminarayana G., Dao T. D., Chen K., Sharma M., Takeda T., Brik M. G., Kityk I. V., Singh S., Nagao T., (2015), Effect of different surfactants on structural and optical properties of Ce^{3+} and Tb^{3+} co-doped $BiPO_4$ nanostructures. *Opt. Mater.*,**39**:110.

Law M., Greene L. E., Johnson J. C., Saykally R., and Yang P.**,**(2005),Nanowire dye-sensitized solar cells, *Nat. Mater.*, **4:**455-459.

Lee E., Terblans J. J., Swart H. C., (2018), The effect of pH on the luminescence properties of Y_2O_3:Bi phosphor powders synthesised using co-precipitation. *Vacuum*, **157**:237.

Lellis B., Polonio C. Z. F., Pamphile J. A., Polonio J. C., (2019), Effects of textile dyes on health and the environment and bioremediation potential of living organisms. *Biotechnol. Res. Innov.,***3(2)**: 275-290.

Li G. S., Li L. P., Boerio-Goates J., Woodfield B. F., (2005), High purity anatase TiO(2) nanocrystals: near room-temperature synthesis, grain growth kinetics, and surface hydration chemistry.*J. Am. Chem. Soc.,***127**: 8659–8666.

Li L., Pan Y., Chen Z., Huang S., Wu M., (2017), Tunable luminescence and energy transfer properties of Bi^{3+} and Mn^{4+} co-doped $Ca_{14}Al_{10}Zn_6O_{35}$ phosphors for agricultural applications. *RSC Adv.,***7**:14868.

LiL., SuY., LiG., (2010), Chemical modifications of red phosphor $LaPO_4$:Eu^{3+}nanorods to generate white light. *J. Mater. Chem.,***20**:459-465.

Li P., Guoa L., Lianga C., Lia T., Chen P., (2018), Enhanced dual-wavelength sensitive upconversion luminescence of $BiPO_4$:Yb^{3+}/Er^{3+} phosphors by Sc^{3+} doping, *Mater SciEng B*, **229**:20–26.

Li P., Yuan T., Li F., Zhang Y., (2019), Phosphate Ion-Driven $BiPO_4$:Eu Phase Transition, *J. Phys. Chem. C.,* **123(7)**:4424–4432.

Lin C., Xiao Z., Guo G., Chan T., Liu R., (2010) Versatile Phosphate Phosphors $ABPO_4$ in White Light-Emitting Diodes: Collocated Characteristic Analysis and Theoretical Calculations. *J. Am. Chem. Soc.,***132**:3020−3028.

Liu S., Zhang W., Hu Z., Feng Z., Sheng X., Liang Y, (2013), Synthesis and luminescent properties of Eu^{3+} and Dy^{3+} doped $BiPO_4$ phosphors for near UV-based white LEDs, *J Mater Sci: Mater Electro*, **24:** 4253-4257.

Liu Y., Luo W., Li R., Chen X., (2010), Optical properties of Nd3+ ion doped ZnO nanocrystals, *J. Nanosci. Nanotechnol.,***10**:1871–1876.

Liu Y., Sun M., Liu Y., Chen G., Zhang X., (2015), Effects of aging time on phase, morphology, and luminescence by two-photon processes of $BiPO_4$:Er^{3+}, Yb^{3+} in the solvothermal synthesis, *Opt mater*., **45**:32-36.

Luo X. B., Hu R., Liu S., Wang K., (2016), Heat and fluid flow in high-power LED packaging and applications. *Prog Energy Combust Sci*, **56**:1–32.

Lu M., Yuan G., Wang Z., Wang Y., Guo J., (2015), Synthesis of $BiPO_4$/Bi_2S_3 Heterojunction with Enhanced Photocatalytic Activity under Visible-Light Irradiation.*Nanoscale Res Lett.,***10(1)**: 385-391.

Luwang M. N., Ningthoujam R. S., Jagannath, Srivastava S. K., Vatsa R. K., (2010), Effects of Ce^{3+}Codoping and Annealing on Phase Transformation and Luminescence of Eu^{3+} Doped YPO_4 Nanorods: D_2O Solvent Effect *J. Am. Chem. Soc.*, **132**:2759–2768.

Ma S., Liu Y., Shi X., Zhao M., Liu D., Wang K., Zuo H., and Li J., (2017), CTAB-assisted hydrothermal synthesis and luminescence properties of $BiPO_4$:Eu^{3+} phosphors., *J Mater Sci: Mater Electron.*,**28:**15154–15160.

Malba C. M., (2013), Synthesis and characterization of lanthanide based luminescent materials, Ca' Foscari University of Venice, Italy, p. 185.

Mass H., Currao A., Calzaferri, G., **(**2002), Encapsulated Lanthanides as Luminescent Materials *Angew. Chem., Int. Ed.*,**41**:2495.

Matsumoto K. and Yuan J. G., (2003), Lanthanide Chelates as Fluorescent Labels for Diagnostics and Biotechnology, *Metal Ions in Biological Systems*,**40**:191-232.

Mills A., Hazafy D., Parkinson J., Tuttle T., Hutchings M. G., (2011), Effect of alkali on methylene blue (C.I. Basic Blue 9) and other thiazine dyes.*Dyes Pigm.*,**88**:149–155.

Morozov V. A., Bertha A., Meert K. W., Rompaey S. V., Batuk D., Martinez G. T., Aert S. V., Smet P. F., Raskina M.V., Poelman D., Abakumo A. M., Hadermann J., (2013), Incommensurately modulated structures and luminescence properties of the $Ag_xSm_{(2-x)/2}WO_4$ (x=0.286, 0.2) scheelites as thermographic phosphors *Chem. Mater.*,**25**:4387.

Murthy K.V.R., Virk H.S., (2014), Luminescence Phenomena: An Introduction, *Defect and Diffusion Forum*,**347**:1-34.

Naciri Y., Chennah A., Jaramillo-Páez C., Navio J. A., Bakiz B., Taoufyq A., Ezahri M., Villian S., Guinneton F., Benlhachemi A., (2019), Preparation, characterization and photocatalytic degradation of Rhodamine B dye over a novel $Zn_3(PO_4)_2$/$BiPO_4$ catalyst. *J. Environ. Chem. Eng.*,**7**:103075-103084.

Naidu B. S., Vishwanadh B., Sudarsan V. and Vatsa R. K., (2012), $BiPO_4$: A better host for doping lanthanide ions.,*Dalton Trans.*,**41**: 3194-3203.

Naorem R. S., Singh N. P., Singh N. M., (2020) Photoluminescence studies of Ce^{3+} ion-doped $BiPO_4$ phosphor and its photocatalytic activity. *Int J Appl Ceram Technol.*,**17**:2744.

Naorem R. S., Singh N. P., Singh N. M., (2020), Photoluminescence properties of Tb^{3+} doped $BiPO_4$ nanophosphor synthesised by co-precipitation method using ethylene glycol, *Mater Technol*,https://doi.org/10.1080/10667857.2020.1866919.

Nazarov M. V., Jeon D. Y., Kang J. H., Popovici E. J., Muresan L. E., Zamoryanskaya M. V., Tsukerblat B. S., (2004), Luminescence properties of europium-terbium double activated calcium tungstate phosphor, *Solid State Commun.*,**131**:307-311.

Neeraj S., Kijima N., Cheetham A. K., (2004), Novel red phosphor for solid state lighting: the system $NaM(WO_4)_{2-x}(MoO_4)_x$: Eu^{3+} (M = Gd, Y, Bi), *Chem. Phys. Lett.*, **387**:2-6.

Ni Y., Hughes J. M. and Mariano A. N., (1995), Crystal chemistry of the monazite and xenotime structures., *Am. Mineral.*,**80:** 21–26.

Ningthoujam R. S., Rai S. B., Dwivedi Y., (2012), Enhancement of Luminescence by Rare Earth Ions Doping in Semiconductor Host, Nova Science Publishers, Inc. Hauppauge, USA.

Okram R., Phaomei G., Singh N. R., (2013), Water driven enhanced photoluminescence of Ln (=Dy^{3+}, Sm^{3+}) doped $LaVO_4$ nanoparticles and effect of Ba2+ co-doping *Mat. Sci. Eng., B***178**:409-416.

Pan C., Xu J., Chen Y., Zhu Y., (2012), Influence of OH-related defects on the performances of $BiPO_4$ photocatalyst for the degradation of rhodamine B. *Appl. Catal. B.*,**115-116**:314-319.

Pan C., Zhu Y., (2010), New Type of $BiPO_4$ Oxy-Acid Salt Photocatalyst with High Photocatalytic Activity on Degradation of Dye. Environ. *Sci. Technol.*,**44**: *5570-*5574.

Pan L., Koehler K., Jacobsohn L. G., (2020), Luminescence of undoped and Ce-doped hexagonal $BiPO_4$. *J. Lumin.*,**228**:117626.

Park K., Heo M. H., Kim K. Y., Dhoble S. J., Kim Y., Kim, J. Y., (2013**),**Photoluminescence properties of nano-sized $(Y_{0.5}Gd_{0.5})PO_4$:Eu^{3+} phosphor powders synthesized by solution combustion method.*Powder Technol.,* **237**:102–106.

Patterson A. L., (1939), The Scheeres formula for X-ray particle size determination, *Phys. Rev.*,**56**:978-982.

Pawlig O., Schellenschlager V., Lutz H. D., Trettin R., (2001), Vibrational analysis of iron and zinc phosphate conversion coating constituents. *SpectrochimActa A.*,**57**:581.

Pust, P., Weiler V., Hecht C., Tucks A., Wochnik A. S., Henb A. K., Wiechert D., Scheu C., Schmidt P. J., Schnick W., (2014), Narrow-band red-emitting $Sr[LiAl_3N_4]:Eu^{2+}$ as a next-generation LED-phosphor material. *Nat Mater.*,**13**:891–896.

Regmi C., Maya-Flores E., Lee S. W., Rodriguez-Gonzalez V., (2018), Cerium-doped *β*-$Ni(OH)_2$ hexagon nanosheets: an effective photocatalyst for the degradation of the emerging water pollutant, naproxen. *Nanotechnology*,**29**: 375603.

Reli M., Ambrozova N., Sihor M., et al. (2014), Novel cerium doped titania catalysts for photocatalytic decomposition of ammonia.*Appl. Catal. B.*,**178**:108-116.

Rendell D., (1987), Fluorescence and Phosphorescence.Crown.

Reyes R. Cremona, M.; Teotonio, E. E. S.; Brito, H. F, Malta, O. L. 2004, Voltage color tunable OLED with (Sm,Eu)-β-diketonate complex blend, *Chem. Phys. Lett.*,**396**:54-58.

Riwotzki K., Meyssamy H., Kornowski A., Haase M., (2000), Liquid-Phase synthesis of doped nanoparticles: Colloids of luminescing LaPO4:Eu and $CePO_4$:Tb particles with a narrow particle size distribution, *J. Phys. Chem. B,***104**:2824-2828.

Rizkalla E.N., Choppin G.R., (1994), Handbook on the Physics and Chemistry of Rare Earths, **18**:529-558.

Romero B., Bruque S., Aranda M. A. G., and Iglesias J. E., (1994), Syntheses, Crystal Structures, and Characterization of Bismuth Phosphates.,*Inorg. Chem.*, **33 (9)**:1869–1874.

Roming M., Feldmann C., (2009), Synthesis and characterization of nanoscaled $BiPO_4$ and $BiPO_4$:Tb, *J Mater Sci*,**44**:1412–1415.

Ronda C., (2009), Luminescence loss mechanisms, *J. Lumin.*,**129**:1824-1826.

Ryadun A., Rakhmanova M., Grigorieva V., (2020), Effect of Cu doping on properties of $PbMoO_4$ single crystals as materials for luminescence thermometry, *Mater Technol*, DOI: 10.1080/10667857.2020.1797325

Sahu M. K., Mula J., (2019), White light emitting thermally stable bismuth phosphate phosphor $Ca_3Bi(PO_4)_3:Dy^{3+}$ for solid-state lighting applications, *J. Am. Ceram. Soc.*, **102**:6087–6099.

Sahu N. K., Ningthoujam R. S. and Bahadur D. (2012), Disappearance and recovery of luminescence in $GdPO_4:Eu^{3+}$nanorods: propose to water/OH- release under near infrared and gamma irradiations.*J. Appl. Phys*., **112**: 014306-12.

Scarangella A., Reitano R., Priolo F., Miritello M., (2019), Bismuth doping of silicon compatible thin films for telecommunications and visible light emitting devices. *Mater. Sci. Semicond. Process.*,**92**:47.

Scherrer P., (1918), Bestimmung der Gross und der Inneren Struktur von Kolloidteilchen Mittels Rontegenstralhen, Nachrichten von der Gesellschaft der Wissenschaften, Göttingen," *Mathematisch-Physikalische Klasse*, **2**: 98-100.

Selvin P. R., (2002), Principles and biophysical applications of lanthanide-based probes. *Annu Rev BiophysBiomolStruct*., **31**:275. doi:10.1146/annurev.biophys.31.101101.140927

Seo H. J., (2014), Line broadening and crystallographic sites for Eu^{3+} in disordered double borate $Ca_3Gd_2(BO_3)_4$. *J. Alloys Compd.*,**604**:100–105.

Shahbazi M. A., Faghfouri L., Ferreira M. P., Figueiredo P., Maleki H., Sefat F., Hirvonen J., Santos H. A., (2020**)**, The versatile biomedical applications of bismuth-based nanoparticles and composites: Therapeutic, diagnostic, biosensing, and regenerative properties. *Chem. Soc. Rev.,* **49**:1253–1321.

Shannon R. D., (1976), Revised Effective Ionic Radii and Systematic Studies of Interatomie Distances in Halides and Chaleogenides.*Acta.Cryst.*,**32**:751-767.

Sharma K. G., Singh N. R., (2013), Synthesis and luminescence properties of $CaMO_4:Dy^{3+}$ (M = W, Mo) nanoparticles prepared *via* an ethylene glycol route.*New J. Chem*.,**37**:2784.

Sharma K. G., Singh T. P., Singh N. R., (2014), Low temperature synthesis, characterization and tunable optical properties of Eu^{3+}, Tb^{3+} doped $CaMoO_4$ nanoparticles. *J. Alloys Comp.,* **602**:275.

Shi X., Liu Y., Zhang J., Zhang K., Li J., Zuo H., Li P. (2015), Enhanced luminescence properties of $BiPO_4:Eu^{3+}$ phosphors prepared by hydrothermal method. *Ceram. Int,* **41(5)**: 6683–6686.

Shi X., Liu Y., Zhang J., Zhang K., Li P., Zuo H., and Li J., (2014), Effects of pH and Sm^{3+} doping on the structure, morphology and luminescence properties of $BiPO_4$: Sm^{3+} phosphors prepared by hydrothermal method.,*Ceram. Int.*,**41(2):** 3162–3168.

Shionoya S., Yen W. M., (1999), Phosphor Handbook, CRC Press Inc., Boca Raton, FL, 33431, USA.

Singh N. P., (2018), Synthesis, characterization and photoluminescence studies of lanthanide doped $MM'O_4$ (M=Zn, Cd; M'=W, Mo) phosphors. Department of Chemistry, Mizoram University, India.

Singh N. P., Devi Y. R., Singh N. R., Singh N. M., (2019), Synthesis of Tb^{3+}ion doped $ZnWO_4$ phosphors and investigation of their photoluminescence properties: concentration effect. *Bull. Mater. Sci*.,**42**:96.

Singh N. P., Singh N. R., Devi Y. R., Sh B. S., Singh T. D., Singh N. R., Singh N. M., (2020), Effects of annealing temperature on structural and luminescence properties of $CdMoO_4:Dy^{3+}$ phosphor synthesized at room temperature by co-precipitation method. *Solid State Sci*.,**102**:106172. https://doi.org/10.1016/j.solidstatesciences.2020.106172

Singh N. P., Singh N. R., Singh N. M., (2018), Synthesis of $CdMoO_4:Sm^{3+}$ phosphors at room temperature and investigation on photoluminescence properties. *Optik*.,**156**:365.

Singh N. P., Singh N. R., Singh N. R., Singh N. M., (2018), Effect of doping ion concentration on the photoluminescence behavior of $CdWO_4:Tb^{3+}$ phosphor synthesized via co-precipitation method. *Indian J Phys*.,**92**:1461.

Singh N. S., (2011), Synthesis and photoluminescence studies of $MVO_4:Ln^{3+}$(M=Gd, Y &Ln^{3+}= lanthanide ions) and CdX(X=S, Se) nanocrystals and thin films, Department of Physics Manipur University, India.

Singh N. S., Ningthoujam R. S., Singh S. D., Viswanadh B., Manoj N., Vatsa R., (2010), Preparation of highly crystalline blue emitting $MVO_4:Tm^{3+}$ (M = Gd, Y) spherical nanoparticles: Effects of activator concentration and annealing temperature on luminescence, life time and quantum yield, *J. Lumin.,* **130**:2452-2459.

Singh S., Lakshminarayana G., Sharma M., Dao T. D., Chen K., Wada Y., Takeda T., Nagao T., (2015),Excitation Induced Tunable Emission in Ce^{3+}/Eu^{3+} Codoped $BiPO_4$ Nanophosphors *J Spectrosc*,2015:Article ID 493607 https://doi.org/10.1155/2015/493607

Stouwdam J. W., Hebbink G. A., Huskens J., Veggel F. C. J. M. V., (2003), Lanthanide doped nanoparticles with excellent luminescent properties in organic media, *Chem. Mater.,* **15**:4604-4616.

Sun B. and Sirringhaus H, (2005), Solution-processed zinc oxide field - effect transistor based on self – assembly of colloidal,nanorods, *Nano Lett.*,**5**: 2408-2413.

Talapin D. V. and Murray C. V., (2005), PbSnanocrystal solids for n- and p- channel thin – effect transistors, *Science,* **310**: 86-89.

Talewar R. A., Mahamuda S. K., Rao A. S., Joshi C. P., Moharil S. V., (2018), Sensitization of Nd^{3+} by 4f-5d transition of Ce^{3+} in $Ba_2Y(BO_3)_2Cl$ phosphor for the prospective NIR applications. *J. Lumin.*,**202**: 1-6.

Tanaka M., Oki T., Koyama K., Narita H., Oishi T., (2013), Recycling of Rare Earths from Scrap, *Handbook on the Physics and Chemistry of Rare Earths,***43:**159-211.

Tang C., Bando Y., Golberg D., and Ma R., (2005), Cerium Phosphate Nanotubes: Synthesis, Valence State, and Optical Properties.,*Angew. Chem. Int. Ed.*,**44:** 576 –579.

Vadivel S., Maruthamani D., Kumaravel M., Saravanakumar B., Paul B., Dhar S. S., Saravanakumar K., Muthuraj V., (2016) Supercapacitors studies on $BiPO_4$ nanoparticles synthesized through a simple microwave approach, *J. Taibah Univ. Sci.*, **11**:661-666.

Valeur B., Mario N., Santos B., (2011), A brief history of fluorescence and phosphorescence before the emergence of quantum theory, *J. Chem. Educ.*, **88**:731-738.

Venkatasubramanian R., Srivastava R. S., Misra R. D. K., (2013), Comparative study of antimicrobial and photocatalytic activity in titania encapsulated composite nanoparticles with different dopants. *Mater Sci Technol.*,**24(5)**:589–595.

Verma B. R., Baghel R. N., (2017), A Review on Luminescence properties in Eu Doped Phosphate Phosphors *IJoMS.*, **12(3)**: 483-489.

Vleck J. H. V., (1937), The Puzzle of Rare-earth Spectra in Solids. *J. Chem. Phys*., **41**:67-80.

Vranjeˇs M., Kuljanin-Jakovljevi J., Ahrenkiel S. P., Zekovi´ I., Mitri´ M., ˇSaponji´ Z., Nedeljkovi´ J.M., (2013), Sm^{3+} doped TiO_2 nanoparticles synthesized from nanotubular precursors luminescent and structural properties, *J. Lumin.*,**143**:453–458.

Wang B., Lin H., Huang F., Xu J., Chen H., Lin Z., Wang Y., (2016),Non-Rare-Earth $BaMgAl_{10-2x}O_{17}$: xMn^{4+}, xMg^{2+}: A Narrow-Band Red Phosphor for Use as a High-Power Warm w-LED. *Chem. Mater.*,**28**:3515–3524.

Wang B., Liu Y., Huang Z., Fang M., (2018), Photoluminescence properties of a Ce^{3+} doped $Sr_3MgSi_2O_8$ phosphor with good thermal stability.*RSC Adv.*,**8**:15587-15594.

Wang X. J., Gao M.Y., (2006), A facile route for preparing rhabdophane rare earth phosphate nanorods, *J. Mater. Chem.*,**16**:1360-1365.

Wang R., Hashimoto K., Fujishima A., et al. (1997), Watanabe, T. Light-induced amphiphilic surfaces. *Nature*,**388:**431–432.

Wang Y., Huang H., Quan C., Tian N., Zhang Y., (2015), Hydrothermal fabrication of multi-functional Eu^{3+} and Tb^{3+} co-doped $BiPO_4$: Photocatalytic activity and tunable luminescence properties, *J. Cryst. Growth*,**433**:1-6.

Wang Y., Zhu G., Xin S., Wang Q., Li Y., Wu Q., Wang C., Wang X., Ding X., Geng W., (2015), Recent development in rare earth doped phosphors for white light emitting diodes. *J Rare Earths*,**33**:1–12.

Wang Z., Feng J., Pang M., Pana S., Zhang H., (2013), Multicolor and bright white upconversion luminescence from rice-shaped lanthanide doped $BiPO_4$ submicron particles, *Dalton Trans*.,**42**:12101–12108.

Wolfert A.,Oomen E.W.J.L., Blasse G., (1985), Host lattice dependence of the Bi^{3+} luminescence in orthoborates $LnBO_3$ (with *Ln* = Sc, Y, La, Gd, or Lu), *J. Solid State Chem*.,**59(3)**:280-290.

Wu Z. C., Liu J., Hou W. G., Xu J., Gong M. L., (2010), A new single-host white-emitting $BaSrMg(PO_4)_2:Eu^{2+}$ phosphor for white-light-emitting diodes *J. Alloys Compd*.,**498**:139-142.

Xia C., Xua Y., Cao M., (2020), A selective and sensitive fluorescent probe for bilirubin in human serum based on Europium(III) post-functionalized Zr(IV)-Based MOFs. *Talanta*, **212**:120795.

Xia C., Yu C., Cao M., Xia J., Jiang D., Zhou G., Zhang D., Li H., (2018), A Eu and Tb Co-Doped MOF-5 Compound for Ratiometric High Temperature Sensing. *Ceram. Int.*,**44(17)**:21040-21046.

Xia J., Zhao H., Pang W. K., Yin Z., Zhou B., He G., Guo Z., Du Y., (2018), Lanthanide doping induced electrochemical enhancement of $Na_2Ti_3O_7$ anodes for sodium-ion batteries. *Chem. Sci*.,**9**:3421.

Xia Z. G., Meijerink A., (2017), Ce^{3+}-doped garnet phosphors: composition modification, luminescence properties and applications. *ChemSoc Rev*,**46**:75–99.

Xiang J., Yang J., Luo N., Zhu J., Huang S., Mao Y., (2019), Optimized photoluminescence and electronic properties of europium doped phosphate red phosphor, *Results Phys*,**13**:102258.

Xie R. J., Li Y. Q., Hirosake N. Yamamoto H., (2011), Nitride phosphors and solid-state lighting(Boca Raton: CRC Press, Taylor & Francis Group, LLC).

Xin S., Gao M., Wang C., Wang X., Zhu G., Zhou F., Li Z., Wang Y., (2018), Efficient and controllable photoluminescence in novel solid solution phosphors $Ca_{1-x}Sr_xHf_4(PO_4)_6:Eu^{2+}$ with high thermal stability for white light emitting diodes *CrystEngComm*, **20**:4383-4394.

Xin S., Wang Y., Zhu G., Ding X., Geng W., Wang Q., (2015), Structure and temperature sensitive photoluminescence in a novel phosphate red phosphor $RbZnPO_4:Eu^{3+}$*Dalton trans*,**44**:16099-16106.

Xu J., Li L., Guo C., Zhang Y., Meng W., (2013),Photocatalytic degradation of carbamazepine by tailored $BiPO_4$: efficiency, intermediates and pathway. *Appl. Catal. B.*,**130-131**:285-292.

XuS., LiP., WangZ., Li T., Bai Q., Sun J., Yang Z., (2015), Luminescence and energy transfer of $Eu^{2+}/Tb^{3+}/Eu^{3+}$ in $LiBaBO_3$ phosphors with tunable-color emission. *J. Mater. Chem. C*, **3:**9112.

Xu X. T., Tang Y. X. Mo F. W., (2014), Synthesis and luminescent properties of $CaTiO_3$: Eu^{3+}, Al^{3+} phosphors. *Ceram. Int.*,**40**:10887–10892.

Xue F., Li H. B., Zhu Y. C., Xiong S. L., Zhang X. W., Wang T. T., Liang X., Qian Y. T., (2009), Solvothermal synthesis and photoluminescence properties of $BiPO_4$ nano-cocoons and nanorods with different phases *J. Solid State Chem.*, **182**:1396.

Yaba T., Wangkhem R., Singh N. S., (2020) Enhanced red emission from Bi^{3+} sensitized $CaWO_4$: Eu^{3+} as red component for near UV/blue LED pumped white light emission. *J Alloys Compd.*,**843**:156022.

Yan S. Q., (2015), Synthesis and Luminescence of $BiPO_4:Tb^{3+}$ Nanowires by a Hydrothermal Process, *Mater. Manuf. Process*,**30(5)**:591-594.

Yan S. Q., Long C. G., (2016), Effects of Sm^{3+} concentration on the microstructure and luminescence properties of $BiPO_4$ phosphor prepared by hydrothermal method, *J Mater Sci: Mater Electron*,**27**:12079–12084.

Yang F., Ma H. G., Liu Y. F., Liu Q. B., Yang Z. P., Han Y., (2013), A new green luminescent material $Ba_3Bi(PO_4)_3:Tb^{3+}$. *Ceram. Int.*,**39(2)**: 2127-2130.

Yang Y., Liu B., Zhang Y., Lv X., Wei L., Wang X., (2016), Fabrication and luminescence of $BiPO_4:Tb^{3+}/Ce^{3+}$ nanofibers by electrospinning, *SuperlatticeMicrost*, **90**: 227-235.

Zhang D., Su C., Yao S., Li H., Pen X., Geng Y., (2020), Facile in situ chemical transformation synthesis, boosted charge separation, and increased photocatalytic activity of BiPO4/BiOCl p-n heterojunction photocatalysts under simulated sunlight irradiation. *J. Phys. Chem. Solids*, **147**:109630.

Zhang J., Yu Z., Guo J., Yan W., Xue W., (2017), Enhanced luminescence properties and morphology evolution of $Bi_{1-x}PO_4:xDy^{3+}$ by introducing excessive PO_4^{3-} ions, *J Alloy Compd*, **703**:156-162.

Zhang Y., Xu J., Cui Q., Yang B., (2017), Eu^{3+}-doped $Bi_4Si_3O_{12}$ red phosphor for solid state lighting: microwave synthesis, characterization, photoluminescence properties and thermal quenching mechanisms *Sci. Rep*,**7**:42464.

Zhang Y. R., Wang S. Q., Shen S. L., Zhao B. X., (2013), A novel water treatment magnetic nanomaterial for removal of anionic and cationic dyes under severe condition. *Chem. Eng. J.*,**233**:258–264.

Zhao M., Li G., Li L., Yang L., Zheng J., (2012), Structures and Polymorph-Sensitive Luminescence Properties of $BiPO_4$/Eu Grown in Hydrothermal Conditions, *Cryst. Growth Des.*,**12**: 3983−3991.

Zhao M., Li G., Zheng J., Li L., Wang H., Yang L., (2011), Preparation and polymorph-sensitive luminescence properties of $BiPO_4$:Eu, Part I: room-temperature reaction followed by a heat treatment, *CrystEngComm*, **13**:6251-6257.

Zhao M., Li L., Yang L., Zheng J., Li G., (2013), Exploring the unique electrical properties of metastable $BiPO_4$ through switchable phase transitions *CrystEngComm*,**15**:609-615.

Zhao M., Li L., Zheng J., Yang L., Li G., (2012), Is BiPO4 a Better Luminescent Host? Case Study on Doping and Annealing Effects, *Inorg chem*., **52**:807−815.

Zheng Y., Li L., Zhao M., Zheng J., Li G., Yanga E., Zhang X., (2014), Enhancement of thermal stability in bismuth phosphate by Ln^{3+} doping for tailored luminescence properties, *CrystEngComm*, **16**:5040-5049.

Zhou X., Wang X., (2011), Preparation, characterization and luminescence properties of BiPO4:Eu nanophosphors, *Luminescence*, **28**: 685–689.

Zukauskas A., Vaicekauskas R., Ivanauskas F., Vaitkevicius H., Shur M. S., (2008), Spectral optimization of phosphor-conversion light-emitting diodes for ultimate color rendering. *Appl. Phys. Lett*.,**93**:051115.

Received: 1 June 2020 | Revised: 7 July 2020 | Accepted: 17 July 2020

DOI: 10.1111/ijac.13600

ORIGINAL ARTICLE

International Journal of Applied Ceramic TECHNOLOGY

Photoluminescence studies of Ce^{3+} ion-doped $BiPO_4$ phosphor and its photocatalytic activity

Ramananda Singh Naorem[1] | **Naorem Premjit Singh**[2] | **Nongmaithem Mohondas Singh**[1]

[1]Department of Chemistry, School of Physical Sciences, Mizoram University, Aizawl, India

[2]Department of Chemistry, A. R. S. D. College, University of Delhi, New Delhi, India

Correspondence
Nongmaithem Mohondas Singh, Department of Chemistry, School of Physical Sciences, Mizoram University, Aizawl-796004, India.
Email: nmdas08@rediffmail.com

Funding information
Science and Engineering Research Board, Grant/Award Number: SB/EMEQ-336/2014

Abstract

Ce^{3+} ion doped $BiPO_4$ phosphors were synthesized by co-precipitation method using ethylene glycol as capping agent. The prepared phosphors were characterized by XRD, SEM, FT-IR, UV-Vis, and PL spectroscopy techniques. The formation of monoclinic phase was confirmed from XRD and FT-IR studies. SEM study revealed the rice shape morphology of $BiPO_4$:Ce^{3+} (7at.%). In the photoluminescence analysis, a broad emission band extending in a wide wavelengths range with maxima around 419 and 470 nm was observed under excitation at 370 and 417 nm, respectively. These emission bands are originated from the electronic transitions, viz., 5d → $^2F_{5/2}$, $^2F_{7/2}$ of Ce^{3+} ion. The emission intensity was accentuated with the increase of Ce^{3+} ion till 7at.% and subsequently attenuated with further increase of Ce^{3+} ion concentration; which is due to the concentration quenching effect. The $BiPO_4$:Ce^{3+} (7at.%) sample was characterized for the feasibility of photocatalytic degradation of methylene blue under UV light irradiation and degradation of 90% of the dye was degraded within 120 minutes was observed. From the results, it is believed that the prepared $BiPO_4$:Ce^{3+} may have potential applications in solid state lighting as well as in photocatalysis for the degradation of organic dyes.

KEYWORDS

$BiPO_4$:Ce^{3+}, concentration effect, photocatalysis, photoluminescence

1 | INTRODUCTION

Rare earth ions-doped luminescent materials have attracted a much attention because their wide applicability in the fields of lighting and display devices, optoelectronics etc.[1–3] Among the rare earth ions, Ce^{3+} is very much sought after due to its low cost, spin, and parity allowed optical 4f-5d transitions and its applications in scintillators, light-emitting diodes and field emission displays etc.[4] Moreover cerium ion-doped phosphors could absorb in UV region with a large cross-section and emitted in the blue region of the visible radiation due to electric dipole allowed transitions, which makes them suitable for applications in the fields of lithography, imaging, optical data recording.[5]

In the last few years, phosphate-based luminescent materials have drawn a considerable attention because of their potential applications in photoluminescence, photocatalysis, super ionic conductors, etc as well as their high physio-chemical stability.[6–8] As a member of phosphate family, $BiPO_4$ is considered as suitable host for doping rare earth ions because of their comparable in size of Bi^{3+} with the trivalent rare earth ions. $BiPO_4$ normally crystallizes in two crystallographic forms: Hexagonal and Monoclinic. Hexagonal phase is generally formed at lower temperature and it can be converted to monoclinic phase on heating above 600°C. Hexagonal and Monoclinic structures of $BiPO_4$ are essentially differed in the co-ordination number of Bi^{3+}. In case of hexagonal phase, Bi^{3+} ions are surrounded by eight neighboring oxygen atoms and forming square anti-prism geometry whereas in case of monoclinic phase nine near oxygen atoms. In hexagonal phase, BiO_8 polyhedra and PO_4 tetrahedra with lattice water molecules located in channels are symmetrically arranged

in a chain form parallel to the c-axis.[7,9] But in the monoclinic phase, the chains are unsymmetrically arranged.[9] Monoclinic phase exhibited superior photoluminescence and photocatalytic activity than the hexagonal phase.[10] Additionally the luminescence arising from the Bi^{3+} species is also quite interesting because of its electron transition between the $6s^2$ ground states and the 6s6p excited states and significant Stoke shift associated with its emission-absorption characteristics.[7]

Semiconductor photocatalysis have become the most attractive research topic among the researchers in the past few years as it is considered as the most promising method to solve the energy problem and the environment related problems.[11,12] It has potential applications in water splitting to generate hydrogen and decomposition of organic dyes in waste water. The organic dyes present in waste water are very stable in natural cycle. Therefore, it causes hazardous effects on living beings (both aquatic and surface environments). It also caused carcinogenic, mutagenic to human being as well.[13,14] Hence, degradation of these organic dyes is of great importance before entering into the fresh water bodies. In this regard, $BiPO_4$ is considered as the good UV-light active photocatalyst semiconductor due to its high efficiency to separate the electrons and holes, low cost, high stability etc. It has also been reported that $BiPO_4$ has greater activity on the degradation of some organic dyes, phenol, benzene than the P25 under UV light irradiation.[15–17] Moreover doping of Ce^{3+} ion into semiconductor leading to increase its surface area and also enhances the electron-hole charge separation which higher its photocatalytic activity.[18,19] Therefore, the present study is focused on the investigation of photoluminescence and photocatalytic properties of Ce^{3+}-doped $BiPO_4$ prepared by co-precipitation method using ethylene glycol as reaction medium.

2 | EXPERIMENTAL DETAILS

2.1 | Materials

The chemicals used in the synthesis are cerium nitrate hexahydrate ($Ce(NO_3)_3{\cdot}6H_2O$) (with 99.99% purity), Bismuth nitrate hexahydrate ($Bi(NO_3)_3{\cdot}6H_2O$) (with 98% purity), Ammonium dihydrogen phosphate ($NH_4H_2PO_4$) (with 98% purity). All chemicals were purchased from Alfa Aesar. The solvent ethylene glycol was purchased from Merck.

2.2 | Preparation of cerium ions doped bismuth phosphate

In a typical synthesis, the stoichiometric amount of $Bi(NO_3)_3{\cdot}5H_2O$ was added into a round bottom flask containing 70 mL of ethylene glycol. The solution was stirred in a magnetic stirrer for 30 minutes. Then, the stoichiometric amounts of $NH_4H_2PO_4$ and $Ce(NO_3)_3$ were added into the above solution and it is refluxed at a temperature of 160°C for 2 hours. The solution was then allowed to cool down at room temperature and then the precipitate thus formed was washed with distilled water for several times and then with ethanol. After that the sample was dried in an oven at a temperature of 80°C for 12 hours.[7] Similar process was followed for preparing different doping concentrations of Ce^{3+}.

2.3 | Characterizations

Bruker D2 phaser XRD machine equipped with Cu Kα radiation (λ = 1.5406 Å, Ni filter, 2Θ = 15°-60° operated at 30 kV and 100 mA) was used to determine the crystal structure of the prepared samples. The vibrational spectra of the prepared sample were analyzed using Shimadzu Iraffinity-1s FT-IR spectrometer using KBr as beam splitter. Field emission scanning electron microscopy (FESEM) was recorded by Jeol JSM-6390 in order to see the morphologies of the samples. The absorption band and the photocatalytic activity of the sample were recorded by Jasco V-730 UV-Visible spectrophotometer. Hitachi (F-7000) fluorescence spectrophotometer having xenon discharge lamp as excitation source was used for the recording of excitation and emission spectra. All the measurements were taken at room temperature.

2.4 | Photocatalytic activity measurement

Methylene blue was chosen as a target pollutant fo**r** evaluating the photocatalytic activity of the prepared $BiPO_4$:7at.% Ce^{3+} because it is one of the most commonly used dye in industries mainly for printing, textiles and leather industries.[20] It causes environmental and biological problems.[21] It also causes headache, shortness of breath, high blood pressure of human being.[22] The photocatalytic activity of the prepared $BiPO_4$:Ce^{3+} (7at.%) sample was analyzed through the degradation of methylene blue dye under UV-light irradiation (Spectroline E-Series UV lamp with 254 nm). The details of the procedure are as follow, 10 ppm of methylene blue solution was prepared in aqueous solution. Then 100 mg of the catalyst was suspended in 100 mL of above methylene blue solution. The solution was stirred using magnetic bar for 15 minutes and then kept in a dark place for about 30 minutes in order to achieve adsorption-desorption equilibrium. Then the solution was irradiated by UV light at a wavelength of 254 nm. Every 10 minutes, the absorbance of the sample was recorded using UV–Vis spectrophotometer. The discoloration efficiency (I%) was calculated using the formula.

$$I(\%) = \frac{C_o - C_t}{C_t} \times 100,$$

where, C_o is the initial concentration of the dye and C_t is the concentration of the dye after UV-light irradiation at time t.

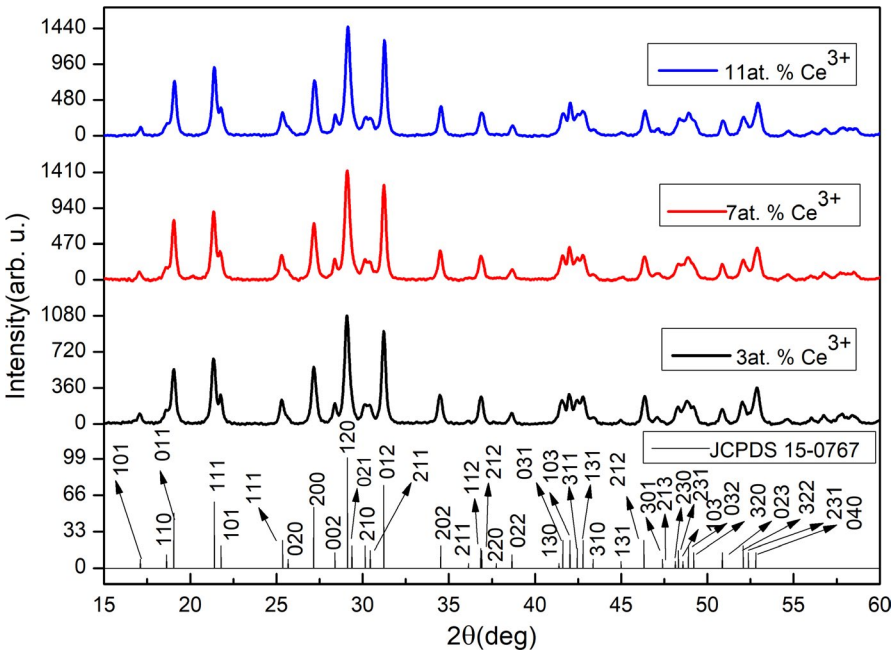

FIGURE 1 XRD patterns of the prepared $BiPO_4$:xCe^{3+} (x = 3, 7, 11at.%)

TABLE 1 Calculated lattice parameters and cell volumes of cerium ions-doped bismuth phosphate

Dopant cerium ion concentrations (atomic percentage)	Lattice parameters			Cell volume (V) Å^3
	a(Å)	b(Å)	c(Å)	
3	6.754	6.937	6.47	294.465
7	6.752	6.936	6.469	294.277
11	6.741	6.934	6.463	293.572

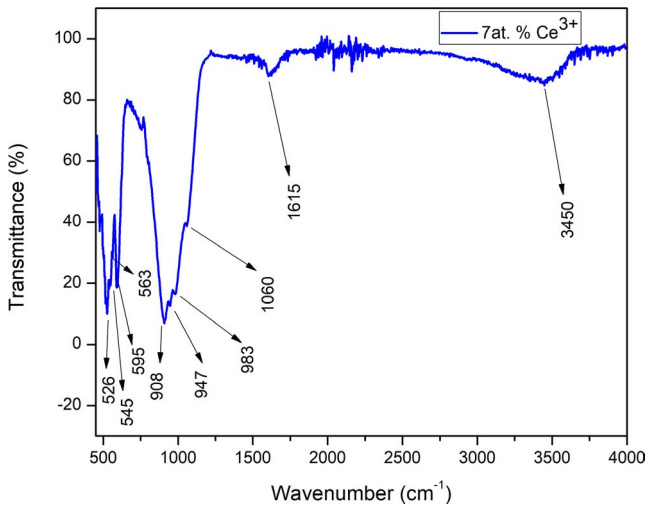

FIGURE 2 FT-IR spectrum of $BiPO_4$:Ce^{3+} (7at.%)

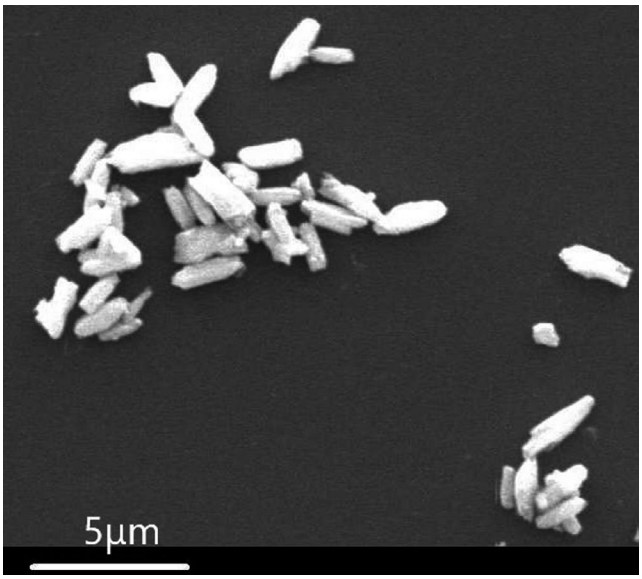

FIGURE 3 SEM image of $BiPO_4$:Ce^{3+} (7at.%)

3 | RESULTS AND DISCUSSIONS

3.1 | XRD study

Figure 1 shows the XRD patterns of Ce^{3+} (3, 7, and 11at.%) ions-doped $BiPO_4$ phosphors. The diffraction peaks of as prepared samples are well matched with the monoclinic phase of the $BiPO_4$ according to the JCPDS No. 15-0767.[8] The observed diffraction peaks were strong and sharp indicating that the prepared samples are well crystallized. Further no possible impurity phases were detected showing that the prepared sample is crystallized in pure monoclinic phase. Figure S1 (Supplementary Information) showed the shifting of diffraction peak to the higher angle as the concentrations of dopant Ce^{3+} ion increases which is due to the smaller size of Ce^{3+} ion (1.07 Å) as compared to Bi^{3+} ion (1.17 Å).[23,24] This shifting of diffraction peaks confirmed the successful doping of Ce^{3+} ions into the interstitial site of $BiPO_4$.[25–27] The calculated lattice parameters and cell volumes are shown in Table 1. It is clearly seen that the cell volume is decreased with the increase of Ce^{3+} ion concentration which is due to smaller size of Ce^{3+}

ion as compare to the Bi^{3+} ion. The substitution of Bi^{3+} ion by Ce^{3+} ion is also supported by reduction in cell volume.

3.2 | FT-IR and SEM Image study

The FT-IR spectrum of $BiPO_4:Ce^{3+}$ (7at.%) is shown in Figure 2. The bands observed at 3450 and 1615 cm^{-1} correspond to the stretching and bending vibrations of O–H bond that is originated from the adsorbed H_2O molecules on the surface of the sample.[28,29] The bands observed at 947, 983, and 1060 cm^{-1} are attributed to the symmetric stretching vibrational modes of P–O bond and the band observed at 908 cm^{-1} can be assigned to the symmetric stretching vibrational mode of P–O bond within the PO_4^{3-} group.[6] The bands observed at 595, 563, 545, and 526 cm^{-1} correspond to the bending vibrational modes of O–P–O linkage.[30] All these observed bands are the characteristic bands of PO_4^{3-} group of a monoclinic structure. So the formation of monoclinic phase is further supported from the above analysis. The rice shape morphology of $BiPO_4:Ce^{3+}$ (7at.%) phosphor was observed from SEM image analysis and the SEM images of $BiPO_4:Ce^{3+}$ (7at.%) is shown in Figure 3.

3.3 | PL study

Figure 4 showed the photoluminescence excitation spectrum of prepared $BiPO_4:Ce^{3+}$ (7at.%). The excitation spectrum was

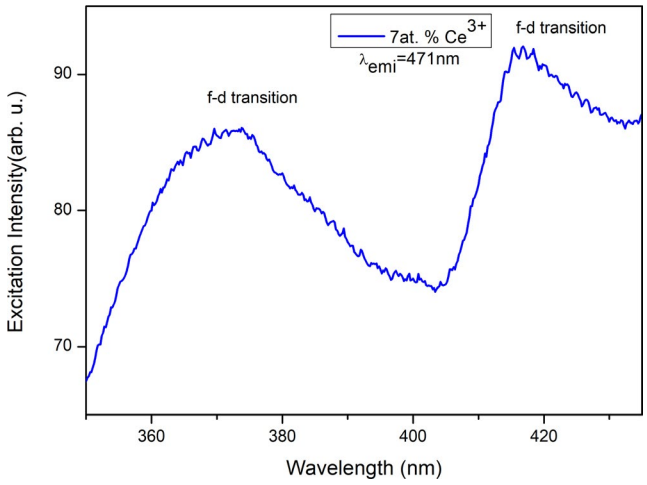

FIGURE 4 PLE spectrum of $BiPO_4:Ce^{3+}$ (7at.%) (λ_{emi} = 471 nm)

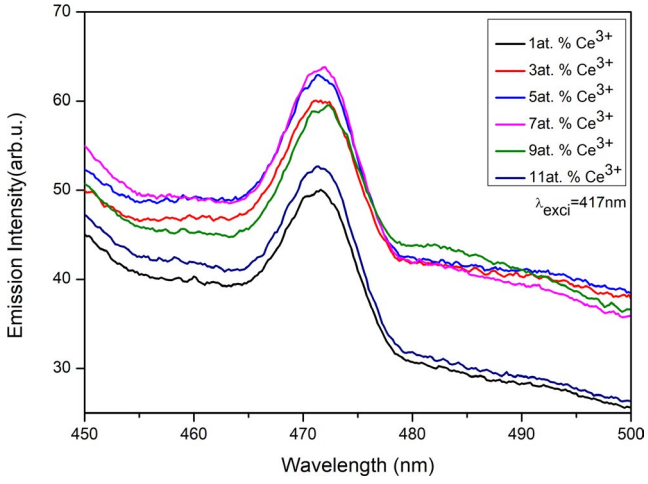

FIGURE 6 PL spectra of $BiPO_4:xCe^{3+}$, (λ_{emi} = 417 nm) (x = 1,3,5,7,9,11at.%)

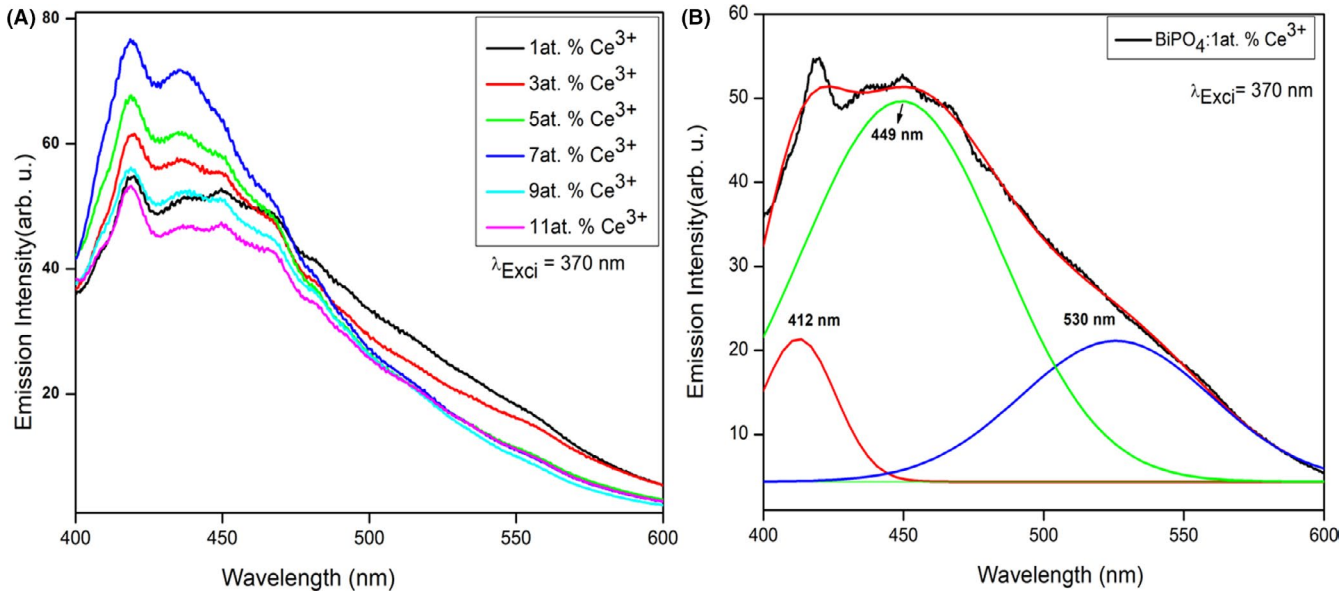

FIGURE 5 (A) PL spectra of $BiPO_4:xCe^{3+}$, (λ_{emi} = 370 nm) (x = 1,3,5,7,9,11at.%) (B) Gaussian fitting of the peak of $BiPO_4$:1at.% Ce^{3+}

recorded by monitoring the emission wavelength at 471 nm. The spectrum consists of two maxima at 370 and 417 nm which correspond to $^2F_{5/2} \rightarrow 5d$ transitions of Ce^{3+} ion.[31–33]

Under excitation at the wavelength of 370 nm, a broad emission band extending upto 600 nm having maximum at 419 nm was observed (Figure 5A) which is due to the $5d \rightarrow {}^2F_{5/2}$, $^2F_{7/2}$ allowed transition resulted from the coupling of 5d electron with the host lattice.[33,34] This broad emission band can be split into three different bands at 412, 449, and 526 nm by Gaussian curve fitting (Figure 5B) and these bands are resulted due to the transition from ground state to different field-splitting 5d levels of Ce^{3+} ions.[30,24,35] However, under excitation at 417 nm (Figure 6) the observed emission band is extended from 465 to 480 nm with maximum peak intensity at 471 which is due to the $5d \rightarrow {}^2F_{7/2}$ transition and is fall in the blue region of the electromagnetic wave.[30] Except the photoluminescence intensity, there is no significant change on the peak profile with the change of Ce^{3+} ion concentration. The photoluminescence intensity was found to increase with the increase of Ce^{3+} till it reaches 7at.%. Beyond this concentration the intensity was found to decrease upon excitation at both the wavelengths 370 and 417 nm. This decreases in the photoluminescence intensity beyond 7at.% Ce^{3+} is due to the concentration quenching.[36] This can be explained as the increase in the concentration of Ce^{3+} ion, inter ionic distances between the Ce^{3+} ions decreases. When the inter ionic distances among Ce^{3+} ions are lower than the critical distance, the non radiative energy transfer among the Ce^{3+} ions increases and results into the quenching of emission intensities.[37]

3.4 | Optical property study

The absorption spectra of $BiPO_4:Ce^{3+}$ (7at.%) is shown in Figure 7A. The figure showed that the absorption band is extended in a wide range from UV to visible with maximum absorption in the UV region which indicates that the sample has the possibility to use as photocatalyst under UV-light irradiation. The energy band gap was determined using the formula for optical absorption:

$$\alpha h\nu = A\left(h\nu - E_g\right)^{n/2},$$

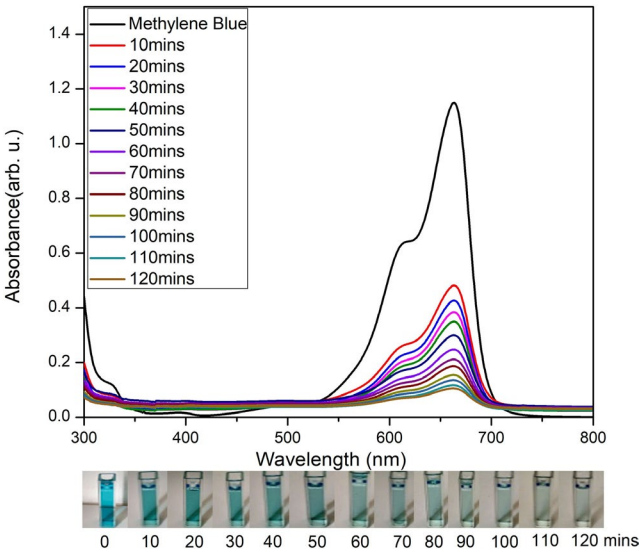

FIGURE 8 Photodegradation of Methylene blue under UV-light irradiation using $BiPO_4$:7at.% Ce^{3+}

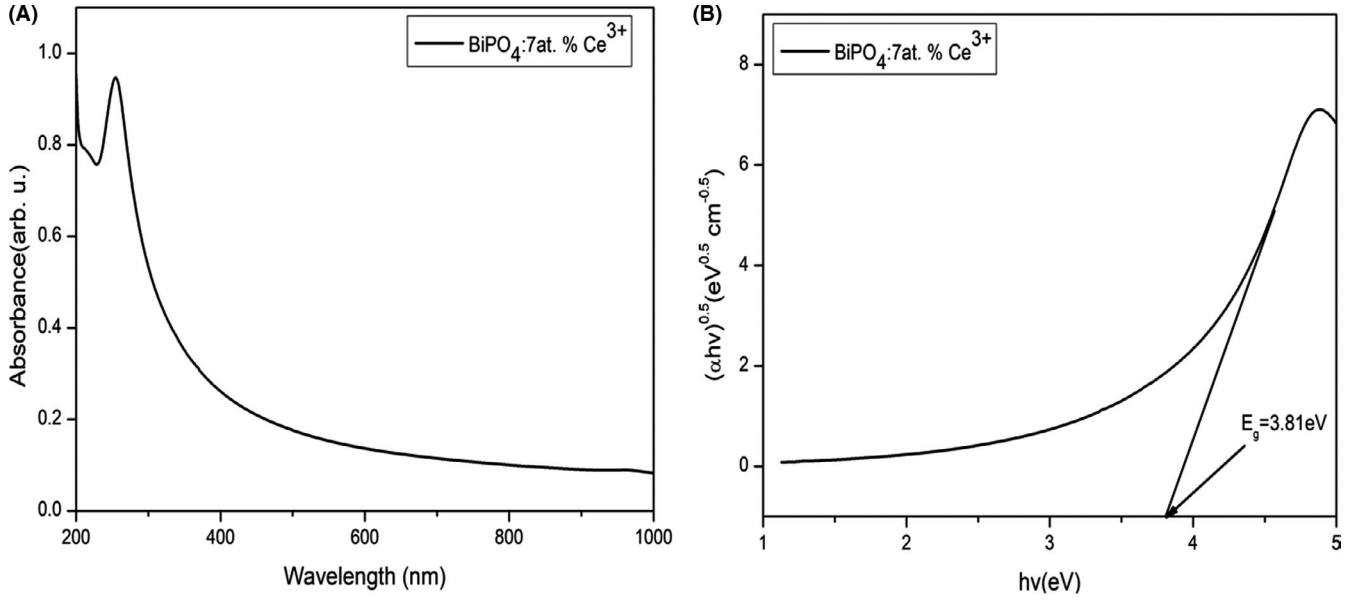

FIGURE 7 (A) Absorbance spectra of $BiPO_4$:7at.% Ce^{3+} (B) Band gap of $BiPO_4$:7at.% Ce^{3+} calculated using Tauc plot. (α, absorption coefficient, h, Plancks constant, ν, photonic frequency, E_g, absorption energy gap, eV, electron volts)

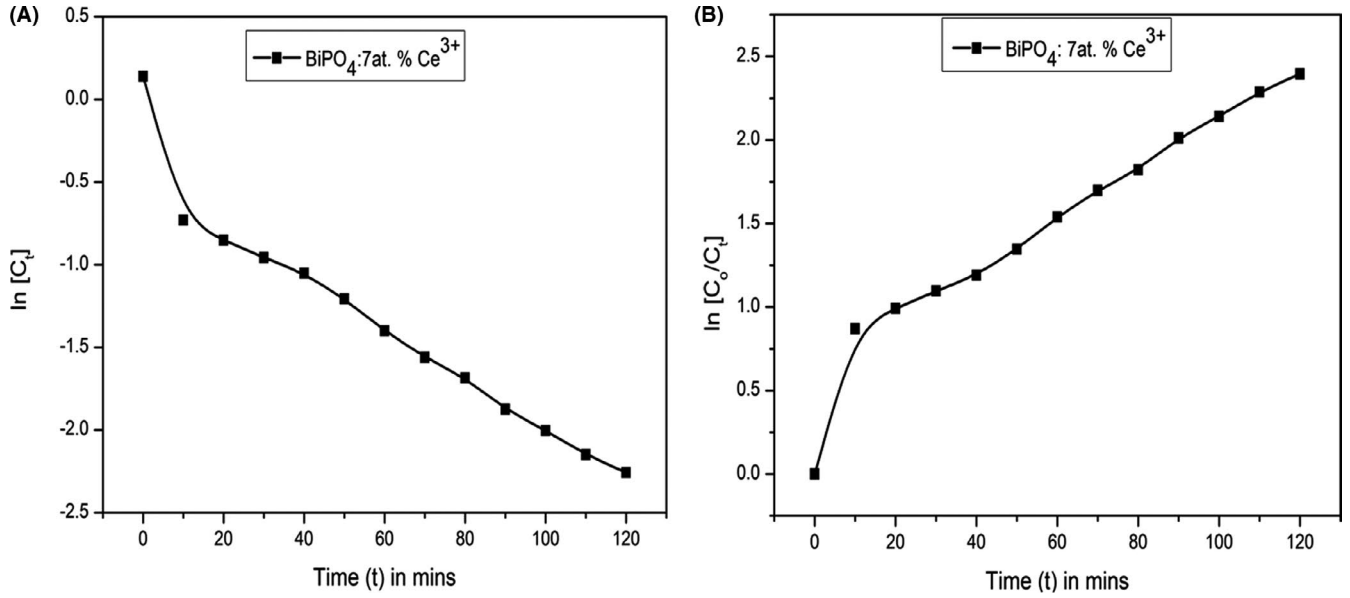

FIGURE 9 (A) Plot of ln[C_o] vs time in minutes (B) Linear transform ln(C_o/C_t) vs time in minutes of the kinetic curves of Methylene blue degradation. (ln, natural logarithm; C_o, initial concentration; C_t, concentration at time t)

where α is the absorption co-efficient, h is the plancks constant, ν is the photonic frequency, A is the constant relative to the material, E_g is the absorption energy gap, and n depends on the type of transitions (for direct transition, $n = 1$ and for indirect transition, $n = 4$). As $BiPO_4$ exhibits indirect transition, the absorption energy band gap is determined by extrapolating the linear portion of the plot of $(\alpha h\nu)^{0.5}$ *vs* $h\nu$ and it is shown in Figure 7B.[15] The estimated energy band gap was found to be 3.81 eV. This observed energy band gap is almost same with that reported in the literature.[38]

3.5 | Photocatalytic activity study

The photocatalytic activity of the prepared $BiPO_4$:Ce^{3+} (7at.%) was examined through the degradation of methylene blue dye under UV-irradiation. Figure 8 shows the absorbance spectra of methylene blue dye at different time intervals. It was reported that methylene blue dye does not degraded itself.[39] However with the addition of the prepared catalyst, the absorption spectrum was significantly decreased. The absorbance was recorded every 10 minutes and after 120 minutes of UV light irradiation 90% of the dye was degraded. On irradiation under UV light, the photogenerated electrons are introduced in the conduction band and photogenerated holes are produced in the valence band which are responsible for the degradation of methylene blue dye.[40] The electrons in the conduction band of $BiPO_4$ adsorbed O_2 from water molecule and formed $O_2^{-\bullet}$, while the holes in the valence band interact with absorbed H_2O molecules to form hydroxyl radicals. The $O_2^{-\bullet}$ and $OH^{\bullet}$ decomposed Methylene blue to CO_2 and H_2O.[41] From this investigation it is believed that the prepared sample may have potential application in degrading the coloring organic dyes present in waste water.

3.6 | Kinetics study

The kinetics involving the rate of degradation of methylene blue under UV-light irradiation was discussed. The order of the reaction was calculated by plotting a graph between ln [C_t] vs time, where C_t is the concentration of the dye at time t. The graph exhibited a negative slope which confirmed the reaction followed a first order kinetic Figure 9A. Furthermore, ln [C_o/C_t] vs time graph was plotted as shown in Figure 9B which showed that the degradation of methylene blue followed first order Langmuir-Hinshelwood kinetics model and pseudo first order kinetics equation is given below.[42]

$$\ln\left(C_o/C_t\right) = kt,$$

where C_o and C_t represent the initial concentration of methylene blue and final concentration of methylene blue at time t, respectively, k represents the first order kinetic rate constant and t is the time. The rate constant was calculated and found to be 2.56395×10^{-2} min^{-1}.

4 | CONCLUSIONS

$BiPO_4$:xCe^{3+} (x = 1,3,5,7,9,11at %) phosphors were synthesized successfully by co-precipitaion method using ethylene glycol as reaction medium as well as capping agent. The prepared phosphors were characterized by

XRD, UV-Vis scpectroscopy, SEM, and PL. The PL study showed a broad emission band extending from blue to green region upon excitation at 370 nm. The optimum concentration of Ce^{3+} was found to be 7 at.%. Photocatalytic analysis of $BiPO_4$:Ce^{3+} (7at.%) sample revealed that 90% of the dye methylene blue could be degraded within 120 minutes of UV light irradiation. From the results it is believe that the prepared samples may have potential applications in solid state lighting as well as photocatalyst for the degradation of organic dyes.

ACKNOWLEDGMENTS

The authors thank the Science and Engineering Research Board (SERB), New Delhi (Vide No. SB/EMEQ-336/2014 dated 04.02.2016) for financial support.

ORCID

Nongmaithem Mohondas Singh https://orcid.org/0000-0001-6086-946X

REFERENCES

1. Park K, Heo MH, Kim KY, Dhoble SJ, Kim Y, Kim JY. Photoluminescence properties of nano-sized $(Y_{0.5}Gd_{0.5})PO_4$:Eu^{3+} phosphor powders synthesized by solution combustion method. Powder Technol. 2013;237:102–6.
2. Singh NP, Devi YR, Singh NR, Singh NM. Synthesis of Tb^{3+} ion doped $ZnWO_4$ phosphors and investigation of their photoluminescence properties: concentration effect. Bull Mater Sci. 2019;42(3):96.
3. Yang F, Ma HG, Liu YF, Liu QB, Yang ZP, Han Y. A new green luminescent material $Ba_3Bi(PO_4)_3$:Tb^{3+}. Ceram Int. 2013;39(2):2127–30.
4. Dabre KV, Dhoble SJ, Lochab J. Synthesis and luminescence properties of Ce^{3+} doped MWO_4 (M=Ca, Sr and Ba) microcrystalline phosphors. J Lumin. 2014;149:348–52.
5. Lai H, Bao A, Yang Y, et al. UV luminescence property of YPO_4:RE (RE = Ce^{3+}, Tb^{3+}). J Phys Chem C. 2008;112:282–6.
6. Ganguli S, Hazra C, Chatti M, Samanta T, Mahalingam V. A highly efficient UV–Vis–NIR Active Ln^{3+}-doped $BiPO_4$/$BiVO_4$ nanocomposite for photocatalysis application. Langmuir. 2015;32:247–53.
7. Naidu BS, Vishwanadh B, Sudarsan V, Vatsa RK. $BiPO_4$: a better host for doping lanthanide ions. Dalton Trans. 2012;41:3194–203.
8. Guan M, Sun J, Tao F, Xu Z. A host crystal for the rare-earth ion dopants: synthesis of pure and Ln-doped urchinlike $BiPO_4$ structure and its photoluminescence. Cryst Growth Des. 2008;8:2694–7.
9. Arunkumar P, Jayajothi C, Jeyakumar D, Lakshminarasimhan N. Structure–property relations in hexagonal and monoclinic $BiPO_4$:Eu3+ nanoparticles synthesized by polyol-mediated method. RSC Adv. 2012;2:1477–85.
10. Achary SN, Errandonea D, Muñoz A, et al. Experimental and theoretical investigations on the polymorphism and metastability of $BiPO_4$. Dalton Trans. 2013;42:14999–5015.
11. Wang R, Hashimoto K, Fujishima A, et al. Light-induced amphiphilic surfaces. Nature. 1997;388:431–2.
12. Kamat P. Photochemistry on nonreactive and reactive (semiconductor) surfaces. Chem Rev. 1993;93:267–300.
13. Lellis B, Polonio CZF, Pamphile JA, Polonio JC. Effects of textile dyes on health and the environment and bioremediation potential of living organisms. Biotechnol Res Innov. 2019;3(2):275–90.
14. Berradi M, Hsissou R, Khudhair M, et al. Textile finishing dyes and their impact on aquatic environs. Heliyon. 2019;5:e02711.
15. Pan C, Zhu Y. New type of $BiPO_4$ oxy-acid salt photocatalyst with high photocatalytic activity on degradation of dye. Environ Sci Technol. 2010;44:5570–4.
16. Pan C, Xu J, Chen Y, Zhu Y. Influence of OH-related defects on the performances of $BiPO_4$ photocatalyst for the degradation of rhodamine B. Appl Catal B. 2012;115–116:314–9.
17. Xu J, Li L, Guo C, Zhang Y, Meng W. Photocatalytic degradation of carbamazepine by tailored $BiPO_4$: efficiency, intermediates and pathway. Appl Catal B. 2013;130–131:285–92.
18. Reli M, Ambrozova N, Sihor M, et al. Novel cerium doped titania catalysts for photocatalytic decomposition of ammonia. Appl Catal B. 2014;178:108–16.
19. Regmi C, Maya-Flores E, Lee SW, Rodriguez-Gonzalez V. Cerium-doped β-$Ni(OH)_2$ hexagon nanosheets: an effective photocatalyst for the degradation of the emerging water pollutant, naproxen. Nanotechnology. 2018;29:375603.
20. Mills A, Hazafy D, Parkinson J, Tuttle T, Hutchings MG. Effect of alkali on methylene blue (C.I. Basic Blue 9) and other thiazine dyes. Dyes Pigm. 2011;88:149–55.
21. Jalali K, Pajootan E, Bahrami H. Elimination of hazardous methylene blue from contaminated solutions by electrochemically magnetized graphene oxide as a recyclable adsorbent. Adv Powder Technol. 2019;30:2352–62.
22. Zhang YR, Wang SQ, Shen SL, Zhao BX. A novel water treatment magnetic nanomaterial for removal of anionic and cationic dyes under severe condition. Chem Eng J. 2013;233:258–64.
23. Li P, Guo L, Liang C, Li T, Chen P. Enhanced dual-wavelength sensitive upconversion luminescence of $BiPO_4$:Yb^{3+}/Er^{3+} phosphors by Sc^{3+} doping. Mater Sci Eng B-Adv. 2018;229:20–6.
24. He X, Liu X, Li R, et al. Effects of local structure of Ce^{3+} ions on luminescent properties of $Y_3Al_5O_{12}$: Ce nanoparticles. Sci Rep. 2016;6:22238–48.
25. Shannon RD. Revised effective ionic radii and systematic studies of interatomie distances in halides and chaleogenides. Acta Cryst. 1976;32:751–67.
26. İlhan M, Keskin İÇ, Çatalgöl Z, Samur R. NIR photoluminescence and radioluminescence characteristics of Nd^{3+} doped $BaTa_2O_6$ phosphor. Int J Appl Ceram Technol. 2018;15:1594–601.
27. İlhan M. Synthesis, structural characterization, and photoluminescence properties of TTB-type PbTa2O6:Eu^{3+} phosphor. Int J Appl Ceram Technol. 2017;14(6):1144–50.
28. Huang XH, Tay CB, Zhan ZY, et al. Universal photoluminescence evolution of solution-grown ZnO nanorods with annealing: important role of hydrogen donor. CrystEngComm. 2011;13:7032–6.
29. Li GS, Li LP, Boerio-Goates J, Woodfield BF. High purity anatase TiO(2) nanocrystals: near room-temperature synthesis, grain growth kinetics, and surface hydration chemistry. J Am Chem Soc. 2005;127:8659–66.
30. Pawlig O, Schellenschläger V, Lutz HD, Trettin R. Vibrational analysis of iron and zinc phosphate conversion coating constituents. Spectrochim Acta A. 2001;57:581–90.
31. Wang B, Liu Y, Huang Z, Fang M. Photoluminescence properties of a Ce^{3+} doped $Sr_3MgSi_2O_8$ phosphor with good thermal stability. RSC Adv. 2018;8:15587–94.

32. Singh S, Lakshminarayana G, Sharma M, et al. Excitation induced tunable emission in Ce^{3+}/Eu^{3+} codoped BiPO4 nanophosphors. J Spectrosc. 2015;2015:1–10.
33. Yang Y, Liu B, Zhang Y, Lv X, Wei L, Wang X. Fabrication and luminescence of $BiPO_4:Tb^{3+}/Ce^{3+}$ nanofibres by electrospinning. Superlattices Microstruct. 2016;90:227–35.
34. Talewar RA, Mahamuda SK, Rao AS, Joshi CP, Moharil SV. Sensitization of Nd^{3+} by 4f–5d transition of Ce^{3+} in $Ba_2Y(BO_3)_2Cl$ phosphor for the prospective NIR applications. J Lumin. 2018;202:1–6.
35. Shi Q, Wang C, Li S, et al. Enhancing blue luminescence from Ce-doped ZnO nanophosphor by Li doping. Nanoscale Res Lett. 2014;9:480–6.
36. Katelnikovas A, Jüstel T, Uhlich D, Jorgensen JE, Sakirzanovas S, Kareiva A. Characterization of cerium-doped yttrium aluminium garnet nanopowders synthesized via sol-gel process. Chem Eng Comm. 2008;195:758–69.
37. Singh NP, Singh NR, Singh NR, Singh NM. Effect of doping ion concentration on the photoluminescence behavior of $CdWO_4:Tb^{3+}$ phosphor synthesized via co-precipitation method. Indian J Phys. 2018;92:1461–6.
38. Xu H, Xu YG, Li HM, et al. Synthesis, characterization and photocatalytic property of $AgBr/BiPO_4$ heterojunction photocatalyst. Dalton Trans. 2012;41:3387–94.
39. Hou C, Hu B, Zhu J. Photocatalytic degradation of methylene blue over TiO_2 pretreated with varying concentrations of NaOH. Catalysts. 2018;8:575–87.
40. Chang W, Xuan Q, Shan L. Enhanced photocatalytic activity of BiPO4 photocatalyst by surface modification of Fe(III) Cocatalyst. J Wuhan Univ Technol Mater Sci Ed. 2018;33:871–5.
41. Lu M, Yuan G, Wang Z, Wang Y, Guo J. Synthesis of $BiPO_4/Bi_2S_3$ heterojunction with enhanced photocatalytic activity under visible-light irradiation. Nanoscale Res Lett. 2015;10(1):385–91.
42. Naciri Y, Chennah A, Jaramillo-Páez C, et al. Preparation, characterization and photocatalytic degradation of Rhodamine B dye over a novel $Zn_3(PO_4)_2/BiPO_4$ catalyst. J Environ Chem Eng. 2019;7:103075–84.

SUPPORTING INFORMATION

Additional supporting information may be found online in the Supporting Information section.

How to cite this article: Naorem RS, Singh NP, Singh NM. Photoluminescence studies of Ce^{3+} ion-doped $BiPO_4$ phosphor and its photocatalytic activity. *Int J Appl Ceram Technol*. 2020;00:1–8. https://doi.org/10.1111/ijac.13600

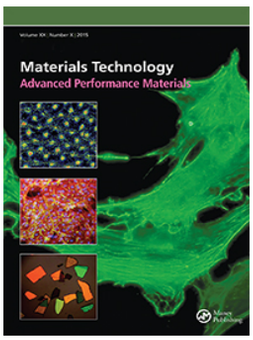

Taylor & Francis
Taylor & Francis Group

Materials Technology
Advanced Performance Materials

ISSN: (Print) (Online) Journal homepage: https://www.tandfonline.com/loi/ymte20

Photoluminescence properties of Tb^{3+} doped $BiPO_4$ nanophosphor synthesised by co-precipitation method using ethylene glycol

Ramananda Singh Naorem , Naorem Premjit Singh & Nongmaithem Mohondas Singh

To cite this article: Ramananda Singh Naorem , Naorem Premjit Singh & Nongmaithem Mohondas Singh (2020): Photoluminescence properties of Tb^{3+} doped $BiPO_4$ nanophosphor synthesised by co-precipitation method using ethylene glycol, Materials Technology

To link to this article: https://doi.org/10.1080/10667857.2020.1866919

Published online: 27 Dec 2020.

MATERIALS TECHNOLOGY
https://doi.org/10.1080/10667857.2020.1866919

Taylor & Francis
Taylor & Francis Group

Photoluminescence properties of Tb^{3+} doped $BiPO_4$ nanophosphor synthesised by co-precipitation method using ethylene glycol

Ramananda Singh Naorem [a], Naorem Premjit Singh [b] and Nongmaithem Mohondas Singh [a]

[a]Department of Chemistry, School of Physical Sciences, Mizoram University, Aizawl, India; [b]Department of Chemistry, A. R. S. D. College, University of Delhi, New Delhi, India

ABSTRACT

This work investigated the photoluminescence behaviour of Tb^{3+} doped $BiPO_4$ nanophosphors synthesised by co-precipitation method using ethylene glycol. The prepared nanophosphors were characterised by XRD, SEM, FT-IR and PL spectroscopy techniques. Monoclinic phase was observed from the XRD and FT-IR studies. SEM image showed agglomeration of nanoparticles. In the emission spectra, band originated from $^3P_1$–$^1S_0$ transition of Bi^{3+} ion and bands due to $^5D_4 \rightarrow {}^7F_{6,5,4,3}$ transitions of doping Tb^{3+} ion were observed upon excitation at 351 nm. The emission intensity was found to accentuate with the increase in Tb^{3+} ion concentration upto 3at. % and subsequently attenuated with further increase in Tb^{3+} ion concentration due to concentration quenching effect. The decay time of the prepared phosphors was also investigated. The CIE chromaticity diagram revealed a nearly white colour emission upon excited at 351 nm. It is possible that the prepared phosphors may be useful for solid-state lighting.

ARTICLE HISTORY
Received 23 September 2020
Accepted 11 December 2020

KEYWORDS
$BiPO_4$:Tb^{3+}; photoluminescence; concentration effect; CIE diagram

Introduction

Nanotechnology is one of the fastest growing technologies in this modern era and it has been becoming an important tool for manufacturing advanced materials. Nano-sized materials exhibited physical and chemical properties rather different from counterpart bulk materials because of their smaller size, large surface area to volume ratio, large number of loosely bound bonds and unsaturated atoms on the surface [1,2]. In addition to this, they also have advantageous features such as reduced scattering of light, surface defect concentration, etc. [2,3]. Moreover, quantum dots or nanomaterials in which the sizes less than 10 nm are becoming hot area of research owing to their outstanding optical and physic-chemical properties and their wide range of applications [4,5]. In past few decades, ZnO, TiO_2 and CuO nanoparticles are widely studied because of their excellent performance in the fields of photocatalysis, sensors, quantum dots, biomedicals, etc. [6–9].

It has been found that rare earth ion-doped inorganic phosphor materials have applications in various kinds of fields including solid state physics, photochemistry, biophysics, etc. [10–12]. These materials consist of two components: host material and activator, doping rare earth ion acts as activator ion [13]. Among the various host materials, phosphate-based materials have been attracted as one the best host due to their high physico-chemical and thermal stability [14,15]. Among phosphate family, $BiPO_4$ has several interesting properties such as high absorption edge, high stability in terms of chemical and mechanical stability as well as similar of ionic size of Bi^{3+} and lanthanide ions [16,17] and also has many potential applications in different fields such as ion sensing, catalysts, radioactive element separation, etc. [17–19]. In addition, $BiPO_4$ can be crystallised in three different crystallographic forms: Hexagonal, low temperature monoclinic and high temperature monoclinic. In hexagonal structure, Bi^{3+} ion is surrounded by eight oxygen atoms whereas in case of monoclinic phase it is surrounded by nine oxygen atoms [17]. The luminescent property of a phosphor is strongly dependent on its phase structure and many researchers have reported that low-temperature monoclinic structure of $BiPO_4$ exhibit strongest luminescent property in comparison with other phases in case of $BiPO_4$ [10].

In lanthanide ions doped luminescent materials, the luminescence property is generally originated from the electronic transition within the 4f electrons of doping lanthanide ions and since the 4f electrons of rare earth ion are shielded by 6s and 5p orbitals, the f-f electronic transitions of rare earth ions is not influenced by the outside environment thereby producing sharp absorption and emission bands. Doping of different rare earth ions into the host lattice exhibited different emission colours. For examples, Ce^{3+} ion doping normally emits blue colour, Eu^{3+} exhibits red colour and Sm^{3+} exhibits orange colour [20–23]. Trivalent terbium ion generally gives green colour

CONTACT Nongmaithem Mohondas Singh nmdas08@rediffmail.com; Ramananda Singh Naorem rmnda.nao@gmail.com Department of Chemistry, School of Physical Sciences, Mizoram University, Aizawl 796004, India

due to the $^5D_4 \rightarrow {}^7F_5$ electronic transition of Tb^{3+} ion [23] and it has potential applications in various fields including traffic signal, decoration, lighting and display, etc. Moreover it is one of the components of white light. Therefore the present study investigated the luminescence property of Tb^{3+} ion-doped $BiPO_4$ synthesised by co-precipitation method using ethylene glycol as reaction medium. Since the luminescence property is strongly influenced by the concentration of doping ion, the effect of Tb^{3+} ion concentration has been investigated in order to get optimum emission. To the best of author's knowledge there is no paper similar to our work reported yet.

Experimental section

Sample preparation

For the synthesis of $BiPO_4$:Tb^{3+} phosphors, the chemicals used were Terbium nitrate hexatahydrate ($Tb(NO_3)_3.6H_2O$) with 99.99% purity (Alfa Aesar), Bismuth nitrate pentahydrate ($Bi(NO_3)_3 \cdot 5H_2O$) with purity of 98% (Alfa Aesar), Ammonium dihydrogen phosphate ($NH_4H_2PO_4$) of 98% purity (Alfa Aesar) and the solvent Ethylene glycol (Merck). The typical synthesis steps are given as follows; first, the stoichiometric amounts of $Bi(NO_3)_3 \cdot 5H_2O$ were mixed with 70 mL of ethylene glycol in a round bottom flask. Stoichiometric amounts of $NH_4H_2PO_4$ and $Tb(NO_3)_3$ were added into the above solution. The solution was then refluxed at a temperature of 170 °C for 2 hrs. The white precipitate thus obtained was centrifuged, washed with distilled water for about 4–5 times and then finally with acetone. The sample was dried in an oven at a temperature of 80°C for 12 hrs. The same procedure was followed for preparing different doping concentrations of Tb^{3+} ion.

Characterisation of sample

The prepared samples were characterised by different characterisation techniques. The crystal structure and the phase composition of the prepared samples were determined using Bruker D2 phaser XRD with Cu Kα radiation (λ = 1.5406 A, Ni filter, 2θ = 15°-60° operated at 30 kV and 100 mA). Shimadzu Iraffinity-1s FT-IR spectrometer was used for recording the vibrational spectra. Field emission scanning electron microscopy (FESEM) image was recorded by FEI Quanta 200 3D to see the morphology of the sample. The photoluminescence excitation spectra, emission spectra and decay time were recorded by Horiba FluoroMax-4CP Spectrofluorometer with 150 W xenon lamp and 25 W μsec flash lamp as excitation light sources. All the measurements were performed at room temperature.

Results and discussions

XRD study

The XRD patterns of the prepared undoped $BiPO_4$ and 0.5, 3 and 7at. % of Tb^{3+} ions doped $BiPO_4$ nanophosphors are shown in Figure 1a, b. The XRD patterns of both doped and undoped $BiPO_4$ nanophosphors showed monoclinic phase according to JCPDS card no. 15–0767 [24,25]. The diffraction peaks are sharp and well defined, revealing that the phosphors are well crystallised. No impurity peaks were detected in the XRD patterns of concentrations of 0.5 and 7at. % while peak due to impurity was detected at 2θ degree around 20 degree in the pattern of 3at. % Tb^{3+} doped $BiPO_4$ and undoped $BiPO_4$ nanophosphors. The diffraction plane [120] is shifted towards the higher angle (as shown in Figure 2) with the increase of Tb^{3+} ion concentration which is because of the substitution of

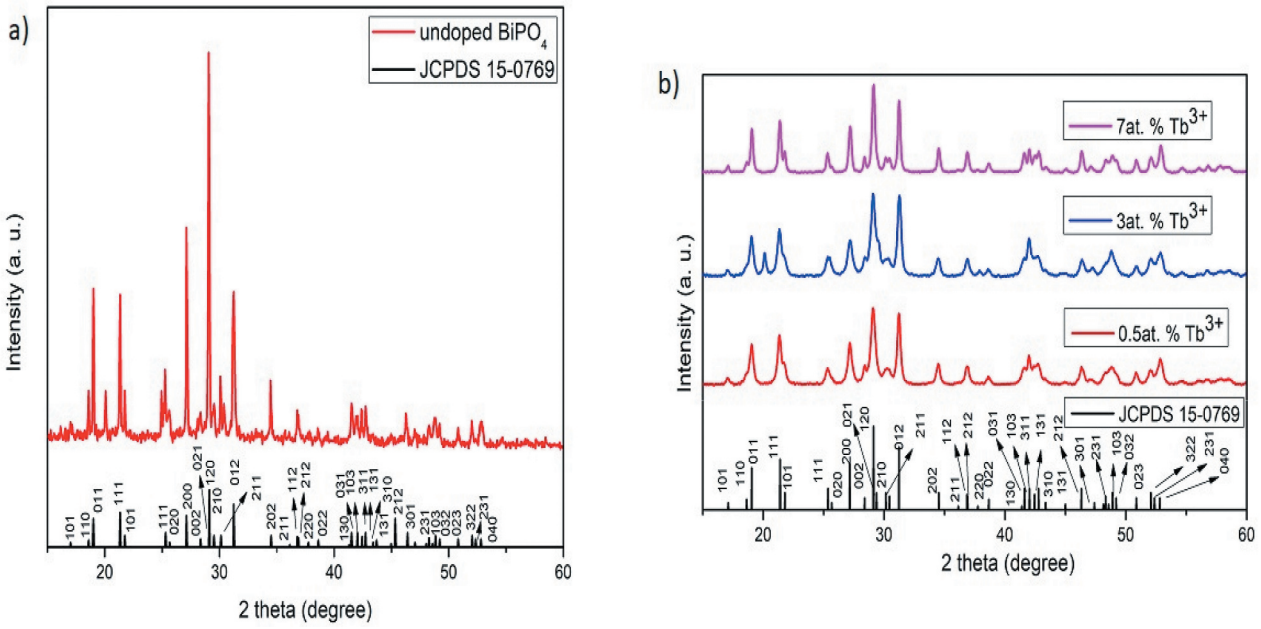

Figure 1. XRD patterns of the prepared a) undoped $BiPO_4$ b) $BiPO_4$:xTb^{3+} (x = 0.5, 3, 7at. %).

larger size Bi^{3+} (1.15 Å) with smaller size Tb^{3+} (1.01 Å) [26,27]. The calculated unit cell volume decreased with the increase in Tb^{3+} ion concentrations. From these above results it is indicated that the dopant Tb^{3+} ion has been successfully doped into the $BiPO_4$. The calculated lattice parameters, cell volume along with average crystallite size are provided in Table 1. The average crystallite size was calculated using Scherrer equation

$$D = 0.9\lambda/\beta\cos\theta$$

Where, D represents the crystallite diameter, λ is the incident x-ray wavelength which has a value of 1.5406 Å, β is the full width at half maximum and θ represents the angle of diffraction.

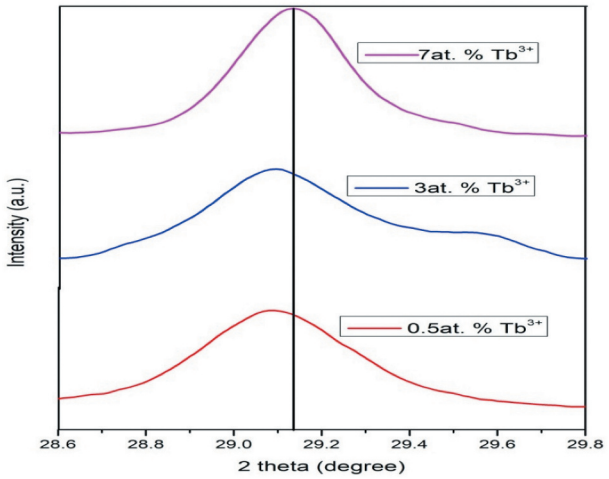

Figure 2. Expanded view of the diffraction peaks in the 2θ range from 28.6 to 29.8 of Figure 1(b) which shows the deflection of the peak with concentrations.

Table 1. Calculated lattice parameters, cell volumes and crystallite sizes of undoped $BiPO_4$ and Tb^{3+} ions doped $BiPO_4$.

Tb^{3+} ion doping concentrations (atomic percentage)	Lattice parameters			Cell volume (V) Å^3	Crystallite size (nm)
	a(Å)	b(Å)	c(Å)		
0	6.801	6.795	6.392	290.584	30.45
0.5	6.790	6.793	6.390	290.250	28.29
3	6.777	6.695	6.386	289.602	20.70
7	6.770	6.691	6.382	289.158	25.02

FT-IR spectroscopy and SEM study

Figure 3 shows the FT-IR spectrum of undoped $BiPO_4$ and $BiPO_4$:Tb^{3+} (3 at. %). The peaks centring at around 1570 and 3550 cm^{-1} are corresponded to the bending and stretching vibrations of adsorbed water molecules [28,29]. The peak observed at around 2360 cm^{-1} is ascribed to the ν3 anti-symmetric stretching mode of CO_2 molecule adsorbed from the atmosphere [30]. The bands observed in the range of 400 cm^{-1} and 1000 cm^{-1} are the characteristic bands of PO_4^{3-}. The bands observed at 937, 960 and 991 cm^{-1} are ascribed to the stretching symmetric vibrations (ν1) of O-P-O linkage whereas the bands observed at 545, 561, and 607 cm^{-1} are attributed to the bending vibrations of O-P-O linkage [28,31]. These observed bands are the characteristic bands of PO_4^{3-} group in monoclinic structure. So the formation of monoclinic structure in the sample was supported by this FTIR study. No significant change in the FT-IR spectra of undoped $BiPO_4$ and $BiPO_4$:Tb^{3+} (3 at. %) was observed, this may be due to very low doping concentration of Tb^{3+}. The field emission scanning electron microscopic image is used to examine the morphology of samples. The FESEM image of the synthesised

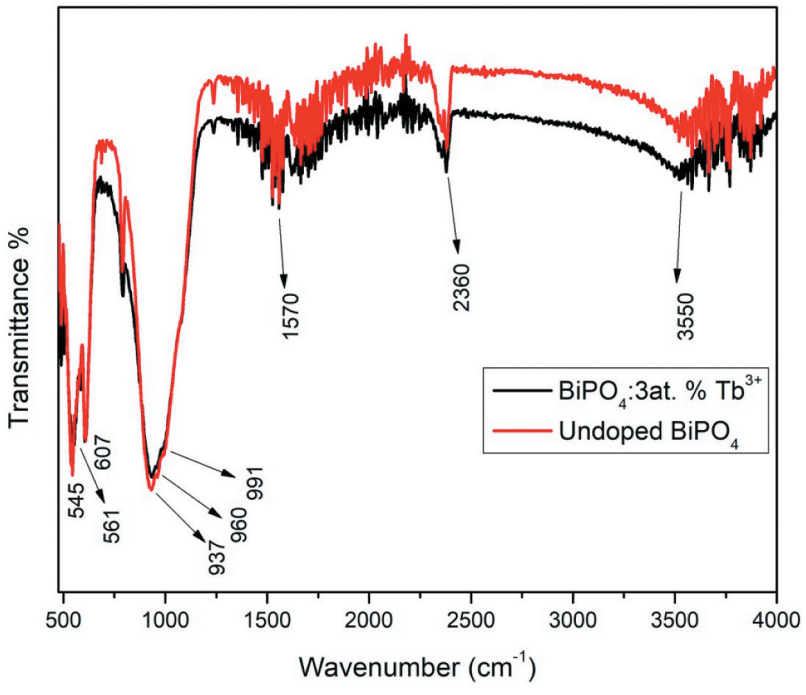

Figure 3. FT-IR spectrum of undoped $BiPO_4$ and $BiPO_4$: Tb^{3+} (3at. %).

$BiPO_4$:Tb^{3+} (3at. %) is shown in Figure 4. It is seen that there is no clear shape observed and the particles exist as agglomeration.

Photoluminescence study

The photoluminescence excitation spectra are shown in Figure 5. The spectra were measured with the emission wavelength of 544 nm. The spectra consist of a broad band at 285 nm originated from the $^1S_0 \rightarrow {}^1P_1$ electronic transition of Bi^{3+} ion [32] and sharp bands due to the electronic transitions within the 4f energy levels of doping Tb^{3+} ion. These sharp bands are observed at 377, 369, 351, 340 and 318 nm and they can be ascribed to the 4f electronic transitions such as $^7F_6 \rightarrow {}^5G_6$, $^7F_6 \rightarrow {}^5L_{10}$, $^7F_6 \rightarrow {}^5L_9$, $^7F_6 \rightarrow {}^5L_8$ and $^7F_6 \rightarrow {}^5H_7$ of Tb^{3+} ion respectively [33,34]. Bi^{3+} can also have an electronic transition, i.e., $^1S_0 \rightarrow {}^1P_3$ at 351 nm [35]. Hence the peak observed at 351 nm may be attributed to the overlapping of $^1S_0 \rightarrow {}^1P_3$ transition with f-f transition of Tb^{3+} ion. As the peak due to $^7F_6 \rightarrow {}^5L_9$ transition is stronger than the other excitation peaks, the emission spectra of all the samples were measured with the excitation wavelength of 351 nm. Figure 6 shows the emission spectra of $BiPO_4$ nanophosphors doped with different concentrations of Tb^{3+} ion. The spectra consist of a broad band with maximum at 419 nm and four sharp peaks centring at 488, 544, 582 and 620 nm, this broad band at 419 nm is due to the electronic transition from $^3P_1$ to $^1S_0$ of Bi^{3+} ion [35,36] and the sharp peaks are attributed to the $^5D_4 \rightarrow {}^7F_6$, $^5D_4 \rightarrow {}^7F_5$, $^5D_4 \rightarrow {}^7F_4$ and $^5D_4 \rightarrow {}^7F_3$ transitions of Tb^{3+} ion respectively [37,38]. It is also known that Bi^{3+} ion exhibited emission band in the wavelength range between 450 and 650 nm [39,40]. Therefore the emission band observed from 450 to 650 nm may be due to the overlapping of emissions from Tb^{3+} ion and Bi^{3+} ion. With increased of Tb^{3+} ion-doping concentration, the emission band at 419 nm originated from Bi^{3+} ion is found attenuated and the emission band at 544 nm originated from Tb^{3+} ion was found increased. This indicates the transfer of energy from Bi^{3+} ion to Tb^{3+} ion [41]. Further, the emission intensity is attenuated beyond 3at. % of Tb^{3+} ion-doping concentration, it is due to the concentration quenching effect. So, the optimum concentration of Tb^{3+} is found to be 3 at. %. Due to the increase in the concentration of Tb^{3+} ion, the inter-ionic distance between the Tb^{3+} ions decreased. When the distance is lower than its critical distance non-radiative energy transfer among the doped Tb^{3+} takes place which leads to attenuation of emission intensity [42].

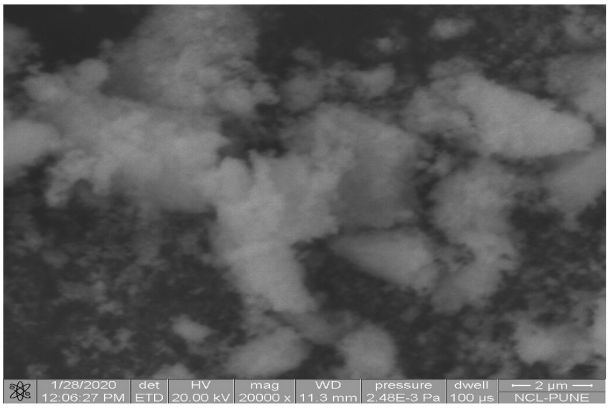

Figure 4. FESEM image of $BiPO_4$: Tb^{3+} (3at. %).

Lifetime study

The luminescence decay curves of the prepared Tb^{3+} ion-doped $BiPO_4$ nanophosphors have been

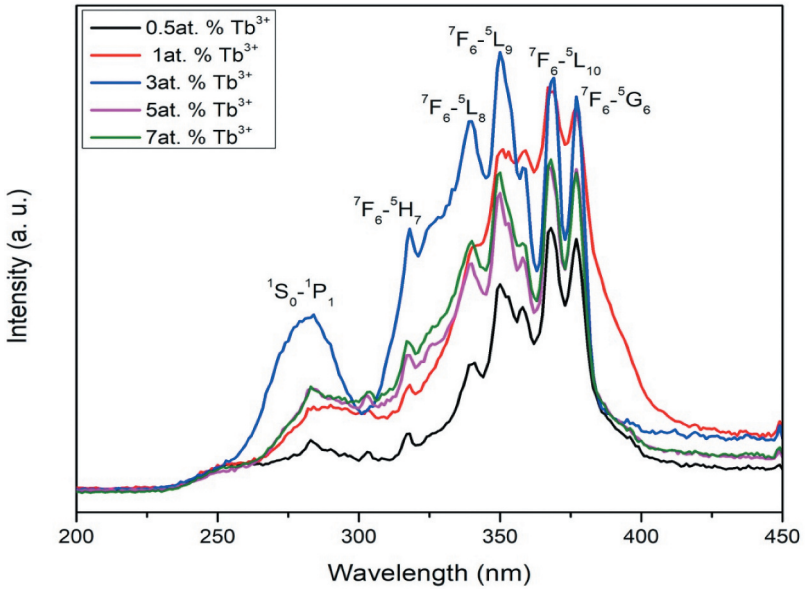

Figure 5. PLE spectrum of $BiPO_4$:x Tb^{3+} (x = 0.5,1,3,5,7at. %) (λ_{emi} = 544 nm).

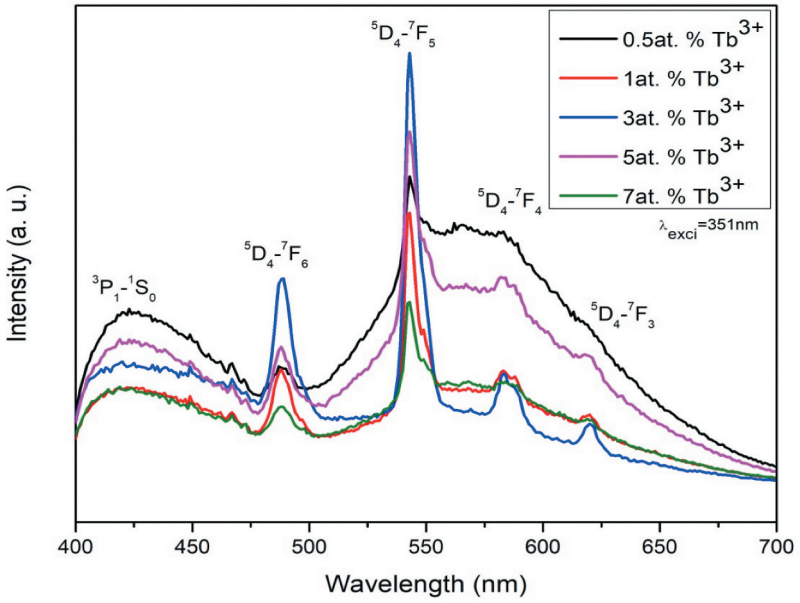

Figure 6. PL spectra of $BiPO_4$:xTb^{3+}, (λ_{exci} = 351 nm) (x = 0.5,1,3,5,7at. %).

evaluated. The decay curves were measured by fixing the excitation and emission wavelengths at 351 and 544 nm respectively for all the concentrations. The measured decay curves are shown in Figure 7. All the observed decay curves are well fitted by using bi-exponential equation [43].

$$I = I_1\exp(-t/\tau_1) + I_2\exp(-t/\tau_2)$$

Here I_1 and I_2 represent the intensities at two different time intervals and τ_1 and τ_2 represent their corresponding decay times. The decay behaviour for bi-exponential curve fitting of a phosphor lies on a) non-homogeneous distribution of dopant ions into the host lattice b) energy transfer from donor atom and c) defects present in the host and the presence of impurity [44]. The average decay time can be evaluated by using the following equation

$$\tau_{ave} = \left(I_1\tau_1^2 + I_2\tau_2^2\right)/(I_1\tau_1 + I_2\tau_2)$$

The calculated average lifetime for the Tb^{3+} concentrations of 0.5%, 1%, 3%, 5% and 7% are found to be 1.31, 1.49, 1.56, 1.76, and 1.83 ms respectively and their goodness of fitting (R^2) for the above concentrations is 0.99958, 0.99978, 0.99994, 0.99972 and 0.99969 respectively. These obtained lifetime values are in agreement with those reported in literatures

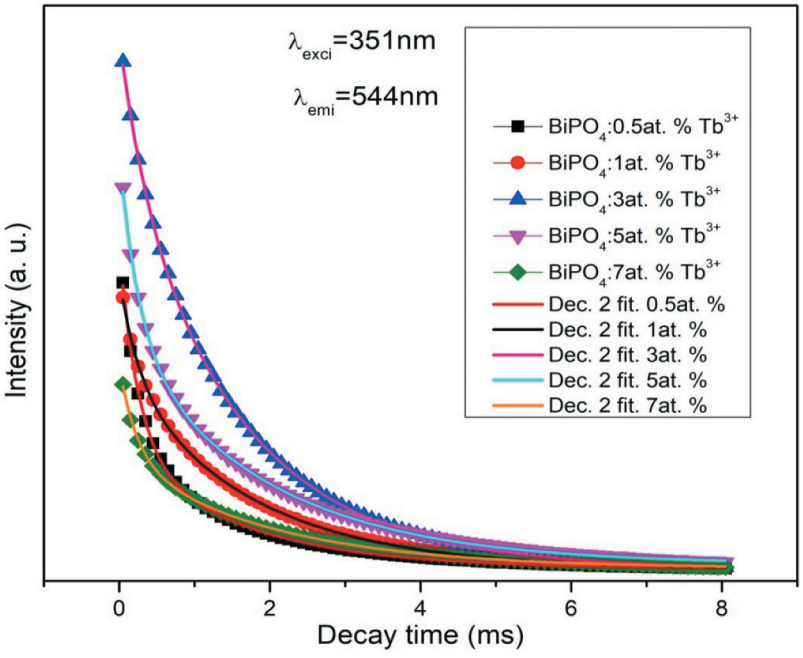

Figure 7. Photoluminescence decay curve of $BiPO_4$:Tb^{3+} with bi-exponential fitting.

Table 2. Parameters involved in the lifetime study.

Sample	y_0	I_1	τ_1	I_2	τ_2
0.5at. % Tb^{3+}	5446.102	148,804.387	1.59449	250,764.978	0.24823
1at. % Tb^{3+}	4920.868	118,326.036	0.24715	242,288.363	1.71372
3at. % Tb^{3+}	5364.018	512,514.805	1.56957	145,013.291	0.35325
5at. % Tb^{3+}	10,654.841	228,505.424	0.25884	279,435.395	1.93152
7at. % Tb^{3+}	5352.537	113,296.454	0.23191	137,220.138	1.98890

[13,17]. And the parameters involved in the lifetime study are listed in Table 2.

CIE study

The Commission International de L'Eclairage (CIE) chromaticity diagram reveals the coordinates are very useful in determining the perceived colour of the emission of a phosphor [45,46]. The calculated colour coordinates from the emission spectra and their corresponding co-related colour temperature are given in Table 3. The co-related colour temperatures (CCT) for Tb^{3+} ions doped $BiPO_4$ were calculated by using McCamy's equation [47,48]:

$$\begin{aligned} CCT &= -437n^3 + 3601n^2 - 6861n \\ &\quad + 5514.31 \text{ and } n \\ &= (x - x_e)/(y - y_e), \end{aligned}$$

Where x and y represent the calculated colour co-ordinates. The CIE chromaticity diagram for the prepared $BiPO_4$ doped with different concentrations of Tb^{3+} ion upon excitation at 351 nm is shown in Figure 8. This diagram showed that the prepared samples emit nearly white colour under excitation at 351 nm.

Conclusion

In conclusion, the monoclinic structure of Tb^{3+} doped $BiPO_4$ nanophosphors has been prepared successfully by co-precipitation method using ethylene glycol as reaction medium. Photoluminescence analysis revealed the typical emission spectra of Tb^{3+} with maximum emission intensity at 544 nm due to $^5D_4$-$^7F_5$ under excitation at 351 nm. The optimum concentration of Tb^{3+} was found to be at 3at. %. Beyond this concentration the emission intensity decreases as a result of concentration quenching effect. The lifetime decay of prepared $BiPO_4$:Tb^{3+} (3at. %) was found to be the maximum lifetime as compared to other prepared concentrations. From the CIE diagram it is observed that all the prepared nanophosphors emitted to nearly white colour. From these above results, it is believed that the prepared nanophosphors may have potential applications in the fields of solid state lighting, displays and other optical devices, etc.

Table 3. CIE chromaticity coordinates and CCT of the $BiPO_4$:Tb^{3+} nanophosphors upon excitations at 351 nm.

% of Tb^{3+} doped into $BiPO_4$ lattice	x	y	CCT
0.5	0.36	0.38	4601
1	0.32	0.36	6007
3	0.27	0.34	8886
5	0.35	0.38	4912
7	0.33	0.36	5596

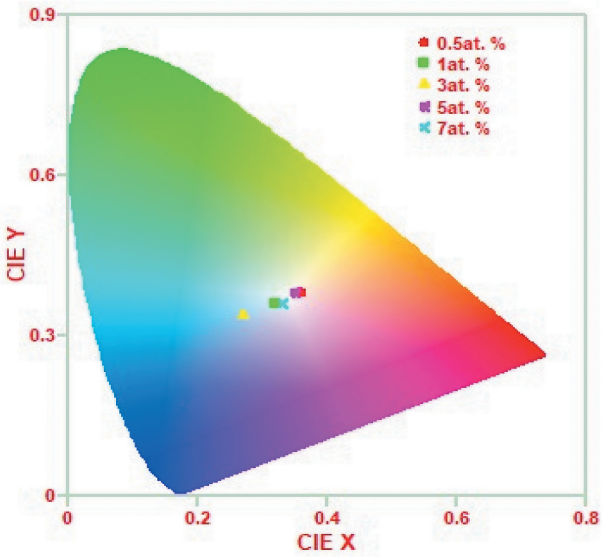

Figure 8. CIE chromaticity diagrams of the $BiPO_4$:xTb^{3+} nanophosphors. (x = 0.5, 1, 3, 5 and 7at. %).

Acknowledgments

The authors thank the Science and Engineering Research Board (SERB), New Delhi (Vide No. SB/EMEQ-336/2014 dated 04.02.2016) for financial support and NCL Pune for providing SEM facility.

Disclosure statement

No potential conflict of interest was reported by the authors.

ORCID

Ramananda Singh Naorem http://orcid.org/0000-0002-8206-9807
Nongmaithem Mohondas Singh http://orcid.org/0000-0001-6086-946X

References

[1] Guisbiers G, Rosales SM, Deepak FL. Nanomaterial properties: size and shape dependencies. J Nanomater. 2012;2012:Article ID 180976, 2.
[2] Hong NH. Introduction to nanomaterials: basic properties, synthesis, and characterization. Nano-Sized Multifunct Mater. 2019;1–19. DOI:10.1016/B978-0-12-813934-9.00001-3.
[3] Khan I, Saeed K, Khan I. Nanoparticles: properties, applications and toxicities. Arabian J Chem. 2017;12:908.
[4] Joshi PN, Mathias A, Mishra A. Synthesis of eco-friendly fluorescent carbon dots and their biomedical

and environmental applications. Mater Technol. 2018;33:10,672–680.
[5] Jia Z, Misra RDK. Tunable ZnO quantum dots for bioimaging: synthesis and photoluminescence. Mater Technol. 2013;28:221–227.
[6] Jayaprakash N, Suresh R, Rajalakshmi S, et al. One-step synthesis, characterisation, photocatalytic and bio-medical applications of ZnO nanoplates. Mater Technol. 2020;35:2,112–124.
[7] Depan D, Misra RDK. Structural and physico-chemical aspects of silica encapsulated ZnO quantum dots with high quantum yield and their natural uptake in hela cells. J Biomed Mater Res A. 2014;102:2934–2941.
[8] Venkatasubramanian R, Srivastava RS, Misra RDK. Comparative study of antimicrobial and photocatalytic activity in titania encapsulated composite nanoparticles with different dopants. Mater Sci Technol. 2013;24(5):589–595.
[9] Gao M, Zhang D, Pu X, et al. Combustion Synthesis and enhancement of BiOCl by doping Eu3+ for photodegradation of organic dye. J Am Ceram Soc. 2016;99(3):881–887.
[10] Naorem RS, Singh NP, Singh NM. Photoluminescence studies of Ce^{3+} ion-doped $BiPO_4$ phosphor and its photocatalytic activity. Int J Appl Ceram Technol. 2020;17:2744.
[11] Singh NP, Singh NR, Devi YR, et al. Effects of annealing temperature on structural and luminescence properties of $CdMoO_4$: dy^{3+}phosphor synthesized at room temperature by co-precipitation method. Solid State Sci. 2020;102:106172.
[12] Selvin PR. Principles and biophysical applications of lanthanide-based probes. Annu Rev Biophys Biomol Struct. 2002;31:275.
[13] Xu S, Li P, Wang Z, et al. Luminescence and energy transfer of Eu^{2+}/Tb^{3+}/Eu^{3+} in $LiBaBO_3$ phosphors with tunable-color emission. J Mater Chem C. 2015;3:9112.
[14] Shi X, Liu Y, Zhang J, et al. Effects of pH and Sm^{3+} doping on the structure, morphology and luminescence properties of BiPO4: sm^{3+}phosphors prepared by hydrothermal method. Ceram Int. 2015;14:3162.
[15] Hou J, Pan C, Chen X, et al. White-light-emitting from single-phased (Ca,Eu,Mn)9Al(PO4)7 phosphor with blue-white-yellow tunable luminescence properties for UV-based LEDs. Mater Technol. 2019;34:135.
[16] Roming M, Feldmann C. Synthesis and characterization of nanoscaled $BiPO_4$ and $BiPO_4$: tbJ. Mater Sci. 2009;44:1412.
[17] Naidu BS, Vishwanadh B, Sudarsan V, et al. BiPO4: a better host for doping lanthanide ions. Dalton Trans. 2012;41:3194.
[18] Charyulu M, Chetty KV, Phal D, et al. Recovery of americium from nitric acid solutions containing calcium by different co-precipitation methods. J Radioanal Nucl Chem. 2002;251:153.
[19] Zhang D, Su C, Yao S, et al. Facile in situ chemical transformation synthesis, boosted charge separation, and increased photocatalytic activity of BiPO4/BiOCl p-n heterojunction photocatalysts under simulated sunlight irradiation. J Phys Chem Solids. 2020;147:109630.
[20] Xia C, Yu C, Cao M, et al. A Eu and Tb Co-Doped MOF-5 compound for ratiometric high temperature sensing. Ceram Int. 2018;44(17):21040–21046.
[21] Xia C, Xua Y, Cao M. A selective and sensitive fluorescent probe for bilirubin in human serum based on europium(III) post-functionalized Zr(IV)-Based MOFs. Talanta. 2020;212:120795.
[22] Cybinska J, Lorbeer C, Mudring AV. Ionic liquid assisted microwave synthesis route towards color-tunable luminescence of lanthanide- doped $BiPO_4$. J Lumin. 2016;170:641.
[23] Huang M, Xu Z, Hou C, et al. Facile synthesis of colloidal photoluminescent $BiPO_4$: ln(Eu,Tb) nanoparticles well-dispersed in polar solvents. Cryst Eng Comm. 2019;21:278.
[24] Guan M, Sun J, Tao F, et al. A host crystal for the rare-earth ion dopants: synthesis of pure and Ln-doped urchinlike $BiPO_4$ structure and its photoluminescence. Cryst Growth Des. 2008;8:2694.
[25] Gao M, Zhang D, Pu X, et al. Surface decoration of BiOBr with BiPO4 nanoparticles to build heterostructure photocatalysts with enhanced visible-light photocatalytic activity. Sep Purif Technol. 2016;170:183–189.
[26] Li P, Guo L, Liang C, et al. Enhanced dual-wavelength sensitive upconversion luminescence of $BiPO_4$: yb^{3+}/Er^{3+}phosphors by Sc^{3+} doping. Mater Sci Eng B-Adv. 2018;229:20.
[27] Singh NP, Singh NR, Singh NR, et al. Effect of doping ion concentration on the photoluminescence behavior of $CdWO_4$: tb^{3+}phosphor synthesized via co-precipitation method. Indian J Phys. 2018;92:1461.
[28] Xue F, Li H, Zhu Y, et al. Solvothermal synthesis and photoluminescence properties of BiPO4 nano-cocoons and nanorods with different phases. J Solid State Chem. 2009;182:1396.
[29] Singh NP, Devi YR, Singh NR, et al. Synthesis of Tb^{3+} ion doped $ZnWO_4$ phosphors and investigation of their photoluminescence properties: concentration effect. Bull Mater Sci. 2019;42:96.
[30] Iskra A, Gentleman AS, Kartouzian A, et al. Infrared spectroscopy of gas-phase $M^{+}(CO_2)_n$ (M = Co, Rh, Ir) ion-molecule complexes. J Phys Chem A. 2017;121:133.
[31] Pawlig O, Schellenschlager V, Lutz HD, et al. Vibrational analysis of iron and zinc phosphate conversion coating constituents. Spectrochim Acta A. 2001;57:581.
[32] Li L, Pan Y, Chen Z, et al. Tunable luminescence and energy transfer properties of Bi^{3+} and Mn^{4+} co-doped $Ca_{14}Al_{10}Zn_6O_{35}$ phosphors for agricultural applications. RSC Adv. 2017;7:14868.
[33] S Q Y. Synthesis and luminescence of $BiPO_4$: tb^{3+}nanowires by a hydrothermal process. Mater Manuf Process. 2015;30:591.
[34] Lakshminarayana G, Dao TD, Chen K, et al. Effect of different surfactants on structural and optical properties of Ce^{3+} and Tb^{3+} co-doped $BiPO_4$ nanostructures. Opt Mater. 2015;39:110.
[35] Kaur G, Kumar B, Verma RK, et al. Bismuth induced enhanced green emission from terbium ions and their complex in thin films. Dalton Trans. 2014;43:11014.
[36] Lee E, Terblans JJ, Swart HC. The effect of pH on the luminescence properties of Y_2O_3: biphosphor powders synthesised using co-precipitation. Vacuum. 2018;157:237.

[37] Yang Y, Liu B, Zhang Y, et al. Fabrication and luminescence of $BiPO_4$: tb^{3+}/Ce^{3+}nanofibers by electrospinning. Superlattices Microstruct. 2016;90:227.
[38] Gayatri SK, Singh NR. Re-dispersible CaWO4: tb3 +nanoparticles: synthesis, characterization, and photoluminescence studies. J Lumin. 2013;139:98.
[39] Scarangella A, Reitano R, Priolo F, et al. Bismuth doping of silicon compatible thin films for telecommunications and visible light emitting devices. Mater Sci Semicond Process. 2019;92:47.
[40] Pan L, Koehler K, Jacobsohn LG. Luminescence of undoped and Ce-doped hexagonal $BiPO_4$. J Lumin. 2020;228:117626.
[41] Yaba T, Wangkhem R, Singh NS. Enhanced red emission from Bi^{3+} sensitized CaWO4: eu^{3+}as red component for near UV/blue LED pumped white light emission. J Alloys Compd. 2020;843:156022.
[42] Chen M, Xia Z, Liu Q. Luminescence properties and energy transfer of Ce^{3+}/Tb^{3+} co-doped $Ca_6Ba(PO_4)_4$ O phosphor for near-UV pumped light-emitting diodes. J Mater Chem C. 2015;3:4197.
[43] Devi CV, Phaomei G, Yaiphaba N, et al. Luminescence behavior of YVO4: dy^{3+}phosphors with enhanced photoluminescence on co-doping Bi^{3+} ions. J Alloys Compd. 2014;583:259.
[44] Sharma KG, Singh NR. Synthesis and luminescence properties of $CaMO_4$: dy^{3+}(M = W, Mo) nanoparticles prepared *via* an ethylene glycol route. New J Chem. 2013;37:2784.
[45] Singh NP, Singh NR, Singh NM. Synthesis of $CdMoO_4$: sm^{3+}phosphors at room temperature and investigation on photoluminescence properties. Optik. 2018;156:365.
[46] Sharma KG, Singh TP, Singh NR. Low temperature synthesis, characterization and tunable optical properties of Eu^{3+}, Tb^{3+} doped $CaMoO_4$ nanoparticles. J Alloys Comp. 2014;602:275.
[47] Du P, Wu S, Yu JS. Synthesis, electronic structure and luminescence properties of color-controllable Dy^{3+}/Eu^{3+}-codoped $CaWO_4$ phosphors. J Lumin. 2016;173:192.
[48] Ryadun A, Rakhmanova M, Grigorieva V. Effect of Cu doping on properties of PbMoO4 single crystals as materials for luminescence thermometry. Mater Technol. 2020.

Publications

1. **Ramananda Singh Naorem**, N. Premjit Singh and N. Mohondas Singh, Photoluminescence properties of Tb^{3+} doped $BiPO^4$ nanophosphor synthesised by co-precipitation method using ethylene glycol, *Materials Technology* (2021), https://doi.org/10.1080/10667857.2020.1866919; ISSN:1066-7857 [IF:3.846] [Taylor & Francis] *First Online Published 27.12.2020.*

2. **Ramananda Singh Naorem**, N. Premjit Singh and N. Mohondas Singh, Photoluminescence studies of Ce^{3+} ion doped $BiPO_4$ phosphor and its photocatalytic activity, *Int J of Appl Ceram Technol*, (2020), 17:27, 2744-2751. https://doi.org/10.1111/ijac.13600. ISSN: 1744-7402 (WILEY-VCH) [IF:1.968]

3. N. Premjit Singh, **N. Ramananda Singh**, Y. Rangeela Devi, Brojendro Singh Sh, Th. David Singh, N. Rajmuhon Singh, N. Mohondas Singh. Effects of annealing temperature on structural and luminescence properties of CdMoO4:Dy^{3+} phosphor synthesized at room temperature by co-precipitation method. *Solid State Sciences* (2020), 102, 106172, 1-7; IF: 3.059 [Elsevier].

4. N. Premjit Singh, **N. Ramananda Singh**, N. Rajmuhon Singh, N. Mohondas Singh. Effect of doping ion concentration on the photoluminescence behavior of $CdWO_4$:Tb^{3+} phosphor synthesized via co-precipitation method, *Indian J Phys*; DOI: 10.1007/s12648-018-1219-z, 92(11) 1461-1466 (2018), ISSN: 0974-9845.IF:1.947 [Springer]

5. **Ramananda Singh Naorem**, N. Premjit Singh and N. Mohondas Singh, Calculation of Energy Parameters for Interactions of Nd(III) and Pr(III) with DL-Serine by using their Absorption Spectra as a Probe in The Presence and Absence of Zn(II) in Different Solvents, ISSN: 0036-0244, *Russian Journal of Physical Chemistry A* (2020), 94:13, 154-158, [IF: 0.691][Springer].

6. **N. Ramananda Singh**, N. Premjit Singh and N. Mohondas Singh. 4f–4f Spectral Analysis and Solvent Effect for the Interaction of Pr(III) with l-Tryptophan Using Different Aquated Solvents in the Presence and Absence of Zn(II). *Chemistry Africa* (2020) 3:171-180. ISSN: 2522-5758 (Print) 2522-5766 (Online). [Springer].

Seminars/conferences presented

1. Presented a paper entitled *Photoluminescence studies of Tb^{3+} ion doped $BiPO_4$ phosphor: concentration effect* in the national conference on "New Trends in Nanotechnology and Applications (NTNA-2020)" organized by Atma Ram Sanatan Dharma College, DU during **February 6-7, 2020.**

2. Presented a paper entitled *Photoluminescence property of Ce^{3+} doped $BiPO_4$ phosphor: concentration effect* in "International Conference on Materials Science (ICMS-2020)" organized by Department of Physics, Tripura University during **March 4-6, 2020.**

3. Presented one paper in *Photoluminescence investigation Tb^{3+} ion doped $BiPO_4$ nanophosphor synthesized by using ethylene glycol* in "International Seminar on Recent Advances in Science and Technology (ISRAST-2020)" organized by Mizoram University during **November 16-18, 2020**

4. Presented a paper entitled *Solvothermal synthesis of SnS_2photocatalyst for organic dye degradation under solar light irradiation* in the Mizoram Science Congress 2018, a National Conference, held at Pachhunga University College during **4-5th October, 2018**.

5. Presented a paper entitled *Solvent Effect on the Photocatalytic Property of SnS_2 for Organic Dye Degradation Under Solar Light Irradiation*in the International Conference on Chemistry & Environmental Sustainability (ICCES-2019) organized by Department of Chemistry, Mizoram University during **February 19-22, 2019.**

BIO-DATA

1. NAME : Naorem Ramananda Singh

2. DATE OF BIRTH : 1st February 1992

3. FATHER'S NAME **:**(L) Naorem Shyamchandra Singh

4. PERMANENT ADDRESS **:**Kakching Wairi Thongam Leikai, Kakching, Manipur-795103

5. EMAIL ADDRESS **:** rmnda.nao@gmail.com

5. EDUCATIONAL QUALIFICATIONS

Examination passed	Year of Passing	Board/ University	Roll No.	Class/ Division	% of Marks	Subjects
High School Leaving Certificate Examination	2007	Board of Secondary Education, Manipur	4791	I	61	Maths, Eng, Sci, S. sci, MAN, Higher Maths
Higher Secondary School Leaving Certificate Examination	2009	Council of Higher Secondary Education, Manipur	8879	I	63	Chem, Phy, Maths, Biolg, Eng, MAN
B. Sc.	2012	Delhi University	6000862	II	58.51	Chem(spl), Phy, Maths, Eng, Computer
M.Sc	2015	ManipurUniversity	1315026	I	71.15	Org.Chem(spl), Ing. chem, Phy. chem, Computer

Work Experience:

Worked as Project Assistant, for 4 years, for the Project entitled SERB-DST-sponsored project entitled ***"Absorption Spectral Analysis and Kinetics Study of 4f-4f Transition for the Complexation of Pr(III)/Nd(III) with the Biologically Important Ligands"*** [Vide Sanctioned order no. SB/EMEQ-336/2014 dated 04.02.2016] from April 2016 to March 2020.

Publications:

1. **Ramananda Singh Naorem**, N. Premjit Singh and N. Mohondas Singh, Photoluminescence properties of Tb^{3+} doped $BiPO^4$ nanophosphor synthesised by co-precipitation method using ethylene glycol, *Materials Technology* (2021), https://doi.org/10.1080/10667857.2020.1866919; ISSN:1066-7857 [IF:1.738] [Taylor & Francis] *First Online Published 27.12.2020*.

2. **Ramananda Singh Naorem**, N. Premjit Singh and N. Mohondas Singh, Photoluminescence studies of Ce^{3+} ion doped $BiPO_4$ phosphor and its photocatalytic activity, *Int J of Appl Ceram Technol*, (2020), 17:27, 2744-2751. ISSN: 1744-7402 (WILEY-VCH) [IF:1.762]

3. N. Premjit Singh, **N. Ramananda Singh**, Y. Rangeela Devi, Brojendro Singh Sh, Th. David Singh, N. Rajmuhon Singh, N. Mohondas Singh. Effects of annealing temperature on structural and luminescence properties of CdMoO4:Dy^{3+} phosphor synthesized at room temperature by co-precipitation method. *Solid State Sciences* (2020), 102, 106172, 1-7; IF: 2.434 [Elsevier].

4. N. Premjit Singh, **N. Ramananda Singh**, N. Rajmuhon Singh, N. Mohondas Singh. Effect of doping ion concentration on the photoluminescence behavior of $CdWO_4$:Tb^{3+} phosphor synthesized via co-precipitation method, *Indian J Phys*; DOI: 10.1007/s12648-018-1219-z, 92(11) 1461-1466 (2018), ISSN: 0974-9845.IF:1.407[Springer]

5. **Ramananda Singh Naorem**, N. Premjit Singh and N. Mohondas Singh, Calculation of Energy Parameters for Interactions of Nd(III) and Pr(III) with DL-Serine by using their Absorption Spectra as a Probe in The Presence and Absence of Zn(II) in Different Solvents, ISSN: 0036-0244, *Russian Journal of Physical Chemistry A* (2020), 94:13, 154-158, [IF: 0.719][Springer].

6. **Ramananda Singh Naorem**, N. Premjit Singh and N. Mohondas Singh. 4f–4f Spectral Analysis and Solvent Effect for the Interaction of Pr(III) with l-Tryptophan Using Different Aquated Solvents in the Presence and Absence of Zn(II). *Chemistry Africa* (2020) 3:171-180. ISSN: 2522-5758 (Print) 2522-5766 (Online). [Springer].

Seminars/conferences presented

1. Presented a paper entitled *Photoluminescence studies of Tb^{3+} ion doped $BiPO_4$ phosphor: concentration effect* in the national conference on "New Trends in Nanotechnology and Applications (NTNA-2020)"organized by Atma Ram Sanatan Dharma College, DU during **February 6-7, 2020.**

2. Presented a paper entitled *Photoluminescence property of Ce^{3+} doped $BiPO_4$ phosphor: concentration effect* in "International Conference on Materials Science (ICMS-2020)"organized by Department of Physics, Tripura University during **March 4-6, 2020.**

3. Presented one paper in *Photoluminescence investigation Tb^{3+} ion doped $BiPO_4$ nanophosphor synthesized by using ethylene glycol* in "International Seminar on Recent Advances in Science and Technology (ISRAST-2020)"organized byMizoram University during **November 16-18, 2020**

4. Presented a paper entitled *Solvothermal synthesis of SnS_2photocatalyst for organic dye degradation under solar light irradiation* in the Mizoram Science Congress 2018, a National Conference, held at Pachhunga University College during **4-5th October, 2018**.

5. Presented a paper entitled *Solvent Effect on the Photocatalytic Property of SnS_2 for Organic Dye Degradation Under Solar Light Irradiation*in the International Conference on Chemistry & Environmental Sustainability (ICCES-2019) organized by Department of Chemistry, Mizoram University during **February 19-22, 2019.**

PARTICULARS OF THE CANDIDATE

NAME OF CANDIDATE	:	Naorem Ramananda Singh
DEGREE	:	Doctor of Philosophy (Ph.D)
DEPARTMENT	:	Chemistry
TITLE OF THESIS:		Synthesis, Characterization and Photoluminescence Properties of Rare Earth Ions Doped $BiPO_4$ Phosphors
DATE OF ADMISSION	:	12th August, 2016

APPROVAL OF RESEARCH PROPOSAL:

1. BOS	:	2nd May, 2017
2. SCHOOL BOARD	:	15th May, 2017
MZU REGN. NO.	:	1600780
Ph.D REGN. NO. & DATE	:	MZU/Ph.D/1005 of 15.05.2017
EXTENSION	:	NIL

Head

Department of Chemistry

ABSTRACT

SYNTHESIS, CHARACTERIZATION AND PHOTOLUMINESCENCE PROPERTIES OF RARE EARTH IONS DOPED $BiPO_4$ PHOSPHORS

A THESIS SUBMITTED IN PARTIAL FULFILLMENT OF THE REQUIREMENTS FOR THE DEGREE OF DOCTOR OF PHILOSOPHY

NAOREM RAMANANDA SINGH
MZU REGISTRATION NO.: 1600780
Ph.D REGISTRATION NO.: MZU/Ph.D/1005 of 15.05.2017

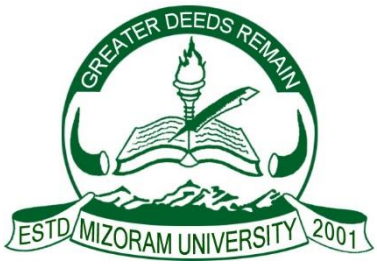

DEPARTMENT OF CHEMISTRY
SCHOOL OF PHYSICAL SCIENCES
MARCH, 2021

The lanthanide are the elements that follow lanthanum in the periodic table. Lanthanides elements are also known as f block elements due to their gradual filling of electron in the antepenultimate shell of f-orbital except lanthanum. The most stable oxidation state of lanthanides ions is +3, but Tb and Ce sometimes show +4 oxidation state. Similarly, Eu and Sm show +2 oxidation state as well. The +2 oxidation state of Eu and Sm are also stable due to their high value of the third ionization energy as compared to the rest of the lanthanides and the stability of +4 oxidation state in Tb and Ce can be explained from their electronic structure. One of the most interesting features of lanthanide ions is their photoluminescence properties. Since the 4f orbital in lanthanides is strongly shielded by the 5s and 5p electrons, their optical properties such as absorption and emission are usually narrow and sharp, which leads to the production of high color purity of the emitted light. Some of the lanthanide ions show luminescence in the visible regions while some others showed luminescence near-infrared spectral region upon UV light excitation such as Tb^{3+} emits in green region, Eu^{3+} in the red region, Tm^{3+} emits blue light and Sm^{3+} in pink or yellow orange region. Yb^{3+}, Er^{3+} and Nd^{3+} are very well known ions that emit in near-infrared region. Some other lanthanide ions such as Sm^{3+}, Pr^{3+}, Dy^{3+}, Tm^{3+} and Ho^{3+} also found transition in near-infrared region. They have potential applications in the fields such as fluorescent lamp phosphors, organic light emitting diodes, optical fibres for telecommunications, contrast agents for magnetic resonance imaging, biological assays. Those lanthanide ions which showed emission near the infrared region are useful for laser applications**,** telecommunication and optical amplifiers.

Lanthanide ions doped materials have drawn particular attention for luminescence properties since they are applicable in laser materials, flat panel displays, cathode ray tube etc. But the optical efficiency of lanthanide ions doped materials is limited by the dynamics of lanthanide ions. The dynamics of dopant lanthanide ions hang on its interaction with the host materials. On the other hand, $BiPO_4$ is considered as one of the best host for lanthanide ion doping owing to their several attractive properties

such as high chemical and mechanical stability, high adsorption edge and similarity in their ionic sizes with the lanthanide ions. Moreover, it has various applications like solid-state lighting, supercapacitor, biomedical, photocatalyst etc. $BiPO_4$ crystallized in three different crystallographic forms namely hexagonal, low-temperature monoclinic and high-temperature monoclinic phases. Normally the hexagonal phase of $BiPO_4$ is obtained at low temperature below whereas low-temperature monoclinic phase and high-temperature monoclinic phase are obtained at higher temperature. Hexagonal and monoclinic phases differ in their co-ordination number of Bi^{3+} ion. Bi^{3+} ions in hexagonal phase are being surrounded by eight oxygen atoms forming square anti-prism geometry while the Bi^{3+} ions in monoclinic phase are co-ordinated by nine oxygen atoms similar with monazite structure of lanthanide phosphate. Therefore, investigation on the photoluminescence properties of lanthanide ions doped $BiPO_4$ is very exciting.

In this research, $BiPO_4:Ln^{3+}$ (Ln=Ce, Tb, Eu, Sm) were synthesized using co-precipitation method and the prepared $BiPO_4:Ln^{3+}$ phosphors were characterized by using XRD, FT-IR, UV-Vis spectroscopy, SEM, TEM EDAX, SAED and PL techniques. The photoluminescence properties of various lanthanide ions doped in $BiPO_4$ were also investigated.

Chapter 1

In this chapter, the general introduction of lanthanides and photoluminescence were reported. The types of different luminescence were listed out in details. The spectroscopic properties, as well as applications of lanthanide ions were also discussed. Different processes which are responsible for quenching of luminescence were also mentioned briefly. The reviews of literatures as well as scope of studies were reported. Researches on the development of lanthanide ions doped $BiPO_4$ in last few decades were reviewed.

Chapter 2

Characterization of the synthesized materials is an important step required to discover the properties of the materials using the required instruments. This chapter discussed in detail about the various instrumentation techniques which were used in our research such as XRD, FT-IR, TEM, SEM, EDAX and Photoluminescence. Materials are characterized in order to find out the properties which they possess. The properties of a material depend on the morphology and size, these can be observed by recording TEM or SEM. Likewise, the property which indeed depending on the crystallinity of the materials can be perceived using XRD analysis.

Chapter 3

The synthesis of Ce^{3+} ion doped $BiPO_4$ phosphors by co-precipitation method using ethylene glycol as capping agent was reported in this chapter. The morphology, phase structure and photoluminescence properties of Ce^{3+} ion doped $BiPO_4$ phosphors were also discussed. The formation of monoclinic phase was confirmed from XRD and FT-IR studies. SEM study revealed the rice shape morphology of $BiPO_4$:Ce^{3+} (7at.%). Photoluminescence analysis showed a broad emission band extending in a wide wavelengths range with maxima around 419 and 470 nm was observed under excitation at 370 and 417 nm, respectively. These emission bands are attributed to $5d \rightarrow {}^2F_{5/2}$, ${}^2F_{7/2}$ transitions of Ce^{3+} ion. The emission intensity was accentuated with the increase of Ce^{3+} ion till 7at.% and subsequently attenuated with further increase of Ce^{3+} ion concentration due to the concentration quenching effect. Hence, the optimum concentration of Ce^{3+} ion doping was found to be 7at. %. The $BiPO_4$:Ce^{3+} (7at.%) sample was characterized for the feasibility of photocatalytic degradation of methylene blue under UV light irradiation and 90% of the dye was degraded within 120 minutes.

Chapter 4

This chapter reports the synthesis, characterization and photoluminescence behavior of Tb^{3+} ions doped $BiPO_4$ phosphors synthesized by co-precipitation method using ethylene glycol as reaction medium. The effect of annealing temperature on the photoluminescence property was also repoted. The formation of low-temperature monoclinic phase was confirmed from XRD and FT-IR studies. From XRD study, change of phase structure from low-temperature monoclinic phase to high-temperature monoclinic phase was observed upon annealing at 1000^oC. SEM image showed agglomeration of nanoparticles. TEM image revealed the formation of hexagonal shape morphology with particle size in the range of 8-20nm. In the photoluminescence study, the emission spectra showed four emission peaks centering at 488nm, 544nm, 582nm and 620nm under excitation at 351nm. These emission peaks were resulted due to $^5D_4 \rightarrow {}^7F_6$, $^5D_4 \rightarrow {}^7F_5$, $^5D_4 \rightarrow {}^7F_4$ and $^5D_4 \rightarrow {}^7F_3$ transitions of Tb^{3+} respectively. The emission intensity was accentuated with the increase of Tb^{3+} ion till 3at. % and subsequently attenuated with further increase of Tb^{3+} ion concentration; which is due to the concentration quenching effect. For annealed samples, the emission peaks profiles were observed same except their emission peak intensities. The emission peaks intensities were found increased with increased of annealing temperature upto 800^oC, then decreased when the annealing temperature reached 1000^oC due to change of phase structure from low-temperature monoclinic phase to high-temperature monoclinic phase. The decay lifetime of the prepared samples were also investigated and found 1.8346 ms as the maximum lifetime.

Chapter 5

This chapter described the synthesis characterization and photoluminescence properties of hexagonal phase of Eu^{3+} doped $BiPO_4$ nanophosphors. XRD study showed the change of phase structure from hexagonal to mixed phase of hexagonal and low-temperature monoclinic phases and later on to pure low-temperature monoclinic phase upon annealing at 500^oC and 800^oC respectively. TEM images revealed the hexagonal

shape morphology of the synthesized nanophosphors. Photoluminescence emission spectra showed the characteristic emission peak of Bi^{3+} at 420nm due to $^3P_1 \rightarrow {}^1S_0$ transition. The other emission peaks at 594nm with a shoulder peaking at 589nm, peaks at 614nm with a shoulder peaking at 618nm, 654nm and the emission band in the range of 687nm to 701nm are attributed to $^5D_0$-$^7F_1$, $^5D_0$-$^7F_2$, $^5D_0$-$^7F_3$, $^5D_0$-$^7F_4$ transitions of Eu^{3+} ion respectively. The optimum concentration of Eu^{3+} was found to be 8at. %. Further, the photoluminescence emission intensity increased with increased of annealing temperature upto 800^{o}C due to the change in their phase structure from hexagonal phase to pure low-temperature monoclinic phase. The effect of pH of the reaction medium on the photoluminescence property of Eu^{3+} doped $BiPO_4$ nanophosphors were discussed and emission intensity was found maximum at pH 7 but there occurred no change in their peaks profile. 0.5mM exhibited maximum emission intensity and the emission intensity decreased as CTAB concentration of the reaction medium increased due to the formation of agglomerated particles and larger particle size of the nanoparticles. The emission peaks profiles were the same only.

Chapter 6

This chapter discussed the synthesis characterization and photoluminescence properties of hexagonal phase of Sm^{3+} doped $BiPO_4$ nanophosphors. XRD study revealed the formation hexagonal phase of the prepared sample and the change of phase structure from hexagonal phase to low-temperature monoclinic phase was observed upon annealing at 800^{o}C. Change of morphology from rod shaped to spherical shape was noticed upon annealing at 800^{o}C and the sizes also found increased upon annealing. The characteristic emission peaks of Sm^{3+} were exhibited at 563nm, 598nm and 645nm which are attributed to $^4G_{5/2}$-$^6H_{5/2}$, $^4G_{5/2}$-$^6H_{7/2}$, $^4G_{5/2}$-$^6H_{9/2}$ transitions respectively. The optimum concentration of Sm3+ was found to be 5at. %. The emission intensity was found accentuated with increased of heating temperature which is due to the change of phase structure from hexagonal to low temperature monoclinic phase.